Dissertationsreihe am Institut für Hydromechanik
der Universität Karlsruhe (TH)
Heft 2006/1

Large Eddy Simulation of Turbulent Swirling Jets

Manuel García-Villalba Navaridas

universitätsverlag karlsruhe

Manuel García-Villalba Navaridas

Large Eddy Simulation of Turbulent Swirling Jets

Dissertationsreihe am Institut für Hydromechanik
der Universität Karlsruhe (TH)
Heft 2006/1

Large Eddy Simulation of Turbulent Swirling Jets

von
Manuel García-Villalba Navaridas

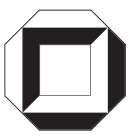

universitätsverlag karlsruhe

Dissertation, Universität Karlsruhe (TH), Fakultät für Maschinenbau, 2006

Impressum

Universitätsverlag Karlsruhe
c/o Universitätsbibliothek
Straße am Forum 2
D-76131 Karlsruhe
www.uvka.de

Universitätsverlag Karlsruhe 2006
Print on Demand

ISSN 1439-4111
ISBN 3-86644-015-4

Large Eddy Simulation of Turbulent Swirling Jets

Zur Erlangung des akademischen Grades eines

Doktors der Ingenieurwissenschaften

von der Fakultät für Maschinenbau

der Universität Karlsruhe

genehmigte

DISSERTATION

von

Manuel García-Villalba Navaridas

aus Spanien

Tag der mündlichen Prüfung: 16.02.06

Hauptreferent: Prof. Dr. U. Maas

Korreferenten: Prof. Dr. W. Rodi

Priv. Doz. Dr.-Ing. habil. J. Fröhlich

Karlsruhe 2006

A mi madre.

Abstract

Swirling annular and co-annular jets are widely used in combustion devices, such as gas turbine combustors, to stabilize the flame by means of a swirl-induced recirculation zone. Previous experimental and numerical studies have demonstrated, however, that such flows are prone to instabilities generating large-scale coherent vortical structures. They have a substantial impact on the mixing of scalar quantities such as fuel and oxidizer or hot and cold gas and hence on efficiency and security of the installation.

In this work large eddy simulations of unconfined annular and co-annular swirling jets are reported. The calculations are performed at high Reynolds number ($Re \sim 80000$) and high Swirl number ($S \sim 0.9$) matching realistic conditions. The simulations are validated by comparison with corresponding experiments. Very good agreement has been obtained for mean flow and turbulent fluctuations. Also, the low frequency range of the power spectral density of velocity fluctuations has been found to be in good agreement with the experiments.

For some of the cases, flow instabilities leading to large-scale coherent structures develop. Two complex shear layers are formed in the flow. An inner one on the boundary of the jet with the recirculation zone and an outer one on the boundary with the surrounding co-flow. Two families of large-scale helical coherent structures appear, an inner structure oriented quasi-streamwise and located in the inner shear layer and an outer structure oriented at a larger angle with respect to the longitudinal axis and situated in the outer shear layer. The Kelvin-Helmholtz instability has been identified as the major source for the generation of the coherent vortices.

In order to obtain further insight into the physics of the flows in question several parametric studies are performed. The level of swirl is varied over a wide range and different vortex systems are formed for each condition. The results of these investigations show that the inner shear layer is less stable than the outer one and the structures first appear in the inner shear layer. The modifications of the coherent structures in the presence of an oscillating flow rate are also investigated. It is found that with pulsation, vortex rings are dominant but the helical coherent structures remain present, especially in the case of pure axial oscillation.

Kurzfassung

Annulare und co-annulare Drallstrahlen werden oft bei Verbrennungsmaschinen wie z.B. von Gasturbinen eingesetzt, um die Flamme mit Hilfe einer drallerzeugten Rezirkulationszone zu stabilisieren. Bisherige experimentelle und numerische Untersuchungen haben jedoch gezeigt dass diese Strömungen zu Instabilitäten neigen, die großskalige kohärente Strukturen erzeugen. Sie bestimmen das Durchmischungsverhalten skalarer Größen wie Brennstoff und Oxidator oder von heißen und kalten Gasen, und damit Effizenz und Sicherheit der Anlage.

In der vorliegenden Arbeit wurden annulare und co-annulare Drallstrahlen mit Hilfe der Large-Eddy Simulation untersucht. Die Berechnungen wurden bei großen Reynoldszahlen ($Re \sim 80000$) und großen Drallzahlen ($S \sim 0.9$) durchgeführt, was realistischen Bedingungen entspricht. Die Simulationen wurden durch den Vergleich mit Experimenten validiert. Für die Statistiken des mittleren Strömungsfelds und die turbulenten Fluktuationen ergab sich dabei eine sehr gute Übereinstimmung. Ebenso wurde eine gute Übereinstimmung im niederfrequenten Bereich des Leistungsdichtespektrums der Geschwindigkeitsfluktuationen gefunden.

In manchen der untersuchten Fälle kam es aufgrund von Strömungsinstabilitäten zur Entwicklung kohärenter Strukturen. Zwei komplexe Scherschichten entstehen in dem Strömungsfeld: im inneren Bereich zwischen dem Freistrahl und der Rezirkulationszone sowie an der äußeren Grenze des Strahls. Es resultieren zwei Familien spiralförmiger kohärenter Strukturen : in der inneren Scherschicht sind diese nahezu in Hauptströmungsrichtung orientiert, in der äußeren Scherschicht bilden sie einen größeren Winkel mit der Axialkoordinate. Die Kelvin-Helmholtz Instabilität wurde als die maßgebende Ursache der Entstehung dieser kohärenten Strukturen identifiziert.

Um einen tiefen Einblick in die Physik der untersuchten Strömungen zu erhalten, wurden zahlreiche Parameterstudien durchgeführt. Die Stärke des Dralls wurde über einen großen Bereich variiert und die jeweils entstehenden Wirbelsysteme untersucht. Es konnte gezeigt werden, dass die innere Scherschicht weniger stabil ist als die äußere und dass die ersten Strukturen in der inneren Scherschicht entstehen. In einer weiteren Studie wurde die Veränderung der kohärenten Struk-

turen aufgrund oszillierenden Massenstroms untersucht. Es zeigte sich, dass mit dem Pulsieren der Strömung Wirbelringe dominanieren, jedoch die spiralförmigen Strukturen immer noch vorhanden sind, besonders im Falle rein axialen Oszillation.

Acknowledgments

This work was funded by the German Research Foundation (DFG) through Project A6 in the Collaborative Research Center SFB 606 at the University of Karlsruhe.

I would like to thank Prof. Wolfgang Rodi for his scientific guidance and continuous support and trust. He also made it possible for me to attend a number of international conferences, which I sincerely appreciate.

I am particularly grateful to Dr. Jochen Fröhlich for all his encouragement and support, his permanent availability for scientific and technical discussions and his patience correcting my reports. Without his experience and advice this work could not have been accomplished.

I also like to thank Prof. Ulrich Maas for being my PhD examiner and facilitating me access to the Faculty of Mechanical Engineering.

Mr. Oliver Petsch and Dr. Horst Büchner are thankfully acknowledged for providing experimental data.

I am indebted to Prof. Javier Jiménez for giving me the possibility to undertake research as an undergraduate in Madrid and for introducing me to the fields of turbulence and computational fluid dynamics.

I would also like to thank Dr. Markus Uhlmann for encouraging me to come to Karlsruhe. Without him this thesis would not have been carried out.

I am grateful to all the people at the Institute for Hydromechanics, in particular, to the members of the Turbulence Group, Antje, Christof, ChunLei, Clemens, Dominic, Minh Duc, Ping and Thorsten. Very special thanks to the president of YHOF.

Desde los tiempos en que éramos gemelos, Juan Carlos ha sido un verdadero estímulo intelectual y por ello siempre estaré en deuda con él.

Quiero agradecer el cariño y comprensión de mis dos familias, y la paciencia con la que han soportado la distancia todos estos años.

Finalmente, me gustaría pedirte perdón, Vickie, por todas las horas que esta tesis te ha robado. Gracias por tu paciencia, apoyo y amor.

Karlsruhe, 13-01-2006

Si se puede simplificar,
se simplifica.
Miguel Pardo

Contents

1 General introduction **1**

1.1 Motivation . . . 1
1.2 High-swirl phenomena . . . 3
1.3 Previous work. State of the art . . . 4
1.4 Objective of the thesis . . . 6

2 LES: equations, boundary conditions and numerical method **9**

2.1 Governing equations . . . 9
2.1.1 Turbulence . . . 10
2.1.2 Computing turbulence: DNS . . . 11
2.1.3 Computing turbulence: RANS . . . 12
2.1.4 Computing turbulence: LES . . . 15
2.1.4.1 Sub-grid scale models . . . 17
2.1.4.2 The Smagorinsky model . . . 17
2.1.4.3 The dynamic model . . . 19
2.1.4.4 Analysis and validation of LES data . . . 20
2.2 Boundary and initial conditions . . . 20
2.2.1 Inflow conditions . . . 21
2.2.2 Outflow conditions . . . 22
2.2.3 Periodic boundary conditions . . . 22
2.2.4 Wall boundary conditions . . . 23
2.2.5 Free-slip condition . . . 24
2.2.6 Initial conditions . . . 24
2.3 Numerical method and validation . . . 24
2.3.1 Numerical method . . . 24
2.3.2 Earlier validation of the code LESOCC2 . . . 25
2.3.3 Validation of LESOCC2 for swirl flows . . . 26

3 LES of a turbulent unconfined annular swirling jet. **27**

3.1 Experimental and numerical configuration . . . 27
3.1.1 Experimental configuration . . . 27
3.1.2 Computational domain, boundary conditions and grid . . . 28
3.1.3 Parameters . . . 30

3.2 Time-averaged results and model validation . . . 32
3.2.1 Averaging procedure . . . 32
3.2.2 Regions of the flow . . . 33
3.2.3 Modelling issues . . . 34
3.2.3.1 Grid . . . 36
3.2.3.2 Sub-grid scale model . . . 37
3.2.3.3 Co-flow . . . 42
3.2.3.4 Conclusions from sensitivity studies . . . 43
3.2.4 Comparison with experimental data . . . 43
3.3 Instantaneous flow . . . 47
3.3.1 Dominant structures . . . 47
3.3.2 Precessing vortex cores . . . 51
3.3.3 Fluctuations of axial velocity component . . . 56
3.3.4 Outer structures . . . 57
3.3.5 Secondary structures . . . 58
3.4 Analysis of spectra . . . 59
3.4.1 Computational procedure and general shape . . . 59
3.4.2 Dominant frequencies . . . 61
3.4.3 Relation between the spectra and the coherent structures . . . 64
3.4.4 Discussion . . . 66

4 Inflow boundary conditions 69
4.1 Generation of inflow conditions for swirling flows . . . 69
4.1.1 Equilibrium swirling inflow conditions . . . 70
4.1.2 Generalization of the method . . . 71
4.2 Description of the simulations . . . 73
4.3 Comparison of results . . . 76
4.3.1 Mean and RMS velocity profiles . . . 76
4.3.2 Visualization and Spectra . . . 77
4.4 Discussion . . . 81

5 Influence of the level of swirl 83
5.1 Overview of the simulations . . . 83
5.2 General features of the flow . . . 84
5.2.1 Streamlines . . . 84
5.2.2 Angle of the flow . . . 86
5.2.3 Fluctuating kinetic energy . . . 88
5.3 Mean Flow and Statistics . . . 90
5.4 Coherent structures . . . 95
5.5 Spectra . . . 98

6 Influence of pulsating inflow **101**
6.1 Motivation . . . 101
6.2 Computational Setup . . . 102
6.3 Phase-averaged flow . . . 103
6.4 Instantaneous structures . . . 109

7 Influence of a pilot jet **115**
7.1 Experimental configuration. New burner . . . 115
7.2 Computational Setup . . . 116
7.3 General features of the flow . . . 118
7.4 Mean and RMS velocity profiles . . . 120
7.5 Flow visualization and Spectra . . . 122

8 Influence of the axial location of the pilot jet **127**
8.1 Physical and Numerical Modelling . . . 127
8.2 Average flow . . . 130
8.2.1 Streamlines . . . 130
8.2.2 Mean and RMS velocity profiles . . . 131
8.2.3 Fluctuating kinetic energy . . . 133
8.3 Instantaneous flow and spectra . . . 134
8.3.1 Coherent structures . . . 134
8.3.2 Spectra . . . 136

9 Analysis of coherent structures using conditional averages **141**
9.1 Motivation . . . 141
9.2 Procedure . . . 141
9.3 Results . . . 143

10 Summary, conclusions and recommendations for future work **155**
10.1 Summary . . . 155
10.2 Conclusions . . . 156
10.3 Recommendations for future work . . . 158

Bibliography **160**

List of Tables **169**

List of Figures **171**

Papers

The content of this thesis is based on the following publications which have been published or have been submitted for publication during the course of the PhD project.

M. García-Villalba, J. Fröhlich, and W. Rodi. Unsteady phenomena in an unconfined annular swirling jet. In H.I. Andersson and P.Å. Krogstad, editors, *Advances in Turbulence X*, pages 515–518, 2004.

M. García-Villalba, J. Fröhlich, and W. Rodi. On inflow boundary conditions for large eddy simulation of turbulent swirling jets. In *Proc. 21st Int. Congress of Theoretical and Applied Mechanics. Warsaw. Poland*, 2004.

M. García-Villalba and J. Fröhlich. On the sensitivity of a free annular swirling jet to the level of swirl and a pilot jet. In W. Rodi and M. Mulas, editors, *Engineering Turbulence Modelling and Experiments 6*, pages 845–854, 2005.

M. García-Villalba, J. Fröhlich, and W. Rodi. Large eddy simulation of an annular swirling jet with pulsating inflow. In *Proc. 4th Int. Symposium on Turbulence and Shear Flow Phenomena. Williamsburg. USA*, 2005.

M. García-Villalba, J. Fröhlich, W. Rodi, O. Petsch, and H. Büchner. Large eddy simulation of flow instabilities in co-annular swirling jets. In *Proc. 6th Direct and Large Eddy Simulation Workshop. Poitiers. France*, 2005.

M. García-Villalba, J. Fröhlich, and W. Rodi. Numerical simulations of isothermal flow in a swirl burner. *accepted, ASME GT2006-90764. ASME Turbo Expo 2006: Power for Land, Sea and Air. Barcelona. Spain*, 2006.

M. García-Villalba, J. Fröhlich, and W. Rodi. Identification and analysis of coherent structures in the near field of a turbulent unconfined annular swirling jet using large eddy simulation. *submitted to Phys. Fluids*, 2006.

M. García-Villalba and J. Fröhlich. LES of a free annular swirling jet – dependence of coherent structures on a pilot jet and the level of swirl. *submitted to Int. J. Heat Fluid Flow*, 2006.

1 General introduction

1.1 Motivation

The present thesis is devoted to isothermal swirl flows in configurations related to gas turbine burners. The motivation for this study originates from combustion applications, which is a field of great economical and ecological relevance. Combustion is the major source for the production of mechanical and electrical energy. More than 90% of primary energy is generated using combustion processes. This thesis has been carried out within the project "Large Eddy Simulation of oscillating flows in combustion chambers". This project belongs to a long-term Collaborative Research Centre (SFB 606 [1]) funded by the German Research Foundation (DFG) (Bockhorn *et al.*, 2003). The focus of the SFB is unsteady combustion. In some cases, as with reciprocating engines, unsteady combustion is an inherent feature of the process. In other cases, as in gas turbine flows, unsteady combustion is related to dysfunctions. In recent years, there has been increased demand for gas turbines that operate in a lean premixed mode of combustion in an effort to meet stringent emission goals. The development of combustion systems to meet this goal, and also to increase the system's efficiency, includes modifications of the combustion process making use of highly turbulent swirl-stabilized flames. Unfortunately, detrimental combustion instabilities are often excited within the combustor when it operates under lean conditions, degrading the performance and reducing the combustor life. To eliminate the onset of these instabilities and to develop efficient approaches for their control, the mechanisms responsible for their occurrence must be understood. Several feedback mechanisms have been identified in the literature as potential candidates responsible for the sustainment of combustion driven oscillations. There is, however, no consensus about the real importance of each of them. Lieuwen *et al.* (2001) suggested that heat release

[1] http://www.sfb606.uni-karlsruhe.de

oscillations excited by fluctuations in the composition of the reactive mixture entering the combustion zone are the dominant mechanism responsible for the instabilities observed in the combustor. Other authors (Paschereit *et al.*, 2000*b*; Külsheimer & Büchner, 2002) stress the relevance of the in-phase formation of large-scale coherent vortical structures as drivers of combustion instabilities. In gas turbines that operate in a lean premixed mode of combustion, these large-scale structures play an important role for reaction and heat-release by controlling the mixing between the fresh fuel/air mixture and hot combustion products.

In this context, Külsheimer & Büchner (2002) studied the formation of large-scale vortices in isothermal swirl flows in dependence of frequency and amplitude of a harmonically modulated mass flow rate. Furthermore, the influence of the vortical structures on the combustion process was investigated by measuring flame transfer functions. They found that the critical frequencies for vortex formation in isothermal measurements and for flame-vortex interaction in the flame measurements are different. In the flame investigations the critical frequency characterizes the beginning of a noticeable interaction of the flow-controlled vortex formation with the combustion process.

In a series of experimental studies (Paschereit *et al.*, 1998, 1999, 2000*b*), the excitation of thermoacoustic instabilities by the interaction between acoustics and unstable swirling flow was investigated. Active combustion control was applied to a swirl-stabilized combustor in which the acoustic boundary conditions were modified to obtain unstable operation. Several axisymmetric and helical unstable modes were identified for fully premixed combustion. Isothermal tests were also performed showing that the dynamics of coherent structures are important, in particular, in the recirculation region near the combustor axis and in the shear layers formed at the sudden expansion.

The formation of large-scale coherent structures is a fundamental problem, which must be understood also in the absence of combustion. This is the starting point of the project A6 in SFB606. In the first phase of the project, covered by the present thesis, the isothermal flow is considered. It lays the foundations for the subsequent study of reactive flows in similar configurations.

1.2 High-swirl phenomena

Swirling flows are widely used in many engineering applications, such as combustion devices, cyclone separators or heat exchangers. One of the most important industrial applications of swirling flows is their use in combustion devices as mentioned in the previous section. Here, they serve to stabilize the flame near the burner exit through a recirculation zone generated by the imposed swirl. This zone can appear detached from any boundary which is advantageous as the walls are then remote from the flame thus reducing their heat load.

Recirculation in a swirling flow generally is the result of so-called vortex breakdown which occurs when, with increasing swirl, the pressure on the axis decreases such that the regular spiralling motion becomes unstable and develops a steady or unsteady stagnation point on or near the axis (Leibovich, 1984). This subject has attracted considerable attention over many years. A comprehensive review is given by Lucca-Negro & O'Doherty (2001) where different regimes are described and the influence of the various parameters is discussed. Numerous experimental and numerical investigations have been published on this issue, but mostly for the laminar case (Harvey, 1962; Sarpkaya, 1971; Billant *et al.*, 1998; Ruith *et al.*, 2003). Recently, spatial stability analyses have been conducted for such cases by Gallaire & Chomaz (2003). Despite all these efforts no conclusive explanation for the onset of vortex breakdown is currently available (Lucca-Negro & O'Doherty, 2001; Gallaire & Chomaz, 2003).

Combustor flows are characterized by high Reynolds numbers and broad-band turbulent fluctuations. The extension of laminar studies of vortex breakdown to turbulent swirling flows is a delicate issue as illustrated by the "conical" vortex breakdown observed by Sarpkaya (1995). Paschereit *et al.* (2000*a*) have made an attempt of a linear stability analysis in the turbulent case starting from a given experimentally observed average turbulent flow field. Experimental investigations of turbulent swirling flows have been performed most often for pipe flow with a sudden expansion (Roback & Johnson, 1983; Sommerfeld & Qiu, 1991; Nejad *et al.*, 1989; Wang *et al.*, 2004). The region of interest, the dump after the expansion, hence is confined and for some of the cited configurations the expansion rate is relatively small. Experiments with unconfined turbulent swirling jets have been

performed for example by Schneider *et al.* (2005). They investigated a series of unconfined swirling premixed natural gas/air flames, and compared with the respective isothermal cases to gain insight into changes of fluid dynamical features caused by combustion. Simulations in an unbound domain are more delicate due to the larger domain and the issue of defining far-field boundary conditions.

Turbulent swirling flows, in particular for high swirl numbers, typically feature pronounced coherent structures (Syred & Beér, 1974; Gupta *et al.*, 1984; Coats, 1996). These are influenced by several effects like internal velocity gradients in form of shear layers on one hand and the level of the angular velocity on the other hand. The latter enhances the occurrence of azimuthal instabilities while non-swirling jets mostly exhibit axisymmetric coherent structures. The most prominent coherent structures in swirling flows are the "precessing vortex cores" (PVC) oriented at a low angle with respect to the axis of rotation (Gupta *et al.*, 1984, p. 191). For low swirl numbers coherent structures are relatively weak (Panda & McLaughlin, 1994) while with higher swirl numbers their intensity increases substantially (Gupta *et al.*, 1984, chap. 3). Helical vortices in swirl flows bounded by solid walls have been studied experimentally and theoretically by Alekseenko *et al.* (1999).

1.3 Previous work. State of the art

Large Eddy Simulation (LES) is a particularly suitable approach for studying the generation and evolution of coherent structures in turbulent swirling flows. It allows to address high-Reynolds number flows and to explicitly compute these structures. If properly conducted, LES should have only limited sensitivity to modelling assumptions. The use of LES for swirling flows is relatively recent, presumably caused by the requirements of computing resources and of specifying unsteady turbulent inflow conditions. The first LES pertinent to the present configuration was performed by Akselvoll & Moin (1996) for a non-swirling confined co-annular jet. Pierce & Moin (1998*a*) subsequently accomplished a corresponding LES with swirl and simulated the experiments of Roback & Johnson (1983) and Sommerfeld & Qiu (1991). Schlüter (2000) performed LES of combustor flows using a compressible formulation in the constant density regime and ob-

served PVC without, however, a corresponding pronounced peak in the spectra computed. McIlwain & Pollard (2002) used LES to compute a turbulent jet with a low swirl number. The swirl was found to increase the number of streamwise braids and therefore it enhanced the breakdown mechanisms of the vortex rings. Apte *et al.* (2003) simulated the confined configuration of Sommerfeld & Qiu (1991) and included the transport of particles. The results for the fluid phase are in good agreement with the experiment but no detailed analysis of coherent structures was performed. Wegner *et al.* (2004*a*,*b*) have performed LES and URANS of an unconfined annular swirling jet and obtained spiralling vortex structures. The agreement with the experimental data for mean flow and fluctuations, however, was not entirely satisfactory. Lu *et al.* (2005) performed LES of a turbulent round jet into a dump combustor. Vortex structures were however only little addressed but analyzed in terms of their interaction with acoustic modes of the combustor. Wang *et al.* (2005) investigated the unsteady flow evolution of a swirl injector. The configuration was very complex involving three radial swirlers, with the flow in one of them counter-rotating with respect to the others. Two swirl numbers were investigated and it was found that for the higher one the flow structures become much more complicated.

This overview shows that there is still substantial need for the simulation and analysis of constant-density swirling flows.

LES for reactive swirling flows was performed by Pierce & Moin (1998*a*). Menon and co-workers (Kim *et al.*, 1999; Sankaran & Menon, 2002) performed several such simulations. Sankaran & Menon (2002) observed a strong unsteady vortex core in the cold flow and quantified the impact of combustion by simulating reactive and non-reactive flow in the same configuration. Huang *et al.* (2003) investigated the interaction between turbulent flow motions and oscillatory combustion of a swirl-stabilized combustor. The flow exhibited a very complex structure, including the bubble and spiral modes of vortex breakdown and a PVC. Roux *et al.* (2005) studied the turbulent flow within a complex swirled combustor using compressible LES, acoustic analysis and experiments for both cold and reacting flows. For their configuration, they found that hydrodynamic structures such as the PVC appearing in cold flow can disappear when combustion starts while acoustic modes are reinforced.

Figure 1.1: Swirl burner used in the experiments of Bender & Büchner (2005).

1.4 Objective of the thesis

The present thesis is concerned with LES of constant-density unconfined flows at high swirl number and high Reynolds number. The first purpose is to demonstrate that LES can simulate these flows with high quality, supported by comparison to a companion experiment. The second and main intention then is to gain understanding of the complex dynamics of the coherent structures in these flows and to provide quantitative results on statistics and mechanisms of instability. Simulations are performed for two similar configurations which correspond to two swirl burners used in companion experiments. The first burner was investigated by Hillemanns (1988). Recently, this burner was used again by Büchner & Petsch (2004) for validating their measurement technique prior to performing experiments on a new burner (Bender & Büchner, 2005). For illustration, a picture of the new burner working in a reactive case is shown in Fig. 1.1.

Once the simulations are validated, the information that can be provided by an LES is larger than that of the corresponding experiment. Full three-dimensional instantaneous velocity and pressure fields are available, which allows a clear physical interpretation of the results. Hence, the goal of the present study is to go

beyond reproducing the experimental conditions and to obtain further insight into the physics of the flows in question. To this end several parametric studies are carried out. First, the level of swirl is varied over a wide range. This gives the possibility to study the different vortex systems formed for each condition. A second investigation is concerned with the influence of an imposed oscillation on the flow. As described in §1.1, when a combustion instability develops in a combustor, pressure oscillations originate. In this context, the aim of the investigation is to characterize the modifications of the large-scale coherent structures in the presence of an external oscillation, bearing in mind that the isothermal flow differs from the reacting flow in a combustor. Another parametric study refers to the addition of an interior co-annular jet, the so-called pilot jet. This jet is usually introduced in combustors which operate under lean conditions and contains a richer mixture to stabilize the flame. In addition to providing stability at baseload, the pilot jet also provides combustion stability during engine startup, load ramping, transients and fuel transfer operations.

2 LES: equations, boundary conditions and numerical method

To a first approximation
all species are insects.

Robert May

In this chapter a brief introduction to the simulation of turbulent flows is provided. The different approaches, DNS, RANS, LES, are schematically introduced and the reasons for chosing LES in the present work are explained. Then, the LES methodology is introduced including sub-grid scale models and boundary conditions. Finally, the numerical method is described briefly and some of the validations of the numerical code are presented.

2.1 Governing equations

The basic equations governing fluid flow for a Newtonian fluid with constant density are the Navier-Stokes equations, which read

$$\frac{\partial u_i}{\partial x_i} = 0, \tag{2.1}$$

$$\frac{\partial u_i}{\partial t} + \frac{\partial u_i u_j}{\partial x_j} = -\frac{1}{\rho}\frac{\partial p}{\partial x_i} + \nu \frac{\partial^2 u_i}{\partial x_j \partial x_j} + f_i. \tag{2.2}$$

Here use has been made of Cartesian tensor notation, where x_i is the i-th spatial coordinate and u_i is the corresponding velocity component, p is the pressure, ρ is the density, ν is the kinematic molecular viscosity and f_i is a body force (like gravity, inertia forces, etc). Einstein summation convention applies.

Equation (2.1) represents the conservation of mass and Equation (2.2) the conservation of momentum. These equations describe the physics of incompressible

fluid motion under laminar as well as turbulent conditions. For a detailed derivation of the Navier-Stokes equations see for example Batchelor (1967).

When making these equations dimensionless it can be shown that the most important parameter arising is the Reynolds number

$$Re = \frac{ul}{\nu}, \tag{2.3}$$

where u and l are a characteristic velocity and a characteristic length, respectively. The Reynolds number is a dimensionless quantity which represents the relative importance of the convective terms in relation to the diffusive terms. Thus, if $Re << 1$ the viscous terms are dominant and the resulting flow is laminar. On the other hand, if $Re >> 1$ the convective terms are dominant, except in regions of small size very close to walls where the viscous terms are always important. Most flows in nature and in engineering applications have a high Reynolds number and are therefore turbulent.

2.1.1 Turbulence

Turbulence is a very complex phenomenon which has been studied for more than 100 years and which is, even today, not fully understood. It is a broad field and in this section only some important characteristics are described. More information can be found in books on the subject like Tennekes & Lumley (1972) and Pope (2000), or in a recent review article (Jiménez, 2000).

Turbulent flows are chaotic and disordered. The diffusivity of turbulence causes rapid mixing and increased rates of momentum, heat and mass transfer. Turbulent flows are always dissipative. Even if it would appear that viscous terms should not be relevant at high Reynolds number, they cannot be neglected because in the momentum equation (2.2), the viscosity multiplies the terms with the highest derivatives and cannot be removed without changing the character of the equations. The kinetic energy of the turbulence is dissipated into heat. To compensate for these viscous losses, turbulence needs a continuous supply of energy. If no energy is supplied, turbulence decays rapidly. A common source of energy is shear in the mean flow; other sources, such as buoyancy, exist too.

The dissipative nature of turbulence was not explained until the work of Kolmogorov (1941); a modern account of his theory can be found in Frisch (1995).

Kolmogorov (1941) introduced the concept of an energy cascade. He suggested that turbulence is formed by 'eddies' of many different sizes. Energy is injected in the largest ones (of size L) but they become unstable and transfer their energy to smaller eddies, which repeat the process to ever smaller sizes. This process of energy transfer is inviscid and no energy is dissipated until the eddies are so small that viscous forces become important and dissipation of energy takes place. The length scale at which dissipation occurs is called the 'Kolmogorov scale'.

In order to estimate the Kolmogorov scale, one of the assumptions which is usually made is that the smallest scales have lost any orientation that might be imposed by the flow geometry or by the initial conditions. Therefore, they are assumed to be locally isotropic. In that case, their physical properties can only depend on the kinematic viscosity ν, and the rate of dissipation ε. It then follows from dimensional analysis that the Kolmogorov scale η is

$$\eta = \left(\frac{\nu^3}{\varepsilon}\right)^{\frac{1}{4}}. \tag{2.4}$$

The different strategies for computing turbulent flows differ in which scales are computed explicitly and which ones are modelled.

2.1.2 Computing turbulence: DNS

Although the turbulent motions are chaotic, we have mentioned that the deterministic Navier-Stokes equations (2.1),(2.2) describe the physics of incompressible fluid motion under turbulent conditions. Therefore, in principle the simplest approach to computing turbulence should be to solve the Navier-Stokes equations for a given set of boundary conditions and initial conditions. Direct numerical simulation (DNS) computes explicitly everything down to, and including, the energy dissipating scales. High-order numerical simulations at resolution of a few Kolmogorv scales provide results so accurate that some people call them 'numerical experiments' (Jiménez, 2003). The quality of DNS is only limited by how much one is willing to spend in resolution, domain size, and running time to collect statistics. When they can be obtained, the results of DNS are indistinguishable from laboratory experiments, although there is always the problem of having exactly the same conditions.

Unfortunately, direct simulations are very expensive. The number of cells required becomes so huge that this approach is not practical in most cases. It is easy to show (see for example Pope, 2000, p. 347) that in order to represent the large-scale as well as the small-scale motion in the three spatial directions, the number of cells N scales with the Reynolds number

$$N \propto Re^{\frac{9}{4}}. \tag{2.5}$$

In spite of their cost, direct simulations are an important tool in basic research. Huge simulations of simple flows are possible for low to moderate Reynolds numbers. For example, del Álamo *et al.* (2004) reported simulations of turbulent channel flow in large computational boxes at $Re_\tau = 950$[1] using $2.725 \cdot 10^9$ grid cells, and for a higher Reynolds number, $Re_\tau = 1900$, in a smaller box using $4.5 \cdot 10^8$ cells. The total time it took to finish the largest simulation was about 9 months. In complex flows, the storage requirements are more demanding and the use of a corresponding number of cells is generally not possible. However, large simulations of complex flows are carried out more and more. For example, Wissink & Rodi (2006) reported a DNS of transitional flow and heat transfer in a turbine cascade with incoming wakes. The Reynolds number of the flow was $Re = 72000$ based on the mean inflow velocity and the axial chord length. The number of grid cells was $9.34 \cdot 10^7$. The total time it took to finish each of the simulations reported was about 3-4 months.

2.1.3 Computing turbulence: RANS

RANS methods are on the other extreme regarding computational cost. They are the oldest, cheapest and least general methods for computing turbulence. This approach is actually the most used in industrial applications because of its low cost which permits the realization of parametric studies. These methods are discussed in detail in books like Rodi (1993), Durbin & Pettersson-Reif (2001) and Wilcox (2002).

In these methods the velocity field is decomposed at each point into the mean

[1] Re_τ is the friction Reynolds number, based on the friction velocity $u_\tau = \sqrt{\tau_w/\rho}$ and the channel half-width h, where τ_w is the whall shear stress.

value (time-averaged) and the fluctuation,

$$u_i(\mathbf{x},t) = \langle u_i(\mathbf{x})\rangle + u_i'(\mathbf{x},t), \tag{2.6}$$

where angular brackets denote the mean value and the prime denotes the fluctuation. With this definition, the mean value of the fluctuation vanishes, $\langle u_i'\rangle = 0$. Averaging the Navier-Stokes equations (2.1),(2.2) and taking into account the decomposition (2.6), the Reynolds-averaged Navier-Stokes (RANS) equations are obtained

$$\frac{\partial\langle u_i\rangle}{\partial x_i} = 0, \tag{2.7}$$

$$\frac{\partial\langle u_i\rangle\langle u_j\rangle}{\partial x_j} = -\frac{1}{\rho}\frac{\partial\langle p\rangle}{\partial x_i} + \nu\frac{\partial^2\langle u_i\rangle}{\partial x_j\partial x_j} - \frac{\partial\langle u_i'u_j'\rangle}{\partial x_j} + \langle f_i\rangle. \tag{2.8}$$

In equation (2.8) the unknown symmetric tensor

$$\tau_{ij} = -\langle u_i'u_j'\rangle, \tag{2.9}$$

acts as a stress tensor, although it actually represents a momentum flux due to the turbulent fluctuations. Estimating these 'Reynolds' stresses is the main problem in the practical computation of turbulent flows. It is possible to write transport equations for these terms, but they contain triple products $\langle u_i'u_j'u_k'\rangle$ and other high-order correlations, which cannot be expressed in terms of simpler quantities. This process leads to an infinite hierarchy of equations of higher moments, which has to be closed at some point with a model. The Reynolds stresses are then determined by a turbulence model, either via the eddy-viscosity hypothesis (see below) or more directly from modelled Reynolds-stress transport equations (not discussed in this text, see references mentioned above).

The Boussinesq eddy-viscosity approximation is the most widely used method to close the equations. The anisotropic part of the Reynolds stress tensor is approximated then by the product of an eddy-viscosity and the mean-strain rate tensor

$$\langle u_i'u_j'\rangle - \frac{1}{3}\delta_{ij}\langle u_k'u_k'\rangle = -2\nu_t S_{ij}, \quad S_{ij} = \frac{1}{2}\left(\frac{\partial\langle u_i\rangle}{\partial x_j} + \frac{\partial\langle u_j\rangle}{\partial x_i}\right). \tag{2.10}$$

Still the eddy viscosity ν_t needs to be determined. Based on dimensional reasoning, it can be expressed as the product of a characteristic velocity of the turbulence

and an integral length scale. These velocity and length scales can be estimated simply using local quantities which leads to the so-called algebraic models. More elaborate models solve transport equations for determining the scales and hence the eddy viscosity. Nowadays, the two-equation models (solving two transport equations) are the most widely used in industrial applications. For example in the so-called $k-\varepsilon$ model, an equation is solved for the fluctuating kinetic energy k and another equation for the dissipation rate ε. The velocity scale is proportional to $k^{1/2}$ and the length scale is proportional to $k^{3/2}/\varepsilon$. The eddy-viscosity is then proportional to $\nu_t \propto k^2/\varepsilon$.

The general problem with RANS models is that they have to model the effect of all the turbulent scales, including the non-universal energy-containing ones. Therefore RANS models are not universal, and often have to be adapted to the different cases. There are usually various empirical coefficients which have been adjusted to give the right results for canonical flows, such as decaying turbulence, boundary layers, etc.

A special problem related to the present work is the inability of RANS models to predict accurately the main characteristics of swirling flows (Jakirlić *et al.*, 2002). These flows present features that are absent in simpler flows in which the models have usually been tuned. One of these features is, for example, the secondary shear strain, i.e. in addition to the common mean shear $\partial\langle u_x\rangle/\partial r$, another shear component is present, $\partial\langle u_\theta\rangle/\partial r$.

Furthermore, in flows with unsteady non-turbulent features, e.g. periodic vortex shedding behind a circular cylinder, the results obtained with RANS models are usually unsatisfactory. For these cases an unsteady approach is mandatory. This can be done within the RANS framework using the so-called Unsteady RANS (URANS) approach. In eq. (2.6) the mean is not time-independent but obtained e.g. by ensemble averaging, and therefore in eq. (2.8) the time derivative of the mean remains present, see for example Durbin (2002). In the flows considered in this work, that is jets involving high levels of swirl, periodic flow instabilities develop. An unsteady approach is therefore required. The performance of URANS for such flows has been evaluated by Wegner *et al.* (2004*b*). They showed that the URANS calculations were able to predict the flow instabilities but the level of fluctuations and the spreading rate of the flow were substantially underpredicted.

Hence, these methods are not used in this work.

2.1.4 Computing turbulence: LES

Large Eddy Simulation (LES) is an intermediate approach between DNS and RANS. While in DNS all scales of motion are computed and in RANS all scales of motion are modelled, in LES some scales are computed and some are modelled. This is possible because the inertial range can be parametrized by just the energy transfer rate. Estimating that rate and using it to model the effect of the inertial range replaces computing the dissipation scales, and also those scales which are approximately isotropic and in equilibrium, i.e those scales which lie in the high-frequency part of the inertial range. This is the principle of LES. The non-universal large scales are computed directly and the effect of the small scales is modelled by a sub-grid scale (SGS) model. More information can be found in books on the subject like Sagaut (2002), which includes an extensive catalog of SGS models, and Geurts (2003), or in a recent review article (Fröhlich & Rodi, 2002). The LES methodology followed in this thesis is described in detail in Fröhlich (2005).

The procedure to obtain the LES equations involves also, as in the case of RANS, a decomposition of the velocity field. In this case it is not obtained by time-averaging the velocity field. Instead, the velocity field is filtered using a low-pass filter. The filtered (or resolved) velocity is defined as

$$\overline{u_i}(\mathbf{x},t) = \int G(\mathbf{x},\mathbf{x}')u_i(\mathbf{x}-\mathbf{x}',t)\,d\mathbf{x}'. \tag{2.11}$$

where the filter $G(\mathbf{x},\mathbf{x}')$ must satisfy the normalization condition

$$\int G(\mathbf{x},\mathbf{x}')\,d\mathbf{x}' = 1. \tag{2.12}$$

Now the decomposition of the velocity field into the sum of the resolved velocity $\overline{u_i}$ and the residual velocity u_i'' is

$$u_i(\mathbf{x},t) = \overline{u_i}(\mathbf{x},t) + u_i''(\mathbf{x},t), \tag{2.13}$$

which is essentially different from the Reynolds decomposition (2.6) for two reasons. First, $\overline{u_i}$ is a time-dependent random field. Second, the filtered residual

velocity is, in general, not zero

$$\overline{u_i''}(\mathbf{x}, t) \neq 0. \tag{2.14}$$

Applying the low-pass filter to the Navier-Stokes equations, the filtered Navier-Stokes equations are obtained, for the resolved velocity $\overline{u_i}$ and the resolved pressure divided by the density which is denoted $\overline{p}$. These equations read

$$\frac{\partial \overline{u_i}}{\partial x_i} = 0 \tag{2.15}$$

$$\frac{\partial \overline{u_i}}{\partial t} + \frac{\partial \overline{u_i}\ \overline{u_j}}{\partial x_j} = -\frac{\partial \overline{p}}{\partial x_i} + \frac{\partial (2\nu \overline{S_{ij}})}{\partial x_j} - \frac{\partial \tau_{ij}}{\partial x_j} + \overline{f_i} \tag{2.16}$$

where $\overline{S_{ij}} = \frac{1}{2}(\partial \overline{u_i}/\partial x_j + \partial \overline{u_j}/\partial x_i)$ is the filtered strain-rate tensor. The term $\tau_{ij} = \overline{u_i u_j} - \overline{u_i}\ \overline{u_j}$ results from the unresolved sub-grid scale contributions and needs to be modelled by a subgrid-scale (SGS) model. A difference with respect to RANS is that in general

$$\tau_{ij} = \overline{u_i u_j} - \overline{u_i}\ \overline{u_j} \neq \overline{u_i'' u_j''} \tag{2.17}$$

as a result of (2.14).

In the present work no explicit filter G is used. Instead, implicit filtering is employed. As discussed in Fröhlich & Rodi (2002), the use of the computational grid as filter amounts to an implicit filtering, since any scale smaller than the grid is automatically discarded. In this approach the filter width is proportional to the mesh size.

One of the main problems of LES appears in wall-bounded flows. In that situation the separation between large scales and small scales close to the wall is not clear because all scales are dynamically relevant. Most flows in which walls are not important, such as jets or mixing layers, can be simulated essentially independent of their Reynolds number. As this is mainly the case in the present thesis, we will not describe the attempts on near-wall modelling. Instead, the reader is referred to the literature (Piomelli & Balaras, 2002).

In the past 30 years, there has been considerable progress in the development of LES, which has been facilitated by the substantial increase in computing power. As pointed out by Pope (2004), advances have been made concerning

- modelling the unresolved processes
- accurate numerical methods on structured and unstructured grids
- detailed comparison of LES with DNS and experimental data in canonical flows
- extensions to include additional phenomena, like turbulent combustion

In spite of these advances, there remain fundamental questions about the conceptual foundations of LES, and about the methodologies and protocols used in its application. For flows in which rate-controlling processes occur below the resolved scales (like near-wall flows or combustion) LES is strongly dependent on the modelling of these processes. In non-reacting free shear flows on the other hand, there are reasons to expect that LES is successful, primarily because both the quantities of interest and the rate-controlling processes are determined by the resolved scales. This is the reason why LES is used in the present work.

2.1.4.1 Sub-grid scale models

In order to close the equations for the filtered velocity, a model for the residual stress tensor is needed. In recent years a great variety of models have been proposed in the literature (see Sagaut (2002)). In this thesis we will only use two of the simplest models: the Smagorinsky model (Smagorinsky, 1963) and the dynamic model (Germano *et al.*, 1991). Both are eddy-viscosity models which follow the RANS tradition, although some of the features of the dynamic model like the use of multi-scale decomposition are not present in RANS. Nowadays, these are well known models so that the description will be very brief.

2.1.4.2 The Smagorinsky model

The Smagorinsky model is the oldest and probably the most widely used SGS model. It is attractive because it is simple and because it is numerically very robust. This model approximates the anisotropic part of the SGS term via

$$\tau_{ij}^a = \tau_{ij} - \frac{1}{3}\delta_{ij}\tau_{kk} = -2\nu_t\overline{S_{ij}}, \tag{2.18}$$

while the trace τ_{kk} is lumped into a modified pressure. The eddy viscosity is given by

$$\nu_t = (C_s\Delta)^2 \, |\overline{S}| \quad , \quad |\overline{S}| = (2\overline{S_{ij}} \; \overline{S_{ij}})^{1/2} \tag{2.19}$$

where $\Delta = (\Delta x \Delta y \Delta z)^{1/3}$ is a measure of the filter width and Δx, Δy and Δz are the mesh sizes in x, y and z direction, respectively. In this equation Δ has been used as the length scale for the eddy viscosity, and $\Delta/|\overline{S}|$ as a time scale. In (2.19) the Smagorinsky constant C_s needs to be estimated. This was first done by Lilly (1967) for the case of homogeneous isotropic turbulence, the value obtained was $C_s = 0.17$ (Pope, 2000, p. 588). In shear flows, which is where LES is really needed, the corrections due to anisotropy are fairly large. This has led to different estimations of C_s. Values of C_s used in simulations of channel flow vary around $C_s = 0.06 - 0.1$ (Deardoff, 1970). Studies of shear flows using experimental data yield similar values (O'Neil & Meneveau, 1997, $C_s \simeq 0.1 - 0.12$). In the present work the value employed is $C_s = 0.1$, unless stated otherwise.

There is however little reason to believe that (2.18) is generally valid, and in particular that the tensors τ_{ij}^a and $\overline{S_{ij}}$ are aligned. As a matter of fact, investigations on real flows show that both tensors are only weakly correlated. Nevertheless, (2.18) works well in many situations. The reason seems to be that all that is needed by the large scales is to have a mechanism which dissipates the correct amount of energy at the end of the energy cascade (Jiménez, 2000). Unfortunately, the Smagorinsky model has some major shortcomings. For instance, it does not work properly close to walls and in transitional regions, where the model is too dissipative. Another potential problem of the Smagorinsky model is the choice of the constant. As already mentioned, different constants are usually employed for different kinds of flow. In complex flows, in particular if these are not well resolved, this is thought to be problematic since the model cannot adjust to varying flow regimes in different areas of the flow field.

It is interesting to note that, actually, the energy cascade is unidirectional, i.e. from large to small scales only in the statistical average. Using explicitly filtered DNS data, it has been shown by Piomelli *et al.* (1991) that the cascade is only direct (large to small) in about 60 % of the points and inverse in the rest (the so-called backscatter). The overall direct energy transfer is the difference between two large opposing fluxes. This is the reason for the main limitations of eddy

viscosity models: as long as $\nu_t > 0$ the cascade is direct everywhere. Locally negative eddy viscosities are generally forbidden for reasons of numerical stability of the solution procedure.

2.1.4.3 The dynamic model

The dynamic Smagorinsky subgrid-scale model, first proposed by Germano *et al.* (1991), with the modification of Lilly (1992) has also been used in the present work. This model is an extension of the Smagorinsky model which overcomes some of the deficiencies described above. The basic idea of the dynamic SGS model is to make use of the information available from the smallest resolved scales. To this end, a double filtering procedure leads to a closed expression, commonly referred to as Germano's identity, relating filter stresses at different filter levels to each other. This additional information is then used to adjust the model parameter C_s locally. The detailed formulation of the model is relatively technical and lengthy and can be found elsewhere (Germano *et al.*, 1991; Pope, 2000; Sagaut, 2002; Fröhlich, 2005).

As first pointed out by Lilly (1992), the numerical computation of C_s is not free from problems. C_s can become highly oscillating and in those cases has to be regularized. When the flow has homogeneous directions, like in the case of channel flow, averaging in horizontal planes can be performed leading to a quite stable formulation of the model. Furthermore, the occurrence of negative values of C_s is possible locally. It was originally suggested that the resulting negative viscosities can be used to simulate backscatter. However, as mentioned before, the use of negative eddy viscosities is forbidden due to numerical considerations, because any small perturbation is amplified. Therefore, it is common practice to clip the eddy viscosity to avoid negative values.

In the present work, the model parameter C_s is determined using a three-dimensional explicit box filter of width equal to twice the mesh size. The eddy-viscosity ν_t is clipped to avoid negative values and smoothed by temporal relaxation (Breuer & Rodi, 1996)

$$\nu_t^{n+1} = \varepsilon \nu_t^* + (1-\varepsilon)\nu_t^n, \tag{2.20}$$

with the relaxation factor $\varepsilon = 5\ 10^{-4}$ and ν_t^* the value determined by the original

model.

In the sequel, overbars denoting the resolved quantities will be dropped for clarity.

2.1.4.4 Analysis and validation of LES data

The solution of the filtered Navier-Stokes equations (2.15),(2.16) provides information on the scales which are resolved. Then, the information that is useful for analysis or validation is what is contained in the scales that are well resolved. An important issue is the influence of the unresolved motions on the turbulent statistics. For a discussion on this topic see Sagaut (2002, chapter 8). Calling the exact statistical values $\langle u_i'^e u_j'^e \rangle$, and assuming that the statistical average of the subgrid modes is very small compared with the other terms so that the exact mean velocity and the mean resolved velocity coincide, the expression for the exact turbulent statistical values is (Sagaut, 2002, p. 262)

$$\langle u_i'^e u_j'^e \rangle \simeq \langle u_i'' u_j'' \rangle + \langle \tau_{ij} \rangle \tag{2.21}$$

where $\langle u_i'' u_j'' \rangle$ results from the resolved motions and $\langle \tau_{ij} \rangle$ is the average of the sub-grid scale model. The term $\langle \tau_{ij} \rangle$ is often negligible, in particular in free shear flows at high Reynolds numbers where the large scales carry most of the kinetic energy. If the grid is fine enough to resolve the scales up to the inertial sub-range, the residual energy is negligible.

2.2 Boundary and initial conditions

So far the governing equations have been introduced. To complete the description of the physical model for LES, initial and boundary conditions are described in this section.

It is well known that the mass conservation constraint in an incompressible flow can be used to remove the pressure as a dependent variable from the momentum equations. Boundary conditions are then only required for the velocity field. Given the velocity field, the pressure field is described to within an unknown constant by a Poisson equation obtained by taking the divergence of the momentum

equations. For this equation the momentum equations provide natural Neumann conditions on the boundaries. Thus, in principle, no boundary conditions are required for the pressure.

The boundary conditions for an LES are determined both by the physics of the problem and computational necessities. Because of the high computational cost it is almost always necessary to confine the computational domain closely around the area of interest in a flow simulation. A realistic specification of the conditions on the boundaries is often essential for a successful flow prediction.

2.2.1 Inflow conditions

In order to simulate successfully a complex flow using LES it is extremely important to employ realistic inflow conditions. Turbulent inflow conditions in an LES have to be prescribed in an instantaneous manner. The three components of the velocity have to be specified at an inflow boundary, i.e. Dirichlet conditions. To obtain realistic unsteady inflow conditions is a topic of current research (Lund *et al.*, 1998; Klein *et al.*, 2003; Druault *et al.*, 2004; Sagaut *et al.*, 2004; Schlüter *et al.*, 2004). Some authors consider that at the present time it is more important to improve the strategies for the specification of inflow conditions than to improve the present SGS-models (which constitutes the basis of an LES!). This gives an idea of the importance of the issue. Several LES reported in the literature impose the mean velocity profile and superimpose random fluctuations with a given spatial variation. This is a rather poor approach, because random fluctuations do not possess spatial nor temporal correlations and therefore decay quickly. In other cases, it is possible to use the solution of a simpler flow problem, such as channel or pipe flow, for which periodic conditions can be used. The solution of a simple flow problem is recorded and these data are used to specify the inflow of the more complex flow problem. (Instead of recording the data, it is possible to carry out both simulations simultaneously). This approach is of course more accurate but also more expensive.

In the present work the specification of the inflow conditions is of paramount importance and Chapter 4 is entirely dedicated to this issue.

2.2.2 Outflow conditions

At the outflow boundary it is important in an LES (also in a DNS) to avoid that the turbulent flow is disturbed by the boundary, i.e. the condition imposed on the boundary should allow flow structures to be convected out of the domain, without spurious reflections. This cannot be achieved by using Dirichlet or Neumann conditions. In the present work the so-called convective boundary condition has been employed. At the boundary the following equation is solved

$$\frac{\partial u_i}{\partial t} + u_c \frac{\partial u_i}{\partial n} = 0, \tag{2.22}$$

where $\partial/\partial n$ is the gradient normal to the boundary and u_c is a convective outflow velocity normal to the boundary. The selection of u_c is not very critical because both limits $u_c \to 0$ and $u_c \to \infty$ are numerically possible, equivalent to a Dirichlet or Neumann condition, respectively (Fröhlich, 2005). The value of u_c is usually taken constant over the whole outflow boundary, and equal to the averaged outflow velocity over the boundary. It appears that this is a reasonable approximation and that this condition allows vortical structures to be convected out of the domain.

2.2.3 Periodic boundary conditions

In geometrically simple flows, like fully developed channel or pipe flow, the difficulty of having to prescribe instantaneous boundary conditions is avoided by assuming that the flow is periodic in space. Thus, it is possible to avoid the simulation of extremely long and wide channels. Instead, a 'relatively' small computational box is employed, and periodic conditions are imposed in the homogeneous directions. The box can be only 'relatively' small because the simulated domain has to be large enough to contain a representative number of large energy-containing structures, in order to avoid that the numerical solution is influenced by the periodicity assumption.

2.2.4 Wall boundary conditions

If the domain boundary coincides with a solid, impermeable wall a no-slip condition can generally be used which for a non-moving boundary is

$$u_i(\mathbf{x}_{boundary}, t) = 0. \tag{2.23}$$

However, while the prescription of a no-slip condition is straightforward, the LES in the vicinity of the wall is not, as pointed out in §2.1.4. The difficulties in calculating the flow close to a wall result from the fact that the basic assumption of scale separation between large and small scales does not hold anymore. Hence, the resolution requirements for an LES close to a wall are often prohibitive for the high Reynolds numbers occurring in engineering practice. In cases where the core of the flow, away from the wall, is of main interest, one can attempt to model the effect of the whole viscous sublayer on the free flow. A number of such wall-models have been proposed on the literature (Piomelli & Balaras, 2002; Sagaut, 2002). Most of these models make use of the logarithmic law of the wall describing the mean streamwise velocity profile in the inertial sublayer. The models therefore assume complete self similarity for the velocity profile, i.e. the mean velocity profile normalized with inner variables (ν,u_τ) is independent of the Reynolds number. These models perform relatively well for quasi-parallel flows without pressure gradients.

In the present work, in most of the calculations reported the inlet duct walls are included in the computational domain (see Fig. 3.2 below). However, the region of interest is always far away from walls as described in Chapter 1. Furthermore, strong pressure gradients are present in the flow due to the swirling motion; curvature effects are important, too. Keeping this in mind, it is likely that the standard wall models used in most calculations are not going to provide improvements with respect to a simple no-slip condition. This was confirmed in preliminary tests using the Werner-Wengle wall model (Werner & Wengle, 1993) for a swirling flow in a confined configuration. In that case no improvement was observed. Therefore, in the present work a no-slip condition will be used in all the cases where a wall boundary condition is needed.

2.2.5 Free-slip condition

In some occasions, it is convenient to use free-slip conditions to minimize the effect of the boundary on the predicted flow by allowing the flow to slide along the boundary. The boundary-normal velocity component is assumed to vanish instantaneously while for the other components a homogeneous Neumann condition is imposed normal to the surface

$$u_n = 0 \;\; ; \;\; \frac{\partial u_i}{\partial n} = 0, \tag{2.24}$$

where u_n indicates the boundary-normal velocity component.

2.2.6 Initial conditions

The specification of initial conditions is relatively unproblematic in LES. The reason is that after a sufficiently long integration time the initial conditions do not have any influence on the numerical solution. Nevertheless, in order to reach a statistically steady state in the flow in a short time, the initial condition should be close to the developed solution. Usually an approximation to the mean flow with some random noise is specified as initial condition. In some cases, this information is not known in the entire domain, as was the case in the present work. Therefore the following strategy was used. First, a random field was imposed as initial condition on a very coarse grid. The simulation was run on this grid for a long time to obtain a good estimation of the velocity field in the whole domain. Then, the velocity field was interpolated onto the final grid and the simulation was run for a few characteristic time units. Only after this start-up period the collection of statistics was undertaken.

2.3 Numerical method and validation

2.3.1 Numerical method

All the simulations in the present work were performed with the in-house code LESOCC2 (Large Eddy Simulation On Curvilinear Coordinates). The code has been developed at the Institute for Hydromechanics. It is the successor of the

code LESOCC developed by Breuer & Rodi (1996) and is described in its most recent status in Hinterberger (2004). The code solves equations (2.15),(2.16) on body-fitted, curvilinear grids using a cell-centered Finite Volume method with collocated storage for the cartesian velocity components. Second order central differences are employed for the convection as well as for the diffusive terms. The time integration is performed with a predictor-corrector scheme, where the explicit predictor step for the momentum equations is a low-storage 3-step Runge-Kutta method. The corrector step covers the implicit solution of the Poisson equation for the pressure correction (SIMPLE). The scheme is of second order accuracy in time because the Poisson equation for the pressure correction is not solved during the sub-steps of the Runge-Kutta algorithm in order to save CPU-time. The Rhie and Chow momentum interpolation (Rhie & Chow, 1983) is applied to avoid pressure-velocity decoupling. The Poisson equation for the pressure increment is solved iteratively by means of the 'strongly implicit procedure' (Stone, 1968). Parallelization is implemented via domain decomposition, and explicit message passing is used with two halo cells along the inter-domain boundaries for intermediate storage. One of the most important features of LESOCC2 is the possibility to use block-structured grids with an unstructured arrangement of the blocks, which was not possible with the previous version of the code. This feature allows the simulation of very complex geometries, like the co-annular burner of Chapter 7.

2.3.2 Earlier validation of the code LESOCC2

Both versions of the code have been validated for a number of flows. Breuer & Rodi (1996) computed turbulent flow through a square duct at several Reynolds numbers, flow through a 180° bend, flow around a surface-mounted obstacle and flow around a circular cylinder. Several flows of engineering interest have been investigated with this version of the code. An overview of some of the cases can be found in Fröhlich (2005). A highly resolved LES of flow over a two-dimensional hill was reported in Fröhlich *et al.* (2005). LESOCC has also been used to investigate transitional flow in turbomachinery (Wissink, 2003; Michelassi *et al.*, 2003; Wissink & Rodi, 2006).

The updated version of the code, LESOCC2, was validated by computing turbulent channel flow at several Reynolds number (Hinterberger, 2004). In this reference, some other flows have been investigated using LESOCC2, like shallow flow around circular cylinders or shallow mixing layers. The flow around a matrix of cubes was investigated in Stoesser *et al.* (2003). Fröhlich & Rodi (2004) computed the flow around cylinders of finite height and Fröhlich *et al.* (2004) investigated the mixing characteristics of a jet in a cross-flow. Encouraging results for complex three-dimensional flows at very high Reynolds number have been obtained. For example, the flow around a simplified car, the so-called Ahmed body, was investigated in Hinterberger *et al.* (2004) and the flow around a three-dimensional axisymmetric bump was reported in Rodi *et al.* (2005). Recently, the flow around two-dimensional dunes has been successfully computed by Braun (2005).

2.3.3 Validation of LESOCC2 for swirl flows

The code has been validated for swirling flows in a combustor-like geometry. The flow in a simplified co-axial swirl combustor has been reported in García-Villalba *et al.* (2005). Two experimental test cases were chosen from the literature, a configuration investigated by Roback & Johnson (1983) and one by Sommerfeld & Qiu (1991). In both cases the configuration consists of coaxial jets which enter into an expansion duct with the annular jet being swirled, the inner jet unswirled. One of the differences between these cases and the ones considered in this thesis is the fact that the domain is confined. The Reynolds number based on the bulk velocity of the outer jet U_b and the diameter of the outer jet D is $Re = 47500$ in the first case and $Re = 65000$ in the second. The swirl number S is $S = 0.41$ and $S = 0.45$, respectively. The flow is highly unsteady and anisotropic and involvs high levels of turbulence. Furthermore, these flows are very sensitive to inflow and outflow conditions which makes them very difficult to simulate. The main features of the flow are a central recirculation zone and a second recirculation zone in the corner of the expansion. Both were well predicted in the simulations. The mean velocities and the turbulent fluctuations were also found to be in good agreement with the experimental data.

3 LES of a turbulent unconfined annular swirling jet.

In this chapter the numerical simulation of the near field of a turbulent unconfined annular swirling jet is presented. This configuration is considered as the reference configuration in the remaining parts of the thesis. In this chapter, first, the experimental configuration is introduced. This is followed by the description of the computational set-up. An overview of the simulations is given in Table 3.1. Several modelling issues are investigated, such as the influence of the grid or the sub-grid scale model. Then, a thorough comparison with the experimental data is presented including mean velocity profiles, turbulent intensities and power spectral densities of velocity fluctuations at selected points. The agreement with the experiment is excellent. This makes possible the analysis of the instantaneous flow in physical terms. Large-scale coherent structures rotating at a constant rate around the symmetry axis are identified in the flow. Furthermore, the connection between the motion of the structures and the power spectral density of velocity fluctuations is explored.

3.1 Experimental and numerical configuration

3.1.1 Experimental configuration

The configuration considered in the present chapter was investigated experimentally by Hillemanns (1988) at the University of Karlsruhe. New measurements of the same configuration have been performed recently by Büchner & Petsch (2004) as a validation of a new test bench. Both sets of measurements were obtained using Laser Doppler Anemometry (LDA). The configuration consists of an annular swirling jet flowing into an ambient of the same fluid which is at rest. A sketch of the burner is shown in Fig. 3.1. The swirl is generated with a mo-

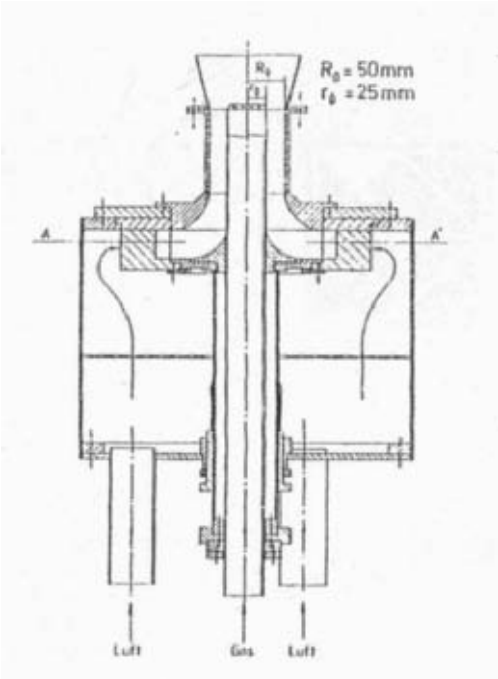

Figure 3.1: Sketch of the burner taken from Hillemanns (1988)

vable block swirl generator (Leuckel, 1967), in which radial flow is fed into the swirl generating device and radial and tangential vane angles are altered to adjust the desired level of swirl. The reported measurements are confined to the near field of the jet. They include first and second order moments of the velocity at several axial stations downstream of the jet exit. The second set of experiments (Büchner & Petsch, 2004) also includes power spectral densities of velocity fluctuations at some points close to the nozzle. The experiments do not provide any measurements of the flow in the region upstream of the jet outlet. This renders the specification of the inflow boundary conditions in the simulation somewhat more difficult.

3.1.2 Computational domain, boundary conditions and grid

The geometry of the computational domain is shown in Fig. 3.2. It features an annular jet issuing with bulk velocity U_b into a large cylindrical domain. The reference length is $R = D/2$ where D is the outer diameter of the annular jet. The inner radius is $0.5R$. The computational domain also includes a crude representation of the inlet duct upstream of the jet exit. A strong idealization is required because a proper representation of the swirl-generating device is computationally

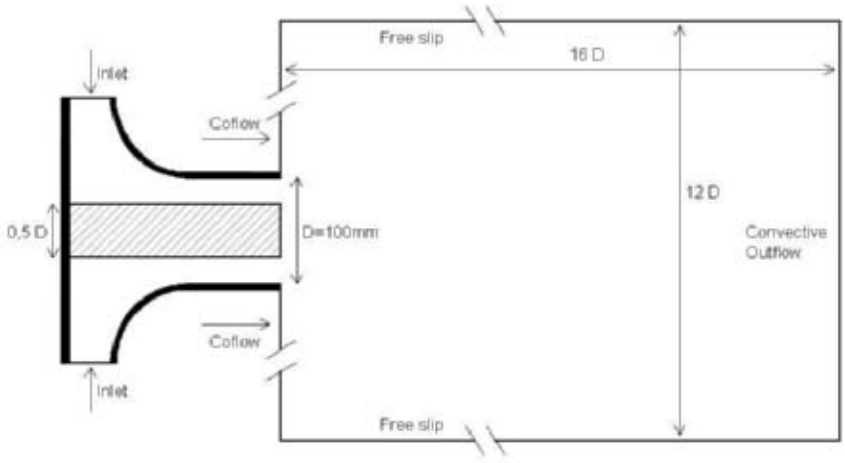

Figure 3.2: Geometry of the computational domain and boundary conditions applied.

too demanding. Instead, the flow is imposed at the circumferential inflow boundary located at the beginning of the inlet duct. The flow enters radially having an azimuthal component. At this position steady, top-hat profiles for the radial and azimuthal velocity components are imposed. This is not an ideal approach because for LES unsteady inflow boundary conditions are usually required. It will be demonstrated, however, that this procedure does not affect the results because turbulence readily develops in the duct upstream of the jet exit. The issue of the specification of inflow conditions will be addressed in detail in Chapter 4. Fig. 3.3 shows the development of the flow in the inlet duct by means of the instantaneous axial velocity and the instantaneous turbulent kinetic energy. The inlet swirl was adjusted such that the computed swirl number at the jet outlet matches the experimental value. No-slip boundary conditions are applied at the walls. At the exit boundary, a convective outflow condition is used. Free-slip conditions are applied at the lateral boundary which is placed far away from the region of interest at $12R$. Note that in the figure the lateral and the downstream boundaries are not positioned to scale. The fluid to be entrained is fed in by a mild co-flowing stream, the influence of which will be addressed in §3.2.3.

Two block-structured grids were used for the simulations discussed in this chapter, C1 and F1 (C Coarse, F Fine). Grid C1 comprises roughly 2.5 million hexahedral cells and grid F1 comprises about 6 million cells. Various views of the grid F1 are shown in Fig 3.4. The grids were generated with the commercial

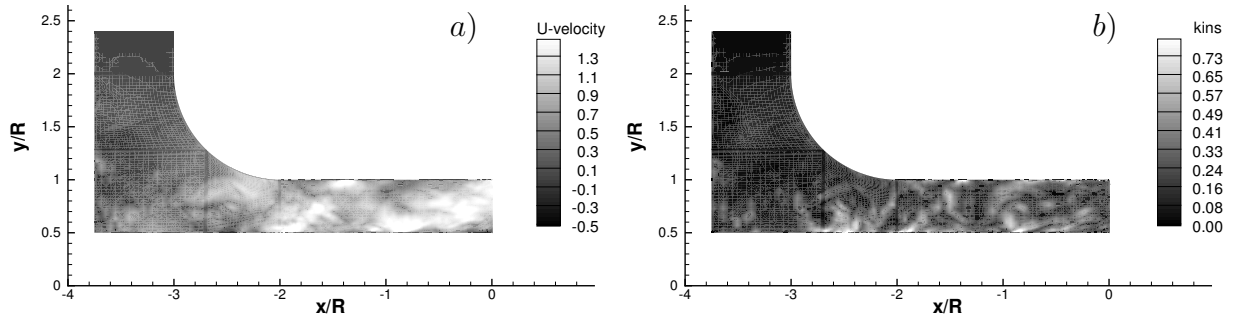

Figure 3.3: Development of the flow in the inlet duct region. a) Instantaneous axial velocity. b) Instantaneous fluctuating kinetic energy.

software ICEM-CFD Hexa. In the azimuthal direction 160 grid points are used in grid F1 while 100 are used in Grid C1. The stretching factor of both grids is everywhere less than 5%. In grid F1, the minimum axial spacing is located at the jet outlet and is $\Delta x = 0.02R$. In the vicinity of the walls, the minimum radial spacing is $\Delta r = 0.008R$. In grid C1, the values of Δx and Δr are slightly larger. As shown in Fig. 3.4d, the region near the symmetry axis consists of a quasi-square mesh, which eliminates the centreline singularity present in grids which use cylindrical coordinates.

3.1.3 Parameters

The following reference quantities are used throughout this chapter: the outer radius of the annulus, $R = 50$ mm, for lengths, the bulk velocity $U_b = 25.5$ m/s, for velocities, and $t_b = R/U_b$ for times.

The Reynolds number of the flow based on the bulk velocity U_b and the outer radius of the jet is $Re = 81500$. The Swirl number is defined as

$$S = \frac{\int_0^R \rho u_x u_\theta r^2 \, dr}{R \int_0^R \rho u_x^2 r \, dr}, \tag{3.1}$$

and is evaluated at a certain axial position x. Table 3.1 assembles the parameters of the computations discussed in this chapter. Simulation H1 is taken as reference because it matches the experimental flow conditions. The value of the swirl number is $S = 1.2$ at $x/R = -2$ and $S = 0.9$ at $x/R = 0$. This decay in the Swirl number is caused by a decay of the tangential velocity in the inlet duct and a

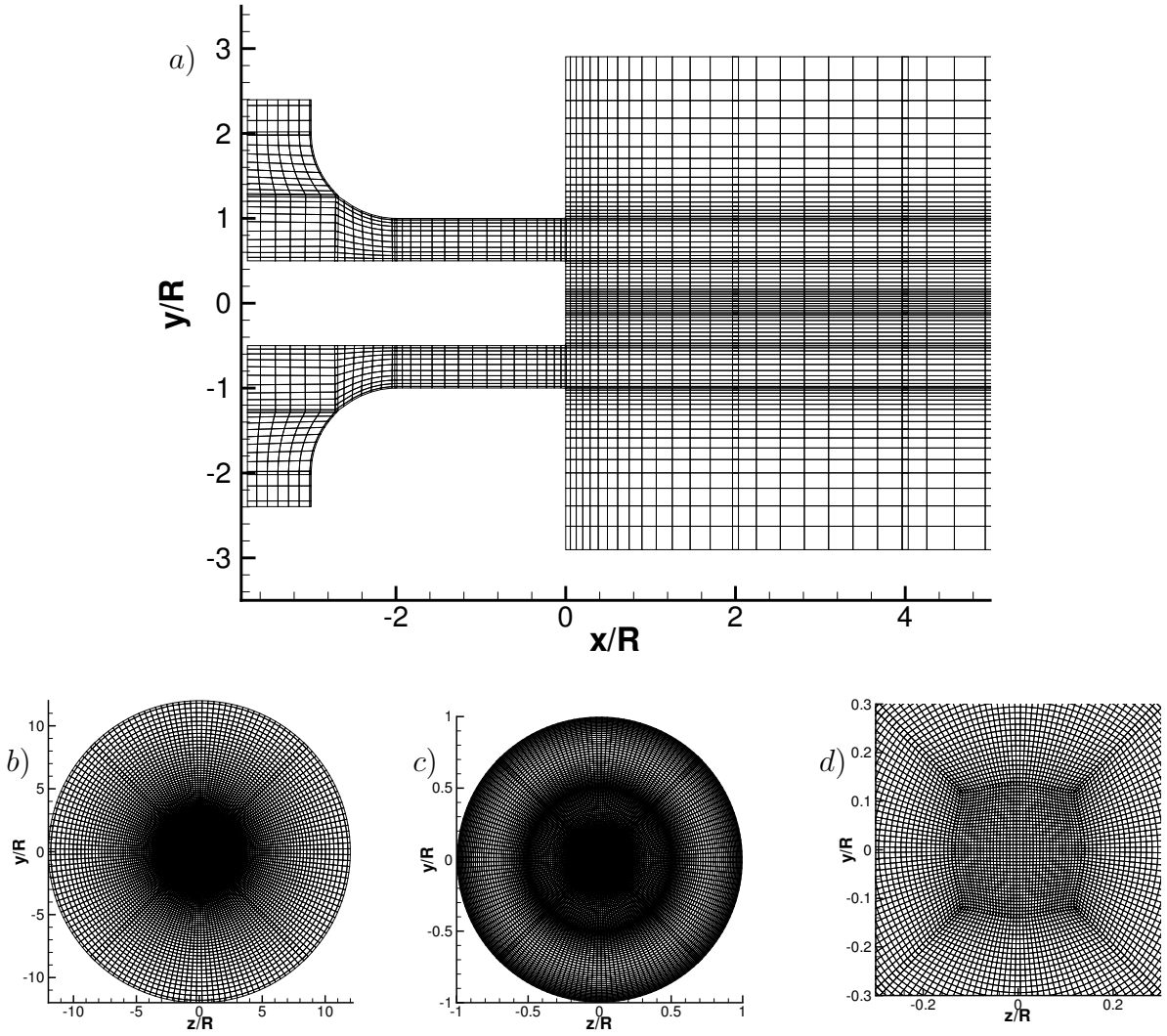

Figure 3.4: Computational grid. $a)$ Axial plane, zoom near the jet exit. Every 4th grid line is shown. $b)$ Cut in the $y-z$ plane through the entire domain with all grid lines being shown. $c)$ same as $b)$ but zoomed around the symmetry axis. $d)$ strong zoom around the axis.

substantial change in the shape of the profiles of both the axial and the tangential velocity components. The same behaviour has also been observed by Sankaran & Menon (2002). Since S represents an integrated quantity, two swirling jets of completely different velocity distributions may have the same swirl number. Although the swirl number hence only provides an incomplete description of the properties of a swirling jet, it is commonly used in the literature and therefore also

employed in the present text.

Simulation	Grid	SGS model	Co-flow	Swirl
H1	F1 (~ 6 mio.)	Dynamic	5%	0.9
H2	C1 (~ 2.5 mio.)	Dynamic	5%	0.95
H3	F1 (~ 6 mio.)	Dynamic	5%	0.95
H4	C1 (~ 2.5 mio.)	Smagorinsky	5%	0.95
H5	C1 (~ 2.5 mio.)	Smagorinsky	2%	0.95
H6	C1 (~ 2.5 mio.)	Smagorinsky	10%	0.95

Table 3.1: Overview of the simulations for the Hillemanns burner. Parameters are explained in the text. H2-H6 have an excess of swirl compared to the experimental flow conditions for historical reasons as discussed in the text.

3.2 Time-averaged results and model validation

3.2.1 Averaging procedure

The simulations were run for several time units t_b to eliminate the effects of the initial conditions. After this period, statistical quantities were collected for 150 t_b in H1, which is long enough to obtain well-converged values in the near field of the jet exit. The averaging time in cases H2-H6 was slightly shorter, in all cases of the order of 100 t_b which is still sufficient. The averaging was performed in time and also along the azimuthal direction. Average quantities are denoted by angular brackets and corresponding fluctuations by a double prime.

Far downstream of the jet exit, for $x/R \geq 6$, the statistical quantities are not fully converged in the vicinity of the symmetry axis because the fluid motions are slower in that region and the impact of azimuthal averaging is low near the axis. Substantially longer averaging times would be necessary to improve in this respect. However, the focus here is the near field of the jet outlet extending roughly up to $x/R = 3$. In this region the averaging period is sufficient. This is supported not only by the smoothness of the results presented below and their good

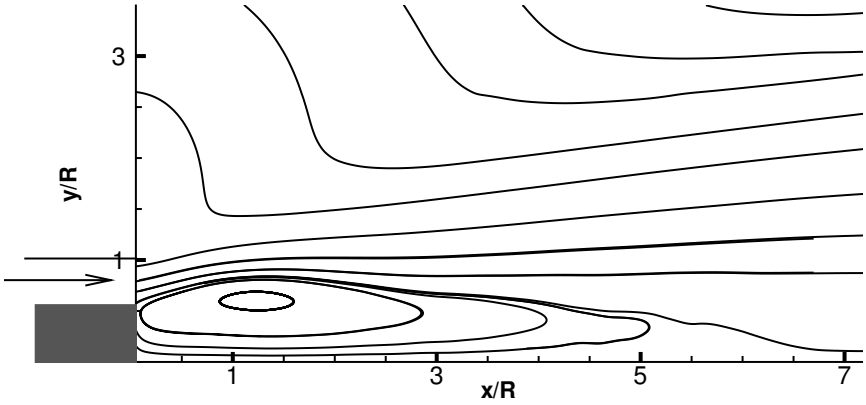

Figure 3.5: Average streamlines in an axial plane obtained from the simulation.

agreement with the experimental data but also by the following reasoning. At $x/R = 3$ the characteristic tangential velocity is about $0.5U_b$ and can be found at $r/R = 1$. Hence, an averaging period of 150 time units yields an average over 12 revolutions of the flow, further supplemented by azimuthal averaging.

3.2.2 Regions of the flow

First of all, a general picture is presented by a brief description of the different regions of the flow.

Fig. 3.5 shows the computed time-averaged two-dimensional streamlines in an axial plane[1] in H1. A long recirculation zone is observed in the central region. The length of the recirculation zone is about $6R$, and its maximum diameter $1.4R$. Note that, as the jet is annular, a recirculation zone is also generated without swirl because the cylindrical center body acts as a bluff body (see Chapter 5). A long recirculation zone is typical for flows with a high level of swirl (Gupta *et al.*, 1984). This phenomenon is related to the presence of a low pressure region generated by the swirl on the symmetry axis of the flow. Further information on the average flow is provided by the vector plot in Fig. 3.6a. It shows that the jet has an outward radial component due to the centrifugal forces and widens substantially further downstream.

The jet produces two shear layers, an inner one on its border with the recirculating flow and an outer one on its border with the surrounding co-flow. This can

[1] In this work, an axial plane is an $x - r-$plane

be seen better in Fig. 3.14a below which shows the mean axial velocity profile at $x/R = 0.2$. The shear layers are not plane shear layers, since they are subject to curvature effects due to the swirl. It is worth noting that the two shear layers formed by the jet are spatially very close to each other. The inner one is wider than the outer one and exhibits a larger change in velocity due to the negative velocity in the recirculation zone. This issue is addressed further in Fig. 3.19 below.

In the outer region, the jet entrains fluid from the ambient in a very intermittent manner, which is visible in the instantaneous vector plot of Fig. 3.6b. This is a complex phenomenon, which is addressed further below. The vanishing slope of the streamlines remote from the jet at $x/R = 0$ and $r > R$ in Fig. 3.5 is due to the co-flow boundary condition. The velocity at this position, however, is only 5 % of the jet axial velocity, so that the influence on the region of interest is negligible. This is also visible in Fig. 3.6 and 3.14.

The swirling jet spreads radially outwards much faster than in the case of a non-swirling jet (Akselvoll & Moin, 1996). In the far field downstream of the recirculation zone, the relevant motions are much slower than in the near field. As stated above, the present integration time is not long enough to study this region which deserves further investigations.

3.2.3 Modelling issues

In this section several modelling choices are validated, namely the effects of the grid, the sub-grid scale model and the co-flow boundary conditions. This is done by means of simulations H2-H6 listed in Table 3.1. For historical reasons, these sensitivity studies were unfortunately performed for a flow condition which did not match exactly the flow condition in the experiment. When simulations H2-H6 were performed, the experimental data of Büchner & Petsch (2004) were not yet available. The swirl level was not adjusted appropriately at the inlet which yielded an excess of mean tangential velocity at the jet outlet. To get an idea of the differing flow conditions between H1 and H2-H6, compare Figs. 3.14b and 3.7b which show the mean tangential velocity profile at $x/R = 0.2$. In Figs. 3.7 to 3.13 the experimental data are still included for reference, but no direct comparison

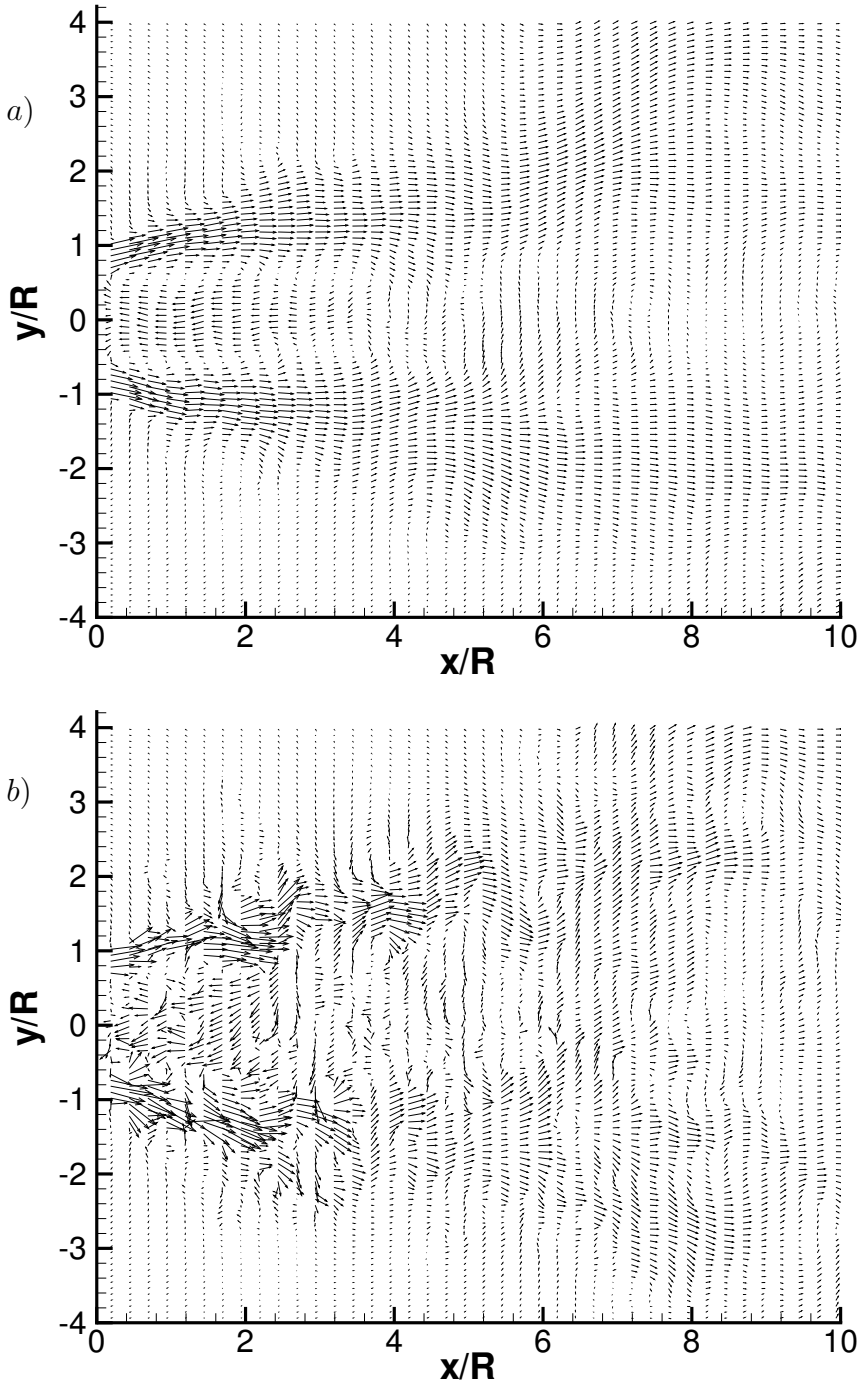

Figure 3.6: Vector plots in an axial plane. a) Average flow. b) Instantaneous flow. (Values are interpolated to a cartesian grid)

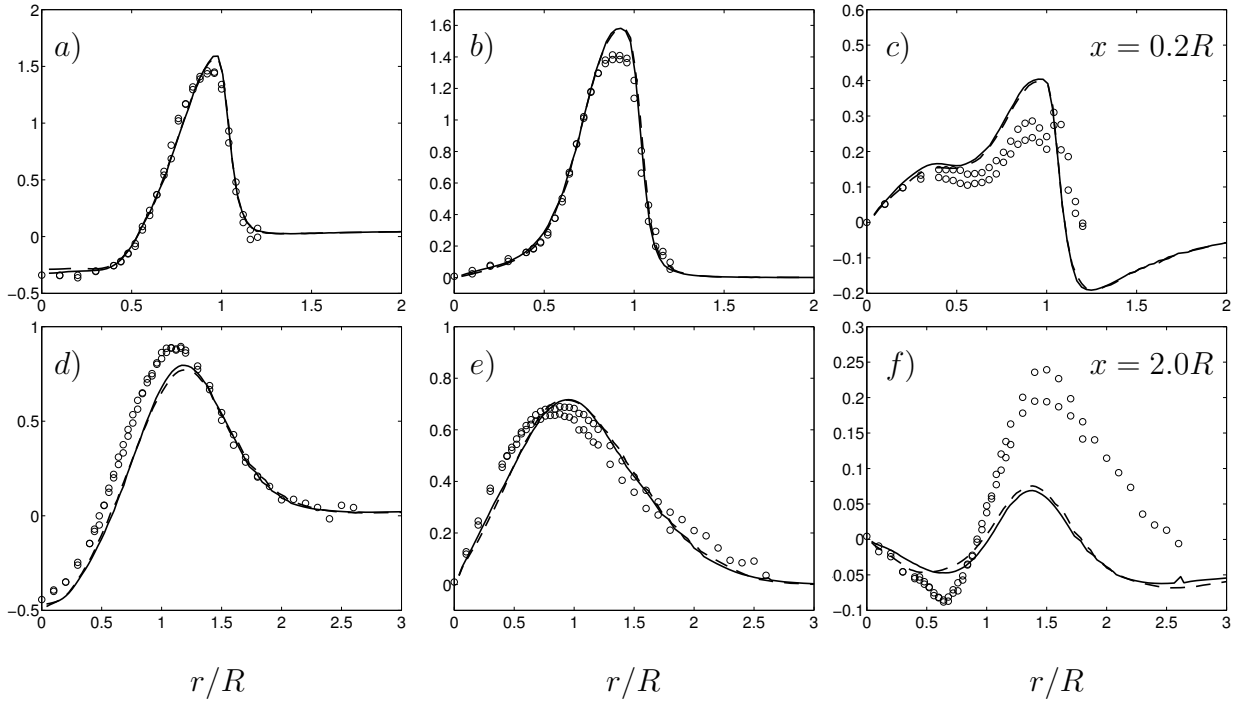

Figure 3.7: Influence of the grid. Radial profiles of mean velocity components at $x/R = 0.2$ and 2.0 (top to bottom as indicated in the rightmost column). Solid line, H3; dashed line, H2; symbols, experimental data from Büchner & Petsch (2004). Left, axial velocity, $\langle u_x \rangle / U_b$. Centre, tangential velocity, $\langle u_\theta \rangle / U_b$. Right, radial velocity, $\langle u_r \rangle / U_b$. Observe that the ranges of the vertical axis have been adjusted individually.

with the experiment is intended. The comparison with the experimental data is performed in §3.2.4.

3.2.3.1 Grid

In order to check the influence of the grid, simulations H2 and H3 were performed, using the same parameters except for the grid, as reflected in Table 3.1. Fig. 3.7 shows profiles of the three components of the mean velocity at two axial stations, at $x/R = 0.2$ very close to the jet exit and at $x/R = 2$ close to the position where the recirculation is strongest. The agreement between both simulations is excellent showing that both grids are good enough for the prediction of the mean flow in the near field of the jet. Hence, if the coarse grid is adequate, the finer is even more so, which validates its use. The same applies for the turbulence statistics,

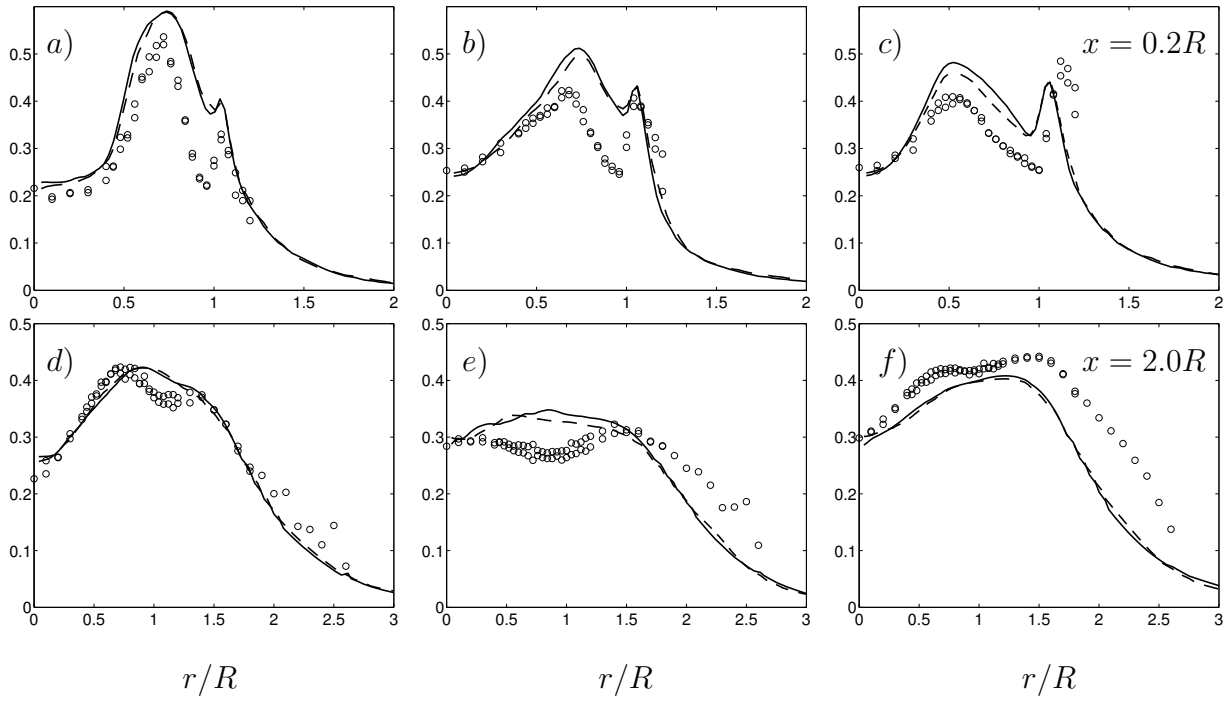

Figure 3.8: Influence of the grid. Radial profiles of rms velocity fluctuations at $x/R = 0.2$ and 2.0 (top to bottom as indicated in the rightmost column). Solid line, H3; dashed line, H2; symbols, experimental data from Büchner & Petsch (2004). Left, axial velocity, $\langle u_x^{rms} \rangle / U_b$. Centre, tangential velocity, $\langle u_\theta^{rms} \rangle / U_b$. Right, radial velocity, $\langle u_r^{rms} \rangle / U_b$.

which are shown in Fig. 3.8. As the graph shows, the differences are insignificant. It is important to note for the subsequent discussion that the simulation with the coarse grid is cheaper than the simulation with the fine grid. This results from the smaller number of operations required by fewer grid points but also from the time step being slightly larger. For example, the time step employed in the simulations with the fine grid is $\Delta t/t_b = 10^{-3}$ while it is $\Delta t/t_b = 2 \cdot 10^{-3}$ with the coarse grid. On the other hand, more scales are resolved in the simulation with the fine grid, and therefore the physical analysis can be richer.

3.2.3.2 Sub-grid scale model

The sensitivity of the simulations with respect to the sub-grid scale model has been investigated in H2 and H4 using the coarse grid, because it is expected that the model will have less impact on the finer-grid solution. Fig. 3.9 shows the

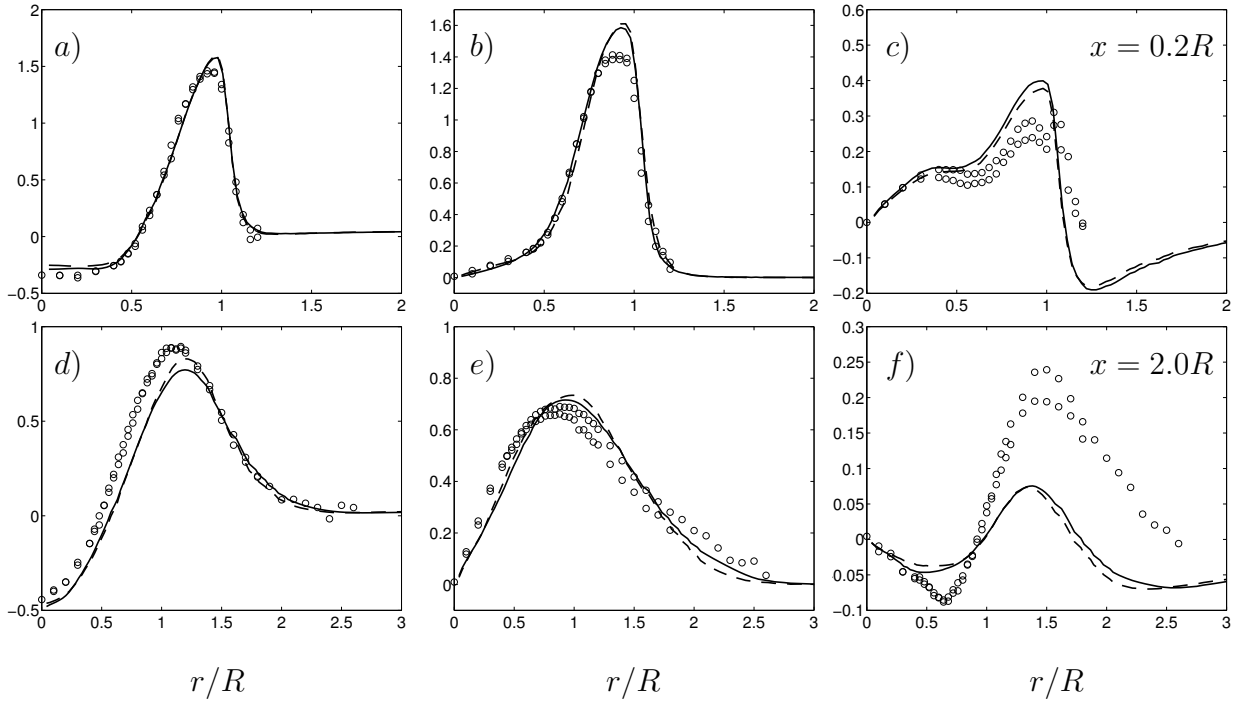

Figure 3.9: Influence of the SGS model. Radial profiles of mean velocity components at $x/R = 0.2$ and 2.0 (top to bottom as indicated in the rightmost column). Solid line, H2; dashed line, H4; symbols, experimental data from Büchner & Petsch (2004). Left, axial velocity, $\langle u_x \rangle / U_b$. Centre, tangential velocity, $\langle u_\theta \rangle / U_b$. Right, radial velocity, $\langle u_r \rangle / U_b$. Observe that the ranges of the vertical axis have been adjusted individually.

mean velocity profiles and Fig. 3.10 the turbulence statistics at the same locations as in the above grid refinement study. Again the agreement is excellent for both mean velocity and the turbulent statistics, which shows that the flow is not very sensitive to the sub-grid scale model. This conclusion was also reached for turbulent swirling flow in a confined configuration by Tang *et al.* (2002). They found that the Smagorinsky model, in spite of its simplicity, gave good results for this kind of flow. Pope (2004) gives an explanation for this. As discussed in Chapter 2, it is reasonable to assume that turbulence possesses scale similarity at high Reynolds numbers, but only over length scales corresponding to the inertial subrange. In the inertial subrange, the Smagorinsky model is, by construction, consistent with the known inertial-range scaling laws. In this circumstance there is, therefore, no substantial need for the dynamic procedure which maintains the

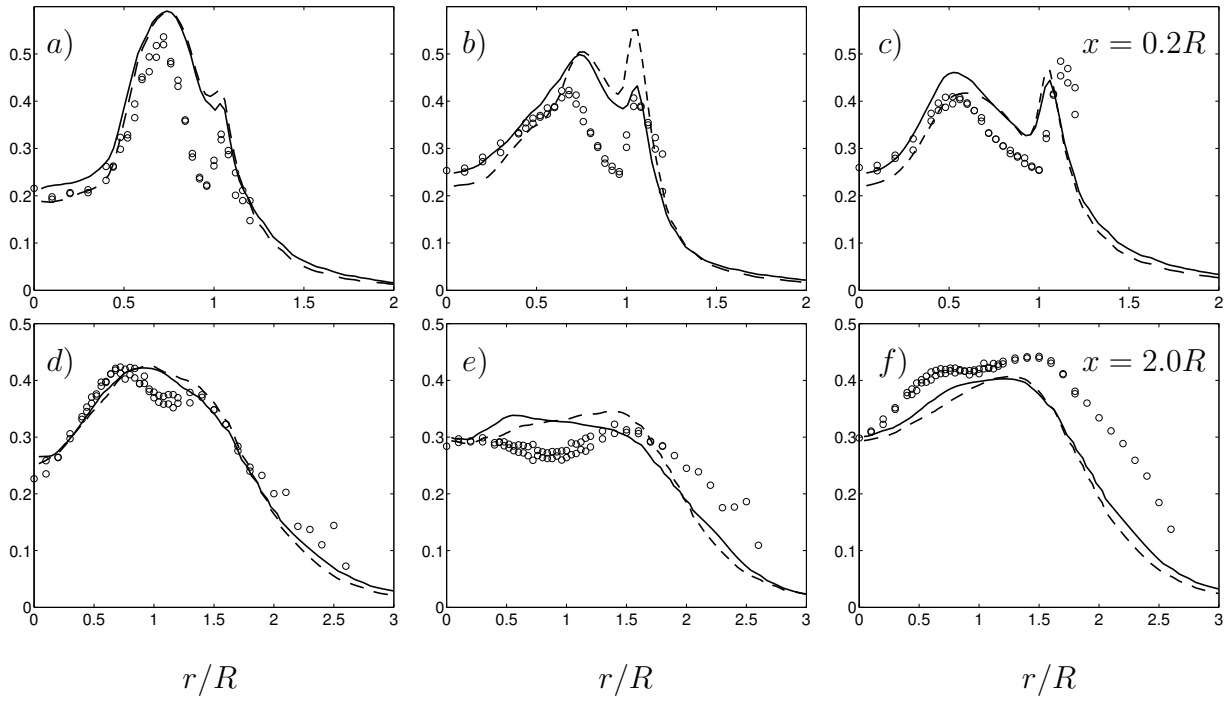

Figure 3.10: Influence of the SGS model. Radial profiles of rms velocity fluctuations at $x/R = 0.2$ and 2.0 (top to bottom as indicated in the rightmost column). Solid line, H2; dashed line, H4; symbols, experimental data from Büchner & Petsch (2004). Left, axial velocity, $\langle u_x^{rms} \rangle / U_b$. Centre, tangential velocity, $\langle u_\theta^{rms} \rangle / U_b$. Right, radial velocity, $\langle u_r^{rms} \rangle / U_b$.

model structure but adds adjustment of the Smagorinsky coefficient. If the grid is fine enough to resolve the large scale motion, so that the unresolved motions lie in the inertial sub-range, the Smagorinsky model should be good enough to obtain satisfactory results. However, it is well known that the dynamic model performs better than the Smagorinsky model in laminar regions, transitional flows and in the viscous near-wall region. The Smagorinsky model is numerically more robust than the dynamic model, the latter can become unstable and lead to numerical instabilities especially when there are no homogeneous directions like in the present investigation. The simulations performed with the Smagorinsky model are also cheaper for two reasons. First, in the dynamic model the determination of the model parameter is relatively expensive because it involves explicit filtering of several fields. Second, the smoothing of the model parameter, which is

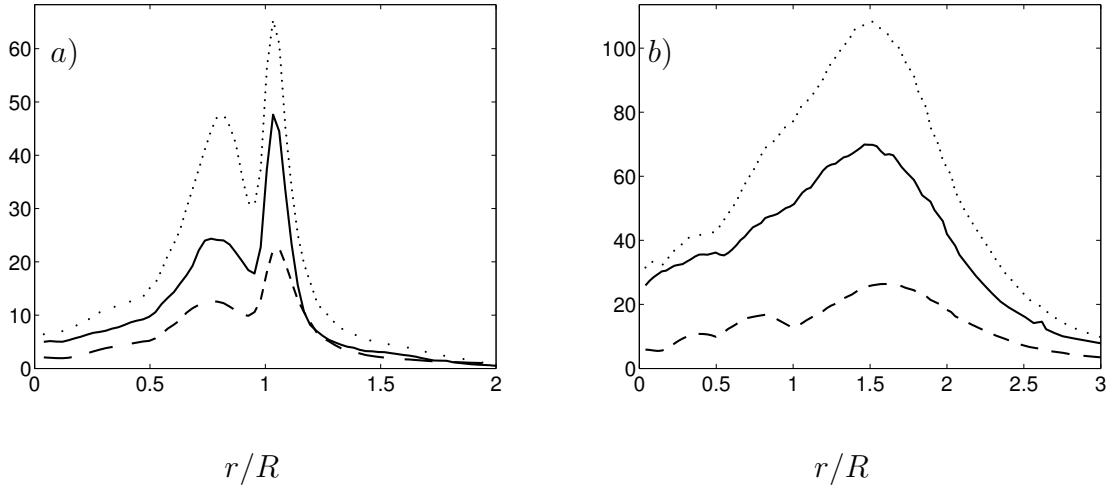

Figure 3.11: Radial profiles of eddy viscosity, ν_t/ν. $a)$ $x/R = 0.2$. $b)$ $x/R = 2.0$. Solid line, H3 with dynamic model on fine grid; dashed line, H4 with Smagorinsky model on coarse grid; dotted line, H2 with dynamic model on coarse grid.

performed in this case by temporal relaxation, §2.1.4.3, is also expensive because it is necessary to discard the initial part of the simulation until the model performs as desired.

To provide an idea of the amount of modelling involved in the simulations, Fig. 3.11 shows the mean eddy viscosity from simulations H2, H3 and H4 at $x/R = 0.2$ and $x/R = 2$. Comparison of simulations H2 (coarse grid, dynamic) and H4 (coarse grid, Smagorinsky) shows that the eddy viscosity in the dynamic model calculations is much larger than when the Smagorinsky model is used. The reason for this might be that with the present numerical method, §2.3, the small-scale motions of the order of the grid spacing are contaminated by numerical error, and the dynamic model, by construction, is able to damp these unphysical motions introducing a higher eddy viscosity. Fig. 3.11 shows that even using the fine grid in H3 the eddy viscosity from the dynamic model is larger than using the Smagorinsky model on the coarse grid in H4.

Another issue related to the sub-grid scale modelling is the influence of the unresolved motions on the turbulence statistics, as discussed in Chapter 2. Recall equation (2.21) which relates the exact turbulence statistics $\langle u_i'^e u_j'^e \rangle$ to the statistics resulting from the resolved motions $\langle u_i'' u_j'' \rangle$ and the average of the sub-grid scale

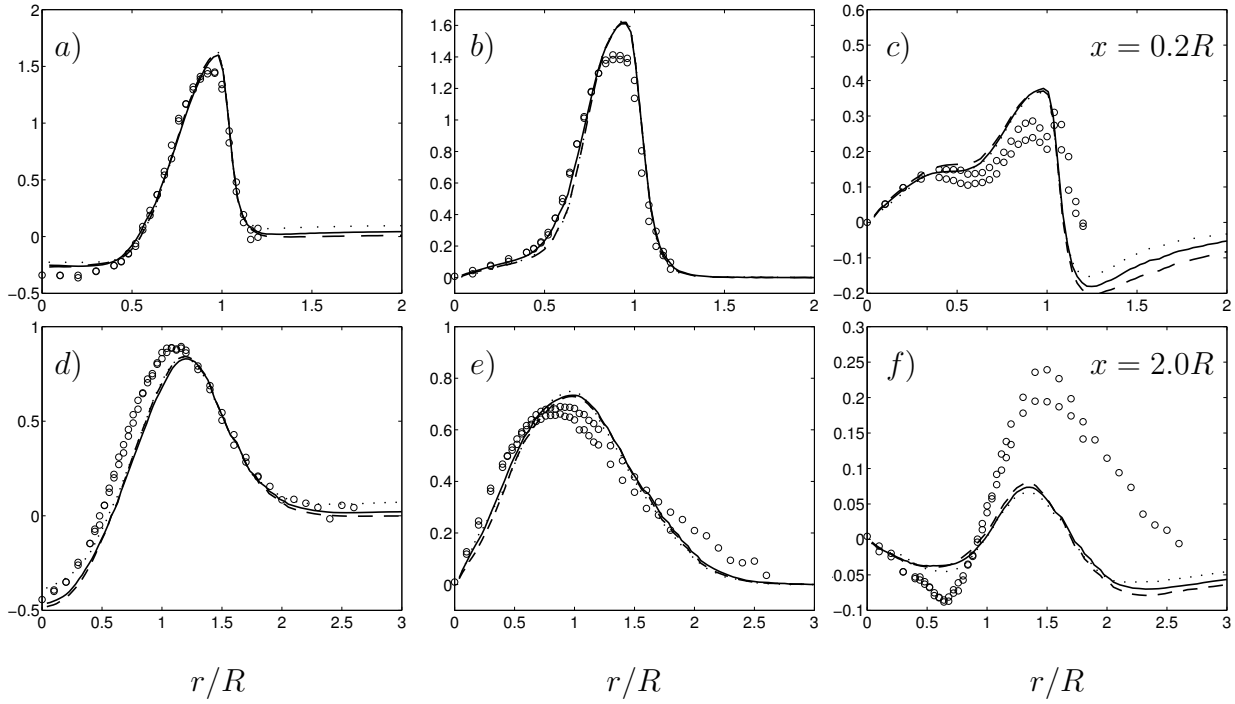

Figure 3.12: Influence of the co-flow. Radial profiles of mean velocity components at $x/R = 0.2$ and 2.0 (top to bottom as indicated in the rightmost column). Solid line, Sim H4; dashed line, Sim H5; dotted line, Sim H6; symbols, experimental data from Büchner & Petsch (2004). Left, axial velocity, $\langle u_x \rangle / U_b$. Centre, tangential velocity, $\langle u_\theta \rangle / U_b$. Right, radial velocity, $\langle u_r \rangle / U_b$. Observe that the ranges of the vertical axis have been adjusted individually.

model $\langle \tau_{ij} \rangle$. In Fig. 3.10 only the resolved motions have been included to compute the turbulence statistics. However, with the high eddy-viscosity of the order of $\nu_t/\nu = 50 - 100$ which occurs in some of the cases, Fig. 3.11, it could be expected that the unresolved motions have some impact on the exact turbulence statistics. The terms $\langle \tau_{ij} \rangle$ have been computed and these contributions turned out to be negligible. In spite of the high ratio of ν_t/ν, the unresolved motions do not have an influence on the turbulence statistics. The large scales carry most of the kinetic energy because the grid is fine enough to resolve the scales up to the inertial sub-range, and then the residual energy is negligible.

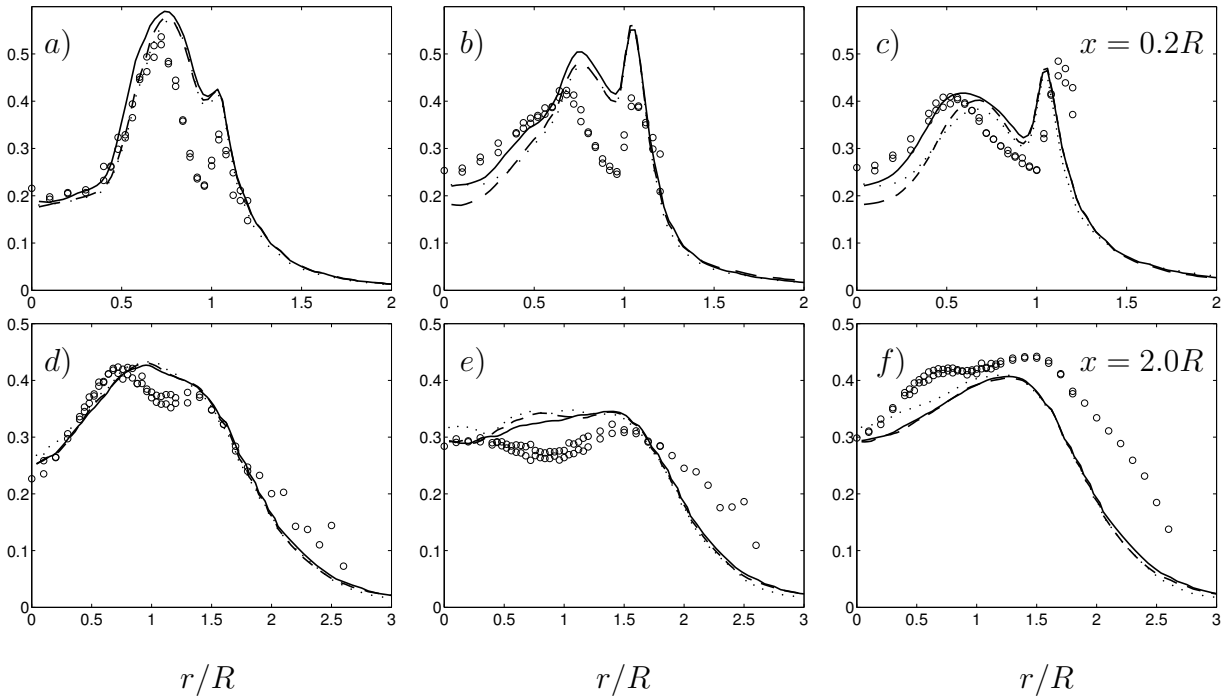

Figure 3.13: Influence of the co-flow. Radial profiles of rms velocity fluctuations at $x/R = 0.2$ and 2.0 (top to bottom as indicated in the rightmost column). Solid line, Sim H4; dashed line, Sim H5; dotted line, Sim H6; symbols, experimental data from Büchner & Petsch (2004). Left, axial velocity, $\langle u_x^{rms} \rangle / U_b$. Centre, tangential velocity, $\langle u_\theta^{rms} \rangle / U_b$. Right, radial velocity, $\langle u_r^{rms} \rangle / U_b$.

3.2.3.3 Co-flow

The sensitivity studies performed in the two previous sections are standard practice in any thorough investigation using LES. In this section we are concerned with an issue more particular to the present configuration, i.e. a jet in an unconfined configuration. A weak co-flow is usually introduced in the simulations of turbulent free jets (see for example Le-Ribault *et al.* (1999); Stanley *et al.* (2002)), in order to feed in the fluid to be entrained. These authors reported that there are no effects on the jet dynamics if the lateral boundaries were placed sufficiently far away and the co-flow is small.

In the present work, three simulations were performed, H4, H5 and H6 (Table 3.1) to check the influence of the co-flow velocity on the results. Figs. 3.12 and 3.13 show the profiles of mean velocity and turbulent statistics at $x/R = 0.2$ and $x/R = 2$ for the three cases. The difference between the cases can be observed

in the profiles of mean axial velocity, Figs. 3.12a and 3.12d, where the velocity in the outer part is slightly different for each case, 0.02U_b, 0.05U_b and 0.1 U_b, respectively. In the profiles of mean tangential velocity, Figs. 3.12b and 3.12e, no difference is observed between the cases, while the difference in the co-flow velocity has a small impact on the entrainment velocity as can be observed in the profiles of mean radial velocity, Figs. 3.12c and 3.12f. Finally, the comparison of the turbulence intensities Fig. 3.13 shows that the influence of the co-flow is minor for these relatively low values of the co-flow velocity.

3.2.3.4 Conclusions from sensitivity studies

The above studies can be summarized as follows. The prediction of the mean flow and the turbulence intensities is satisfactory with both grids and both models showing satisfactory agreement. On the other hand, the simulations with the fine grid and with the dynamic model are more expensive but they offer the possibility to analyze the flow field in more detail because more scales of motion are resolved. This information will be used in the following way. The objective of the rest of this chapter is the detailed analysis of both mean flow and instantaneous flow. For this purpose H1 (fine grid, dynamic model) is used. In Chapter 5 many simulations are used to estimate the influence of the swirl parameter. To perform many simulations is very expensive and therefore these analyses are performed on the coarse grid using the Smagorinsky model.

Finally, from the study of sensitivity to the co-flow velocity, no major differences were found for the three values studied. Thus, in the rest of the thesis all the simulations are performed with a co-flow velocity of 0.05 U_b.

3.2.4 Comparison with experimental data

The remainder of this chapter discusses simulation H1, which uses the fine grid F1 and the dynamic model. In H1 the boundary conditions match the experimental conditions. Fig. 3.14 shows mean velocity profiles at four axial measurement stations in the near field of the jet, ranging from $x/R = 0.2$ to $x/R = 3$. Measurements were performed along a radial line on both sides of the axis. All velocity data are plotted versus the radial coordinate so that points of measurement at op-

posite sides of the symmetry axis appear together. This provides an estimation of the experimental uncertainty. The overall agreement between experiment and simulation is very good at most stations. Particularly good is the agreement at $x/R = 0.2$, Fig. 3.14a-c. This suggests that the experimental inflow conditions are modelled properly. The available experimental data are confined to the range between $x/R = 0.2$ and $x/R = 3$. Therefore, the length of the recirculation zone cannot be compared, but the mean axial velocity profiles in Fig. 3.14 show that until $x = 3R$ the shape of the recirculation zone is well predicted. The spreading of the jet is also in good agreement with the experimental data.

The radial velocity component was the most difficult component to measure in the experiment (Büchner & Petsch, 2004), reflected by the scatter in these data. The agreement close to the jet outlet is quite good, as seen in Figs. 3.14c and 3.14f, whereas a fairly significant difference is observed at $x/R = 2$ and $x/R = 3$, Figs. 3.14i and 3.14l. In order to investigate this issue, the continuity equation for the averaged flow

$$\frac{\partial \langle u_x \rangle}{\partial x} + \frac{1}{r}\frac{\partial (r\langle u_r \rangle)}{\partial r} = 0, \tag{3.2}$$

can be used. Defining $q_1 = -r\partial\langle u_x\rangle/\partial x$ and $q_2 = \partial(r\langle u_r\rangle)/\partial r$, it reads $q_1 = q_2$. These terms are estimated from the experimental data. At $x = 2R$, q_1 has been estimated using central differences and the experimental profiles of $\langle u_x \rangle$ in Figs. 3.14d and 3.14j. The profile of $\langle u_r \rangle$ in Fig. 3.14i has been used to estimate q_2. Fig. 3.15 shows the profiles of q_1 and q_2 at $x = 2R$. It is clear that these data do not fulfill continuity. In this figure, q_1 obtained from the simulation is also shown and the agreement with the experiment is remarkable. The analysis therefore hints to a systematic error in the measurement of the radial velocity component at this location.

Fig. 3.16 shows the turbulent fluctuations of the three velocity components (for the LES only the resolved part). The qualitative agreement between experimental and computational results is good for all three components. As with the mean velocities, the agreement is better for the axial and azimuthal fluctuations than for the radial component. Although the qualitative agreement is good, the calculation tends to slightly under-predict the turbulent intensities. As the eddy viscosity in the present formulation of the dynamic model is clipped to avoid negative values,

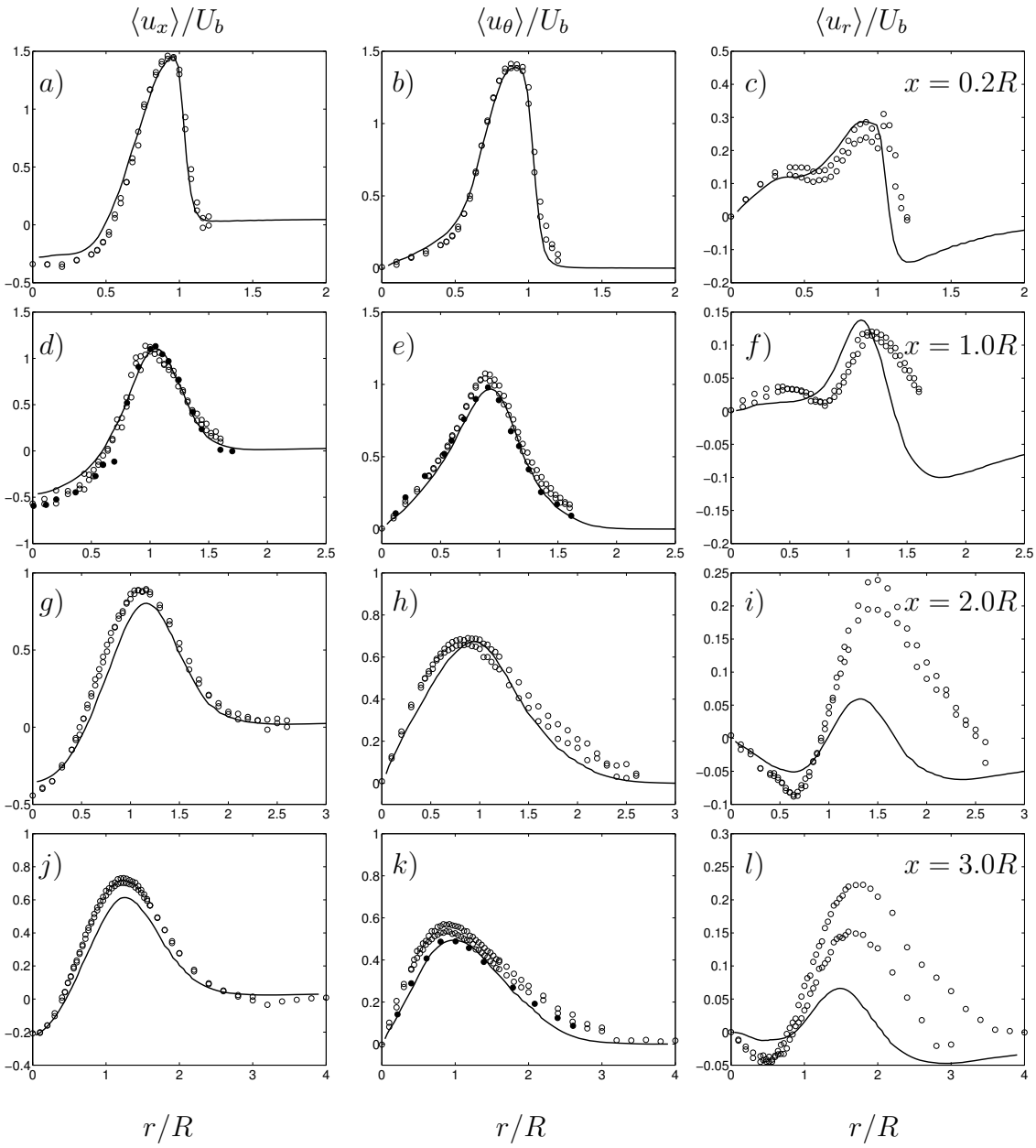

Figure 3.14: Radial profiles of mean velocity components at $x/R = 0.2, 1.0, 2.0$ and 3.0 (top to bottom as indicated in the rightmost column). Solid line, H1; open symbols, experimental data from Büchner & Petsch (2004); closed symbols, experimental data from Hillemanns (1988). Left, axial velocity, $\langle u_x \rangle / U_b$. Centre, tangential velocity, $\langle u_\theta \rangle / U_b$. Right, radial velocity, $\langle u_r \rangle / U_b$. To enhance readability the range of the vertical axis has been adjusted individually.

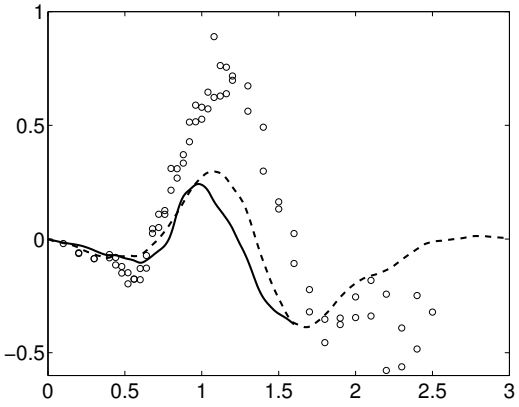

Figure 3.15: Radial distribution of the terms in the continuity equation for the averaged flow eqn. (3.2) at $x = 2R$. Solid line $q_1 = -r\partial\langle u_x\rangle\partial x$ estimated from the experiment. Dashed line q_1 from the simulation. Symbols $q_2 = \partial(r\langle u_r\rangle)\partial r$ estimated from the experiment.

backscatter is not accounted for, and this results in an excess of dissipation, especially in the region of the jet where the fluid is entrained. It is well known that eddy-viscosity models are deficient in such a region because the entrainment is a very intermittent phenomenon. Nevertheless, this is not the only reason for the disagreement. It is well known that the experimental technique has also difficulties in the outer region of the flow (Jones, 2005). LDA measurements are based on the tracking of micro-particles which are seeded, in this case, within the jet. In the surrounding ambient on the other hand no particles are seeded. When a particle is detected at the interface between the jet and the ambient, it comes from the jet and hence it has a high velocity. Patches of fluid which originate in the ambient flow have a low velocity and are not accounted for in the measurement proccess because they are void of particles. A bias towards high velocities is produced in the interface region.

It should be stressed, as in the case of the mean velocities, that the agreement at $x = 0.2R$ is very good, Figs. 3.16a-c. Hence, in spite of the strong idealization applied to the inlet geometry, avoiding the swirl-generating device, and the specification of steady laminar inflow conditions at the entry of the inlet duct, this procedure yields the correct turbulent fluctuations at the inlet into the main

domain, i.e. at the jet exit. The fluctuations induced in the shear layers can be observed in Fig. 3.16a-c. The inner layer generates substantial fluctuations between $r/R \simeq 0.5$ and $r/R \simeq 0.9$, while in the central region of the domain the level of turbulence is much smaller. The outer layer is much thinner than the inner one, but there is also a peak of turbulence intensity associated with it around $r/R \simeq 1.1$.

3.3 Instantaneous flow

3.3.1 Dominant structures

In this section the instantaneous flow is discussed with special emphasis on coherent structures. Fig. 3.6, already discussed above, shows velocity vectors in an axial plane of the time-averaged flow and a snapshot of the instantaneous flow. The comparison of these two plots gives an impression of the high level of turbulence, especially in the near field of the jet.

It is well known that coherent structures are associated with local minima of the pressure field (Jehong & Hussain, 1995; Dubief & Delcayre, 2000). Previous studies (Fröhlich *et al.*, 2005) have shown that the pressure fluctuation is more suitable for the visualization of coherent structures than the commonly used instantaneous pressure. Iso-surfaces of the latter are influenced by the spatially-variable average pressure field which is unrelated to instantaneous structures. This is avoided when $\langle p \rangle$ is substracted from the instantaneous value. Fig. 3.17a shows an iso-surface of the instantaneous pressure fluctuation $p'' = p - \langle p \rangle$. In order to facilitate the interpretation, additional smoothing was applied to p'' in post-processing. This was achieved through two consecutive applications of a three-dimensional box filter of size 2Δ, which is in fact the test filter used in the dynamic procedure. Fig. 3.17b displays the smoothed field and shows that the filtering procedure does not affect the large-scale coherent structures, which validates this procedure for the present case.

Two families of structures are visible in Fig. 3.17. In the inner region of the jet, elongated helical vortices are observed (labeled I) while those in the outer region (labeled O) are also helical but oriented at a substantially larger angle with

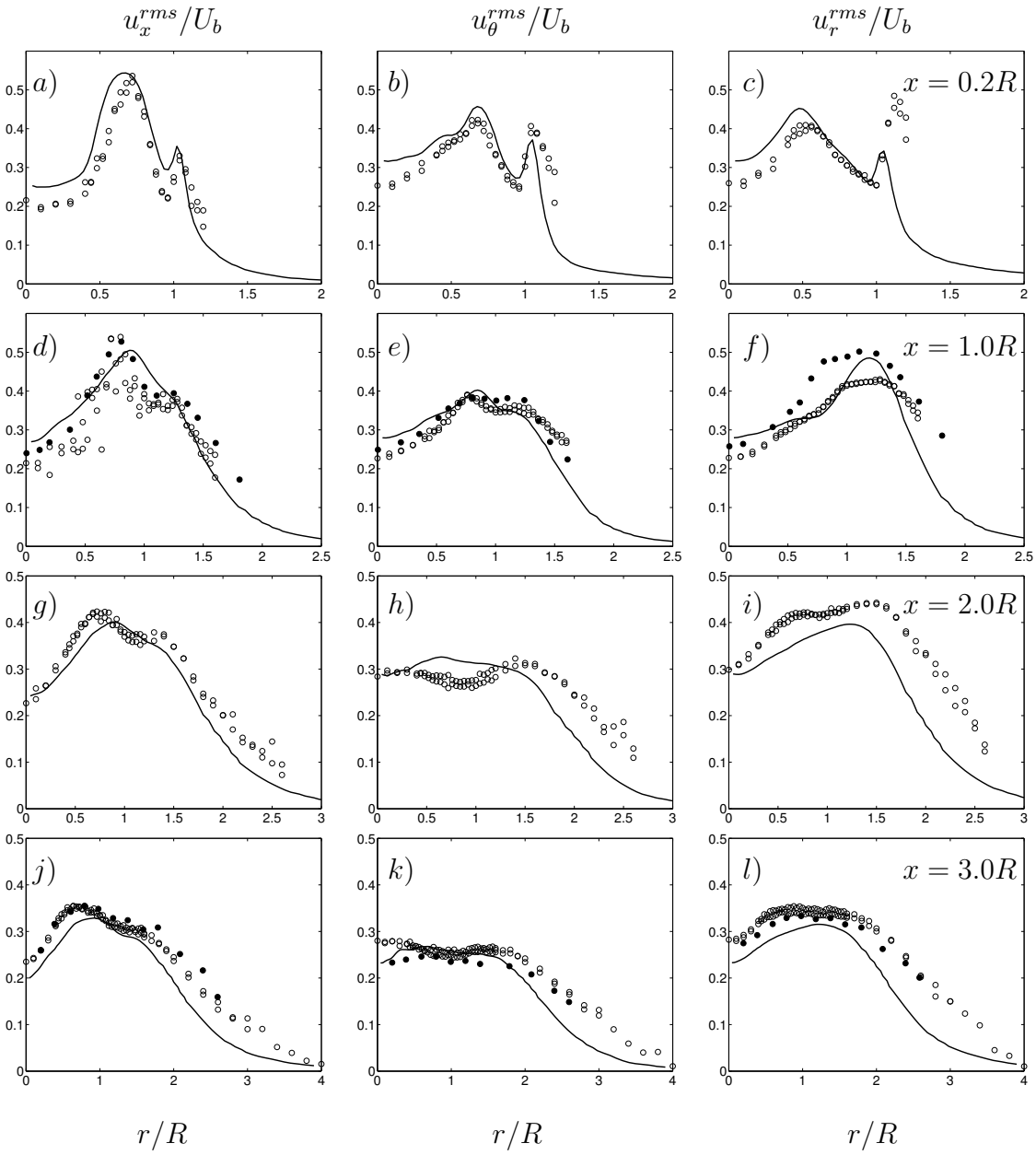

Figure 3.16: Radial profiles of rms velocity fluctuations at $x/R = 0.2, 1.0, 2.0$ and 3.0 (top to bottom as indicated in the rightmost column). Solid line, H1; open symbols, experimental data from Büchner & Petsch (2004); closed symbols, experimental data from Hillemanns (1988). Left, axial component, u_x^{rms}/U_b. Centre, tangential component, u_θ^{rms}/U_b. Right, radial component, u_r^{rms}/U_b.

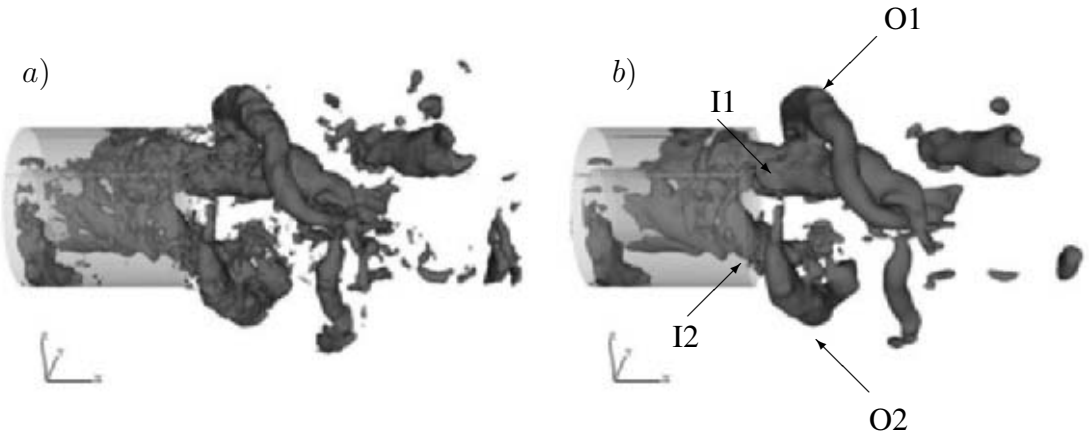

Figure 3.17: Isosurface of instantaneous pressure fluctuations, $p - \langle p \rangle = -0.3$. a) Original field computed in H1. b) Filtered field employed for visualization.

respect to the x-axis. In this snapshot two structures of each type co-exist. One of the inner vortices (labeled I1) is more pronounced than the other (labeled I2). In animations of the flow it has been observed that up to three of these vortices can co-exist at certain instants in time (see Fig. 3.21 below). Most of the time, however, a single vortex is dominant as in Fig. 3.17b. Both families of vortices are rapidly damped further downstream. At $x/R \simeq 2$ they are already very weak. It is worth noting that the inner structures extend considerably upstream of the jet outlet into the annular pipe. The prescription of inlet conditions at the position of the jet exit, e.g. by assuming fully developed turbulent annular pipe flow, is therefore not adequate for the present case. Rather, the inflow conditions need to be specified substantially upstream of the exit, as will be discussed in Chapter 4.

In order to show the evolution of the vortices in time, Fig. 3.18 displays the same isosurface as Fig. 3.17b at three different instants. For clarity, views from two different angles are provided. The structures rotate around the symmetry axis at a constant rate, clockwise when looking upstream. The pictures in the figure cover an interval of roughly half a rotation period in time.

The inner and outer vortices in Figs. 3.17 and 3.18 are very close to each other and it is difficult to distinguish if they are actually two structures, or if it is just one complex vortex. The computations and analyses performed yield the following conceptual picture: the annular jet creates two shear layers, one on

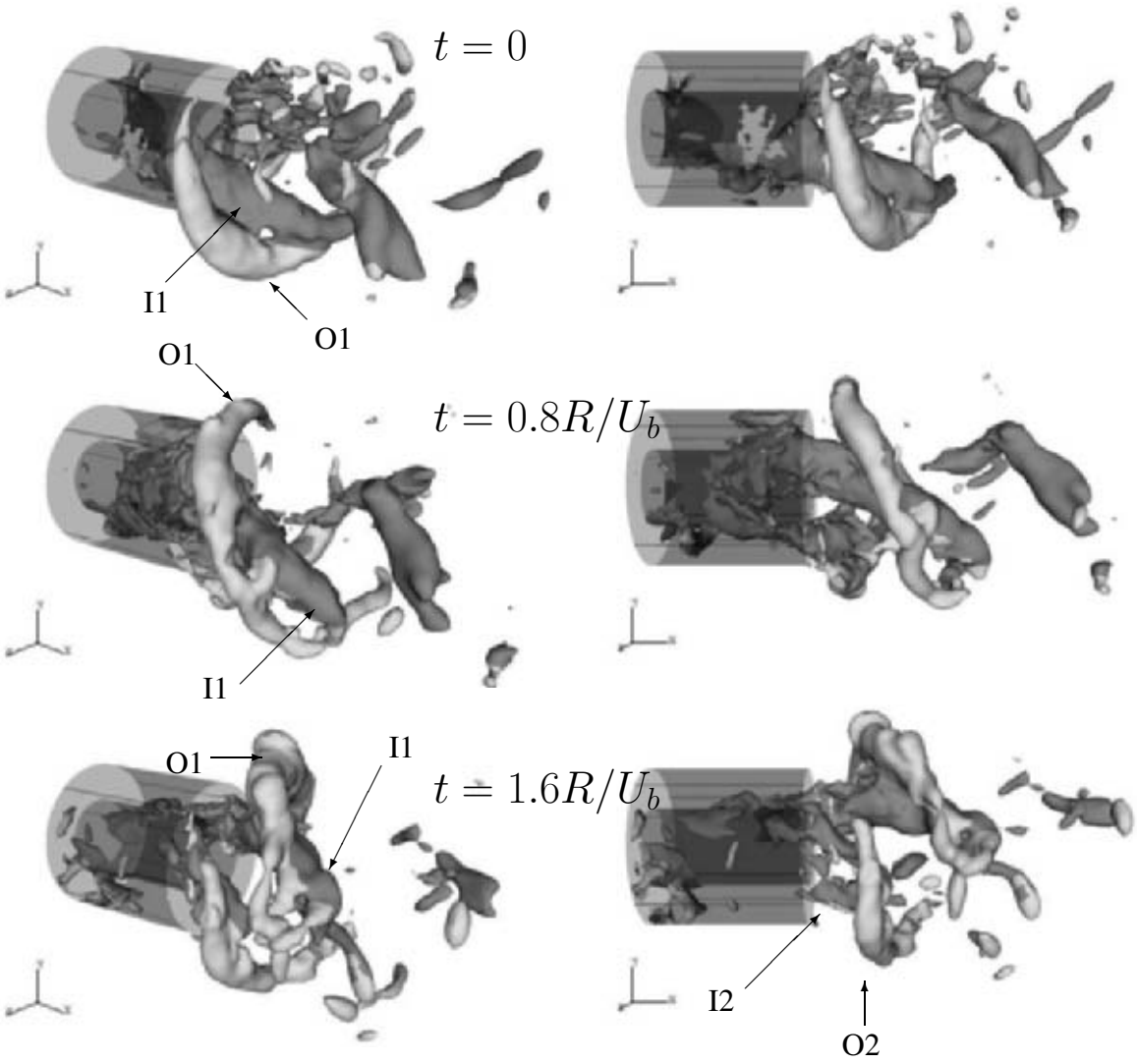

Figure 3.18: Isosurface of instantaneous pressure fluctuations (smoothed), $p - \langle p \rangle = -0.3$ from H1 at three instants in time. The colour is given by: $(\partial \langle u_x \rangle / \partial r) > 0$, dark; $(\partial \langle u_x \rangle / \partial r) < 0$, bright. Swirl is clockwise when looking upstream in axial direction.

its border with the recirculation zone and the other one on its border with the surrounding ambient fluid. Both are prone to the Kelvin-Helmholtz instability. Fig. 3.14a, above, shows the mean axial velocity at $x/R = 0.2$. At this axial station, the inner shear layer extends from $r/R \simeq 0.4$ to $r/R \simeq 1$. The outer one from $r/R \simeq 1$ to $r/R \simeq 1.2$. Both shear layers can be distinguished by the radial derivative of the mean axial velocity, i.e. $\partial\langle u_x\rangle/\partial r$. In the inner shear layer this quantity is positive and in the outer one it is negative. Therefore, the iso-surface in Fig. 3.18 has been coloured with the sign of $\partial\langle u_x\rangle/\partial r$. The fact that the inner and outer structures are so close is due to the small separation between the shear layers. To support this interpretation, an additional simulation has been performed with a Swirl number of $S = 0.85$ at $x/R = -2$, i.e. 30 % below the value used for the main simulation discussed here. When S is lower, the shear layers are more separated than in the original case. This can be seen in Fig. 3.19, which shows the mean axial velocity profile at $x/R = 0.2$ for both simulations, together with a rough estimation of the widths of the shear layers and the radial separation between the inner and the outer one for each case. The two kinds of vortex structures should therefore be further apart. This is indeed observed in Fig. 3.20, which shows an instantaneous snapshot of an iso-surface of pressure fluctuations in a similar way as the previous ones.

3.3.2 Precessing vortex cores

In the literature on the subject, the inner structures, labeled I in Fig. 3.18, are known as precessing vortex cores (PVC) (Gupta *et al.*, 1984; Coats, 1996). The motion of the PVC can be decomposed into two components. The swirling motion of the main flow rotates the vortex core around the symmetry axis, at the same time the vortex spins around its own axis. An idealized sketch of this motion is shown in Fig. 3.21d. As the vortex is oriented preferentially in streamwise direction for this level of swirl (see Fig. 3.18d), its presence generates radial and tangential velocity fluctuations. In addition to this motion a high level of axial velocity fluctuations is observed in the interior of the PVC. This is visualized in Fig. 3.21 which shows contour plots of axial velocity fluctuations and pressure fluctuations close to the outlet at $x = 0.2R$. This plane was chosen since plots

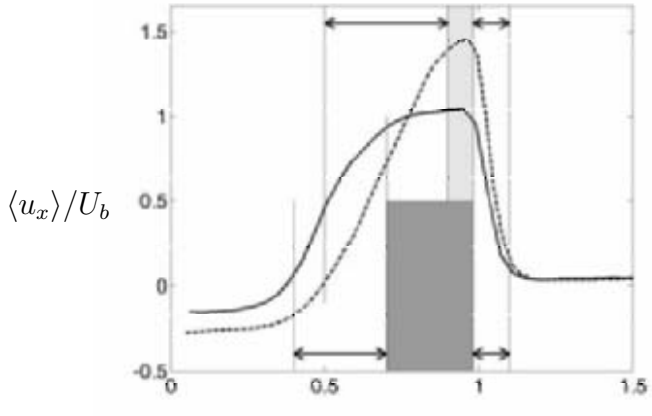

Figure 3.19: Mean axial velocity $\langle u_x \rangle / U_b$ at $x/R = 0.2$. Dashed line, original simulation H1. Solid line, simulation with a lower level of swirl, $S = 0.85$. The arrows indicate the approximate width of the inner and outer shear layers for both simulations. The patches show the resulting radial separation between the inner and the outer shear layer. Light patch, original simulation H1. Dark patch, simulation with lower swirl.

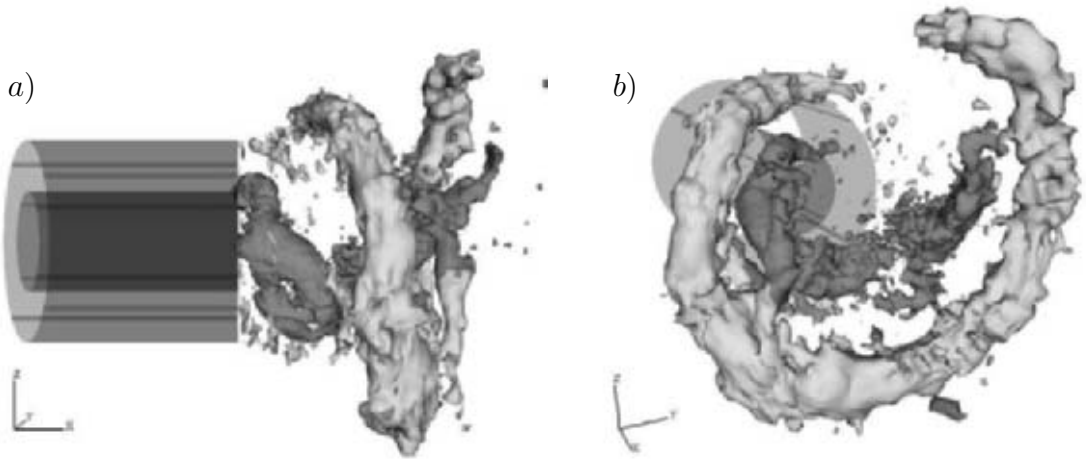

Figure 3.20: Coherent structures from a simulation with a lower level of swirl, $S = 0.85$ at $x/R = -2$, visualized by instantaneous pressure fluctuations (unsmoothed), coloured as in Fig. 3.18. $a)$ Side view. $b)$ View from downstream.

like those in Fig. 3.18 show that the inner structures are strongest in this part of the domain. The PVC can be identified as the region of low pressure fluctuations in Fig. 3.21b, which is marked with an arrow. At the same position, a region of positive axial velocity fluctuations can be seen in Fig. 3.21a, while a large region of negative fluctuations is also present with a phase difference of approximately $180°$. Fig. 3.22 shows time signals of pressure and axial velocity close to the jet exit and Fig. 3.23 its corresponding cross-correlation. In the signals the minima of the pressure represents the quasi-periodic passing of the PVC through the point in which the signal has been recorded. As Fig. 3.21 already suggests, there is a strong correlation between the minima of the pressure and the maxima of the axial velocity. Observe the large amplitude of the velocity signal and the occurrence of negative values. This issue will be discussed further below.

The PVC was detected experimentally some thirty years ago (Syred & Beér, 1974) but the origin of these structures it is still not totally clear. In a series of experimental studies (Syred *et al.*, 1994; Froud *et al.*, 1995; Syred *et al.*, 1997) a possible mechanism for the formation of the PVC in a confined configuration was proposed. However, this cannot explain why the PVC is also observed in open configurations, and why it is possible that several PVCs coexist at the same instant. Schlüter (2000), without further support, mentions that the vortex could develop as a Taylor-Görtler instability, or as a shear layer instability in the circumferential direction, like in the Kelvin-Helmholtz instability.

To address the issue it should be recalled that in the Taylor-Görtler instability, the vortex axis is parallel to the mean flow (Schlichting & Gersten, 1996), while in the Kelvin-Helmholtz instability the vortex axis is perpendicular to the mean flow. Fig. 3.24 shows the inner coherent structures in the present LES and selected three-dimensional streamlines of the mean flow. The origin of the latter has been positioned in the inner region of the jet. The streamlines were computed only downstream. Obviously, the vortex axis is not parallel to the streamlines but orthogonal to them. This fact supports the interpretation that the precessing vortex core is generated by a shear-layer instability, i.e. a Kelvin-Helmholtz instability, of the inner shear layer.

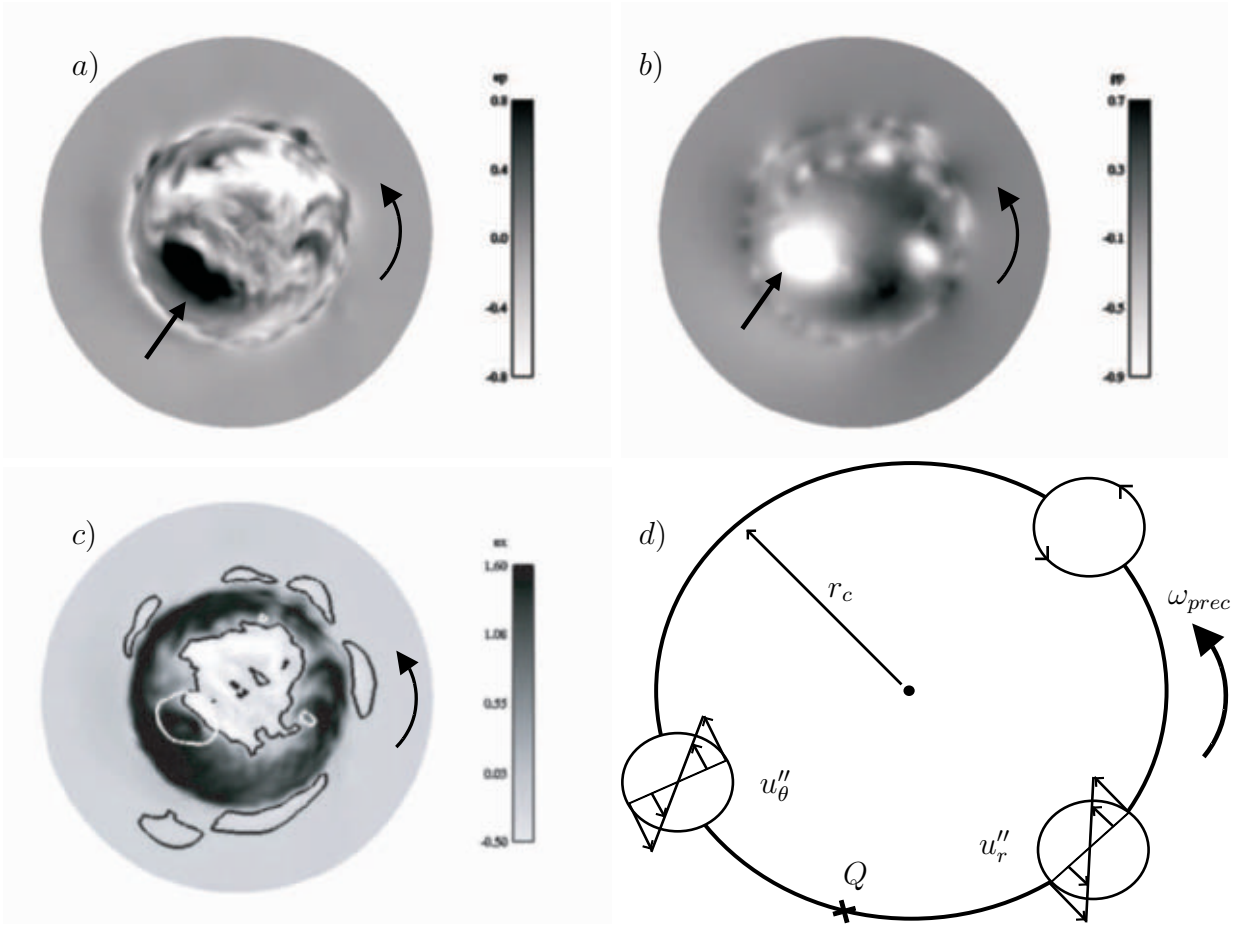

Figure 3.21: $a-c)$ Contour plots in a transverse plane at $x/R = 0.2$ and the same instant in time. The straight arrows point at the dominant PVC observed at this instant. The curved arrows indicate the sense of rotation. $a)$ Instantaneous axial velocity fluctuations. $b)$ Instantaneous pressure fluctuations. $c)$ Instantaneous axial velocity component. The white line is a pressure fluctuation contour $p - \langle p \rangle = -0.7$ extracted from the data shown in $b)$. The black line is the boundary of the recirculation zone $u_x = 0$. $d)$ Idealized sketch of the PVC motion in the transverse plane.

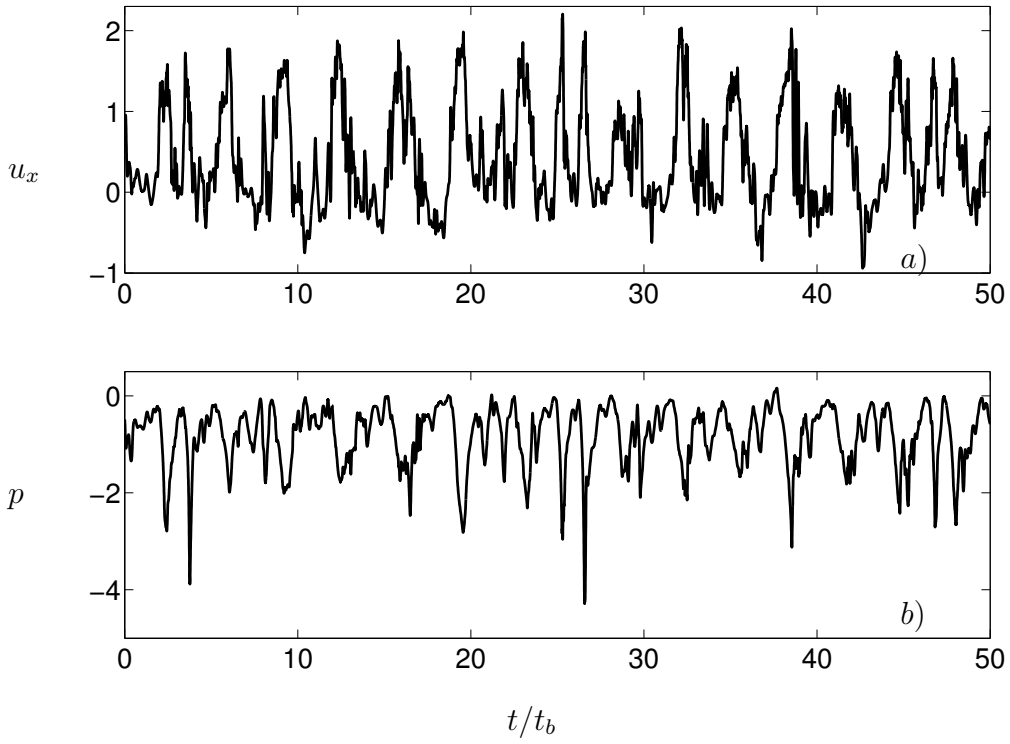

Figure 3.22: Time signal at $x/R = 0.1$, $r/R = 0.6$. a) Axial velocity. b) Pressure.

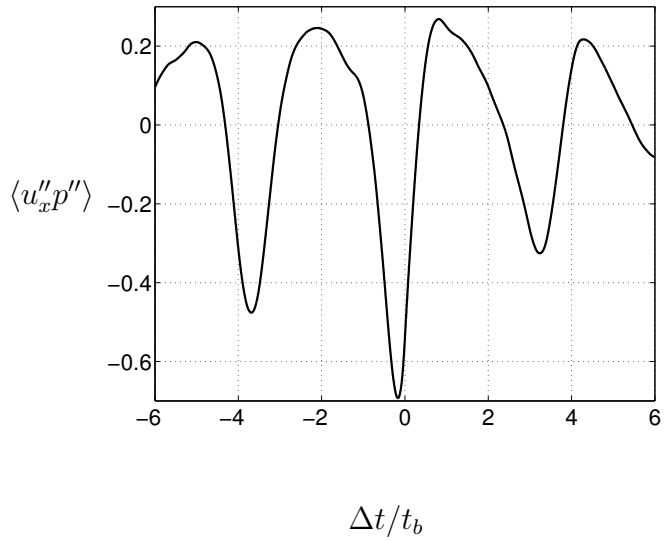

Figure 3.23: Temporal cross-correlation of axial velocity and pressure fluctuations $\langle u_x''(t)p''(t + \Delta t)\rangle$ at $x/R = 0.1$, $r/R = 0.6$.

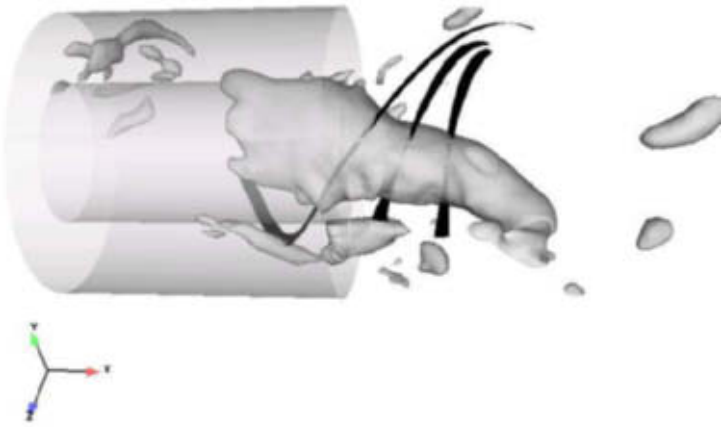

Figure 3.24: Coherent structures of the instantaneous flow as in Fig. 3.18 but the level of the iso-surface is $p - \langle p \rangle = -0.5$. Only the inner region $r < R$ is shown. The black lines represent stream ribbons of the averaged flow issued at different positions in the inner region of the jet around $r/R \sim 0.5$.

3.3.3 Fluctuations of axial velocity component

Phase-averaged measurements in a typical swirl-burner configuration have shown that the distribution of axial velocity was asymmetric (Froud *et al.*, 1995). The highest forward velocities were measured near the outer edge of the swirling flow but the forward velocities in the region containing the PVC were up to 50% larger than the velocities in the diametrically opposite region. The region of reverse flow was found to be located on the opposite side of the core from this region of highest forward velocity. Fig. 3.21c shows a contour plot of an instantaneous axial velocity field together with a white line showing the position of the PVC and a black line corresponding to $u_x = 0$. This plot confirms the findings of Froud *et al.* (1995). However, by comparison of Figs. 3.21a and 3.21c it is observed that the region of highest forward velocity does not correspond to the region of highest forward velocity *fluctuations* u_x''; the highest values of forward velocity fluctuations in Fig. 3.21a are substantially remote from the outer edge of the annular jet while the largest values of u_x in Fig. 3.21c are observed very close to the outer edge (see also Figs. 3.14a and 3.16a). The axial velocity fluctuations

are very large with velocity differences of up to $2.5U_b$. A typical time signal is shown in Fig. 3.22a. In order to see that the region of highest forward velocity fluctuations is indeed associated with the PVC, Fig. 3.23 shows the temporal cross-correlation between the axial velocity and the pressure $\langle u_x''(t)p''(t+\Delta t)\rangle$. The negative correlation shows that the low pressure which is related to the vortex core is correlated with the high forward velocity. The maximum correlation is not achieved for $\Delta t/t_b = 0$ but for $\Delta t/t_b = 0.16$. This is due to the fact that the pressure is minimum at the vortex core while the velocity fluctuation is maximum at the outer edge of the PVC and lags somewhat behind it. The time $2\Delta t/t_b = 0.32$ gives an estimation of the time it takes for a PVC to pass through a point at this radial location. (The factor 2 appears in the expression because Δt accounts only for the radius of the vortex)

Fig. 3.25 shows spatial two-point auto-correlations of the three velocity components with respect to the angular separation $\Delta\theta$ at $x/R = 0.1$ $r/R = 0.6$. The axial velocity autocorrelation is different with respect to the other two components. It does not go to zero when the angular separation increases but saturates at a negative value of -0.2 for $\Delta\theta = 120^\circ$ to 180°. This is explained by the two regions of positive and negative axial fluctuations which were observed in Fig. 3.21a. The radial location where the correlations are computed, $r/R = 0.6$, is positioned slightly radially outwards of the center of the PVC (see also Fig. 3.32a below). Therefore, as illustrated by the sketch in Fig. 3.21d, u_θ'' is always positive and the tangential-velocity autocorrelation does not become negative. On the other hand, the radial fluctuations decay from positive to zero at $\Delta\theta = 35^\circ$ and remain negative for larger angles approaching zero. The minimum of the radial-velocity auto-correlation at $\Delta\theta = 60^\circ$ provides an estimate of the angular size of the vortex.

3.3.4 Outer structures

The outer structures are not mentioned as often in the literature as the precessing vortex core. Gupta *et al.* (1984) described them as "a large eddy in the radial-axial direction which is shed in a continuous process behind the passing PVC". Fig. 3.26 shows the coherent structures and selected three-dimensional streamlines of

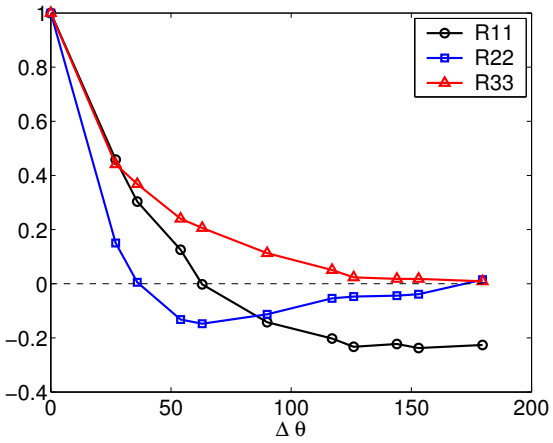

Figure 3.25: Spatial two-point autocorrelation as a function of angular separation at $x/R = 0.1$, $r/R = 0.6$. R11, axial velocity. R22, radial velocity. R33, tangential velocity.

the mean flow passing through the outer structures. The origins of the streamlines are at $x/R = 0$, $r/R = 0.95$, i.e. in the outer region of the jet, at four different angles. It can be seen, as in the case of the inner structures, that the structures are ortoghonal to the average streamlines. This explains the creation of the outer structures by a Kelvin-Helmholtz instability of the outer shear layer, as described above for the inner structures. In Fig. 3.18 and corresponding animations, it is possible to see that the appearance of the outer structure is indeed 'locked' to the presence of the inner one. A possible explanation is that the inner structures are associated with high axial velocities, and as they pass the high velocity region triggers the formation of the outer structures.

3.3.5 Secondary structures

To conclude the analysis of the coherent structures, Fig. 3.27 shows an isosurface of unfiltered pressure fluctuations. The color in the figure just represents the radial distance from the symmetry axis and has been included to facilitate the visibility of the vortices discussed. It can be seen that the large-scale coherent structures generate secondary instabilities oriented in streamwise direction and located at the outer boundary of the outer spirals. Only accidentally, the smoothed plot in Fig. 3.26 exhibits "blobs" reminiscent of these, near the crossings of the

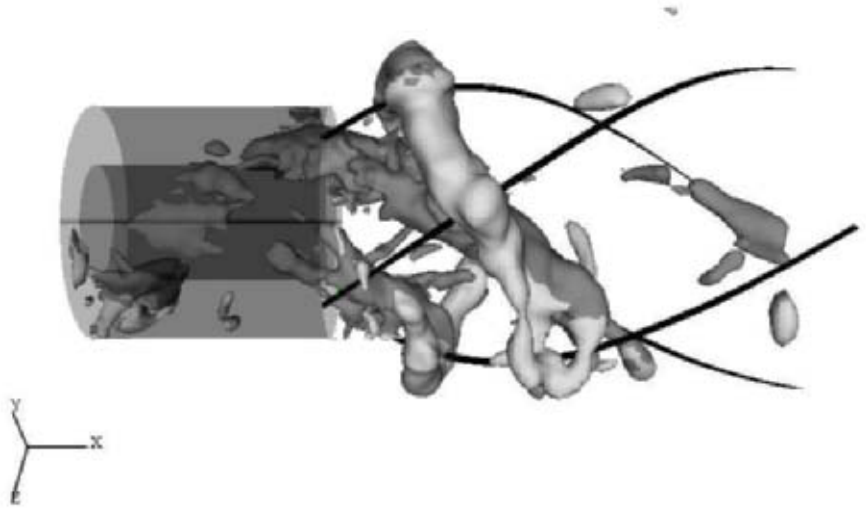

Figure 3.26: Coherent structures of the instantaneous flow as in Fig. 3.18. The black lines represent stream ribbons of the averaged flow issued at $x/R = 0$, $r/R = 0.95$ and four angular positions with an angular distance of $\Delta\varphi = 90^o$.

average streamlines plotted in this figure. These secondary structures resemble the structures in a plane shear layer where counter-rotating vortex pairs, oriented preferentially in streamwise direction and usually known as "braids", are formed between the spanwise primary structures due to the stretching of the flow. In the present simulation, the secondary vortices observed seem to appear at a relatively large spacing, but so far quantitative statements cannot be made.

3.4 Analysis of spectra

3.4.1 Computational procedure and general shape

In the experiment (Büchner & Petsch, 2004), time signals of velocity have been recorded close to the jet exit at $x/R = 0.1$, $r/R = 0, 0.6, 0.8$. During the simulation, velocity and pressure signals were recorded at the same positions for a duration of 115 t_b. Furthermore, signals were recorded for each of these positions at 12 different angular locations over which additional averaging was performed. Fig. 3.22 shows a small part of a time signal of the axial velocity and the pressure

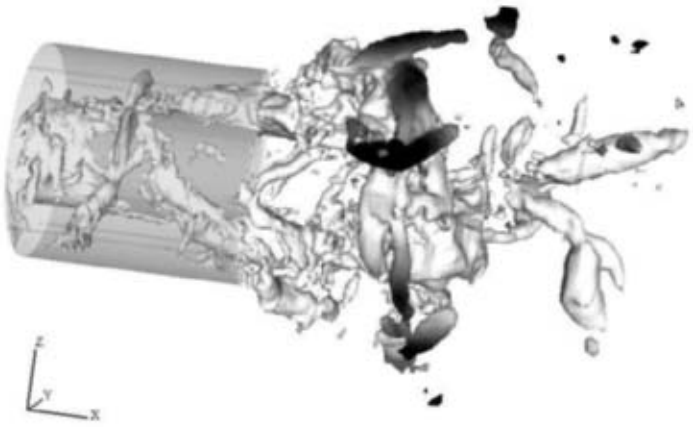

Figure 3.27: Unsmoothed iso-surface of pressure fluctuations $p'' = -0.3$. It has been coloured according to the radial coordinate to highlight secondary structures in streamwise direction which are located at the outer boundary of the outer spiraling vortices.

at $x/R = 0.1$, $r/R = 0.6$. The precessing vortex cores discussed in the previous section are expected to pass right through this point. Indeed, the presence of the structures is indicated by the large oscillations observed in the time signals of both axial velocity and pressure. An analysis of the power spectral density (PSD) is used to obtain the frequencies of rotation. The analysis was performed using a windowed Fourier transform with a Hann window (Oppenheim & Schafer, 1989) and segments of length 2^{11}, i.e. spanning a length of 32.8 time units. The full signal was decomposed into eight such overlapping segments over which averaging was performed. These parameters were selected so as to obtain the best-possible compromise between smoothness of the spectra and width of the frequency windows covered.

Fig. 3.28 shows the power spectral density of the axial velocity fluctuations at $x/R = 0.1$, $r/R = 0.6$, i.e. very close to the jet exit and in the region of the inner shear layer. It exhibits several ranges. At low frequencies several peaks appear which represent the energetic content of the coherent structures. This is followed by a region in which a regular decay of slope -5/3 takes place over about

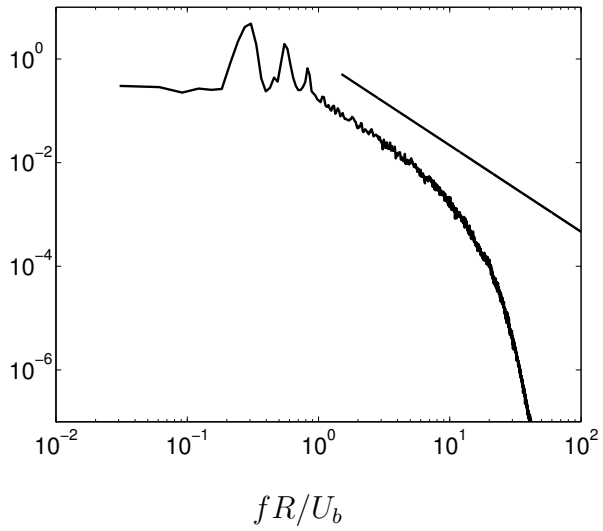

Figure 3.28: Power spectral density of axial velocity fluctuations at $x/R = 0.1$, $r/R = 0.6$. The straight line has a slope of $-5/3$.

one decade in frequency. Finally there is a high-frequency region of faster decay which is related to the effective filter of the LES. In the experiment it was not possible to measure frequencies in the turbulent inertial subrange. The maximum resolved frequency was about $fR/U_b = 2$. In the graphs below the comparison with the experiment is therefore performed only in this range.

3.4.2 Dominant frequencies

Fig. 3.29 shows a comparison of power spectral densities of velocity fluctuations between experiment and simulation at $x/R = 0.1$, $r/R = 0.6$ (later it will be important that in the simulation the position actually was $r/R = 0.605$). The inner structures are expected to pass through this point, as evidenced by the previous visualizations. Indeed, they generate a pronounced peak and higher harmonics. All power spectral densities are normalized with the energy of the signal up to the frequency which was available in the experiment. As the energy at higher frequencies in the simulation is not negligible, its inclusion in the normalization would affect the comparison with the experiment. The agreement is excellent for the axial and radial velocity components in terms of the dominant frequency, even with respect to the amplitude of the corresponding peaks. Concerning the tangential velocity component, the frequency is in good agreement, but the shape

of the spectrum is different with respect to the amplitude of the peaks. This will be addressed further below. The precessing frequency of the vortices corresponds to the first peak, and the higher harmonics correspond to the number of vortices present in the flow field. In visualizations as displayed in Figs. 3.18 and 3.21 up to three precessing vortex cores of different strengths were observed at certain instants. Most of the time, however, only one PVC is present and this is why the first peak is more pronounced. In the spectrum of the radial velocity, Fig. 3.29b, the first two peaks have similar amplitude. This is due to the following effect. For the axial fluctuations u_x'', a dominant structure such as seen in Fig. 3.21a yields a single temporal increase of the signal measured at a point like Q in Fig. 3.21d. For the radial fluctuations u_r'', a single passage of a vortex first produces negative then positive radial fluctuations as sketched in Fig. 3.21d, hence a spectrum with doubled frequency. The simulation predicts very accurately the frequencies of the principal peak: $f_{peak} = 0.31U_b/R$ in the LES and $f_{peak} = 0.32U_b/R$ in the experiment. In the experiment, the latter corresponds to a dimensional value of $f = 160$ Hz.

Fig. 3.30 shows the power-spectrum density of velocity fluctuations at $x/R = 0.1$ on the symmetry axis. At this position only two spectra are shown because all directions perpendicular to the centreline are statistically equivalent. Also at this point the simulation is in very good agreement with the experiment although the agreement is not as impressive as above. This is due to the fact that on the axis no azimuthal averaging is possible and therefore a longer time signal would be needed to provide similar averaging quality. The spectrum of fluctuations orthogonal to the centreline, Figs. 3.29b and 3.29d, exhibits a pronounced peak at the same frequency as the precessing vortex core. In the spectrum of the axial velocity fluctuations at this position no pronounced peak is observed, Figs. 3.29a and 3.29c. At this location, the axial component is blocked by the wall, suppressing the periodic oscillation.

As mentioned above in relation to Fig. 3.29, the agreement with the experimental data is excellent for the axial and radial velocity components and less good for the tangential velocity component. To investigate this issue, time signals have been recorded at $x/R = 0.1$ and $x/R = 0.4$, at several radial positions but each time only at one azimuthal location for technical reasons. Therefore no azimuthal

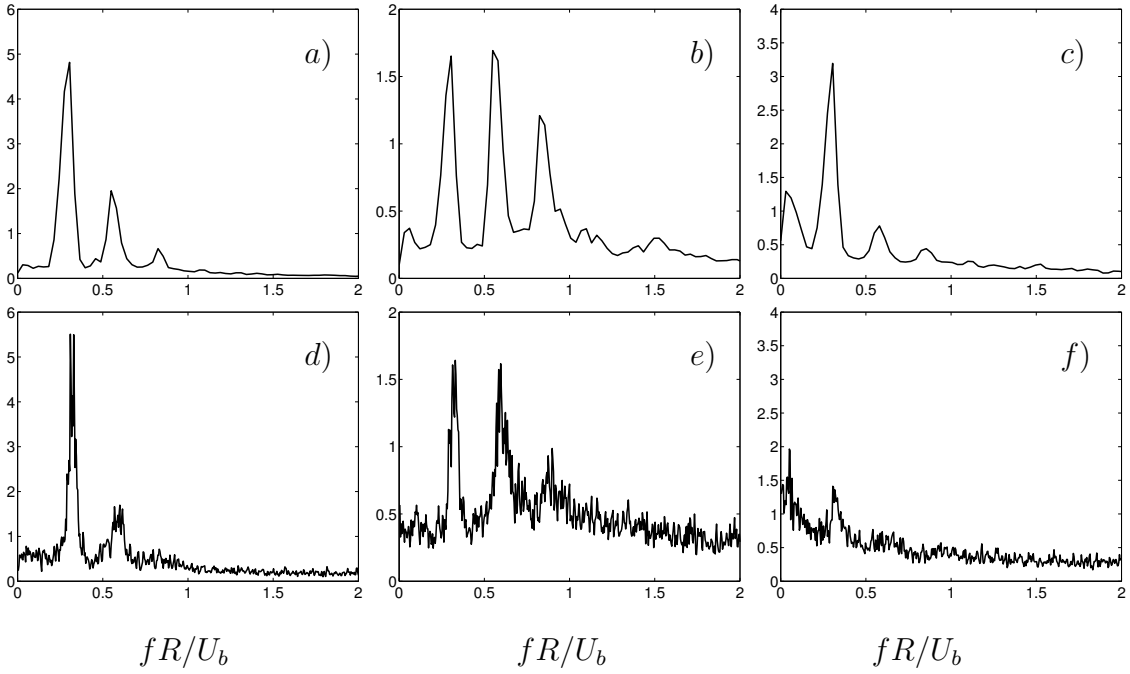

Figure 3.29: Power spectral density of velocity fluctuations at $x/R = 0.1$, $r/R = 0.6$ in the experiment. At $x/R = 0.1$, $r/R = 0.605$ in H1. $a) - c)$ Simulation $d) - f)$ Experiment Büchner & Petsch (2004). $a)$ and $d)$ Axial velocity fluctuations. $b)$ and $e)$ Radial velocity fluctuations. $c)$ and $f)$ Azimuthal velocity fluctuations.

averaging is possible with these time series and the spectrum is less smooth. Fig. 3.31 shows the PSD of axial and tangential velocity fluctuations at $x/R = 0.1$ and $r/R = 0.594$. The PSD of the axial velocity fluctuations is close to the one in Fig. 3.29a, defined at $r/R = 0.605$ and with azimuthal averaging. This provides an impression of the impact of the averaging. The PSD of tangential velocity fluctuations exhibits a significant difference with respect to Fig. 3.29c. Note that the change in radial position is only $\Delta r = 0.01$. In fact, the shape of the PSD of tangential velocity is closer to the experimental spectrum, Fig. 3.29f, than the spectrum obtained at $r/R = 0.605$, Fig. 3.29c. For this component the spectrum is very sensitive to the radial location. This issue is discussed in the following section

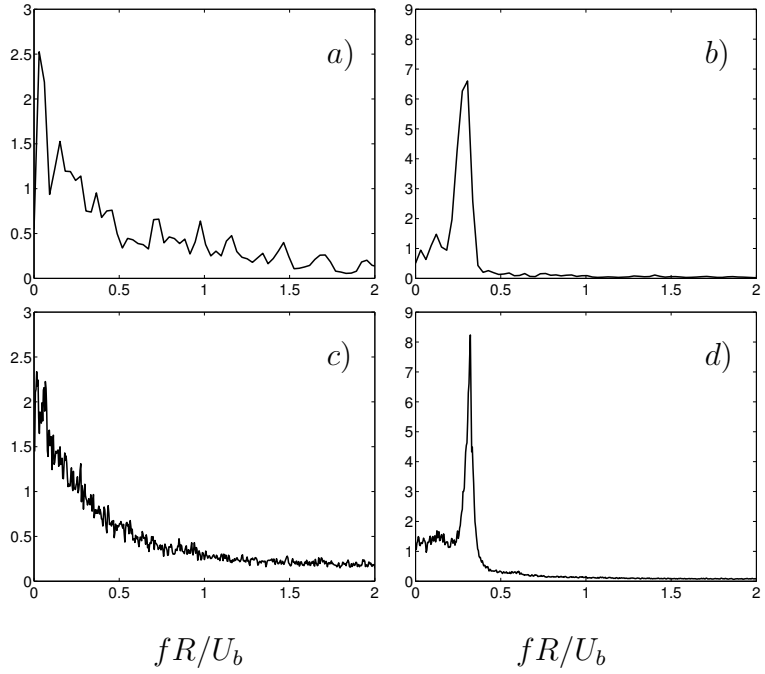

Figure 3.30: Power spectral density of velocity fluctuations at $x/R = 0.1$, $r/R = 0$. $a)-b)$ Simulation $c)-d)$ Experiment Büchner & Petsch (2004). $a)$ and $c)$ Axial velocity. $b)$ and $d)$ Radial velocity. (Note that all directions orthogonal to the centreline are statistically equivalent. Therefore only two spectra are shown in this figure.)

3.4.3 Relation between the spectra and the coherent structures

Fig. 3.32 shows the amplitude of the power spectrum at the fundamental frequency f_{peak} as a function of the radial position. This figure provides information on the organized fluctuations while in the statistical data, Fig. 3.16, the organized fluctuations are mixed with the turbulent fluctuations. It is apparent that the power spectrum amplitude of the tangential velocity fluctuations changes rapidly with radial position around $r/R = 0.6$, explaining the sensitivity to the radial location observed in Figs. 3.29c and 3.31.

The shape of the curves shown in Fig. 3.32 is different for the three velocity components. In order to understand the figure it is necessary to consider the motion of the PVC in the transverse plane $x/R = 0.1$ by means of the sketch in Fig. 3.21d. In the ideal case of a vortex core rotating at a regular rate around the symmetry axis, the spectrum of azimuthal velocity fluctuations u''_θ at a point

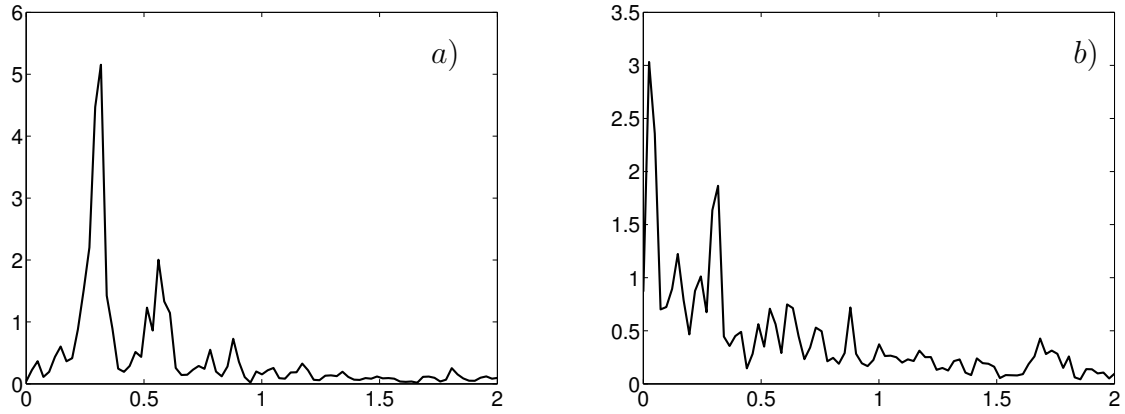

Figure 3.31: PSD of velocity fluctuations at $x/R = 0.1$, $r/R = 0.594$. $a)$ Axial velocity fluctuations. Compare to Fig. 3.29a, d. $b)$ Tangential velocity fluctuations. Compare to Fig. 3.29c, f.

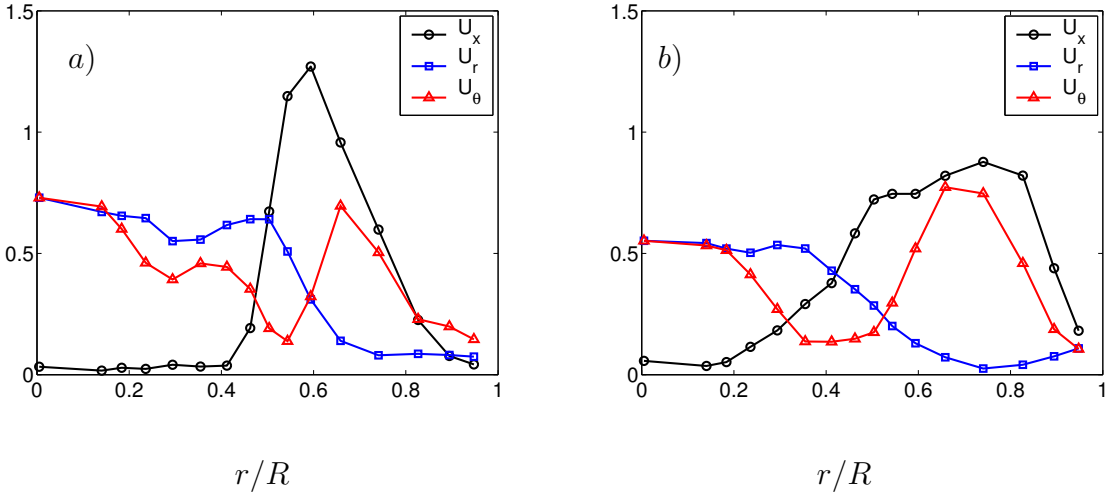

Figure 3.32: Value of the power spectrum at the fundamental frequency f_{peak} as a function of r/R. $a)$ $x/R = 0.1$, $b)$ $x/R = 0.4$

like Q in Fig. 3.21d should not contain any peak, because the center of the vortex is passing always through this point. Therefore, the minimum in the curve for u_θ observed at $r/R = 0.55$ in Fig. 3.32a indicates the mean radial location of the PVC centre. For $r/R < 0.5$, the axial velocity component is blocked by the wall while the radial and tangential ones are not. This blocking is reduced further downstream due to the larger distances from the wall. The radial and tangential components have a similar behaviour for $r/R < 0.5$, and they converge in the centreline as expected due to radial symmetry. For $r/R > 0.6$, the spectrum amplitude of the radial fluctuations decays with r . Due to the regions of positive and negative axial fluctuations observed in Fig. 3.21a, the amplitude of the axial component is significantly higher than the amplitude of the other components for $r/R > 0.5$.

Once the mean radial location of the PVC centre has been established, it is interesting to note that at $x/R = 0.1$ and $r/R = 0.6$ there is an accumulation of energy in the spectrum of tangential velocity fluctuations at low frequencies, one order of magnitude lower than the fundamental, precessing frequency, which does not appear in the other components. It can be observed both in the experiment and the simulation (see Figs. 3.29c and 3.29f). This phenomenon is likely to be related to the unsteady location of the vortex core. In the mean, its radial position at $x/R = 0.1$ is revealed by the minimum in Fig. 3.32a, but it is not constrained in radial direction and can exhibit low frequency oscillations of its position in this direction. These oscillations are most likely responsible for the accumulation of energy at low frequencies.

3.4.4 Discussion

There have been several studies concerned with the dynamics of the near field of non-swirling coaxial jets (Ko & Kwan, 1976; Kwan & Ko, 1977; Dahm *et al.*, 1992; Akselvoll & Moin, 1996; da Silva *et al.*, 2003). In particular Dahm *et al.* (1992) have shown that as soon as the velocity ratio of the two coaxial streams is large enough, the two layers do not evolve independently but the development of the layers is locked. Evidence of this effect is provided by the fact that the vortex passage frequency ratio $F = f_i/f_o$ between the inner and outer layer differs from

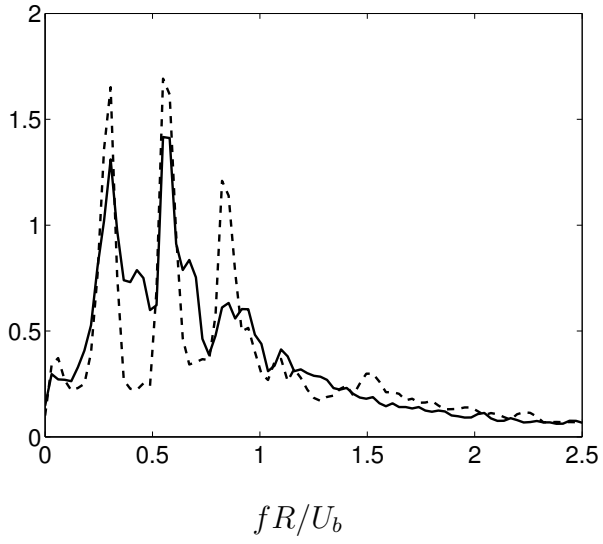

Figure 3.33: Power spectral density of radial velocity fluctuations. Outer shear layer, solid line $x/R = 1.0$, $r/R = 1.2$. Inner shear layer, dashed line $x/R = 0.1$, $r/R = 0.6$.

the values predicted by assuming that the shear layers evolve independently. In Dahm *et al.* (1992) the authors found a value $F \simeq 1$ for this ratio when the velocity ratio between inner and outer jet was about 4 and $F \simeq 2$ when the velocity ratio was about 1.15. This was confirmed by numerical simulations (Akselvoll & Moin, 1996; da Silva *et al.*, 2003).

In the present case of an annular swirling jet, instead of a non-swirling coaxial jet, only a qualitative analysis is possible. Although an annular jet can be considered as a coaxial jet in which the outer-to-inner-stream velocity ratio tends to infinity, it is to be stressed that the dynamics of the present case are very different due to the curvature effects induced by the swirl and the corresponding central recirculation zone. No experimental time signals in the region of the outer shear layer are available. This information, on the other hand, can be extracted from the LES. Fig. 3.33 shows a comparison of the power spectral densities of radial velocity fluctuations at two different points, one in each shear layer. From the figure it is clear that the main frequency and the higher harmonics are the same in both shear layers. This result supports the previous visual impression of Fig. 3.17 that the inner and outer structures are locked. It is also consistent with the findings of Dahm *et al.* (1992) mentioned before.

Finally, as the inner structures rotate at a constant rate, an estimation of the precessing velocity of the structures can be made using the precessing frequency of the vortices, to yield $u_{prec} = \omega_{prec}\, r_c = 2\pi\, r_c\, f_{peak}$ where ω_{prec} and u_{prec} are the angular velocity and precessing velocity of the inner structures, respectively, and r_c is the radial position of the vortex center (see Fig. $3.21d$). In Gupta *et al.* (1984), for a configuration which exhibited similar phenomena as the present one, it was found that at the radius of the center of the vortex core the precessing velocity of the PVC was equal to the measured mean tangential velocity at that radius. However, the present results point into a different direction. In the current simulation the value $u_{prec} = 2\pi\, r_c\, f_{peak} \simeq 1.15 U_b$ is obtained at $x/R = 0.1$. This precessing velocity is higher than the mean tangential velocity at this point, which is $\langle u_\theta \rangle = 0.65 U_b$. The structures are hence moving faster than the mean flow at the center of the shear layer. An explanation can be obtained from the mean tangential velocity profile in Fig. $3.14b$. In high velocity regions (at $r \sim R$) the area ($2\pi\, r$) is larger than in low velocity ones (at $r \sim 0.5R$), and therefore the center of inertia of the velocity distribution through the shear layer is displaced towards higher speed. Another explanation could be related to the previous discussion of the frequency ratio. As the shear layers interact, the precessing velocity of the PVC could be the result of such interaction. Furthermore, the curvature of the shear layer may also play a role. To clarify this issue, stability analyses using the mean flow as base flow as undertaken by Paschereit *et al.* (2000a) may be helpful, but they are beyond the scope of the present thesis.

4 Inflow boundary conditions

In this chapter the use of approximate inflow boundary conditions is assessed. First, the general problem of specifying swirling inflow conditions is discussed and the methods proposed in the literature are described. Then, the results of three simulations are compared in terms of velocity profiles, visualization and spectra. It is shown that good agreement of mean and rms velocities is not, in general, sufficient for a realistic representation of the experimental conditions. The unsteady large scale structures of the flow must also be taken into account.

In the previous chapter the approach employed for the specification of inflow conditions has proven to be successful. The geometry of the burner was simple enough to allow for the inclusion of the inlet ducts up to the swirl-generating device in the computational domain. However, in a more complex burner this might not be the case leading to an excessive cost of the inflow region. Therefore, in this chapter more general approaches are considered which could be used in such cases.

4.1 Generation of inflow conditions for swirling flows

LES of spatially inhomogeneous flows require unsteady inflow boundary conditions with a proper representation of the turbulent fluctuations, as discussed in §2.2.1. Such turbulent inflow conditions must therefore reflect the three-dimensional, unsteady nature of turbulence. The results are often highly sensitive to these boundary conditions.

In order to obtain the most accurate predictions of the velocity field in the region of interest, the computational domain should ideally be extended to include all upstream geometry that may influence flow properties further downstream. This includes all flow conditioning devices, like tangential jets or swirl vanes in the case of a swirling flow. This is generally not practical and computationally too

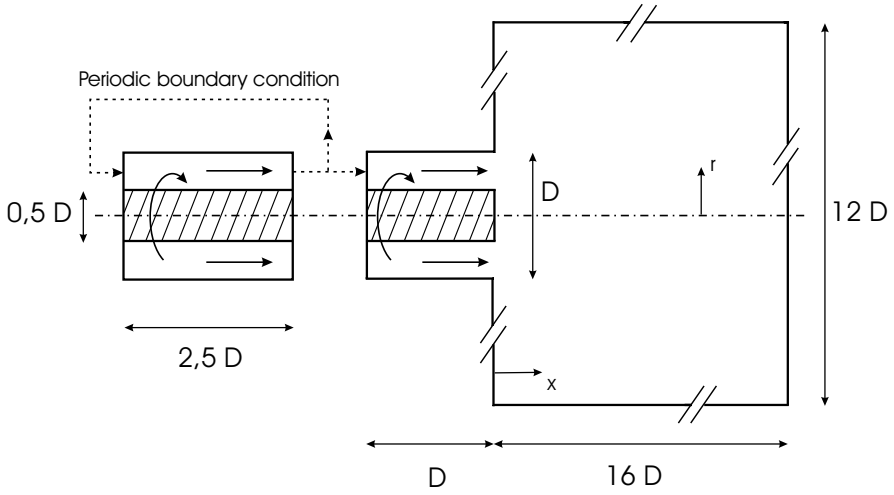

Figure 4.1: Generation of inflow data.

demanding. Nevertheless, some examples are reported in the literature like Wegner *et al.* (2004*a*). In that reference, simulations of flow in a swirl burner were reported, in which the swirler device was included in the computational domain. Therefore, a very complex grid was required.

4.1.1 Equilibrium swirling inflow conditions

It is often necessary or desirable to consider approximate inflow conditions. In many cases, the flow at the inlet is a developing turbulent stream in a duct that can be approximated as fully developed. The unsteady inflow conditions can then be generated by simulating a spatially periodic section of a pipe. This approach was generalized for swirling flows by Pierce & Moin (1998*b*). As these authors point out, swirling flows are not self-sustaining and must eventually decay, independent of the initial forcing that created them. If this relaxation process is sufficiently fast or if the forcing device is located sufficiently far upstream, then an equilibrium swirling inflow condition that is easier to model will result. This is also the closest flow to a fully developed swirling flow. The method for generating swirling flows numerically is to solve for the flow driven by fictitious axial and azimuthal body forces in a spatially periodic duct, from which data are fed as the inflow boundary condition into the main computational domain. This is illustrated in Fig. 4.1.

The axial body force represents the mean pressure gradient that drives the physical flow and has long been established as a means of driving spatially periodic

pipe or channel flows (see for example Wille, 1997, chap. 5). On the other hand, the azimuthal body force used to drive the swirl component is not realistic and should be thought of as existing only to provide the swirl. The resulting flow is a stationary approximation to slowly decaying swirl. As the swirling force is not physically producible, there is some freedom in choosing the forcing profile. Pierce & Moin (1998*b*) tried several profiles, constant forcing, linear and quadratic profiles with respect to the radial coordinate, with the same overall strength of the applied force. They found that the resulting swirl velocity was rather insensitive to changes in the forcing profile. A spatially constant forcing appeared to be adequate and for simplicity is the usual choice for this kind of simulations.

The strength of the applied force still needs to be specified. In a channel flow configuration, there are two obvious ways of doing this. First, the mean pressure gradient can be fixed, then the mass flow through the channel has to adjust to give a wall shear stress corresponding to the mean pressure gradient. (Since in fully developed turbulent channel flow the mean streamwise pressure gradient $\partial\langle p\rangle/\partial x$ has to balance the mean wall shear stress $\langle\tau_w\rangle$ (Pope, 2000, p. 267)). Alternatively, as suggested by Benocci & Pinelli (1990), the mass flow rate can be fixed by adjusting the forcing term appropriately. Thus, the mean wall shear stress is allowed to adjust to the specified flow rate. The second approach is used in the present work. The reason is that the wall shear stress is not always known a priori and it is usually part of the desired solution. In a similar way, the strength of the swirl body force is adjusted to achieve the desired level of swirl, i.e. to get the desired swirl number defined as

$$S = \frac{\int_0^R \rho u_x u_\theta r^2 \mathrm{d}r}{R \int_0^R \rho u_x^2 r \mathrm{d}r}. \tag{4.1}$$

4.1.2 Generalization of the method

When the inflow conditions cannot be approximated as fully developed, their specification becomes significantly more difficult. Usually, some specified mean velocity or turbulence statistics profiles are known from an experiment or a RANS calculation, and it is desired to have the same profiles of statistical quantities applied to the inflow boundary of the LES. However, as already mentioned, LES

requires instantaneous data as inflow conditions and not only statistical data. To overcome this difficulty, the usual approach is the specification of statistically constrained random numbers superimposed on the desired mean flow (Akselvoll & Moin, 1995; Le *et al.*, 1997) although more sophisticated approaches are available too (Klein *et al.*, 2003).

A more attractive approach, first suggested by Pierce (2001), is to generalize the "fully developed" approximation described above to include the larger class of parallel flows having arbitrarily specified velocity statistics profiles. The desired flow is created by simulating a spatially periodic, parallel duct flow and constraining it using a corrective body forcing technique. The resulting flow has the desired statistical properties, and it provides realistic turbulence data which are in equilibrium with the specified mean statistics. Assume that a desired mean velocity profile $T(r)$ and fluctuation intensity profile $T'(r)$ are given (T is used as an abbreviation for target and it is assumed that the profiles only depend on the radial coordinate). The forcing technique then proceeds as follows. At each time step, the streamwise averaged velocity $\langle u_x \rangle(r, \theta, t)$ and fluctuation variance $\langle u_x'^2 \rangle(r, \theta, t)$ are computed

$$\langle u_x \rangle(r, \theta, t) = \langle u_x(x, r, \theta, t) \rangle_x, \tag{4.2}$$

$$\langle u_x'^2 \rangle(r, \theta, t) = \langle u_x(x, r, \theta, t)^2 \rangle_x - \langle u_x \rangle(r, \theta, t)^2, \tag{4.3}$$

where $\langle \cdot \rangle_x$ denotes the operation of averaging in streamwise direction. Then, the following step would be to rescale and shift the instantaneous velocity field so that it has the specified mean and fluctuating velocity profiles

$$u_x(x, r, \theta, t) \rightarrow \frac{T'(r)}{\sqrt{\langle u_x'^2 \rangle(r, \theta, t)}} \left[u_x(x, r, \theta, t) - \langle u_x \rangle(r, \theta, t) \right] + T(r), \tag{4.4}$$

where the arrow indicates the operation of rescaling and shifting. However, this rescaling is not possible because the velocity field obtained in that way will not in general fulfill continuity. An equivalent approach is to add an appropriately defined body force $f_x(x, r, \theta, t)$ to the momentum equation

$$f_x = \frac{T'(r)}{\sqrt{\langle u_x'^2 \rangle(r, \theta, t)}} \left[u_x(x, r, \theta, t) - \langle u_x \rangle(r, \theta, t) \right] + T(r) - u_x(x, r, \theta, t). \tag{4.5}$$

If only the mean velocity profile is constrained, then the body force (4.5) is simplified,

$$f_x = -\langle u_x \rangle(r, \theta, t) + T(r). \tag{4.6}$$

This approach, as noted by Pierce (2001), appears to be an attractive alternative for generating realistic turbulent inflow conditions having specified mean statistical properties. In the case of swirling flow in a pipe, the method can be used to impose given profiles of axial and tangential velocity, by adjusting corresponding body forces in axial f_x and azimuthal f_θ directions. It is not possible however to impose a given mean radial velocity profile with the present formulation. In order to see this, first, imagine that body forces are applied to the momentum equations in axial, azimuthal and radial direction, f_x, f_θ and f_r, respectively, to impose given profiles of U_x, U_θ and U_r. In the continuity equation for the mean flow

$$\frac{\partial u_x}{\partial x} + \frac{1}{r}\frac{\partial (r u_r)}{\partial r} + \frac{1}{r}\frac{\partial u_\theta}{\partial \theta} = 0 \tag{4.7}$$

the first and third term are identically zero due to the periodic boundary conditions in streamwise and azimuthal directions. Therefore,

$$\frac{\partial (r u_r)}{\partial r} = 0 \tag{4.8}$$

and using the boundary conditions at the pipe walls, it is found that u_r is identically zero. Thus, although a body force has been applied in radial direction, the continuity equation forces the radial velocity to be zero. Numerically, the force in radial direction must be absorbed by the pressure. This drawback, however is not very serious because the radial component is usually much smaller than the other two components for this kind of flows (see for example Fig. $3.14a - c$).

4.2 Description of the simulations

It has been common practice in the literature on LES and DNS of jets to locate the inflow plane at the jet exit (Olsson & Fuchs, 1996; McIlwain & Pollard, 2002; da Silva *et al.*, 2003). While this is a validated approach for non-swirling jets, its use in swirling jets is dubious because the dynamically relevant processes occur closer to the jet exit (e.g. recirculation zone). Nevertheless, the location of the

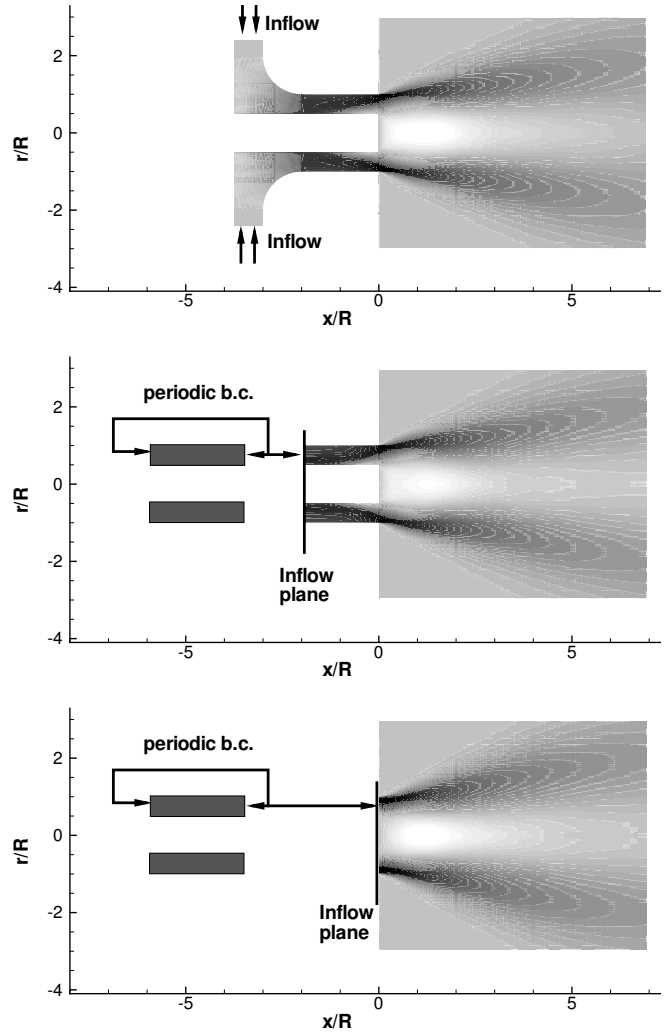

Figure 4.2: Description of the three approaches for the specification of inflow conditions considered in the present chapter . The contour plots show the mean axial velocity component.

inflow plane at the jet exit is the cheapest option from the computational point of view. Therefore, it is interesting to assess whether this approach is feasible for the present case. This was done using the method of the previous section, i.e. by using body forces to impose the profiles of axial and tangential mean flow from the experiment of Hillemanns (1988) measured very close to the jet exit.

Alternatively, the inlet plane can be located upstream of the jet exit. This approach maintains the simplicity of the grid while the computational cost is slightly higher, because the domain to be simulated is larger. In this case, as demonstrated by Akselvoll & Moin (1995), the resolution close to the expansion is critical. For the present configuration it is not possible to use the generalized method of the

Sim.	Grid	SGS m.	Inf. method	Inf. boundary
H1	F1 ($\sim$ 6 mio.)	Dyn.	Inf. geo.	$-3.75 < x/R < -3$
H7	F2 ($\sim$ 6 mio.)	Dyn.	fixed S	$x/R = -2$
H8	F3 ($\sim$ 6 mio.)	Dyn.	fixed prof.	$x/R = 0$

Table 4.1: Overview of the simulations to assess the inflow conditions.

previous section, because no measurements are available in the upstream duct. Therefore, to locate the inflow plane upstream of the jet exit it is necessary to use equilibrium swirling inflow conditions, with a given value of S such that the swirl at the jet outlet corresponds to the one in the experiment.

Three simulations are considered in the present chapter which are summarized in Table 4.1 and represented in Fig. 4.2. The first simulation, H1, is the reference case of Chapter 3. The computational domain includes a representation of the inlet duct upstream of the jet exit up to the swirl generating device. At that location, the flow is imposed at the circumferential inflow boundary, by using laminar top-hat profiles for the radial and azimuthal velocity components. In the second simulation, H7, the inflow plane is located at $x/R = -2$ and equilibrium swirling inflow conditions are employed imposing the value of $S = 1.2$ in the precursor simulation. Finally in the third simulation, H8, the inflow plane is located at $x/R = 0$ and the generalized method is employed, using body forces in the axial and azimuthal directions as described in eq. (4.6) to obtain the desired mean axial and tangential velocity profiles at the jet exit. It was also planned to perform a simulation imposing the turbulent statistics using eq. (4.5), but it turned out that it was not necessary for reasons that will become clear in the following sections.

Downstream of the jet exit, i.e. for $x/R > 0$, the grids employed in the simulations, F1, F2 and F3, have the same distribution of cells. The difference between the grids is due to the different inlet geometry in each case. Nevertheless the number of cells in that region has been kept similar in all cases.

4.3 Comparison of results

4.3.1 Mean and RMS velocity profiles

A comparison of the results obtained with the different methods is reported in Figs. 4.3 and 4.4. The present results show good agreement with the experimental data for the three cases considered. Mean velocity profiles are displayed in Fig. 4.3 at $x/R = 0.2$, $x/R = 1$ and $x/R = 3$. For H8, the flow at $x/R = 0.2$ can not influence the flow upstream because the inlet plane is too close. Also for H8 at the inflow plane, $\langle u_r \rangle$ is identically zero as explained in the previous section, while in the experiment (and both H1 and H7) this is not necessarily the case, because the flow has already started to expand. As a consequence, H8 presents small discrepancies with respect to the experimental data Figs. $4.3(a1)$ and $4.3(a2)$, in particular the backflow is underpredicted and the tangential velocity component is underpredicted for $r/R < 0.5$ and overpredicted for $r/R > 0.5$. H1 and H7 at this axial location present excellent agreement with the experiment. Further downstream, at $x/R = 1$ and $x/R = 3$, not only H1 and H7 yield good agreement but so does H8. This suggests that the three approaches are appropriate to obtain good predictions of mean velocity profiles.

The RMS axial and tangential velocities are reported in Fig. 4.4 at the same locations as the mean velocity profiles. Recall that in H8 only the mean velocity profiles were imposed at the inflow plane. No effort was made to adjust the turbulence statistics. This is the reason why at $x/R = 0.2$ Figs. $4.4(a1)$ and $4.4(a2)$, the disagreement between H8 and the experiment is large. In that simulation, the level of turbulence is substantially larger in the outer shear layer and it is smaller in the inner shear layer. H1 and H7, on the other hand are both in good agreement with the experiment, with a slight overprediction of the turbulence level in H1 and underprediction in H7. However, these results do not invalidate H8 because, as explained in the previous section, in principle it would be possible to modify the body forces in the precursor simulation to obtain the desired levels of turbulence. Furthermore, a bit downstream, at $x/R = 1$, the turbulence statistics are in good agreement with the experiments for the three cases. The level of turbulence is well captured in the three simulations, and only in H8 a small bump remains as left-over of the higher level which was present upstream. At $x/R = 3$ the differences

between the cases are almost negligible.

4.3.2 Visualization and Spectra

In the previous section it has been shown that the three methods provide good predictions of the mean flow and the turbulence statistics in the near field of the jet beyond $x/R = 1$. Now, the instantaneous flow is discussed and the analysis is complemented with the PSD at a monitoring point ($x/R = 0.1$, $r/R = 0.6$). Fig. 4.5 displays iso-surfaces of unsmoothed pressure fluctuations on the left side and the corresponding PSD of axial velocity fluctuations on the right side. Following the analysis performed in Chapter 3, the structures are colored dark in the region where $\partial\langle u_x\rangle/\partial r > 0$ and colored light in the region where $\partial\langle u_x\rangle/\partial r < 0$. Only one snapshot is provided, but animations were generated and the following comments are based on these. In H1 Fig. $4.5(a1)$ two families of structures are identified (labeled I1 and O1 in the figure) which lie on the inner and outer shear layers respectively. In the corresponding PSD a pronounced peak is present and some energy is concentrated in higher harmonics. The frequency of the first peak has been identified as the precessing frequency of the inner structures in their rotation around the symmetry axis. (For more details see Chapter 3). Likewise in H7, Fig. $4.5(b1)$, two families of structures are identified in the flow. The corresponding PSD exhibits peaks at the same frequencies as H1. The energy content of the second harmonic, however, is substantially larger than in H1. This suggests that although the flow instability has been captured in H7, some features are different in both simulations. Animations show that one important difference between H1 and H7 is the fact that in H1 coherent structures extend eventually further upstream into the inlet duct reaching sometimes the plane $x/R = -2$ where the inflow plane is located in H7. Excursions of coherent structures into the inlet duct also occur in H7, but of course to a more limited extent. This indicates that it would have been better to locate the inflow plane of H7 even further upstream, increasing therefore the computational cost. Nevertheless, the differences between H1 and H7 are minor when compared to H8.

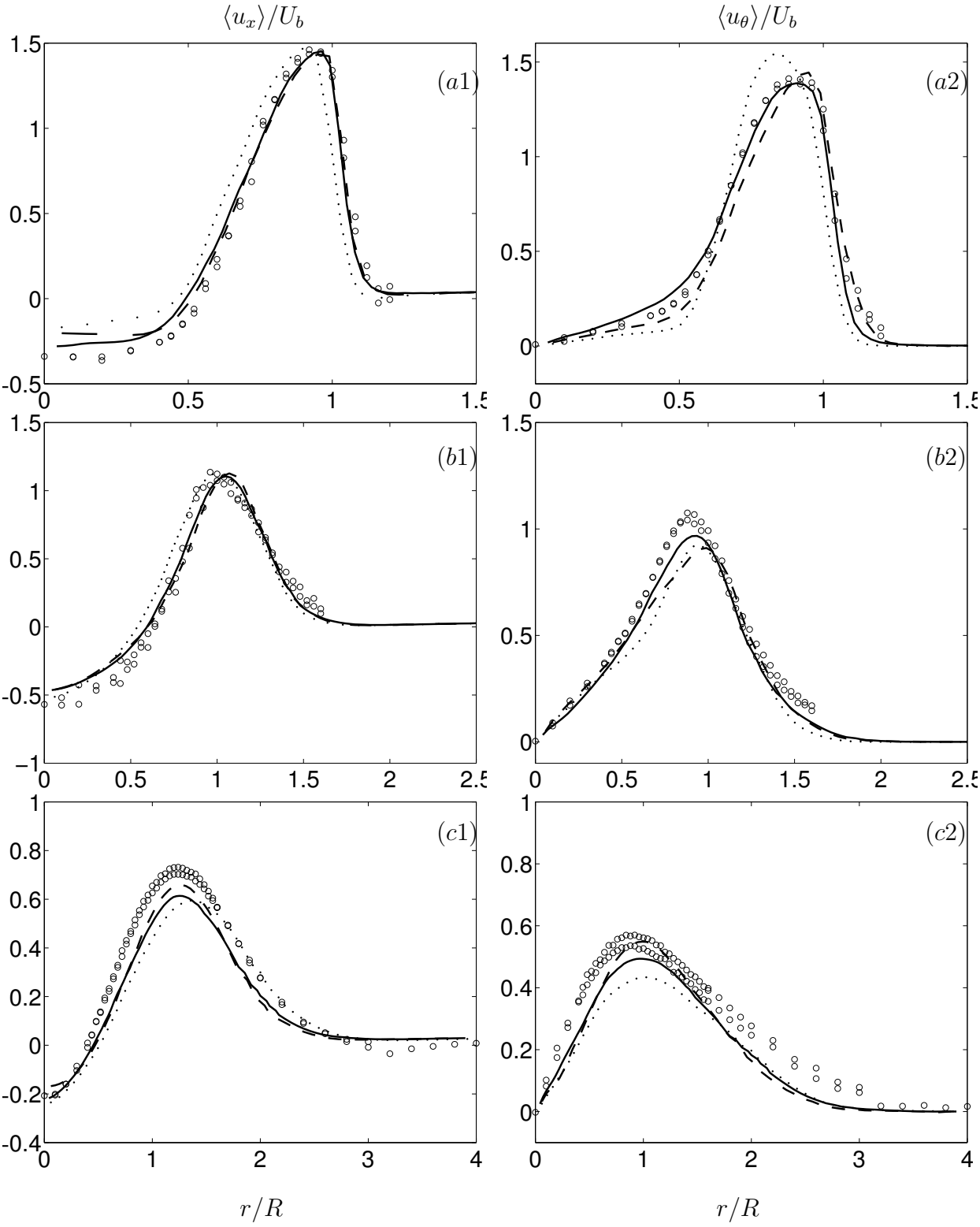

Figure 4.3: Radial profiles of mean velocity obtained with different inflow conditions. Left, axial velocity component. Right, tangential velocity component. *a)* $x/R = 0.2$ *b)* $x/R = 1$ *c)* $x/R = 3$. H1, solid. H7, dashed. H8, dotted.

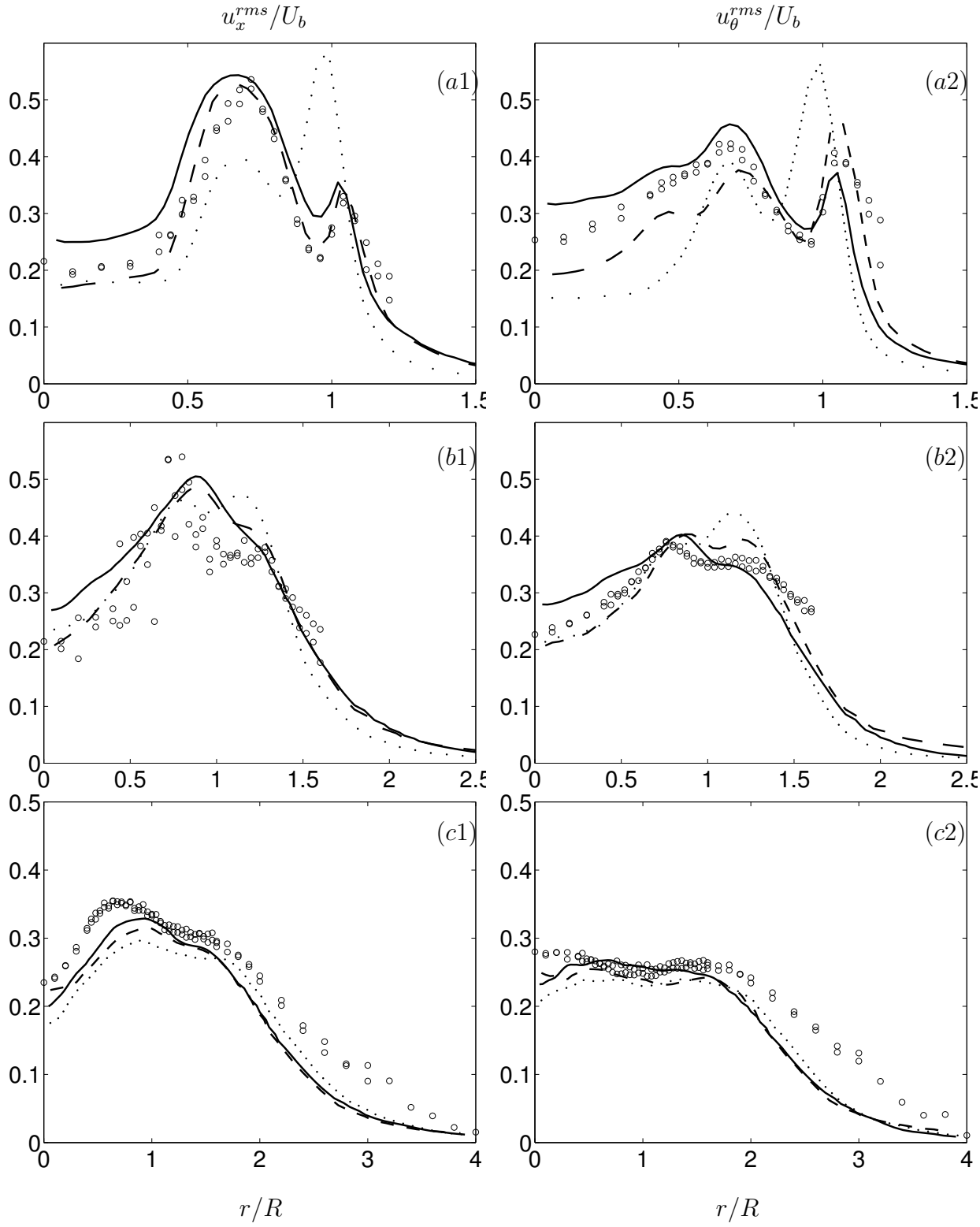

Figure 4.4: Radial profiles of RMS velocity obtained with different inflow conditions. Left, axial velocity component. Right, tangential velocity component. $a)$ $x/R = 0.2$ $b)$ $x/R = 1$ $c)$ $x/R = 3$. H1, solid. H7, dashed. H8, dotted.

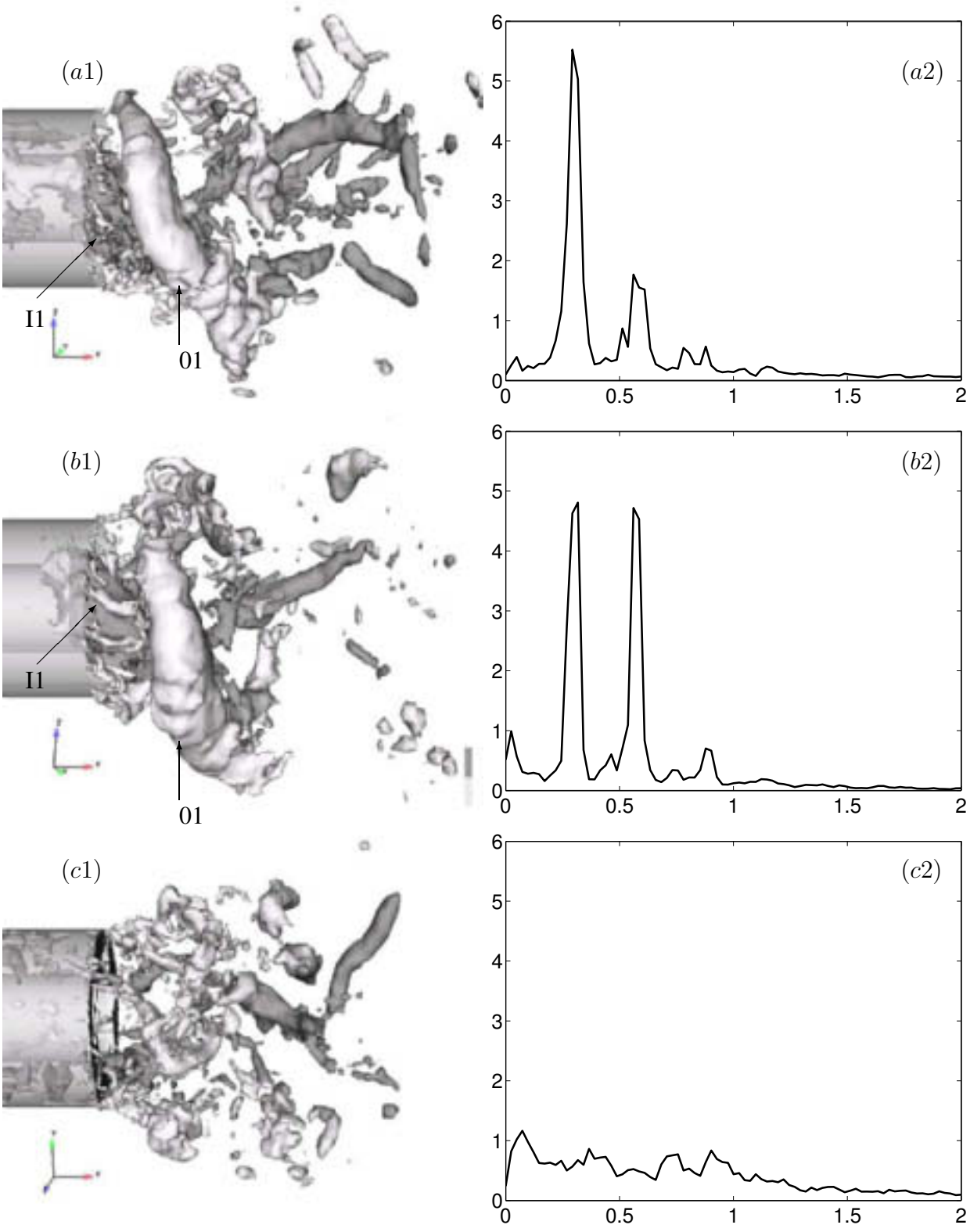

Figure 4.5: Results with different inflow conditions. Left, iso-surfaces of pressure fluctuations. Right, PSD of axial velocity fluctuations at $x/R = 0.1$, $r/R = 0.6$. a) H1. b) H7. c) H8.

In H8 the structures are more irregular than in H1 and H7, Fig. 4.5$(c1)$. They cannot enter the inlet duct because the inlet plane is located at the jet exit. This constrains the formation of large-scale coherent structures in the inner part. In the present case, the inner structures cannot form in the physically correct manner and therefore also the outer structures do not form. Instead, as hinted in Fig. 4.5$(c1)$ and confirmed in animations, only irregular short-living structures are formed in both shear layers. This is confirmed by the corresponding PSD in Fig. 4.5$(c2)$ where no peak is observed.

4.4 Discussion

It has been already mentioned several times that LES of spatially inhomogeneous flows require unsteady inflow boundary conditions with a proper representation of the turbulent fluctuations. In the validation of the different approaches to the problem (Klein *et al.*, 2003; Schlüter *et al.*, 2004), it is usual to compare first and second order moments of the velocity field with the corresponding experimental data. When the agreement is good, the method is usually considered validated. In the present chapter it has been shown that in flows containing unsteady (quasi-periodic) large-scale coherent structures, a good representation of the mean flow and turbulence statistics does not guarantee a good representation of the coherent structures. Indeed, the predictions of H8 were in reasonably good agreement with the experimental data as far as the mean flow and turbulence statistics are concerned, while no large-scale coherent structures were present in the flow. For highly swirling flows it is therefore not possible to apply inflow boundary conditions at the jet exit. A similar conclusion was obtained recently by Wegner *et al.* (2004*b*) and by Freitag & Klein (2005). The good agreement with the experiment shown by H7 together with the prediction of the flow instability show that an elaborate treatment of the flow in the actual swirl-generating device is not necessarily needed. Less expensive and, what is more important, more universal strategies can be employed.

5 Influence of the level of swirl

In this chapter the impact of the swirl on the mean flow and the precessing vortex structures is analyzed. First, the general features of the flow are discussed in a qualitative way, including 2D-streamlines in an axial plane, angle of the flow with respect to the $x-$axis and fluctuating kinetic energy. Then, the mean and RMS velocity profiles are studied at several axial locations. Finally, the coherent structures for each case are studied and complemented by the temporal spectra at a monitoring point.

5.1 Overview of the simulations

An overview of the simulations performed is shown in Table 1. The flow characteristics correspond to the experiment of Hillemanns (1988) discussed in Chapter 3. The Reynolds number of the flow based on the bulk velocity $U_b = 25.5$ m/s and the outer radius of the jet $R = 50$ mm is $Re = 81500$. The swirl number is defined at the inflow plane $x/R = -2$. The range covered by the simulations is very wide, including a simulation without swirl, H9, another with a low level of swirl, H10, and four simulations with a high level of swirl, H12, H13, H14 and H15. There is also a simulation with an intermediate level of swirl, H11. For orientation it should be recalled that for a round jet (i.e. not featuring a bluff body in the centre) recirculation is observed for $S \geq 0.6$ with S being measured at the outlet plane (Gupta *et al.*, 1984).

Fig. 5.1 addresses the inflow conditions for the main simulation imposed at $x/R = -2$. It shows the mean axial and azimuthal velocity components of the unsteady inflow generated by the precursor simulation. In the latter the swirl number was fixed, i.e. equilibrium swirling conditions were applied (see Chapter 4). Fig. 5.1 shows that the mean azimuthal velocity increases almost proportional to S with little change in the shape of the profile. The mean axial velocity is

Sim.	Grid	SGS	S ($x = -2R$)	Line style
H9	C2 (~ 2.5 mio.)	Smag.	0	solid(thin)
H10	C2 (~ 2.5 mio.)	Smag.	0.4	dashed-dotted
H11	C2 (~ 2.5 mio.)	Smag.	0.55	dashed-$\times$
H12	C2 (~ 2.5 mio.)	Smag.	0.7	dotted
H13	C2 (~ 2.5 mio.)	Smag.	0.85	
H14	C2 (~ 2.5 mio.)	Smag.	1	dashed
H15	C2 (~ 2.5 mio.)	Smag.	1.2	solid(thick)

Table 5.1: Overview of the simulations performed to investigate the impact of the swirl number

almost unchanged in all cases.

The grid C2 employed in the simulations has the same distribution of cells for $r/R > 0$ as the grid C1 described in Chapter 3. The inflow part is different because a precursor simulation is used. Nevertheless, the total amount of cells is similar to grid C1.

5.2 General features of the flow

5.2.1 Streamlines

Fig. 5.2 shows the two-dimensional streamlines of the average flow in an axial plane for the simulations in Table 5.1. As the jet is annular, the flow characteristics differ from those of a usual round jet. In the non-swirling case, Fig. 5.2a, a geometry-induced recirculation zone (GRZ) is formed due to the bluff-body effect of the cylindrical centre body. The length of this GRZ is roughly R and its maximum width is $0.5R$ imposed by the geometry. These values agree well with data from the literature (Rehab *et al.*, 1997). Fig. 5.2b shows the case of low swirl, $S = 0.4$. In this case, additional to the GRZ, a very thin central recirculation zone (CRZ) appears close to the axis. The length of the GRZ decreases with respect to the non-swirling case to $0.5R$. The CRZ extends up to about $x/R = 4$. For this level of swirl, $S = 0.4$, no CRZ is expected in a round jet (Gupta et al 1984), but

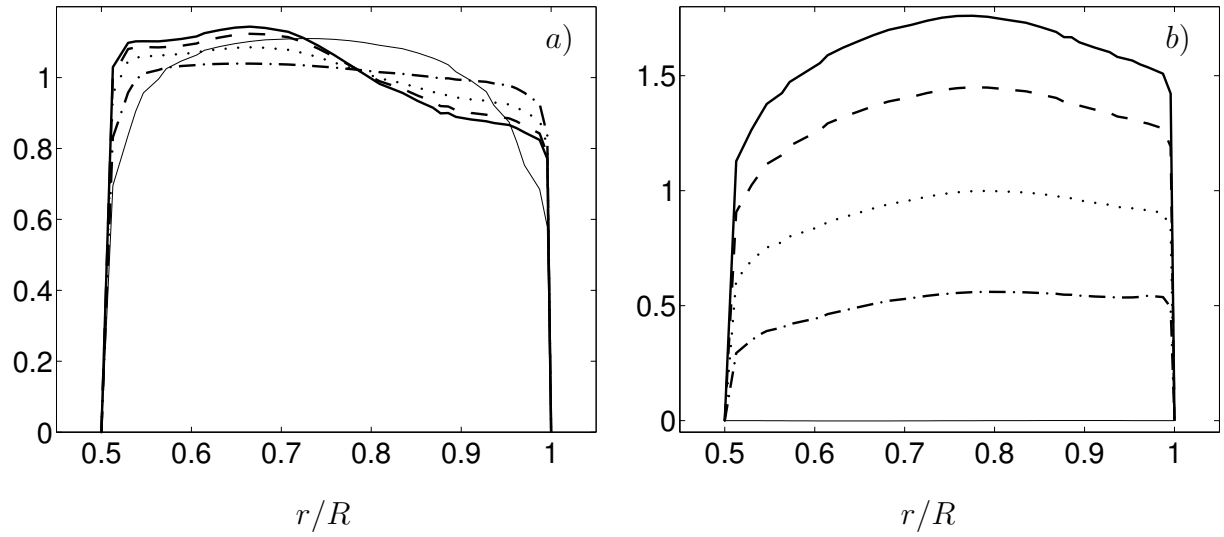

Figure 5.1: Mean velocity deduced from the fluctuating inflow conditions imposed at $x/R = -2$ for different levels of swirl. The line styles are defined in Table 5.1. a) Mean axial velocity. b) Mean tangential velocity.

in the present case the GRZ facilitates the formation of the CRZ. The length and width of the CRZ for each case is summarized in Table 5.2, together with other quantities of interest. Increasing S leads to an increase in the size of the CRZ. For the intermediate swirl case, $S = 0.55$, which is shown in Fig. 5.2c, the length of the CRZ is about $7R$ and the maximum width $0.35R$, i.e. substantially wider and longer than in the case $S = 0.4$. For these two levels of swirl, $S = 0.4$ and 0.55, the GRZ is not as simple as in the non-swirling case. This is hardly visible in Figs. 5.2b and 5.2c, so that a zoom of the region behind the centre body is presented in Fig. 5.3 for both cases. For $S = 0.4$, apart from the GRZ, a secondary recirculation zone is observed at $x/R < 0.2$ between $r/R = 0.15$ and $r/R = 0.3$. Closer to the axis, at $r/R < 0.1$ another bubble is visible which is connected to the CRZ by the line $\langle u_x \rangle = 0$. For $S = 0.55$, this third bubble has disappeared. The secondary recirculation zone has grown, reaching the symmetry axis. The CRZ in this case starts at $x/R = 0.4$.

Some trends can be determined from the streamlines of the high-swirl cases, Fig. 5.2d-g. First, when increasing S, the CRZ widens and lengthens. The values for the length of the CRZ with $S \geq 0.85$ have to be considered with care: the CRZ reaches into a part of the domain where the grid is comparatively coarse and

Sim.	H9	H10	H11	H12	H13	H14	H15
S	0	0.4	0.55	0.7	0.85	1	1.2
Length CRZ	-	$4R$	$7R$	$6.5R$	$> 8R$	$> 8R$	$> 8R$
Width CRZ	-	$0.1R$	$0.35R$	$0.65R$	$0.7R$	$0.8R$	$0.8R$
$\langle u_x \rangle_{max}/U_b$	1.11	1.09	1.11	1.09	1.1	1.25	1.5
$\langle u_x \rangle_{min}/U_b$	-0.3	-0.21	-0.25	-0.31	-0.37	-0.34	-0.47
k_{max}/U_b^2	0.06	0.1	0.14	0.21	0.34	0.35	0.32

Table 5.2: Variation of characteristic quantities with the swirl parameter

where the fluid motion is substantially slower so that the available averaging time can only provide estimates of the average flow. Hence, only an approximate value is provided here. On the other hand, the maximum width of the CRZ is always attained close to the jet exit, and is therefore reliable. With increasing swirl, the axial location of the maximum width moves upstream. For $S = 0.7$, 0.85, 1 and 1.2, the maximum width $0.65R$, $0.7R$, $0.8R$ and $0.8R$, is attained at $x/R = 2$, 1.5, 1.4 and 1, respectively.

For $S = 0.7$, 0.85 and 1, the bubble pattern is similar. The recirculation region encompasses the CRZ and the GRZ exhibiting two 'eyes' or centres. For the highest swirl cases the CRZ has reached $x/R = 0$, and the GRZ has merged into the CRZ. Fig. 5.2 shows that with increasing swirl number the jet spreads further outwards in radial direction.

Let us finally address the slope of the streamlines in Fig. 5.2 remote from the jet, starting at $x/R = 0$ and $r > R$. Their shape is due to the co-flow boundary condition. Note that the velocity at this location is only 5% of the jet axial velocity, so that the influence on the region of interest is negligible, as will be seen in Fig. 5.7. This was also checked with different amounts of co-flow in Chapter 3.

5.2.2 Angle of the flow

Due to the swirl of the jet the average streamlines are highly three-dimensional. So far, only the two-dimensional streamlines of the flow projected onto the $x - r$

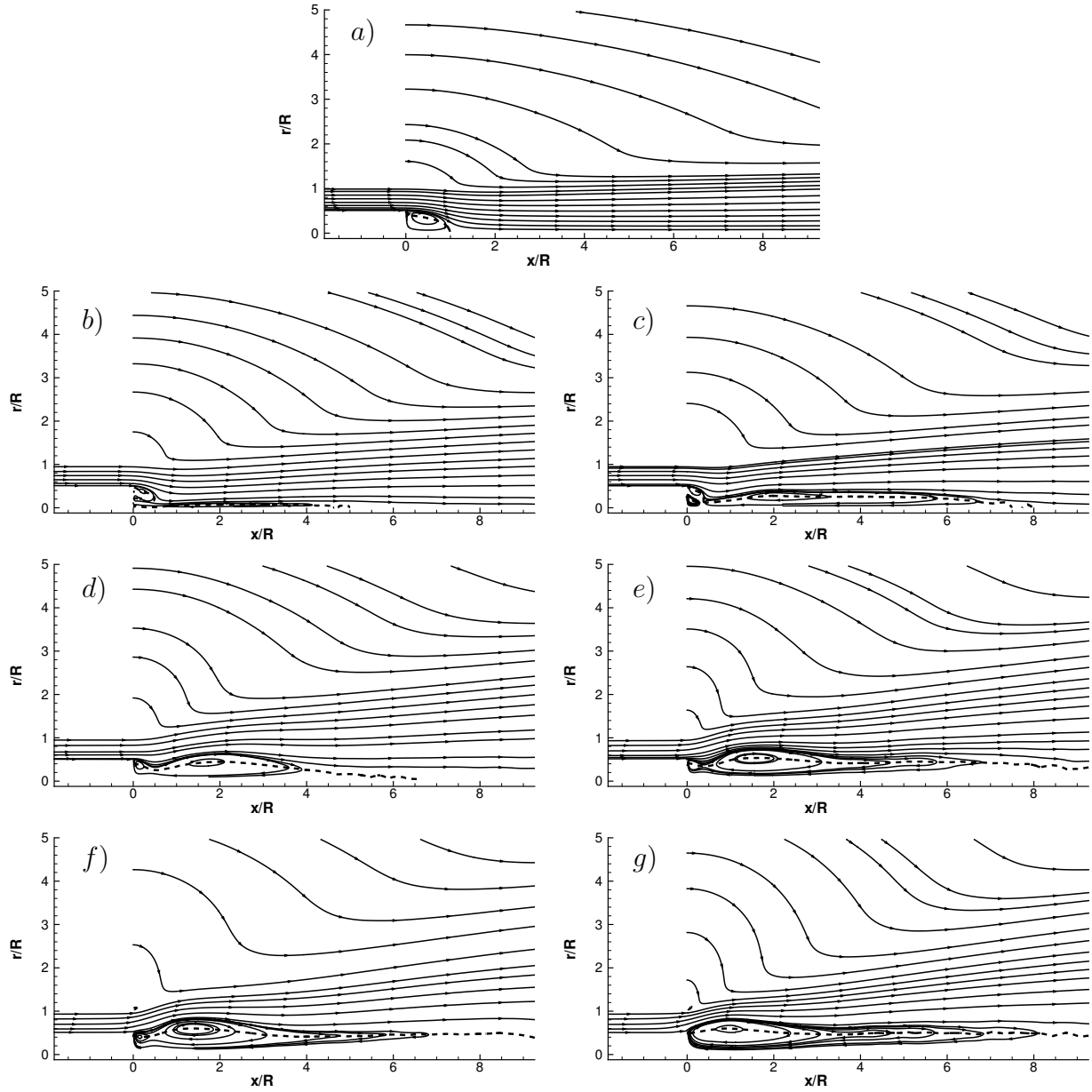

Figure 5.2: Streamlines of the average flow, solid lines. $\langle u_x \rangle = 0$, dashed line. $a)$ $S = 0$. $b)$ $S = 0.4$. $c)$ $S = 0.55$. $d)$ $S = 0.7$. $e)$ $S = 0.85$. $f)$ $S = 1$. $g)$ $S = 1.2$.

plane were addressed. To complete the picture the angle

$$\alpha = \text{arc tan} \left(\frac{\langle u_\theta \rangle}{\langle u_x \rangle} \right) \tag{5.1}$$

between the mean flow and the x-axis is displayed in Fig. 5.4 (in the non-swirling case $\alpha = 0$ so that the picture is dropped). These plots all exhibit a similar

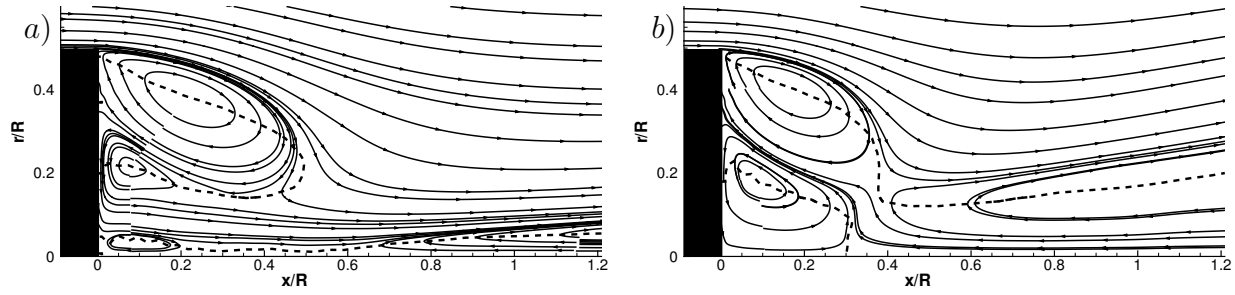

Figure 5.3: Streamlines of the average flow, solid lines. $\langle u_x \rangle = 0$, dashed line. Zoom close to the jet exit. $a)$ $S = 0.4$. $b)$ $S = 0.55$.

structure, for large radii, $\alpha = 0$ in the outer flow. At the outer border of the jet a steep increase is observed with a local maximum. For $S = 0.4$, the maximum occurs around $x/R = 1$ while for the cases with higher swirl the local maximum occurs further downstream at about $x/R = 2$. Inward from this zone a local minimum of α is observed which coincides with the interior of the jet and the maximum of $\langle u_x \rangle$ in the high-swirl cases (see Fig. 5.7$(a1)$). Further towards the axis the flow angle increases again, now beyond 90° which corresponds to the boundary between forward and backward flow. The value of the local maximum in the outer part increases with the swirl number and this zone gets broader and straighter. It in fact identifies the outer border of the jet and its spreading even clearer than the $x - r$ streamlines.

5.2.3 Fluctuating kinetic energy

To conclude the general description of the flow, Fig. 5.5 displays grayscale contours of the fluctuating kinetic energy. The same scale has been used for all simulations to stress the fact that with increasing swirl the level of fluctuating kinetic energy increases dramatically. The maximum kinetic energy for each case is summarized in Table 5.2. In the case $S = 0$ it is characterized by $k_{max} = 0.05U_b^2$ while $k_{max} = 0.32U_b^2$ in case $S = 1.2$. The value of k_{max} increases monotonically with S until $S = 0.85$ where it saturates.

For $S = 0$, the kinetic energy is concentrated in the recirculation zone (GRZ) and in the outer shear layer, Fig. 5.5a. The same happens for $S = 0.4$ but now the recirculation zone, which is the CRZ in this case, is substantially longer. With

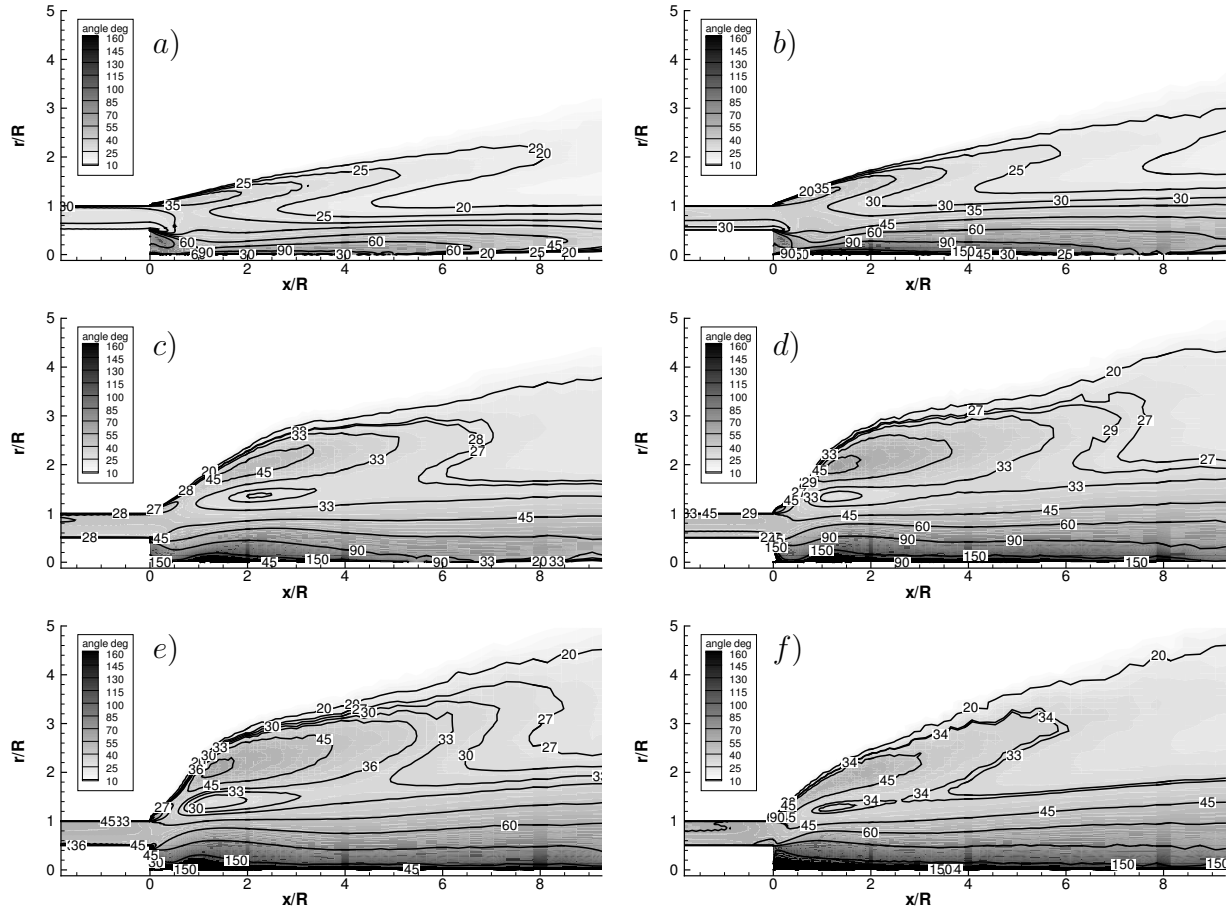

Figure 5.4: α, angle of the average flow with respect to the $x-$axis as detailed in the text. $a)$ $S = 0.4$. $b)$ $S = 0.55$. $c)$ $S = 0.7$. $d)$ $S = 0.85$. $e)$ $S = 1$. $f)$ $S = 1.2$.

increasing swirl, the kinetic energy concentrates in the two shear layers and close to the jet outlet, $x/R < 2$. The concentration of kinetic energy behind the centre body appears to be connected with the existence of the GRZ. A zoom close to the jet exit is shown in Fig. 5.6 for the three cases with $S \geq 0.85$. The value at that location is particularly high for $S = 0.85$ and $S = 1$, Fig. 5.6a, b, while it is very low for $S = 1.2$, Fig. 5.6c. Thus, when the GRZ and the CRZ merge for $S > 1$ the fluctuating activity ceases behind the body. The concentration of kinetic energy is displaced then to the inner shear layer, which is particularly visible for $S = 1$ and $S = 1.2$, and moves upstream entering the inlet duct. The fluctuating kinetic energy for the high swirl cases decays fast with axial direction, i.e. for $S = 1.2$ it decays from $k/U_b^2 \sim 0.3$ at $x/R = 0.5$ to $k/U_b^2 \sim 0.15$ at

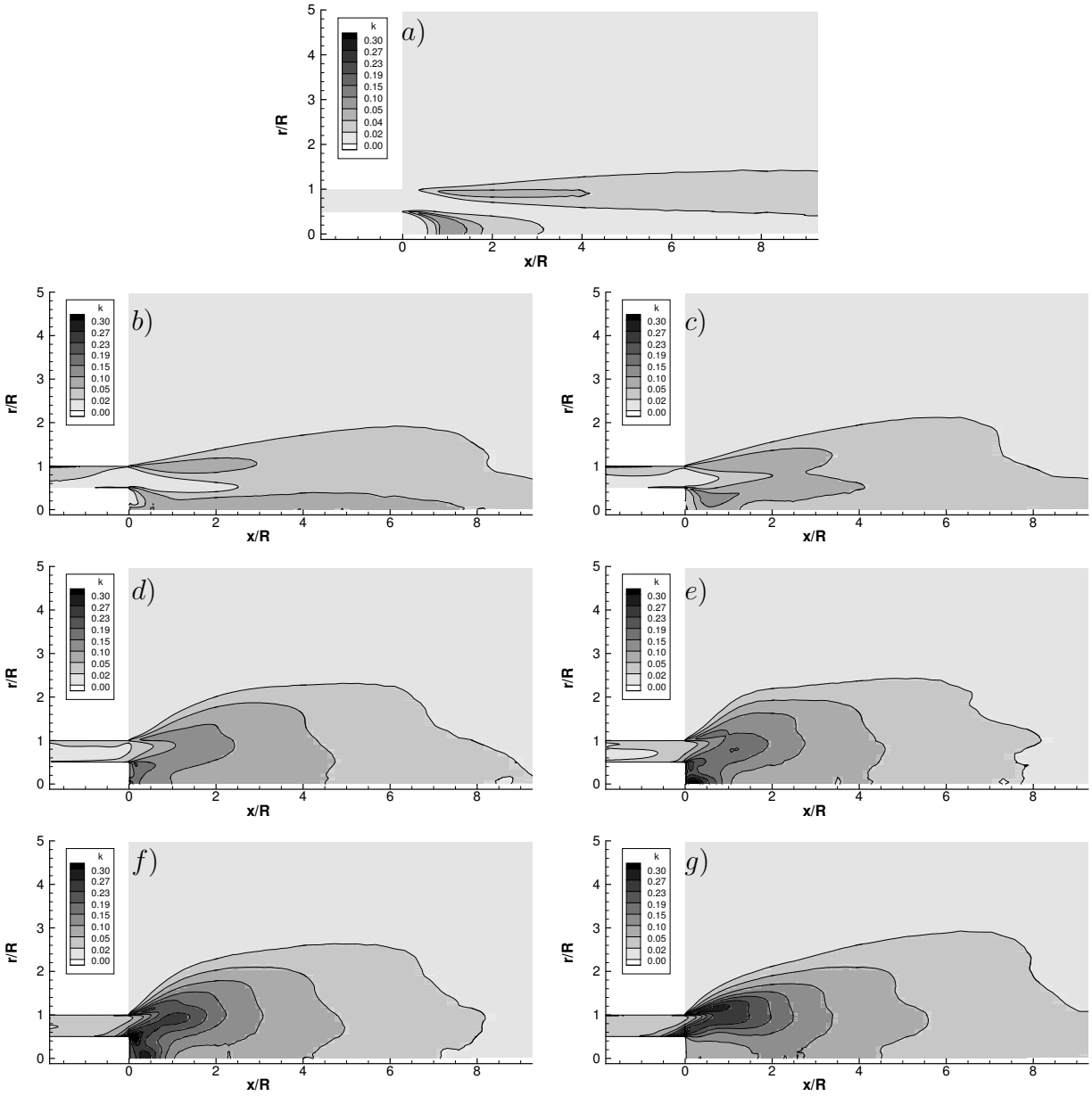

Figure 5.5: Fluctuating kinetic energy. $a)$ $S = 0$. $b)$ $S = 0.4$. $c)$ $S = 0.55$. $d)$ $S = 0.7$. $e)$ $S = 0.85$. $f)$ $S = 1$. $g)$ $S = 1.2$.

$x/R = 2$ and $k/U_b^2 \sim 0.05$ at $x/R = 4$.

5.3 Mean Flow and Statistics

Figs. 5.7 and 5.8 show mean velocity and turbulent intensity profiles at three axial positions: very close to the jet exit at $x/R = 0.2$, within the CRZ in the

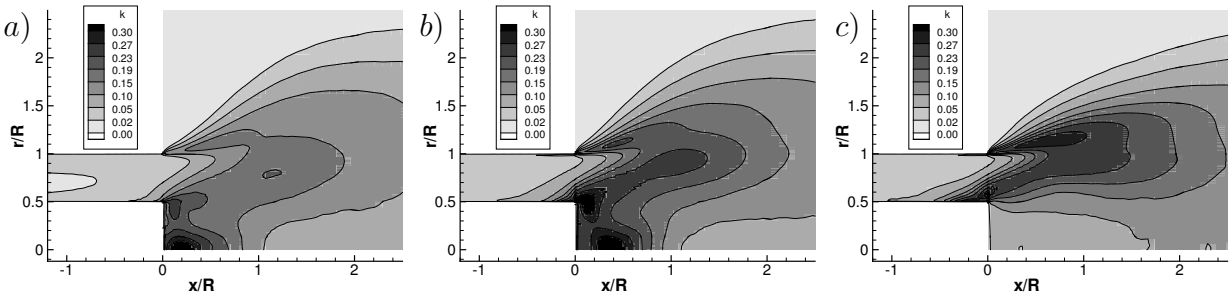

Figure 5.6: Fluctuating kinetic energy. $a)$ S=0.85 $b)$ S=1 $c)$ S=1.2

simulations with swirl at $x/R = 3$ and far downstream of the jet exit at $x/R = 6$. Fig. $5.7(a1 - a2)$ shows mean velocity profiles very close to the jet exit at $x/R = 0.2$. Here, the jet forms two complex three-dimensional shear layers, the inner one with the recirculation zone, and the outer one with the surrounding co-flow. At this position, $x/R = 0.2$, the inner one increases in thickness with S, reaching $0.5R$ for $S = 1.2$. This reflects the growth of the recirculation zone with S discussed above. The outer shear layer remains thin and is just slightly displaced radially outwards with increasing S since close to the jet outlet it is determined by the geometry.

At $x/R = 3$, Fig. $5.7(b1 - b2)$, a qualitative difference between the simulations with low swirl and the simulations with high swirl is observed in all data. The spreading and decay rate is much lower in the former, Fig. $5.7(b1)$. The profiles of mean axial velocity in simulations H12-H15 do not present substantial differences at this location. As soon as the swirl is high enough to produce a strong recirculation zone, a kind of saturation of the profiles is reached. It is also apparent that the backflow in the inner region increases with the level of swirl, and the width of the recirculation region as well. It is interesting to note that the maximum tangential velocity, Fig. $5.7(b2)$, is similar for all cases (except the non-swirling case) despite the difference of swirl at the inlet. The profiles of tangential velocity are displaced radially outwards with increasing swirl. Thus, although the maximum tangential velocity is similar for all cases, the angular momentum increases with increasing swirl.

At $x/R = 6$, Fig. $5.7(c1 - c2)$, the characteristics of the profiles are similar to those at $x/R = 3$. At $x/R = 6$, the basic effects of swirl which are descri-

bed in textbooks (Gupta *et al.*, 1984, chap. 1) are clearly evident. In particular, jet growth, entrainment and decay are enhanced progressively as the degree of swirl is increased. To illustrate, for example, the decay, consider that, in the non-swirling case, the maximum axial velocity at this location is roughly $0.9U_b$ and in the highest swirl case the maximum axial velocity is $0.4U_b$. Thus, in the non-swirling case, the mean axial velocity is still comparable to that at the jet exit while in the highest swirl case the mean axial velocity has decayed by a factor of 3. Note that the maximum and minimum values of mean axial velocity in the whole domain are summarized in Table 5.2. The maximum value increases substantially for the two highest swirl cases as also illustrated by Fig. 5.7$(a1)$.

The axial fluctuations close to the outlet in Fig. 5.8$(a1)$ exhibit a peak in the region of the inner shear layer. The thicker the shear layer, the more pronounced and wider is the peak. The outer shear layer does not present these variations, but with increasing S, the velocity difference is larger, and therefore the turbulence intensity is also larger. Similar conclusions as for the axial fluctuations hold for the azimuthal ones in Fig. 5.8$(b1)$. In the inner part, for $r/R < 0.5$, the fluctuations increase with the swirl until the case $S = 1$. Further increase of S leads to a drop of intensity by a factor of 2 for $S = 1.2$. This is consistent with the previous discussion of the contours of kinetic energy, Fig. 5.6$f - g$.

At $x/R = 3$, the shape of the turbulent intensities is similar for all high-swirl cases, Fig. 5.8$(b1-b2)$, with a slight increase of intensity with S. At this position, the distinction between shear layers is not reflected by the profiles of the fluctuations. Only for the low swirl cases it is still possible to distinguish the peaks due to the fact that these flows develop slower in space than the others. Further downstream at $x/R = 6$, the decay of the jet induced by the swirl is again illustrated by the RMS values. For $S = 1.2$ the maximum of the rms axial fluctuations is $0.3U_b$ at $x/R = 3$ and $0.2U_b$ at $x/R = 6$. On the other hand, for $S = 0$ the maximum of the rms axial fluctuations is $0.2U_b$ at $x/R = 3$ and $0.2U_b$ at $x/R = 6$. The enhanced spreading of the jet with the swirl is also evident from these profiles. In the non-swirling case, the amount of fluctuations at $x/R = 6$ is negligible for $r/R > 2$. For the swirling cases, the radial position where the amount of fluctuations become negligible increases monotonically with S, reaching beyond $r/R > 4$ for $S = 1.2$.

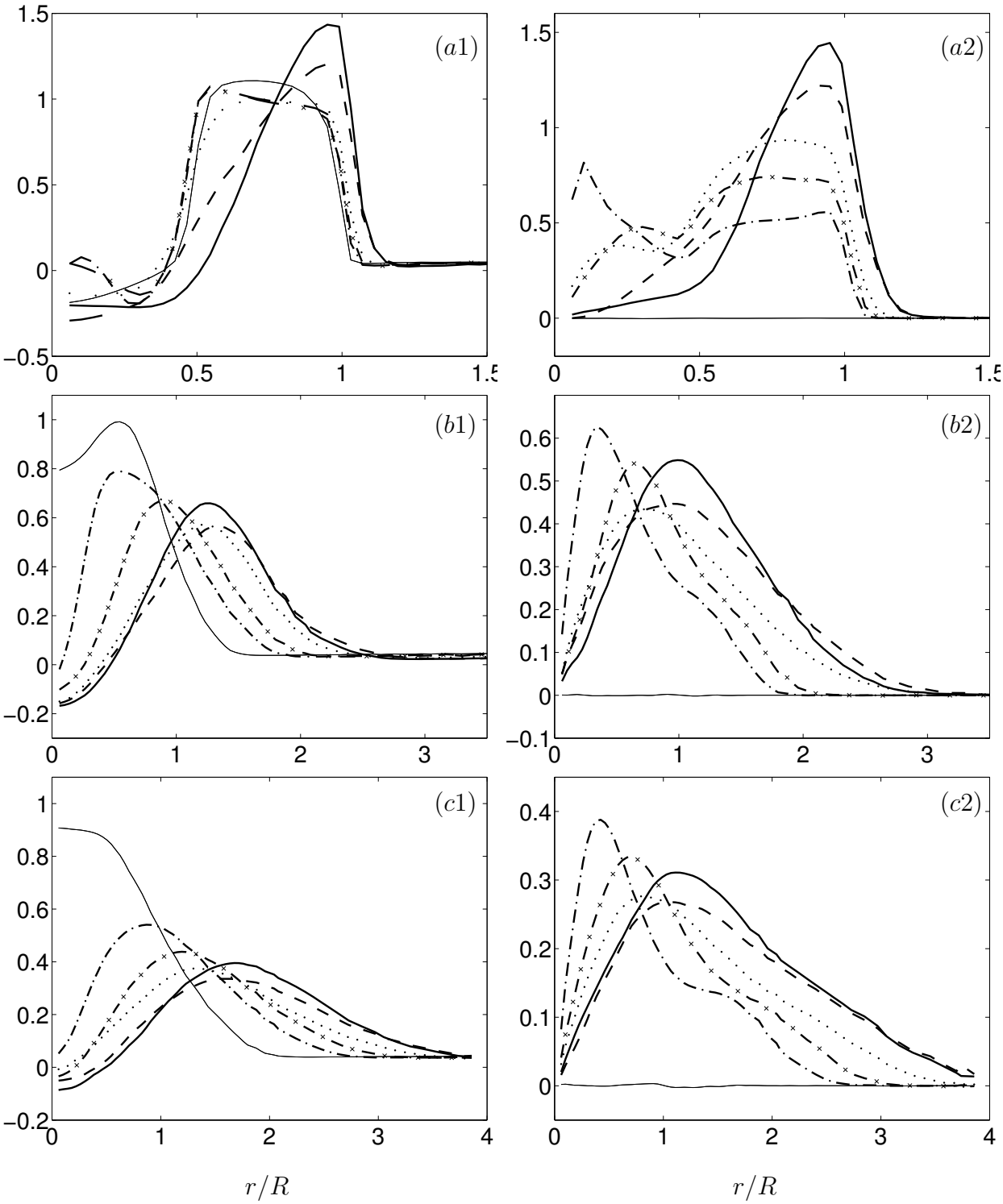

Figure 5.7: Radial profiles of mean velocity for different swirl numbers. Left, axial velocity component. Right, tangential velocity component. $a)$ $x/R = 0.2$. $b)$ $x/R = 3$. $c)$ $x/R = 6$. To enhance readability the range of both axes has been adjusted individually. The line styles are defined in Table 5.1

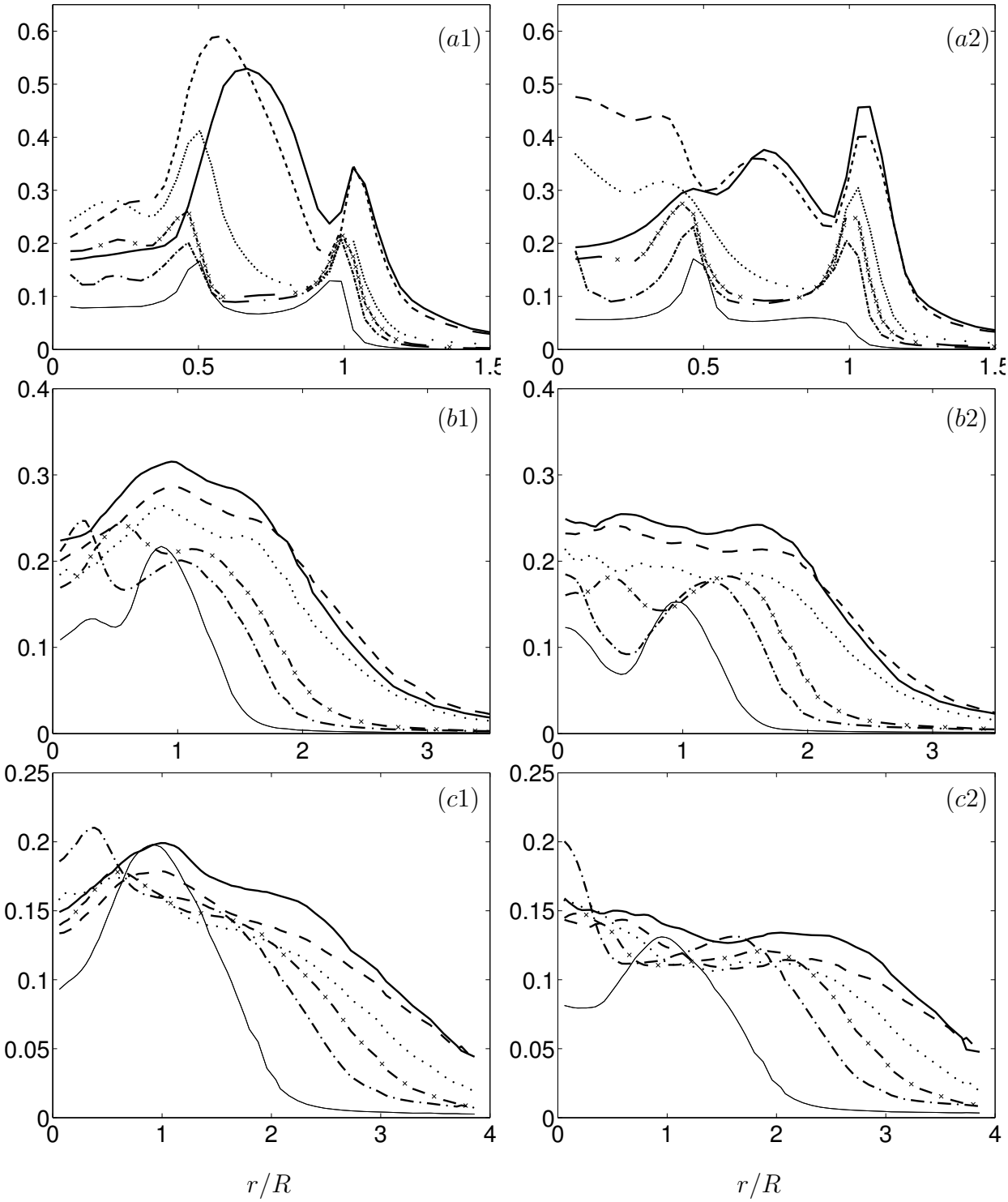

Figure 5.8: Radial profiles of RMS velocity for different swirl numbers. Left, axial velocity component. Right, tangential velocity component. $a)$ $x/R = 0.2$. $b)$ $x/R = 3$. $c)$ $x/R = 6$. To enhance readability the range of both axes has been adjusted individually for each position. The line styles are defined in Table 5.1

5.4 Coherent structures

In Chapter 3 large scale coherent structures were identified and their evolution and interaction described for a high swirl number case, equivalent to H15. It was shown that two families of structures appear resulting from a Kelvin-Helmholtz instability in the inner and the outer shear layer. It is now interesting to study how these structures are modified when varying the swirl number. This is reported in Fig. 5.9 where the same visualization technique is applied as in Fig. 3.18, except that no smoothing was applied. Only one snapshot is included but further views and animations were produced upon which the following comments are based. In the case of low swirl, precessing vortex cores are not expected. However, as in the present case a very thin CRZ is produced, a thin elongated structure can be seen in Fig. 5.9a for $S = 0.4$. Larger values of $p'' < 0$ do not show any large scale structure in these data.

In the case of strong swirl both structures mentioned above are observed. For $S = 0.7$, a single inner and a single outer structure are present. Animations of the flow show that their rotation is in phase and very regular. Upon increasing S, Figs. 5.9e and 5.9f, the irregularity of the flow grows in the sense that the PVCs change in number during their evolution. For $S = 1.2$, up to three of them can co-exist at certain instants. Furthermore, with increasing S, the inner structures enter the inlet duct, slightly for $S = 1$, and in a more pronounced way for $S = 1.2$. At the same time the PVC is displaced off the symmetry axis since the shear layers are shifted outwards. This is consistent with the previous discussion of the kinetic energy contours. In cases $S = 0.7$ and $S = 0.85$, the inner structure is attached to the centre body, Fig. 5.6$c - d$, and its rotation around the symmetry axis is responsible for the high level of fluctuating kinetic energy observed behind the body in Fig. 5.6$d - e$. This is also the case in case $S = 1$ although it is less clear in Fig. 5.9e that the inner structure is always attached to the back of the body. As a consequence, the tangential fluctuations near the axis increase from $S = 0$ to $S = 1$ while decreasing for the larger value $S = 1.2$. The radial fluctuations behave similarly.

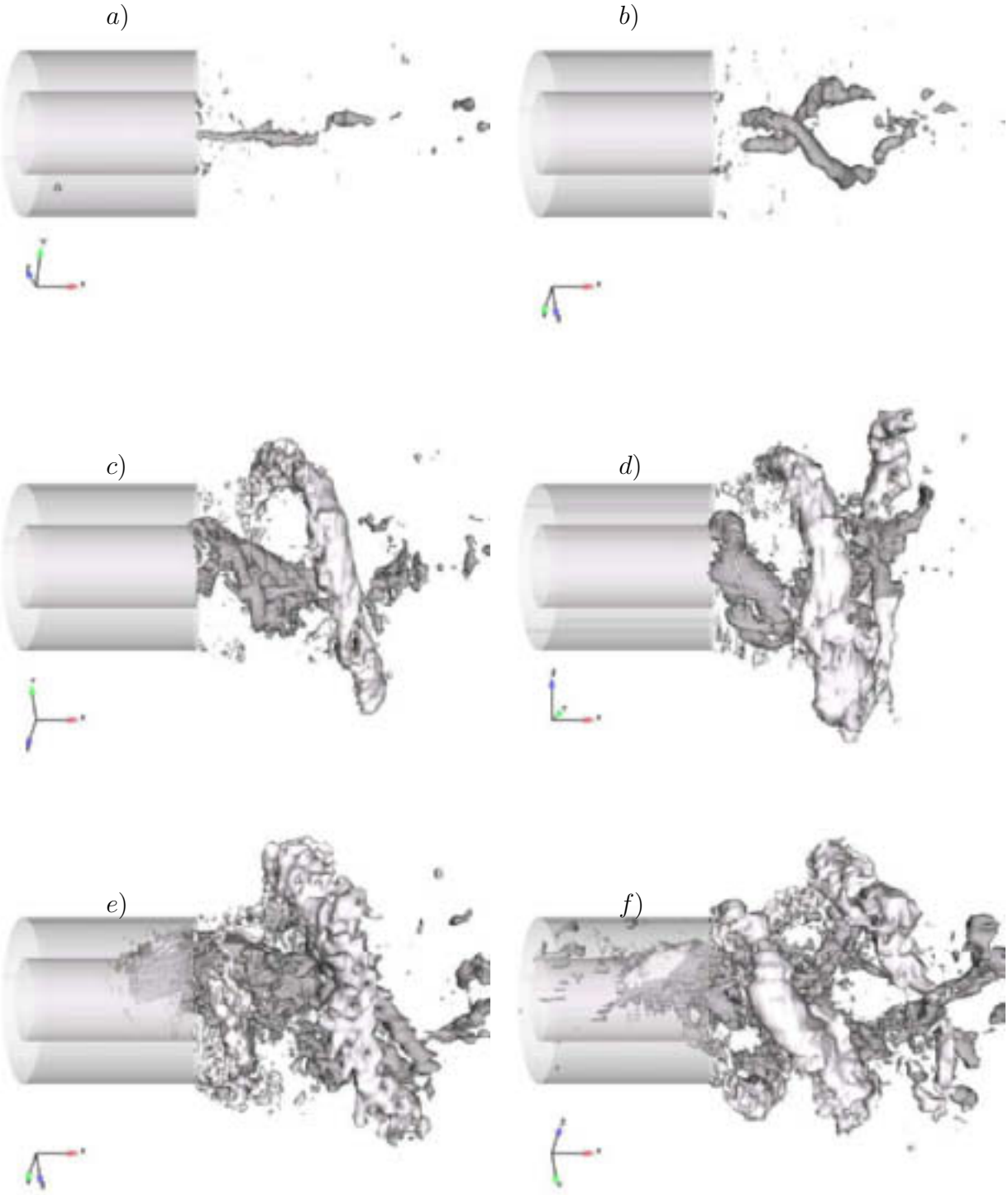

Figure 5.9: Isosurfaces of pressure fluctuations $p'' = -0.3$. $a)$ S=0.4 $b)$ S=0.55 $c)$ S=0.7 $d)$ S=0.85 $e)$ S=1 $f)$ S=1.2 (f)

The outer structures consist of a long spiral for $S = 0.7$ and also become more irregular with increasing swirl. Another interesting feature is that the separation between the inner and the outer structures decreases with increasing S, to the point that in absence of colour it is difficult to distinguish them when $S = 1.2$. The reason for this behaviour is that the two shear layers, identified as the origins and locations of both types of structures, approach each other with increasing S, as seen in Fig. 5.7a.

The case $S = 0.55$ constitutes an intermediate situation between the two regimes of low and high swirl discussed so far. Here, structures are only generated in the inner shear layer, more precisely two of them, and none in the outer shear layer. These structures are located closer to the axis than the PVC for $S = 0.7$ to $S = 1.2$ and also start further downstream. They precess around the axis in a very regular manner. The fact that in this simulation only inner structures are observed suggests that the inner shear layer is more unstable than the outer one, although the thickness of the latter is substantially smaller (Fig. 5.7). This issue, as well as the synchronization between both types of structures, furthermore suggest that the structures in the outer layer are generated by the inner ones. With increasing swirl number, the scenario would then be the following. For low swirl, the CRZ is formed and no instability occurs. Further increasing the swirl, the inner shear layer becomes unstable so that the inner structures are formed. In this case the two shear layers are far from each other (Fig. 5.7a) and the inner structures are relatively weak. Hence, their impact on the outer shear layer is small and not able to generate the large-scale instability there. With $S = 0.7$ and larger, the two layers get closer so that the inner structures generate the outer ones with a synchronized rotation of both.

Comparing the three cases $S = 0.7$, 1, 1.2 in Fig. 5.9 shows that the outer spiralling structures form an increasing angle with the plane x =const. when the swirl increases. By close visual inspection a typical angle of 26°, 30° and 33° has been determined from such pictures for $S = 0.7$, 1, 1.2, respectively. It is now interesting to relate these values to the flow angle α displayed in Fig. 5.4. In the above discussion it was noted that the local minimum of α is located roughly in the interior of the main jet. The corresponding inner-most level lines are $\alpha = 26°$ for $S = 0.7$ and $\alpha = 30°$ for $S = 1.$, respectively, while the same plot for

$S = 1.2$ yields $\alpha = 33°$ in this point. Hence, the angles of the coherent structures correspond very well to the local minima of the flow angle. This supports the observations in Chapter 3 where streamlines of the average flow were inserted into plots of the coherent structures to show that the latter are perpendicular to the average flow thus supporting their generation by a Kelvin-Helmholtz instability (see Figs. 3.24 and 3.26). The present way of investigating this issue complements the previous approach and yields a precise picture.

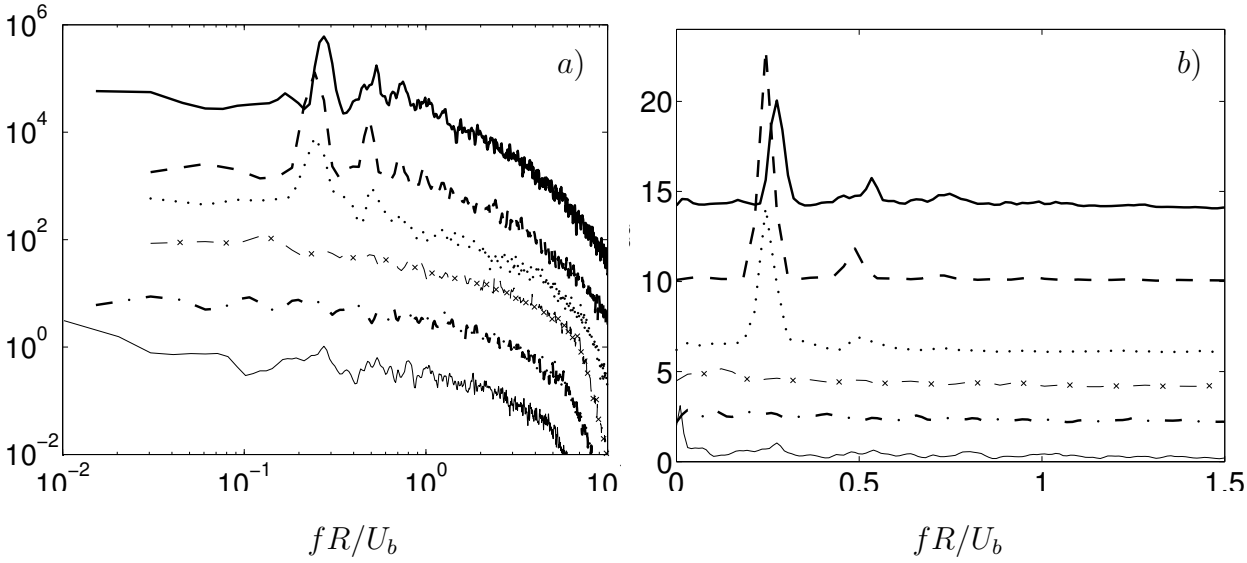

Figure 5.10: PSD of axial velocity fluctuations at $x/R = 0.1$, $r/R = 0.7$ for different swirl numbers. Arbitrary units are used in the vertical axis and the curves have been shifted vertically for readability. $a)$ Diagram with logarithmic axes. $b)$ The same diagram with linear axes. The line styles are defined in Table 5.1.

5.5 Spectra

Fig. 5.10 shows the power spectrum density (PSD) of axial velocity fluctuations at $x/R = 0.1$, $r/R = 0.7$, i.e. very close to the jet exit and in the region of the inner shear layer for the high swirl cases. In the cases of low swirl the spectra do not show a pronounced peak. When the level of swirl is high, i.e., a dominant peak and its higher harmonics appear in the spectrum. This peak reflects the precessing structures observed in Fig. 5.9. Its frequency is almost constant with

increasing swirl number, more precisely $f_{peak} = 0.24U_b/R$ for $S = 0.7$ and $S = 1$ and $f_{peak} = 0.28U_b/R$ for $S = 1.2$. This constancy is unexpected at first sight since the level of swirl is increased by about 70%. Even if the swirl is attenuated between $x/R = -2$ and $x/R = 0.2$ due to friction as can be appreciated by comparing Fig. 5.1b and Fig. 5.7b, the variation of swirl and hence circumferential velocity remains substantial between the three cases.

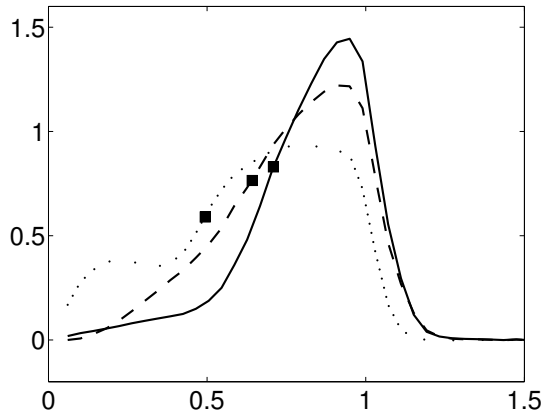

Figure 5.11: Radial profiles of the mean tangential velocity at $x/R = 0.2$ for the cases $S = 0.7$, 1 and 1.2. Symbols identify the middle of the shear layer as detailed in the text.

The reason for the observed behaviour of f_{peak} is presented in Fig. 5.11. The shape of the profiles of $\langle u_\theta \rangle$ at $x/R = 0.2$ changes substantially from $S = 0.7$ to $S = 1.2$, turning from a top-hat-like shape to a more triangular shape. As discussed above, the inner structures are generated by an instability of the inner shear layer. The center of this layer has been marked with a dot in Fig. 5.11 displaying the azimuthal velocity. This position has been obtained by first adding vectorially $\langle u_x \rangle$ and $\langle u_\theta \rangle$, then visually determining the velocity values at both boundaries of the shear layer and choosing their mean value. It turns out that the center of this shear layer shifts outward with increasing S. At the same time the angular velocity at this center increases. While it is not possible to apply the theory of plane shear layers directly, as discussed above, it can be stated that qualitatively the increased swirl is located further outward in the annular jet so that the circumference to be covered is larger. With the same number of structures along the circumference the frequency can then remain constant. If only the azimuthal

velocity at the location of the symbol would matter constant frequency would require the symbols to lie on a straight line going through the origin. This indeed is almost the case. For $S = 0.55$ precessing structures are also observed, Fig. 5.9b, and this should be reflected by the PSD. The monitoring point, however, selected *a priori* at $r/R = 0.7$ for all runs is not crossed by the structures in this case. They occur closer to the axis and further downstream as discussed above. As a consequence, no peak is observed in the PSD provided in Fig. 5.10 for $S = 0.55$.

6 Influence of pulsating inflow

In this chapter the effect of oscillating inflow on an annular swirling jet is studied. The results are compared to the same configuration with constant inflow. Analysis of phase-averaged velocity components, vorticity, turbulent kinetic energy and spectra provides detailed information about the flows considered.

6.1 Motivation

Swirling flows, as discussed in Chapter 1, are prone to instabilities which can trigger combustion oscillations and degrade the performance of the combustor. In the case of a thermo-acoustic combustion instability, temporal oscillations of the pressure in the combustion chamber induce substantial fluctuations of the mass flow rate into the combustion chamber at the burner outlet. It is therefore of crucial importance to investigate the effect of a pulsating flow rate in the presence of swirl. For non-swirling pulsating jets, experiments and simulations (Tang & Ko, 1994; Wicker & Eaton, 1994) have shown dominant ring vortices.

Only few attempts have been made so far to compute and analyze swirling flows with pulsating inflow. Düsing *et al.* (2002) performed LES of a swirling confined diffusion flame with oscillating inflow. The averaging time, however, was not long enough to obtain definite conclusions. Wang *et al.* (2005) studied the flow evolution of a swirl-stabilized injector and its dynamic response to external forcing using LES. In this case, the configuration was very complex, however, involving three radial swirlers, with the flow in one of them counter-rotating with respect to the others. Furthermore, the forcing was weak with respect to the flow intensity, and had only a small impact on the flow characteristics.

Sim.	Grid	SGS	B	TU_b/R	Mass flow	S
H7	F2 (~ 6 mio.)	Dyn.	–	–	Fixed	Fixed
H16	F2 (~ 6 mio.)	Dyn.	0.4	3.5	Osc.	Fixed
H17	F2 (~ 6 mio.)	Dyn.	0.4	3.5	Osc.	Osc.

Table 6.1: Overview of the simulations performed to investigate the influence of pulsating inflow

6.2 Computational Setup

The flow configuration is based on the simulation H7 discussed in Chapter 4. The pulsating inflow was prescribed by imposing an oscillating flow rate in the precursor simulation according to

$$Q = Q_0 \left(1 + B \ \sin\left(\frac{2\pi t}{T}\right)\right), \tag{6.1}$$

where Q_0 is the flow rate without pulsation. The amplitude of the disturbance is $B = 0.4$ in the present configuration which corresponds to experimentally observed values (Koch, 2004). The oscillation period was set to $T = 3.5R/U_b$ which roughly equals the precessing period of the coherent structures observed in the non-pulsating simulations and is also motivated by experimental data from thermo-acoustic instabilities (Büchner, 2005).

Table 6.1 provides an overview of the simulations performed. Two cases were considered depending on the specification of the inflow conditions. Both correspond to modifications of H7. In H16, the mass flow oscillates periodically while the swirl number is kept fixed so that both, the axial and the azimuthal velocity component oscillate periodically (see equations (3.1) and (6.1)). In H17, the body force in the azimuthal direction is kept constant while only the axial flow rate pulsates, Fig.6.1. As a consequence, the swirl number oscillates. Note that different scenarios of pulsation are realistic since the swirl-generating devices in a burner can be different. An axial swirl generator with helical vanes maintains the angle of the flow so that the swirl number will change only little as in H16. With a radial swirler, on the other hand, the axial component can be influenced independently of the angular component upon the occurrence of a thermo-acoustic instability

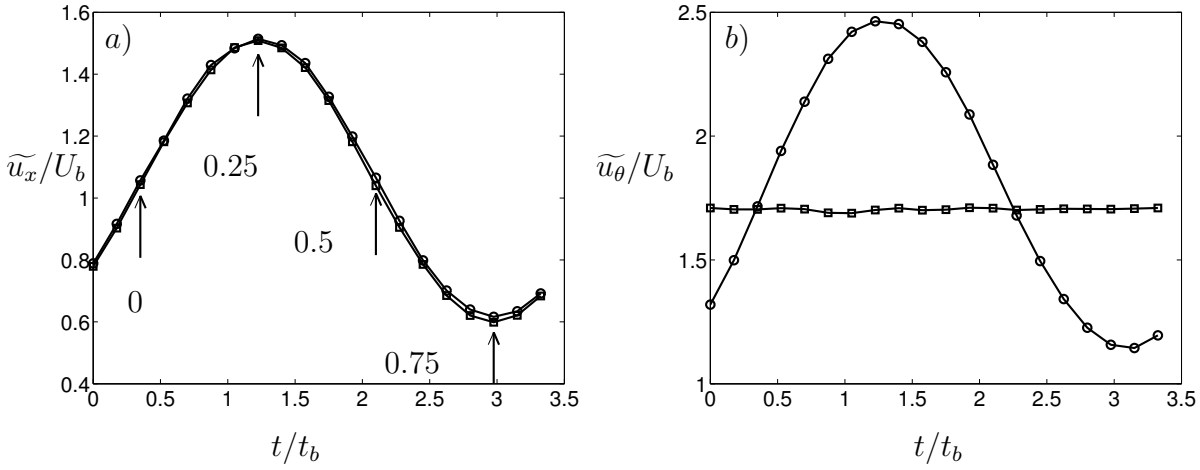

Figure 6.1: Phase-averaged velocity at the inflow plane $x/R = -2$ at $r/R = 0.75$, i.e. in the middle of the annular duct, as a function of time over one period. $a)$ Axial component $\widetilde{u_x}/U_b$ and phases discussed below. $b)$ Tangential component $\widetilde{u_\theta}/U_b$. H16: circles. H17: squares.

resulting in an oscillating flow angle and an oscillating swirl number. Hence, the two cases considered here are representative of extreme cases in applications and allow to assess the sensitivity of the observations with respect to the method of swirl generation. Fig. 6.1 displays characteristic values of phase-averaged velocity generated by the precursor simulation.

6.3 Phase-averaged flow

In order to analyze the flow, each quantity ϕ is decomposed as

$$\phi = \widetilde{\phi} + \phi'' \quad , \tag{6.2}$$

where $\widetilde{\phi}$ denotes the phase average. The phase itself is defined as

$$\psi = \mathrm{mod}\left(\frac{t}{T}, 1\right) \quad . \tag{6.3}$$

With equation (6.1) this implies that $Q(\psi = 0) = Q_0$ while for $\psi = 0.25$ and $\psi = 0.75$ the flow rate is maximal and minimal, respectively. All averaged quantities given below are the resolved ones.

After the computation of several periods, the phase-averaged statistics were gathered during 15 periods of pulsation, and averaging was also performed in azimuthal direction. Each period was divided into 20 phases and the four phases indicated by an arrow in Fig.6.1a are selected for discussion here. Figs. 6.2-6.4 show velocity profiles from the three simulations at two axial stations in the near field of the jet exit. The influence of the pulsation decreases with distance from the jet exit. The most important characteristics of the simulation without pulsation, H7, are a recirculation zone, typical for flows with a high level of swirl, and two shear layers, an inner one bordering the recirculation zone and an outer one between the jet and the surrounding co-flow. Due to the swirl, both shear layers are subject to curvature effects.

The impact of the pulsating inflow on the recirculation zone can be observed in Fig.6.2$c-f$ displaying phase-averaged axial velocity profiles, $\widetilde{u_x}(\psi)$. In H17, the shape of the recirculation zone is almost unaffected by the pulsation as revealed by comparison of Fig.6.2b and Fig.6.2f for $r/R < 0.5$. In H16, the backflow region widens with the deceleration of the flow indicating that the recirculation zone is affected by the oscillation of the azimuthal component. The influence of the pulsation on the shear layers is more difficult to quantify because it involves both axial and tangential velocity components. The latter is shown in Fig.6.3. As expected, the tangential profile changes substantially in H16 at $x/R = 0.1$. This is not only related to a change in amplitude but also a substantial change in shape and affects mainly the inner shear layer. Further downstream, the phase-averaged tangential component also oscillates in the outer part of the jet (Fig.6.3d). With fixed tangential forcing in H17, the inter-phase changes in the inner part are very small, but in the outer part, $r > R$, say, they attain amplitudes comparable to H16. Comparing results at $x/R = 0.1$ and $x/R = 1$, a time lag between the flow at the inlet and the tangential component downstream of the inlet is observed. When the flow at the inlet starts to accelerate (shortly after $\psi = 0.75$) the tangential component attains its maximum in both H16 and H17, although the effect is better seen in H16. During the acceleration phase ($\psi = 0.75 \rightarrow 0.25$), the tangential profile spreads radially outwards.

In the simulation without pulsating inflow, the radial velocity component, shown in Fig.6.4, is very small compared to the other two components. In the pulsating

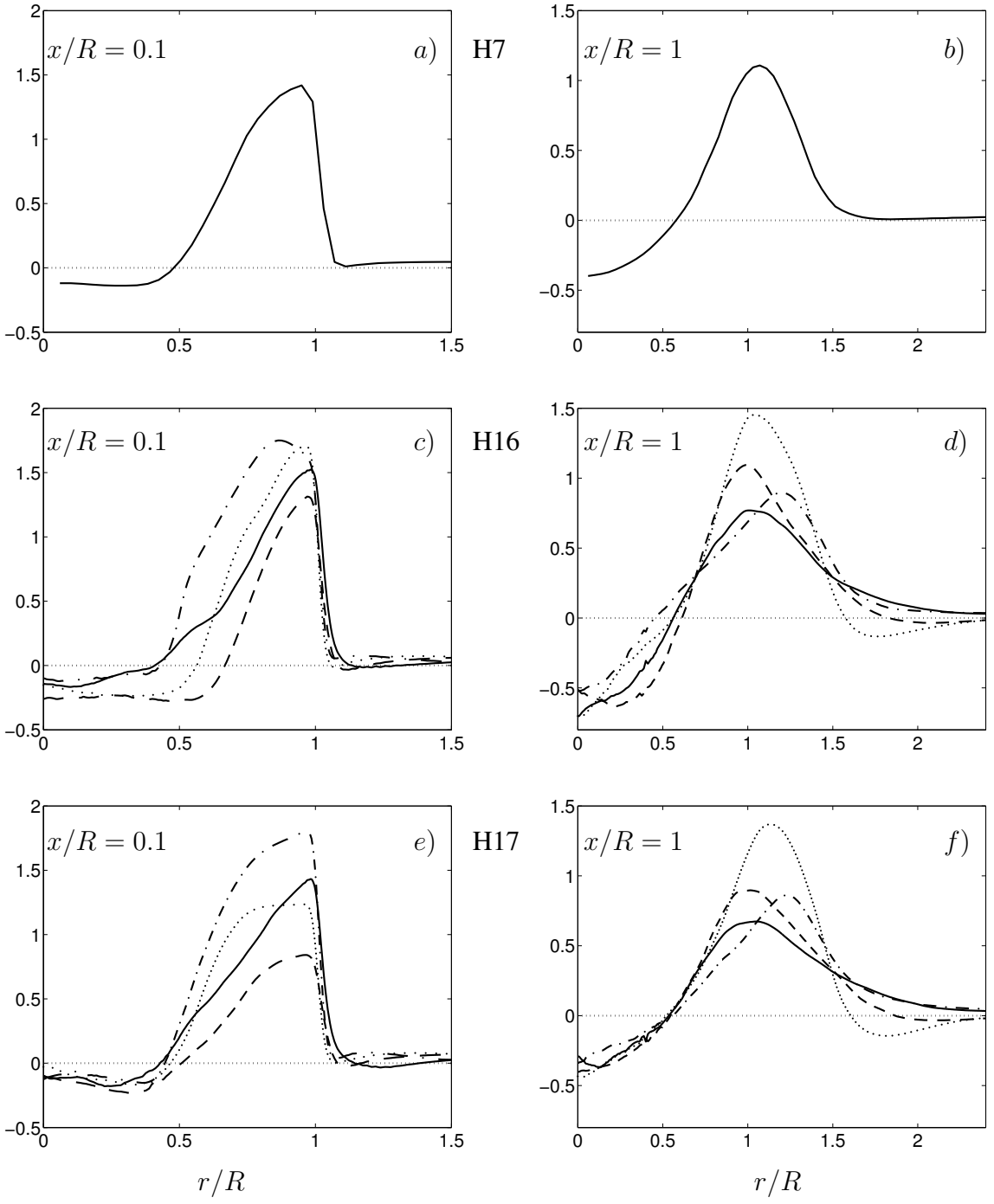

Figure 6.2: Radial profiles of axial velocity u_x/U_b at $x/R = 0.1$ (left) and $x/R = 1$ (right). $a-b)$ Time-averaged velocity in H7. $c-d)$ Phase-averaged velocity in H16. $e-f)$ Phase-averaged velocity in H17. Phases as indicated in Fig.6.1. $\psi = 0$ ——. $\psi = 0.25$ —·—. $\psi = 0.5$ ·····. $\psi = 0.75$ – – –.

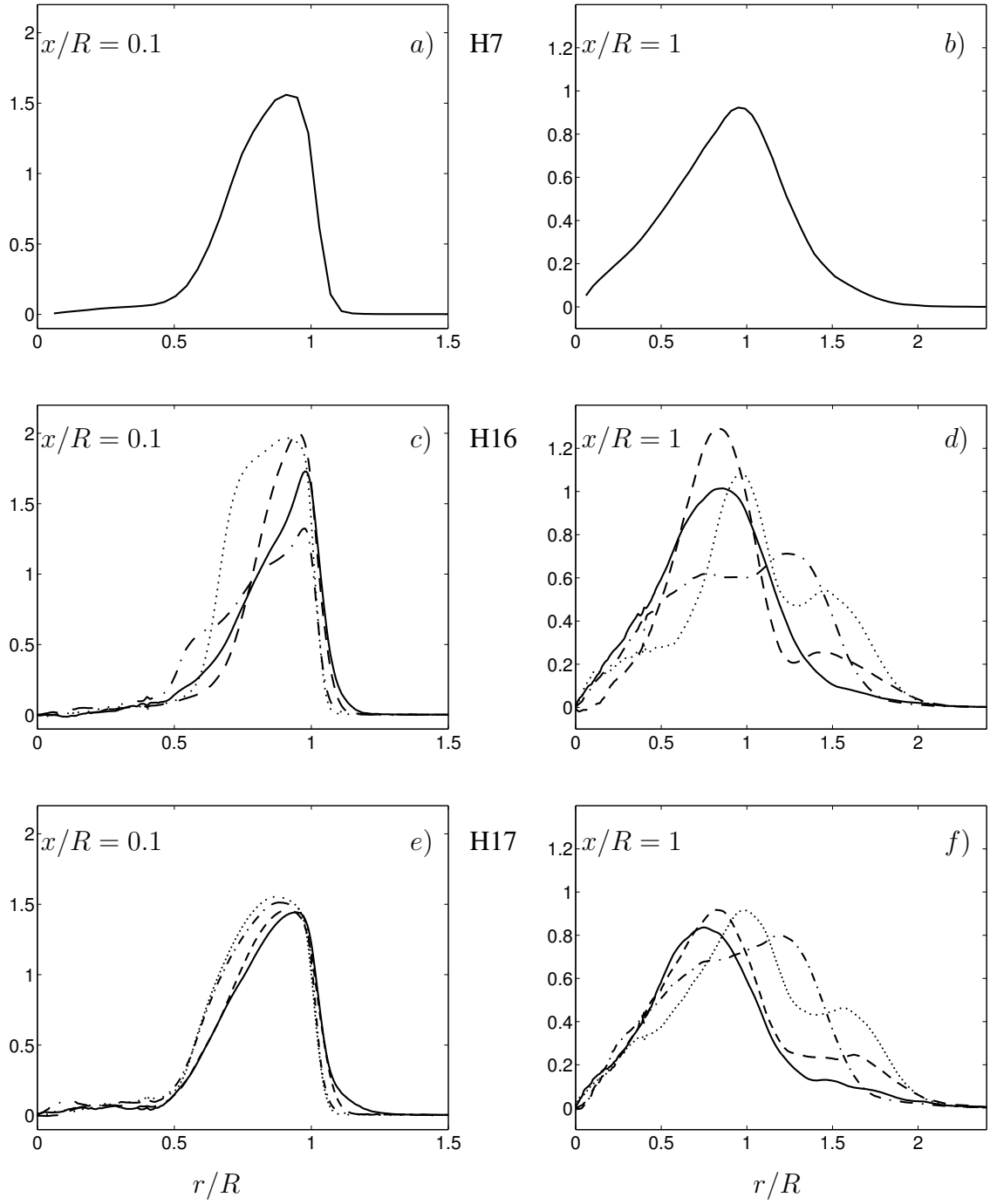

Figure 6.3: Profiles of tangential velocity u_θ/U_b at $x/R = 0.1$ (left) and $x/R = 1$ (right). $a - b)$ Time-averaged velocity in H7. $c - d)$ Phase-averaged velocity in H16. $e - f)$ Phase-averaged velocity in H17 Phases as indicated in Fig.6.1. $\psi = 0$ ——. $\psi = 0.25$ —·—. $\psi = 0.5$ ·····. $\psi = 0.75$ – – –.

cases, however, it exhibits substantial variations. At $x/R = 1$, it varies between $\widetilde{u_r}(0.75) \sim -0.4$ and $\widetilde{u_r}(0.25) \sim 0.4$ in H16, and similar values occur in H17. This is related to the roll-up of the outer shear layer, in which a ring vortex is produced.

Fig.6.5 shows a series of contour plots of phase-averaged tangential vorticity $\widetilde{\omega_\theta}$. Its behaviour is very similar in both simulations. When the flow accelerates at the inlet ($\psi = 0.75 \rightarrow 0.25$) the sheet of negative azimuthal vorticity moves radially outwards and during the deceleration process ($\psi = 0.25 \rightarrow 0.75$) the ring vortex is shed.

Fig.6.6 reports contour plots of the turbulent kinetic energy k. In the non-pulsating simulation it is defined by the fluctuations with respect to the time average. In this case the kinetic energy is concentrated in the two shear layers of which the inner one extends substantially into the inlet duct. The maximum is about $k/U_b^2 = 0.3$ and k rapidly decays with distance from the jet exit. At $x/R > 3$, the results show that $k/U_b^2 < 0.1$. In the simulations with oscillating inflow, k is defined by means of the fluctuations with respect to the phase average. Again, most of this kinetic energy is concentrated in the shear layers. In both H16 and H17 the turbulent fluctuations in the outer part are observed at the locations of the vortex ring discussed above, as revealed by comparing corresponding plots in Fig.6.5 and Fig.6.6. During the phases $\psi = 0$ and $\psi = 0.25$, to a smaller extent also for $\psi = 0.5$, an accumulation of kinetic energy is visible further downstream, moving towards the axis which results from the vortex ring shed during the previous period. The main differences between H16 and H17 are noticed in the inner shear layer. In H16, the kinetic energy in the inner part oscillates with the flow. In the acceleration phase ($\psi = 0.75 \rightarrow 0.25$) the kinetic energy is substantially reduced in this region, re-appearing in the inlet duct during the deceleration phase ($\psi = 0.25 \rightarrow 0.75$). In H17, the overall level of k is higher. An accumulation of kinetic energy in the region of the inner shear layer is observed in all phases. It remains at this location and is only little affected by the pulsation, except for the intensification and elongation during the deceleration phase, i.e. for $\psi = 0.5$. These observations are in line with the discussion of the profiles of phase-averaged velocity components above.

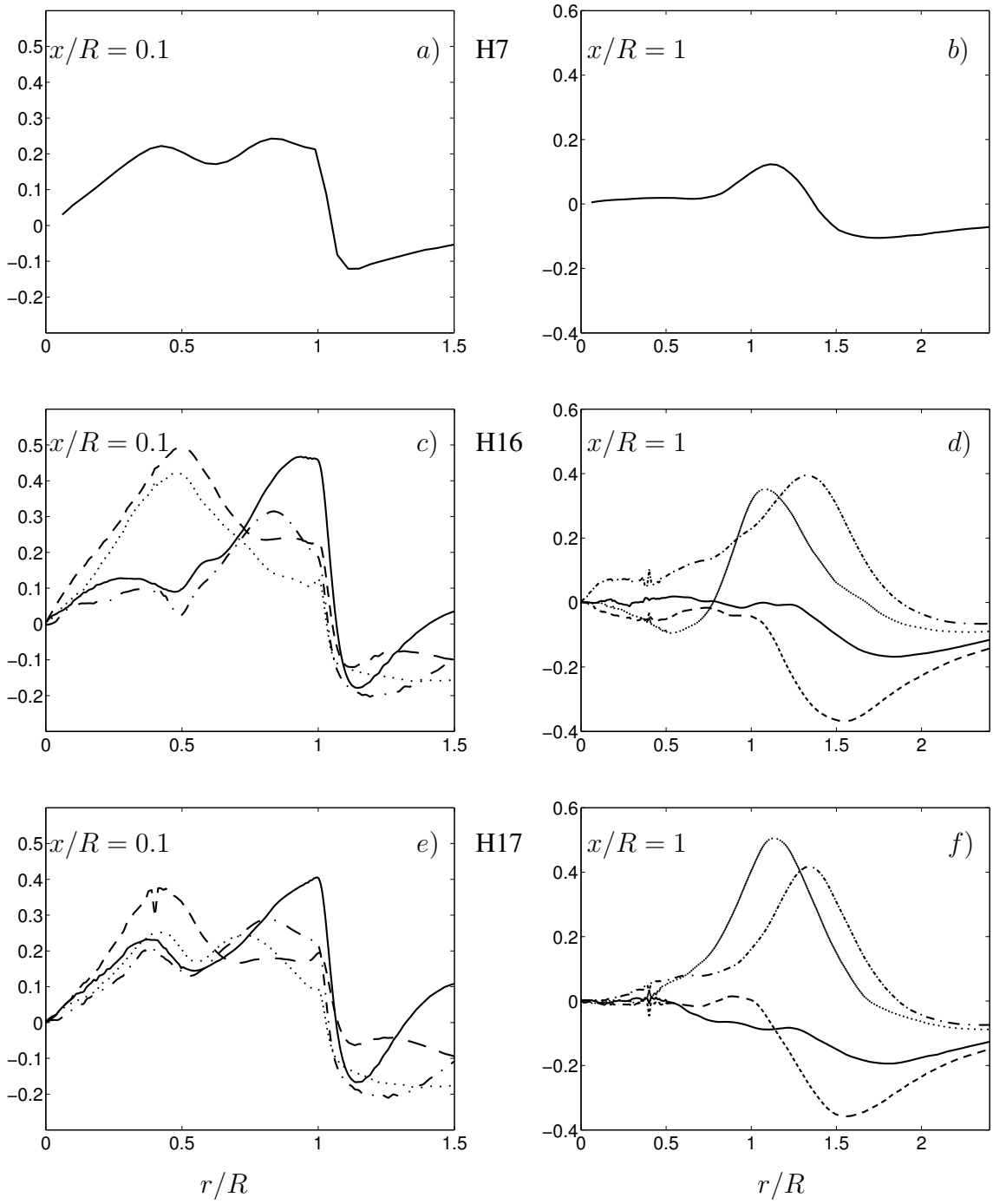

Figure 6.4: Profiles of average radial velocity u_r/U_b at $x/R = 0.1$ (left) and $x/R = 1$ (right). $a - b)$ Time-averaged velocity in H7. $c - d)$ Phase-averaged velocity in H16. $e - f)$ Phase-averaged velocity in H17 Phases as indicated in Fig.6.1. $\psi = 0$ ——. $\psi = 0.25$ —·—. $\psi = 0.5$ ·····. $\psi = 0.75$ – – –.

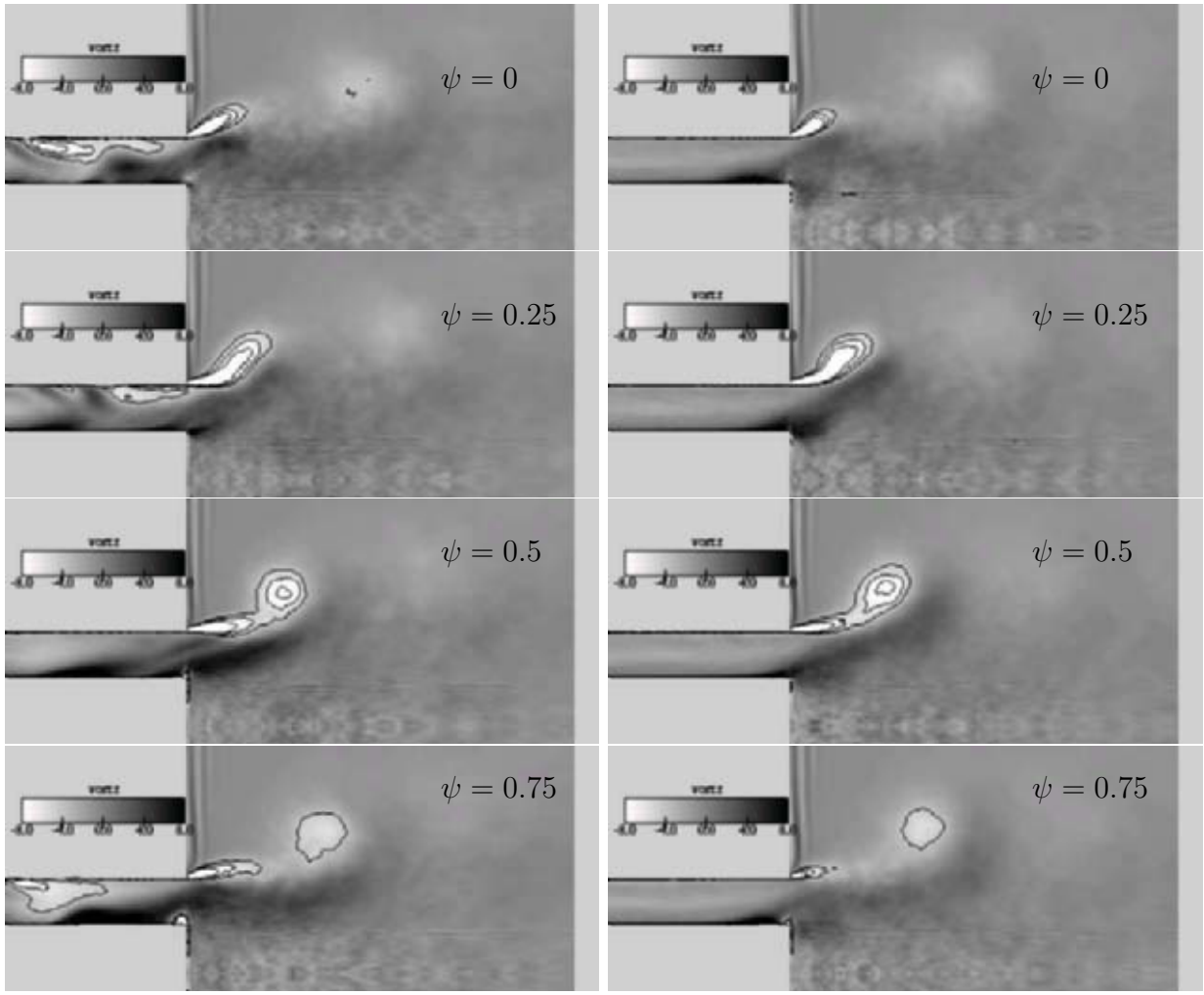

H16 H17

Figure 6.5: Phased-averaged tangential vorticity $\widetilde{\omega_\theta}$ in a plane $\theta = const.$

6.4 Instantaneous structures

In order to visualize instantaneous coherent structures, iso-surfaces of the instantaneous pressure deviation $p'' = p - \tilde{p}$ are reproduced in Fig.6.7. To enhance visibility, the pressure was filtered by applying twice a top hat filter of width equal to twice the grid spacing. The same visualization technique is applied as in Fig. Fig. 3.18. In H7 without pulsation large-scale coherent structures rotating at a constant rate around the symmetry axis can be identified (Fig.6.7a).

The influence of the oscillating inflow on the coherent structures is illustrated in Fig.6.7b, c. For conciseness, only one snapshot is included here for each simulation. As in the case without pulsation, coherent structures located in both shear

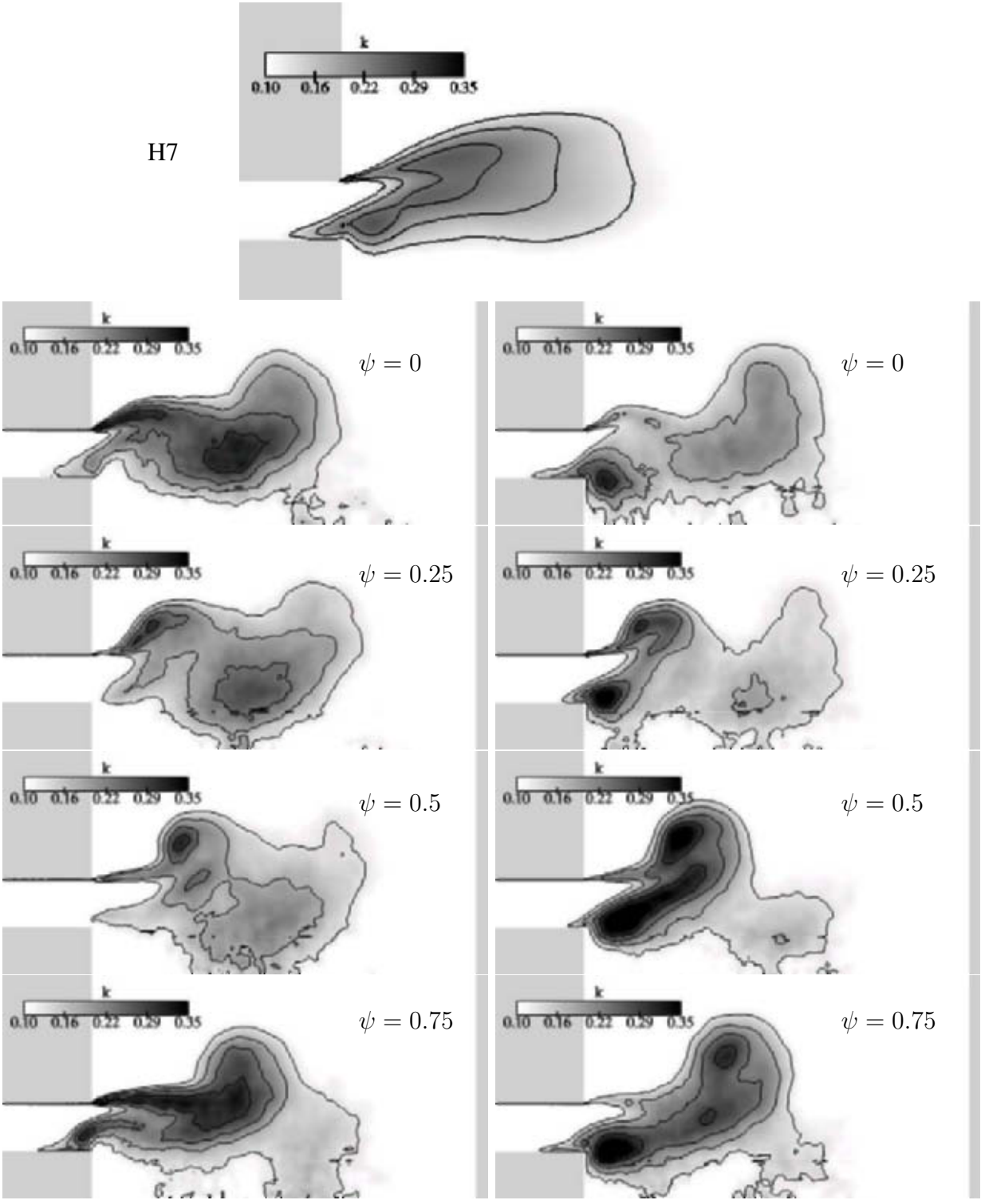

Figure 6.6: Turbulent kinetic energy k/U_b^2 in a plane $\theta = const$. Top : H7 without pulsation. Left: Four phases from H16, Right: the same phases from H17.

layers are visible. In H16, Fig.6.7b, the structures are less organized and persist over shorter lapses of time than for H7. In H17, Fig.6.7c, the structures resemble those of H7, both in shape and regularity. Here, the pulsation has more impact on the outer structures than on the inner ones. Due to the successive processes of acceleration and deceleration, the outer structures are subject to stretching. Thus, secondary instabilities oriented in streamwise direction are formed to a larger extent than in the non-pulsating case. Two of these structures can, e.g., be seen at the outer boundary of the outer spiral in Fig.6.7c.

The visualization technique used in Fig.6.7 requires some discussion. In previous studies such as Fröhlich *et al.* (2005), e.g., it was found advantageous to use pressure fluctuations instead of the instantaneous pressure itself to identify vortices: subtracting the average pressure helps in assuring that the chosen pressure level visualizes vortex structures in a wider range of the domain. The average pressure field is not related to turbulent structures and can hence be subtracted without problem. Here, in contrast, the phase-averaged pressure is subtracted in Fig.6.7$b-c$ which by itself may contain dynamic structures. In the present case these have the form of the rings as discussed above. For validation and comparison, iso-surfaces of the pressure have been generated for the same data sets and are reported as well (Figs. 6.7$d)-e$)). Their behaviour is similar, showing that the vortex rings generated by the pulsation do not overwhelm the swirl-generated structures in the flows considered. Iso-surfaces of p'' are not closed here and allow better identification of the structures. Application of this technique in general cases, however, is not warranted without preliminary validation.

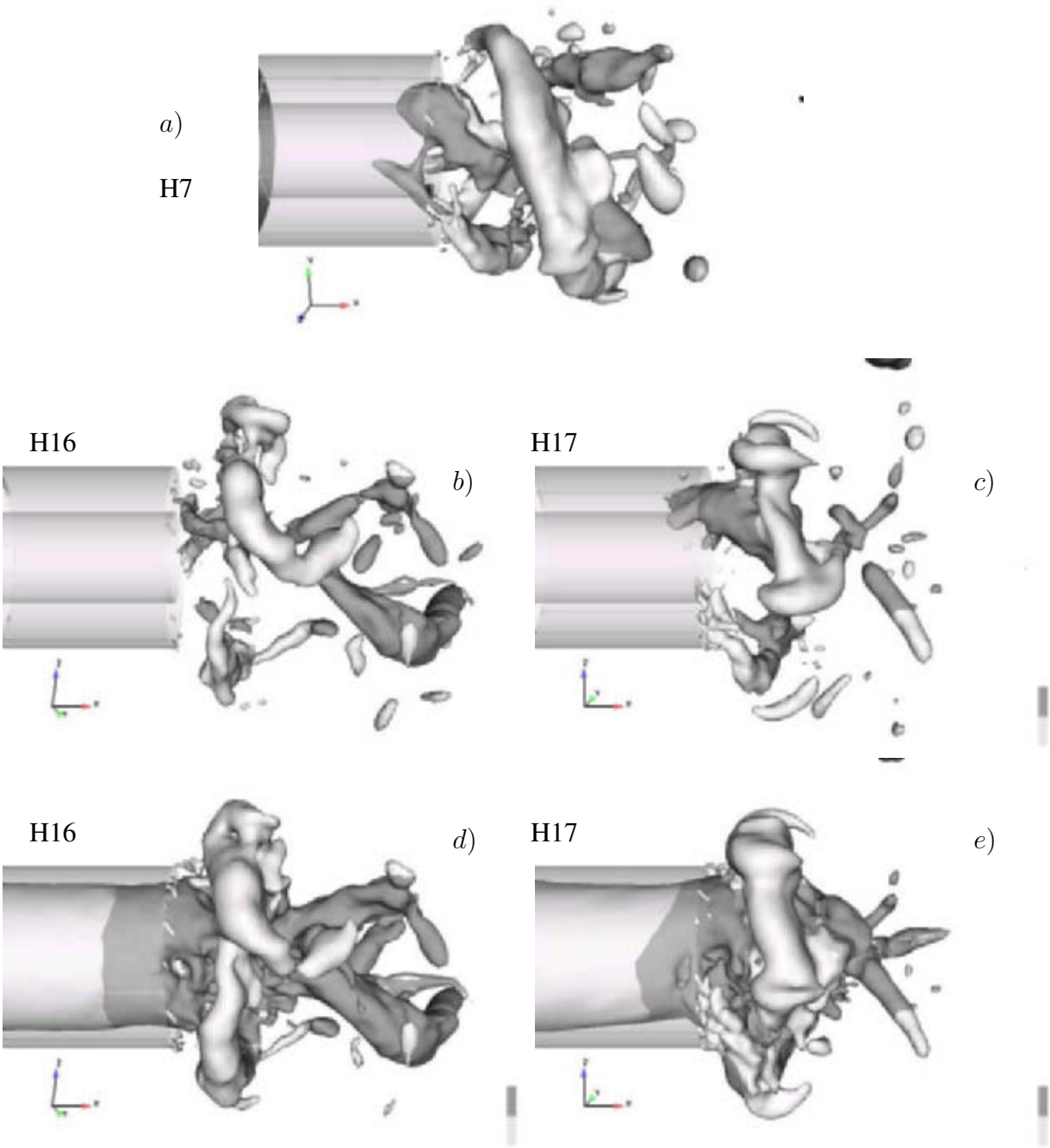

Figure 6.7: Instantaneous coherent structures at $\psi = 0.25$ (arbitrary instant for H7). $a - c$) Iso-surface of pressure fluctuations $p'' = -0.3$, $d - e$) Iso-surface of pressure $p = -0.5$ for the same data sets. The color is determined by the sign of the radial gradient of the phase-averaged axial velocity (in H7 the time-average).

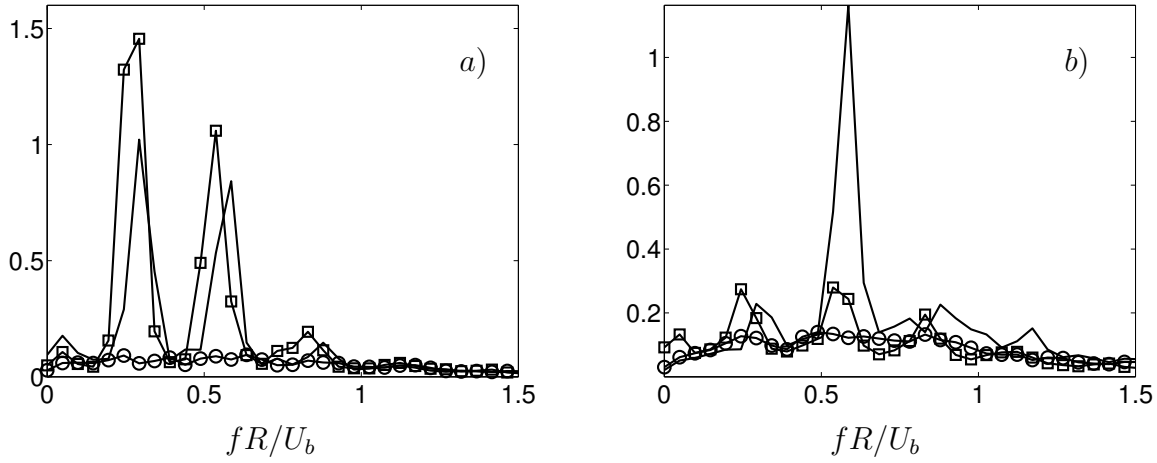

Figure 6.8: PSD of velocity fluctuations. $a)$ PSD of axial velocity fluctuations at $x/R = 0.1$, $r/R = 0.6$. $b)$ PSD of radial velocity fluctuations at $x/R = 0.9$, $r/R = 1.2$. Solid line: H7, circles: H16, squares: H17. Arbitrary units are used in the vertical axis.

The previous observations of instantaneous structures are confirmed by analyses of the power spectral density of the velocity fluctuations. To compute the PSD, the phase-averaged velocities have been removed from the signals. Fig.6.8a presents a comparison between the three cases at $x/R = 0.1$, $r/R = 0.6$, i.e. in the inner shear layer. The pronounced peaks which are observed in H7, are also present in H17 while they do not occur in H16. First of all, Fig.6.7b shows that the inner structures in H16 are substantially weaker and more distorted which would reduce the intensity of corresponding peaks in the spectrum. Second, the rotation rate of the structures is not constant in time since the angular velocity pulsates, so that a pronounced peak cannot be expected. In H17 the tangential velocity is roughly constant at the inlet. Therefore the coherent structures rotate at a constant rate as in the case without pulsation, generating pronounced peaks in the spectrum.

Fig.6.8b presents a comparison of the PSD of radial velocity fluctuations between the three cases at $x/R = 0.9$, $r/R = 1.2$, i.e. in the outer shear layer. In H7, the regularity of the outer structures in Fig.6.7a generates a peak in the spectrum. This is not the case for the pulsating simulations. Note that the vortex rings of the phase-averaged flow do not influence these spectra, because the phase-averaged

signals have been removed to compute the PSD. This figure demonstrates that the outer structures in H17 (Fig.6.7c) are substantially less regular than those of H7 without pulsation.

7 Influence of a pilot jet

The flow configuration considered in the previous chapters consists of an annular jet. In this chapter the effect of an additional inner jet is studied. Nowadays, lean premixed burners in modern gas turbines often make use of a richer pilot flame typically introduced near the symmetry axis. The purpose of this pilot flame is to stabilize the main flame. This raises the question of how the additional jet modifies the fluid mechanical behaviour of the system and in particular the occurrence of coherent structures. Mean flow, turbulence statistics, coherent structures and spectra are reported.

7.1 Experimental configuration. New burner

In the companion project C1 of the Collaborative Research Centre SFB606 [1] a new co-annular swirl burner was developed (Bender & Büchner, 2005). The advantage of this burner is its versatility. The burner is composed of two co-annular jets, a central pilot jet and a concentrically aligned main jet. In both jets the swirl can be adjusted individually. In the outer jet, the burner is designed to allow two different ways of generating the swirl:

- Axially, using warped vanes in an annular duct.
- Tangentially, using rectangular channels as illustrated in Fig. 7.1 where a sketch of the burner is shown in the configuration with tangential swirl generation.

For the generation of swirl in the central pilot jet, axial swirlers with blades at various angles of attack may be inserted in the pilot lance. Furthermore, it is possible to impose different senses of rotation for each jet which leads to co-swirl

[1] http://www.sfb606.uni-karlsruhe.de/index.pl/projekt_ansicht/Teilprojekt+C1

or counter-swirl configurations. Another possibility is to change the axial location of the inner jet. A picture of the burner working in a configuration with retraction of the inner jet was shown in Fig. 1.1.

A large number of experiments were performed with the new burner in several configurations including isothermal and reactive cases (Bender & Büchner, 2005; Habisreuther *et al.*, 2005). For the present numerical investigation the most suitable ones have been selected. In particular, measurements taken with LDA are available for the configuration with tangential swirl generation and co-rotating swirl. Three different axial positions of the inner jet were experimentally investigated by Bender & Büchner (2005). In the present chapter, only one of this is studied, namely the one without retraction of the inner jet. The influence of the location of the inner jet is investigated in Chapter 8.

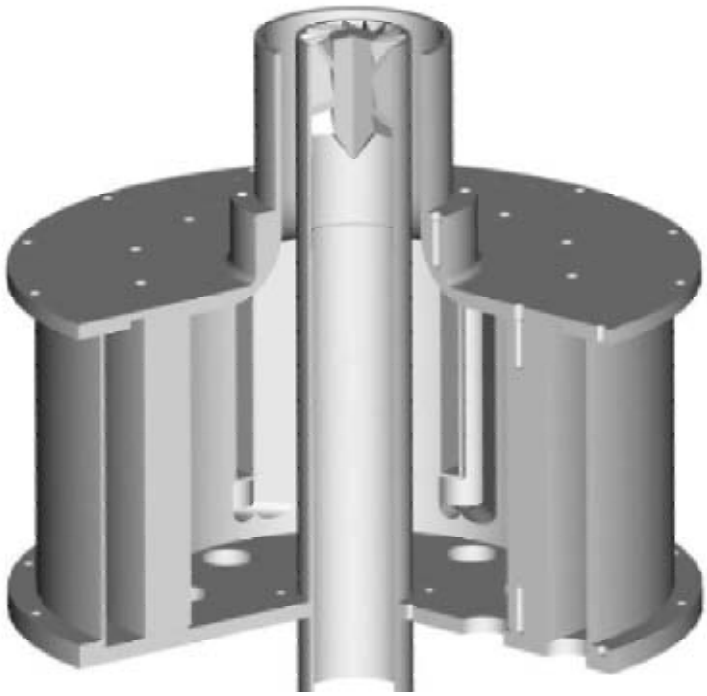

Figure 7.1: Sketch of the new burner in configuration with tangential swirl generation (from Bender & Büchner (2005))

7.2 Computational Setup

The computational domain is essentially the same as for the simulation of the Hillemanns configuration discussed so far. The exit of both inner and outer jets

is located at $x/R = 0$. The geometry only differs with respect to the inlet part which is shown in Fig. 7.2. As in simulation H1 in Chapter 3, the computational domain includes a crude representation of the inlet duct reaching to the tangential channels which generate the swirl in the experiment. The flow is prescribed at the circumferential inflow boundary located at the beginning of the inlet duct. It comes in radially, having a non-zero azimuthal component. At this position, where the swirl generating device is located in the experiment, steady top-hat profiles for the radial and azimuthal velocity components are imposed in the simulations. The flow undergoes a rapid transition as displayed in Fig. 7.2 so that the kinetic energy in the annular pipe corresponds to the level observed in a developed annular jet. The coherent structures downstream of the outlet are substantially more energetic than the ones in the pipe flow so that the levels of kinetic energy k in this figure were restricted to low values to make this transition visible. The results of Chapter 4 show that this approach provides an adequate model of the inflow. With appropriate adjustment of the swirl at the inflow boundary the experimental profiles of mean flow as well as fluctuations in the main jet near the outlet are very well reproduced, as displayed in Fig. 7.4 below.

The grid employed for the simulations in the present chapter, C3, was selected to be very similar to the grid C1 used in the simulations for the Hillemanns configuration in Chapter 3.

In the experiment of Bender & Büchner (2005), a co-annular pilot jet was introduced featuring an axial swirl generator, Fig. 7.1. The end of its nozzle coincides with the end of the outer tube surrounding the main jet. The annular flow leading to this jet is modelled with a precursor simulation here, similar to the inflow in the previous section, which also ends at $x = 0$, as indicated in Fig. 7.2. The direction of swirl is co-rotating with the main jet. In this configuration the inner and outer diameter of the pilot jet are $0.27D$ and $0.51D$, respectively, while the inner and outer diameter of the main jet are $0.63D$ and D, respectively. Hence, the flow conditions are very similar to those of the Hillemanns configuration. The Reynolds number is $Re = 81000$ based on the bulk velocity of the main jet alone, $U_b = 22.1$ m/s in the experiment, and on the outer radius of the main jet $R = 55$ mm. To allow comparison with the simulations of Chapter 5, the resulting swirl number in the main jet at $x = -2R$, has been determined. Its value is $S = 1.05$,

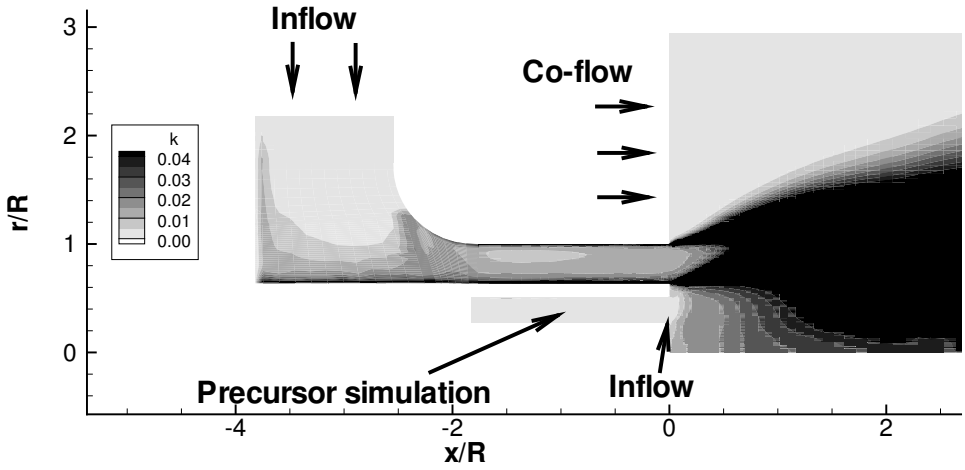

Figure 7.2: Inflow conditions and geometry for the computations assembled in Table 7.1. Development of the fluctuating kinetic energy in the inlet duct for Sim NB3. Only the lower levels of k are considered as discussed in the text.

almost exactly the same as for H14. The different width of the main jet, however, precludes direct comparison with the computations of Chapters 3 and 5. The mass flux of the pilot jet is 10% of the total mass flux (which corresponds to a bulk velocity of $U_b^{pilot} = 7.7$ m/s) and the swirl number defined at $x/R = 0$ for the pilot jet alone is $S = 1$. The kinetic energy of the flow in the precursor simulation in Fig. 7.2 is by a factor of about 10 smaller than the kinetic energy in the main pipe.

The purpose of the simulations in this section is to clarify the impact of the inner jet on the stability of the entire flow. This is investigated by consideration of three cases which are summarized in Table 7.1: the reference case is again an annular jet with a slightly different geometry compared to the Hillemanns configuration studied in Chapters 3 to 6. It is labeled NB1 in the following. A non-swirling inner jet is introduced in case NB2 and a swirling inner jet in case NB3. Experimental data are available only for the last case.

7.3 General features of the flow

The streamlines for the three cases investigated are displayed in Fig. 7.3. As already mentioned, the flow falls into the high-swirl regime and is expected to be similar to H14 in Chapter 5 due to the similar value of S. The geometry is

Sim.	Grid	SGS m.	IJ present	Swirl in IJ	Line
NB1	C3 (~ 2.5 mio.)	Dyn.	No	–	dotted
NB2	C3 (~ 2.5 mio.)	Dyn.	Yes	No	dashed
NB3	C3 (~ 2.5 mio.)	Dyn.	Yes	Yes	solid
Exp	–	–	Yes	Yes	○

Table 7.1: Overview of the simulations performed to investigate the influence of an inner jet (IJ).

slightly different, however, and this introduces a difference in the flow. While in H14 the GRZ and the CRZ are not merged yet, Fig. 5.2f, the GRZ and the CRZ are already merged in NB1, Fig. 7.3$(a1)$, and the pattern is more similar to H15, Fig. 5.2g. As before, a CRZ starting directly behind the cylindrical centre body occupies a long region near the symmetry axis.

In NB2, featuring a non-swirling pilot jet, the resulting streamlines in Fig. 7.3$(b1)$ are very similar to the ones without pilot jet. The streamlines issuing from the pilot duct just enter the inner shear layer without generating substantial alteration. In the case of the swirling pilot jet, NB3, the shape of the recirculation zone is slightly modified in the region of its maximum width. Here, the streamlines are shifted outward due to the higher total swirl which is also observed for the dotted line indicating the location where $\langle u_x \rangle = 0$. Beyond $x/R = 3$ the flow is mostly unchanged.

The right column in Fig. 7.3 shows grayscale contours of fluctuating kinetic energy. As for the streamlines, the shape of the contour levels for the simulation without pilot jet, Fig. 7.3$(a2)$, is close to the case with highest swirl of the previous configuration, Fig. 5.5g. The levels are slightly lower for NB1. As in H15, the graphs show a concentration of kinetic energy close to the nozzle and a fast decay in axial direction. The data for k from all three simulations are very much alike. The differences between the three simulations occur in a small zone close to the jet outlet ($x/R < 2$). In this region, NB1 features a higher level of kinetic energy than NB2 which in turn shows higher k than NB3, especially in the inner shear layer. For NB1 and NB2, the inner shear layer shows considerable values of k with $k_{max} = 0.2U_b^2$ and $k_{max} = 0.18U_b^2$, respectively, and is stronger than the

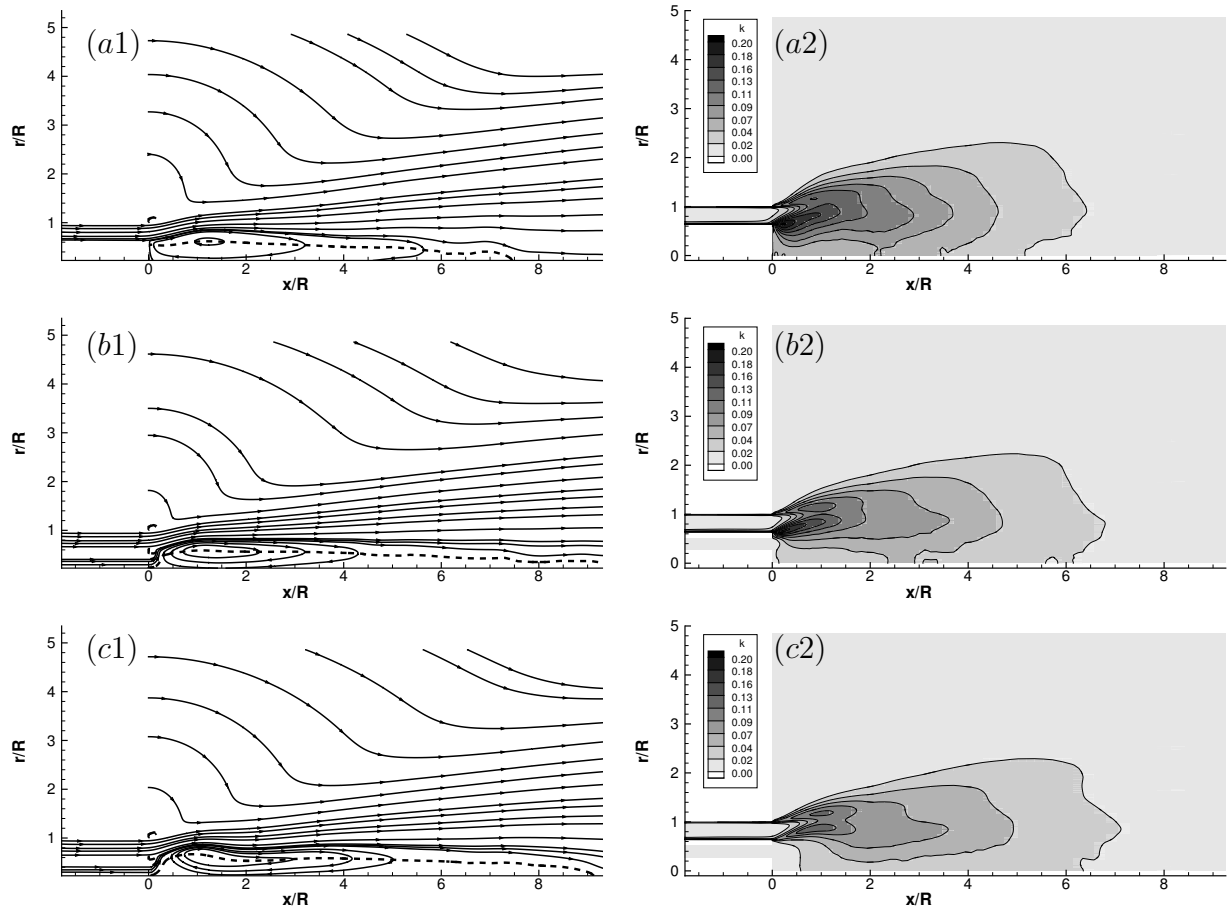

Figure 7.3: Influence of the pilot jet on the mean flow. Column 1: Streamlines of the average flow, solid lines. $\langle u_x \rangle = 0$, dashed line. Column 2: Fluctuating kinetic energy. (a) NB1. (b) NB2. (c) NB3.

outer one. The kinetic energy is lower for NB3 with $k_{max} = 0.13U_b^2$ occurring in the inner shear layer. The latter also is narrower and located further outward, in compliance with the above discussion of streamlines. The turbulent kinetic energy immediately behind the center bluff body is substantially lower than in the case without pilot jet. The properties observed here originate from the vortical structures present in the respective cases which will be discussed below.

7.4 Mean and RMS velocity profiles

Fig. 7.4 shows radial profiles of mean velocity and the corresponding fluctuations at three axial positions in the near flow field of the jet for the three cases.

Note also that only one of the simulations, NB3, corresponds to the experimental condition. The strength of the pilot jet can be appreciated by the mean axial and tangential velocity at $x/R = 0.1$ in Fig. 7.4$(a1)$ and Fig. 7.4$(a2)$. The deviation with respect to the experimental data in this range results from the model for the pilot jet. Its inflow condition is imposed at $x/R = 0$, while in the experiment the flow at this position can be influenced by the downstream flow. Moreover, the guide vanes of the axial swirl generator for the pilot jet, 26 in the experiment, are not represented here since this would render the grid generation very complicated. A slightly different model of the pilot jet employed in Chapter 8 together with a somewhat finer grid yields an improvement in this respect. The results in Chapter 8 support the ones in this chapter. Downstream, at $x/R = 1$, the simulation overpredicts the backflow while the major part of the profile is very well captured, Fig. 7.4$(b1)$. The mean tangential component is also in good agreement with the experiment, Fig. 7.4$(b2)$. At this position the difference between the three cases is small for the mean profiles, with the tangential velocity profile displaced radially outwards for the simulation with swirling inner jet, NB3, compared to the simulation without inner jet, NB1. At $x/R = 3$, the agreement with the experiment is very good and the difference between the three cases is only marginal, Fig.7.4$(c1 - 4)$.

Fig. 7.4$(a3 - 4)$ shows profiles of the RMS fluctuations of axial and tangential velocity profiles at $x/R = 0.1$. It can be appreciated that the region where the agreement is worst is precisely where the pilot jet is located, between $0.27R$ and $0.51R$. This is again due to the model for the pilot jet. The comparison of these turbulence intensity profiles for the three simulations shows higher values in the simulation without pilot jet, as expected from the contour plots of kinetic energy in Fig. 7.3. The disagreement is constrained to a small region close to the exit of the pilot jet. In Fig 7.4$(b3 - 4)$ which shows profiles of the RMS fluctuations at $x/R = 1$, the fluctuations are already very close to the experimental data. At this location, it is still possible to appreciate a higher level of fluctuations in the simulation without inner jet, but the difference is smaller than at $x/R = 0.1$. In conclusion, Figs. 7.3 and 7.4 show that the influence of the pilot jet on the average flow and the second moments is only small.

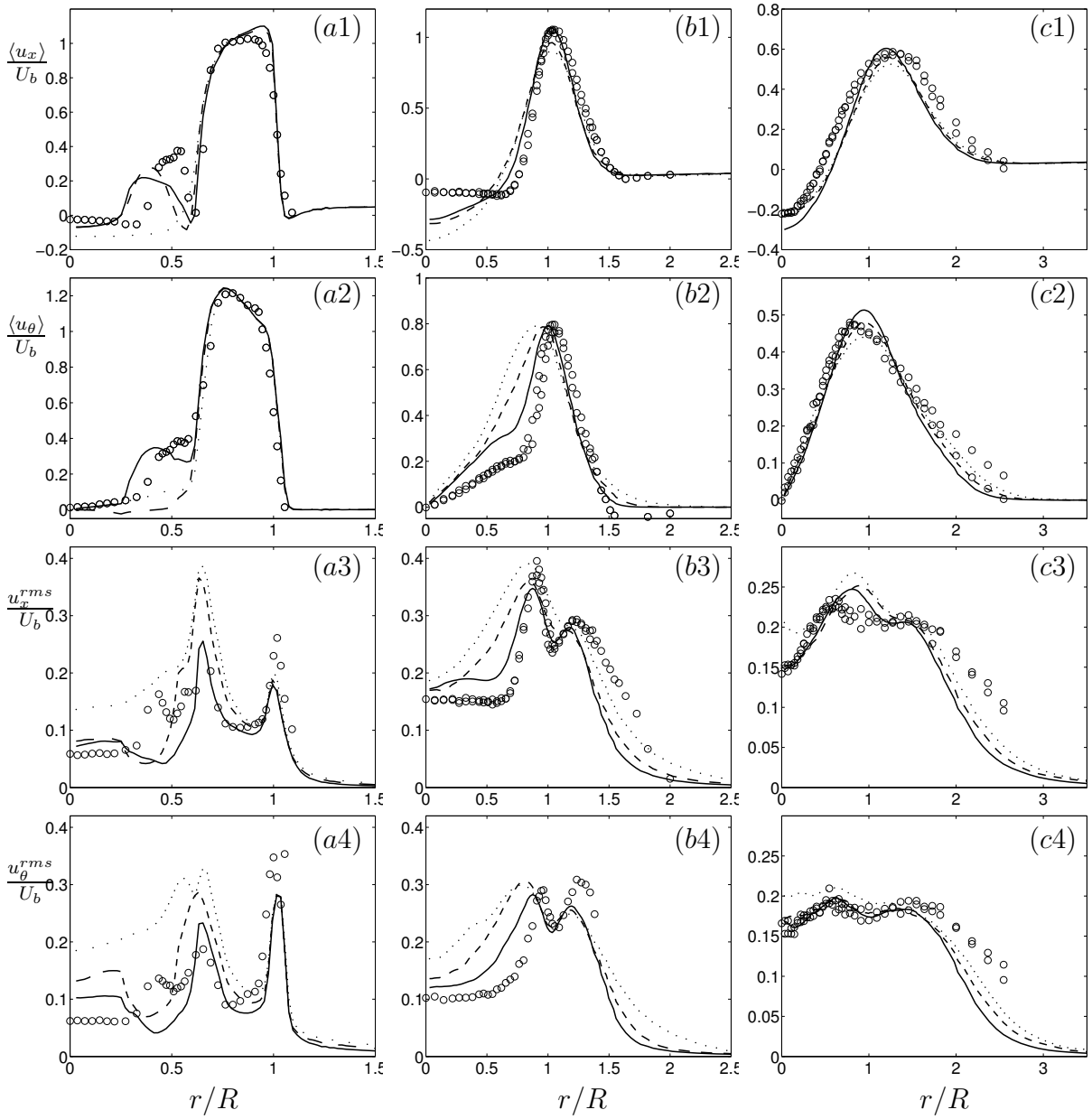

Figure 7.4: Radial profiles of mean velocity and corresponding turbulent intensities. (a) $x/R = 0.1$. (b) $x/R = 1$. (c) $x/R = 3$. Row 1: Mean axial velocity. Row 2: Mean tangential velocity. Row 3: RMS axial velocity. Row 4: RMS tangential velocity. The line styles are defined in Table 7.1. Symbols represent experimental data of Bender & Büchner (2005). To enhance readability the range of the vertical axis has been adjusted individually.

7.5 Flow visualization and Spectra

The instantaneous flow is now visualized in a similar way as in the previous chapters using iso-surfaces of pressure fluctuations, Fig. 7.5. Here, the pressure field

was additionally smoothed in space by a two-fold application of a box filter of width twice the step size of the grid. Obviously, there are important differences between the three cases. Without pilot jet, Fig. 7.5a, the structures have the characteristics described in Chapters 3 and 5. They are very coherent, precess at a quasi-regular rate and persist over long time intervals. When the non-swirling pilot jet is introduced, Fig. 7.5b, it is still possible to recognize similar structures as in the case without pilot jet. These are however substantially less coherent, much thinner, and do not reach downstream that far. In particular, the PVC are smaller and are more numerous along the circumference. In this case, four or five small PVC can co-exist at certain instants. Finally, the addition of swirl to the pilot jet has a dramatic impact on the flow, Fig. 7.5c. The regularity is substantially reduced and the appearance of the structures is more random. Here, even the outer structures are affected and have almost vanished or, when they appear, exhibit only small coherence. The addition of near-axis swirl hence has a strong influence on the instantaneous flow characteristics. Recently, in a different context, the addition of near axis swirl has been proposed as a strategy to control vortex breakdown (Husain *et al.*, 2003).

The previous analysis of the coherent structures is confirmed by analyzing the PSD of the radial velocity fluctuations at two points close to the outlet at $x/R = 0.4$. Experimental spectra are unfortunately not available for these cases. Fig. 7.6a shows the PSD of the three cases on the symmetry axis. Note that, in spite of the difference in geometry with respect to the configuration studied in Chapter 5, the peak in the spectrum for NB1 also appears at a frequency $f_{peak} = 0.24U_b/R$. The difference in geometry hence does not have much influence in the precessing rate of the structures. A pronounced peak can also be observed for NB2. The spectrum of NB3 also shows a peak but at substantially larger time scales. These are not well resolved with the length of the time segments employed for the computation of the spectra mentioned above. Also note that no averaging over angular positions is possible for $r/R = 0$. Repeating the analysis with longer segments shows that, indeed, a low frequency contribution with $f_{peak} \sim 0.025U_b/R$ exists. This issue deserves further investigations, possibly relating it to work of Rehab *et al.* (1997) who observed low frequency oscillations with similar Strouhal number of the recirculation bubble created by

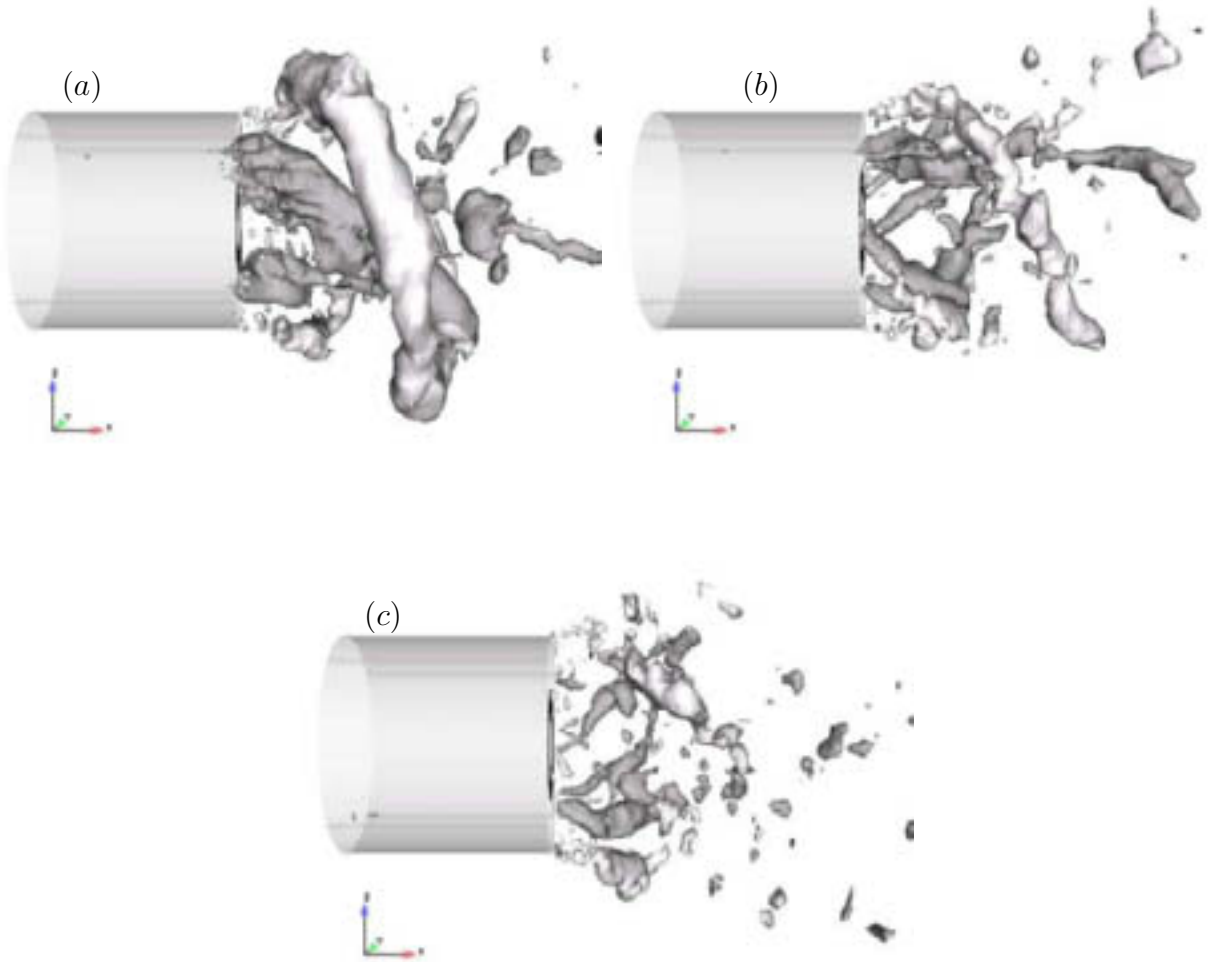

Figure 7.5: Instantaneous coherent structures visualized using an iso-surface of the filtered instantaneous pressure deviation $p' = p - \langle p \rangle = -0.2$. (a) NB1. (a) NB2. (a) NB3. Colour is given by the sign of the radial gradient of the mean axial velocity.

an annular free jet without swirl.

Fig. 7.6b displays the PSD at $r/R = 0.6$, i.e. in the inner shear layer of the main jet. The spectrum of NB1 shows a pronounced first and second harmonic (both label A). The spectrum of NB2 also exhibits peaks at these frequencies, but their energy content is much smaller. Instead, more energy is displaced to the next harmonic, which shows that the PVC are more irregular in this case. For NB3 the energy is contained in substantially higher frequencies (the most dominant ones with label B) and much less in low-frequency modes. The analysis of this section

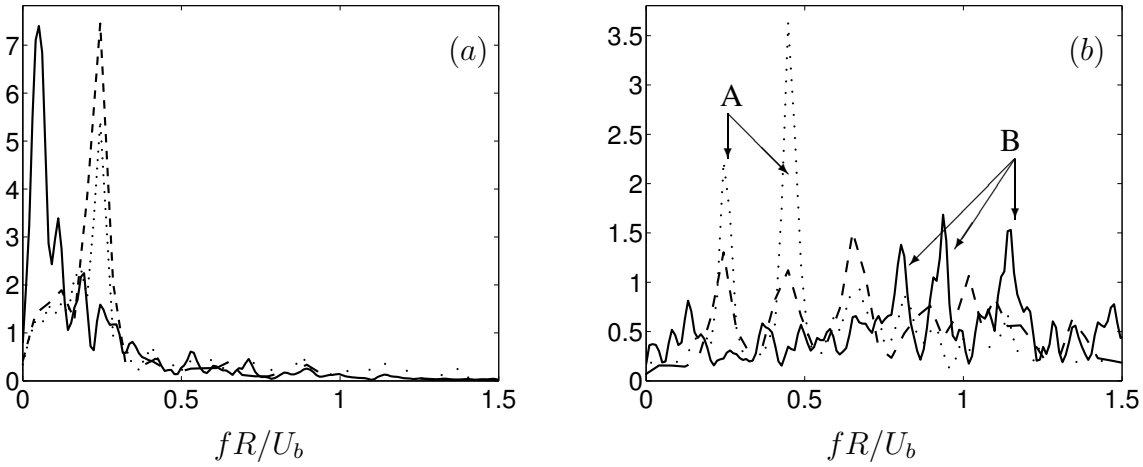

Figure 7.6: PSD of radial velocity fluctuations at $x/R = 0.4$. (a) Location on the symmetry axis, $r/R = 0$. (b) Location in the inner shear layer, $r/R = 0.6$. Line styles are defined in Table 7.1.

hence explains the different levels of fluctuating kinetic energy encountered close to the nozzle in Fig. 7.3: the strong coherent structures observed in NB1 are destroyed by the addition of a non-swirling and even more of a swirling pilot jet.

8 Influence of the axial location of the pilot jet

In this chapter, the analysis of the previous chapter is complemented by varying the axial position of the pilot jet. This position is found to have a strong impact on the formation of coherent structures.

8.1 Physical and Numerical Modelling

In the experiments of Bender & Büchner (2005) three different axial positions of the pilot jet were studied. For the isothermal flow without external forcing, it was observed that axial retraction of the central jet into the duct leads to an increased amplitude of flow oscillations reflected by audible noise. In order to investigate this phenomenon, two of the cases were selected. The first one corresponds to the configuration studied in Chapter 7, i.e. both jets exit at the same position. In the second case, the pilot jet is retracted by 40 mm, i.e. $-0.73R$. This retraction of the pilot jet generates a double expansion for the main jet visualized in Fig. 8.1b. LDA measurements are available for both cases. In particular, radial profiles of mean and RMS velocities have been measured at four axial stations in the near field of the burner. Only for the case with retraction, power spectra of velocity fluctuations were recorded.

The flow conditions are described in the previous chapter. The simulations discussed in this chapter are summarized in Table 8.1. In § 7.4 discrepancies between the results of NB3 and the experiment were observed close to the burner exit at $x/R = 0.1$. This was mainly due to the model used for the pilot jet. An attempt to improve the agreement was made by slightly changing the boundary conditions. Fig. 8.1a displays a zoom of the inflow region for the case NB4. The case NB3 was displayed in Fig. 7.2. In NB4 the inflow plane for the pilot jet was shifted upstream to $x/R = -0.73$, i.e. the annular duct is included in the main LES. To compensate for the additional relaxation of swirl between $x/R = -0.73$

Sim.	Grid	SGS m.	x_{pilot}	S in pilot jet
NB3	C3 (~ 2.5 mio.)	Dyn.	0	1 at $x/R = 0$
NB4	F4 (~ 8.5 mio.)	Dyn.	0	2 at $x/R = -0.73$
NB5	F4 (~ 8.5 mio.)	Dyn.	$-0.73R$	2 at $x/R = -0.73$

Table 8.1: Overview of the simulations performed to investigate the influence of the retraction of the pilot jet.

and $x/R = 0$ the swirl number has been increased to $S = 2$ in NB4, while in NB3 it was $S = 1$. The same boundary conditions were employed in NB4 and NB5. Fig. 8.1b displays a zoom of the inflow region for $x_{pilot} = -0.73R$. In the case $x_{pilot} = 0$ the inflow region differs because the wall separating main and pilot jet and the cylindrical centre body reach until $x = 0$, with the inflow plane for the pilot jet still located at the same position $x/R = -0.73$. This is illustrated in Fig. 8.3 below.

The same grid F4 was employed in NB4 and NB5. In NB4, the wall separating the annular ducts for main and pilot jet, and the cylindrical centre body were introduced by blocking corresponding cells. The distribution of cells is similar to the grid F1 employed in Chapter 3 for the simulations of the Hillemanns configuration. But the grid stretching is reduced and also the concentration of points in the rear part of the central recirculation zone is increased. This leads to an increase in the number of cells of the order of 1.5 with respect to the grid F1. The grid C3 employed for NB3, as noted in the previous chapter, is similar to the grid C1 in Chapter 3.

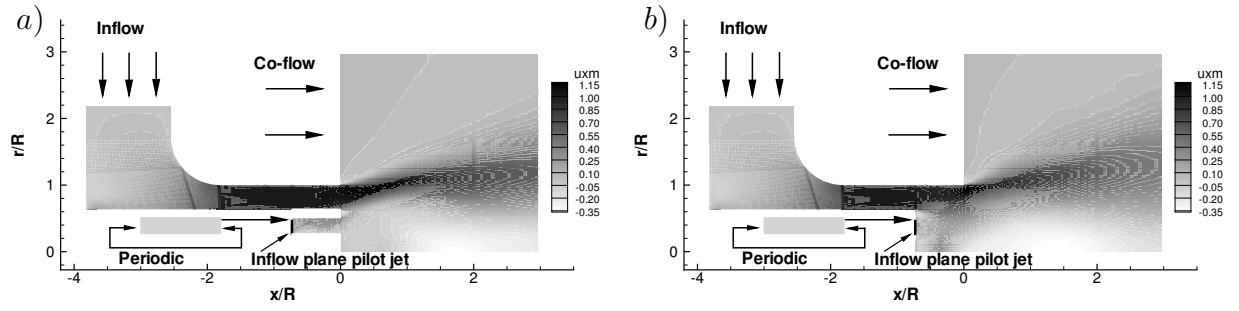

Figure 8.1: Numerical setup and boundary conditions. Gray scale represents mean axial velocity $a)$ $x_{pilot} = 0$. $b)$ $x_{pilot} = -0.73R$.

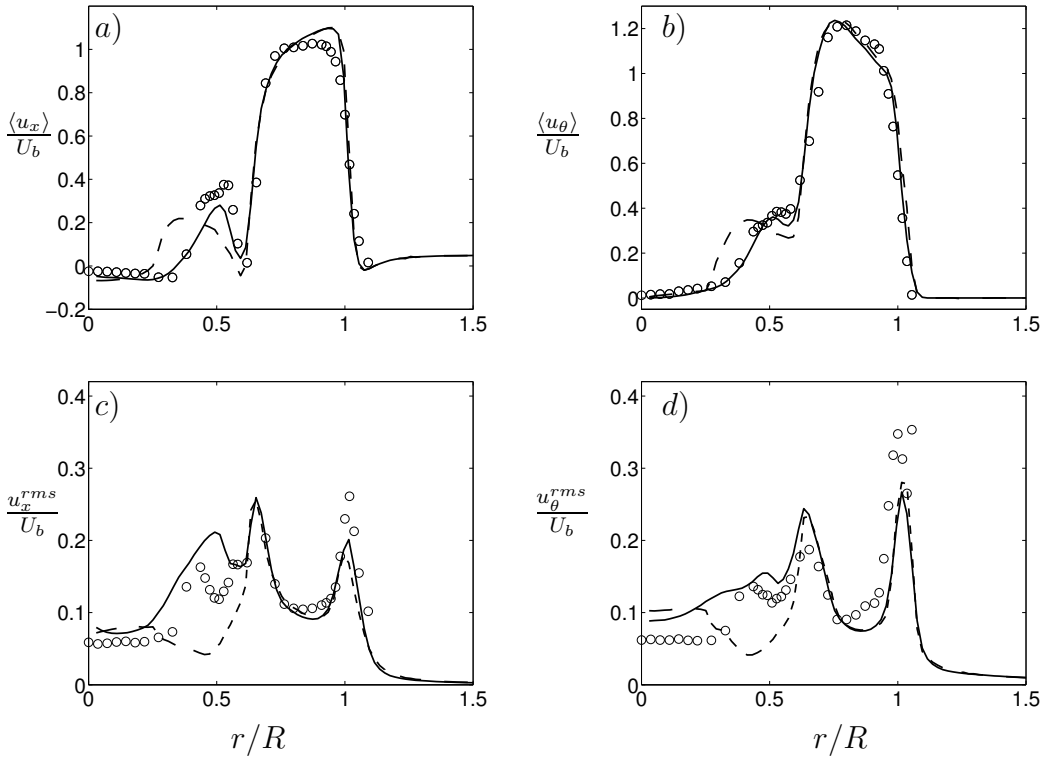

Figure 8.2: Comparison of velocity profiles from simulations NB3 and NB4 at $x/R = 0.1$. Dashed line, NB3. Solid line, NB4. Symbols, experiment. $a)$ Mean axial velocity. $b)$ Mean tangential velocity. $c)$ RMS axial velocity. $d)$ RMS tangential velocity.

Fig. 8.2 shows the improvement of the results at $x/R = 0.1$ in NB4 compared to NB3. As a result of the change in boundary conditions and the grid refinement both mean velocity components and the corresponding turbulent fluctuations are substantially improved in the region of the pilot jet. In Fig. 8.2a the mean axial velocity component in the region of the pilot jet is still slightly smaller than the experimental value. At this stage it should be mentioned that the determination of the ratio of the mass flux in the main jet and in the pilot jet is subject to measurement uncertainties. It seems to have been slightly smaller than the nominal value 9:1. This issue, however, is unimportant for the following discussion.

8.2 Average flow

After discarding initial transients, statistics were collected for $100t_b$.

8.2.1 Streamlines

Fig. 8.3 shows the two-dimensional streamlines of the average flow in an axial plane for both cases. The influence of the retraction of the inner jet is remarkable. For $x_{pilot} = 0$ the recirculation forms immediately behind the cylindrical centre body and the length of the recirculation zone is about $9R$. In the case $x_{pilot} = -0.73R$ the length of the recirculation zone is only about $5R$. The two streams mix before the final expansion and the recirculation is detached from the burner. The maximum width of the recirculation bubble is about $0.8R$ in both cases and it is attained at $x/R = 1.2$ for $x_{pilot} = 0$ and at $x/R = 1.5$ for $x_{pilot} = -0.73R$.

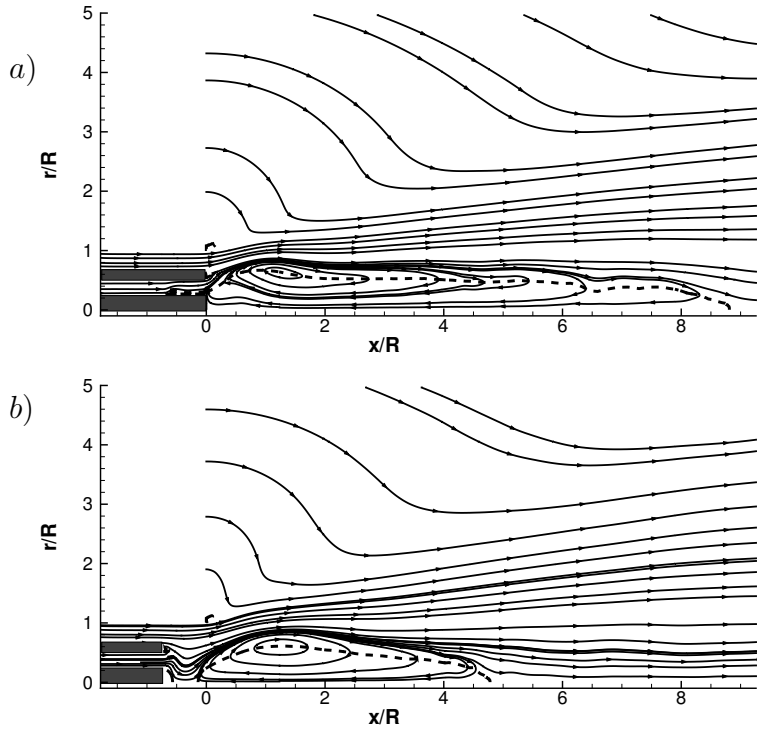

Figure 8.3: Streamlines of the average flow in an axial plane $a)$ $x_{pilot} = 0$, NB4 $b)$ $x_{pilot} = -0.73R$, NB5. The dashed line indicate the location where $\langle u_x \rangle = 0$.

8.2.2 Mean and RMS velocity profiles

A comparison of simulations with experiments is reported in Figs. 8.4-8.7, showing radial profiles of mean velocity and turbulent fluctuations at several axial stations for both cases. The agreement with the experimental data is in general good for the mean flow. The case $x_{pilot} = 0$ is well reproduced in the simulation, Fig. 8.4, which is noteworthy in spite of the strong idealization in setting up the inflow conditions for the pilot jet. In the case $x_{pilot} = -0.73R$, Fig. 8.5, a discrepancy is evident at $x/R = 0.1$; the backflow is overpredicted in the simulation. This implies that the recirculation zone in Fig. 8.3b does not correspond exactly to the experimental one, which was measured to be slightly further downstream. Nevertheless, other characteristics are very well predicted so that this simulation is still close to the experiment. For example, the spreading of the jet is in good agreement with the experiment and so are the turbulent fluctuations of the axial and the tangential velocity components, Fig. 8.7. The agreement is also good for the turbulent fluctuations in the case $x_{pilot} = 0$, Fig. 8.6.

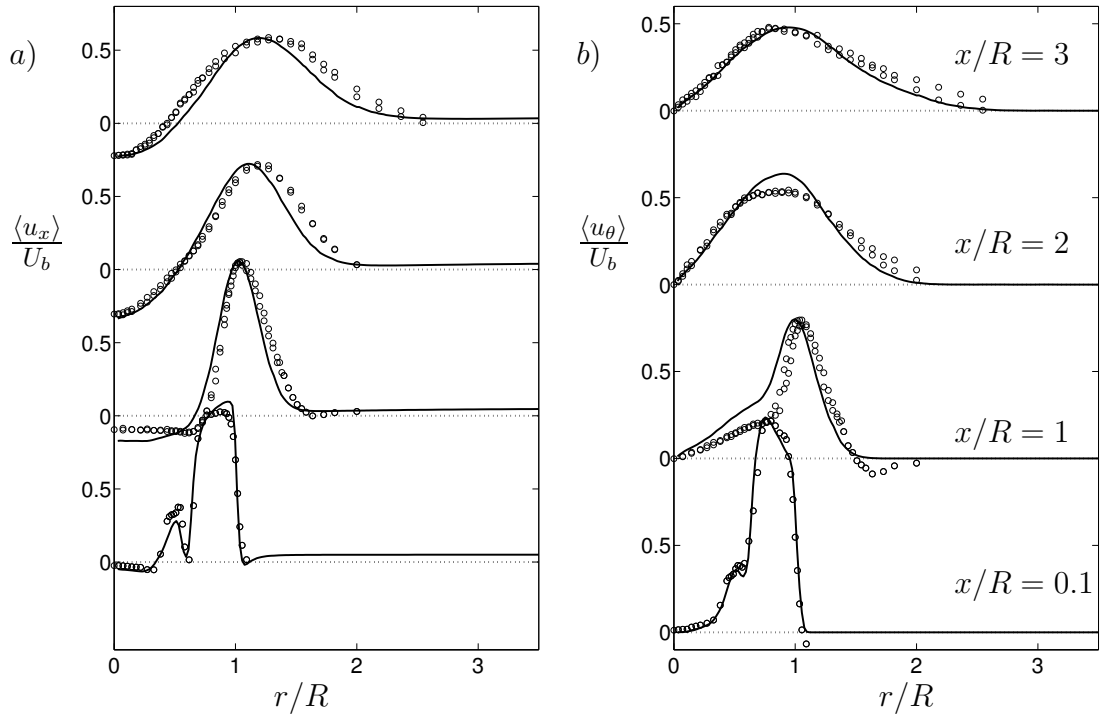

Figure 8.4: Radial profiles of mean velocity for $x_{pilot} = 0$, NB4 a) Axial velocity b) Tangential velocity

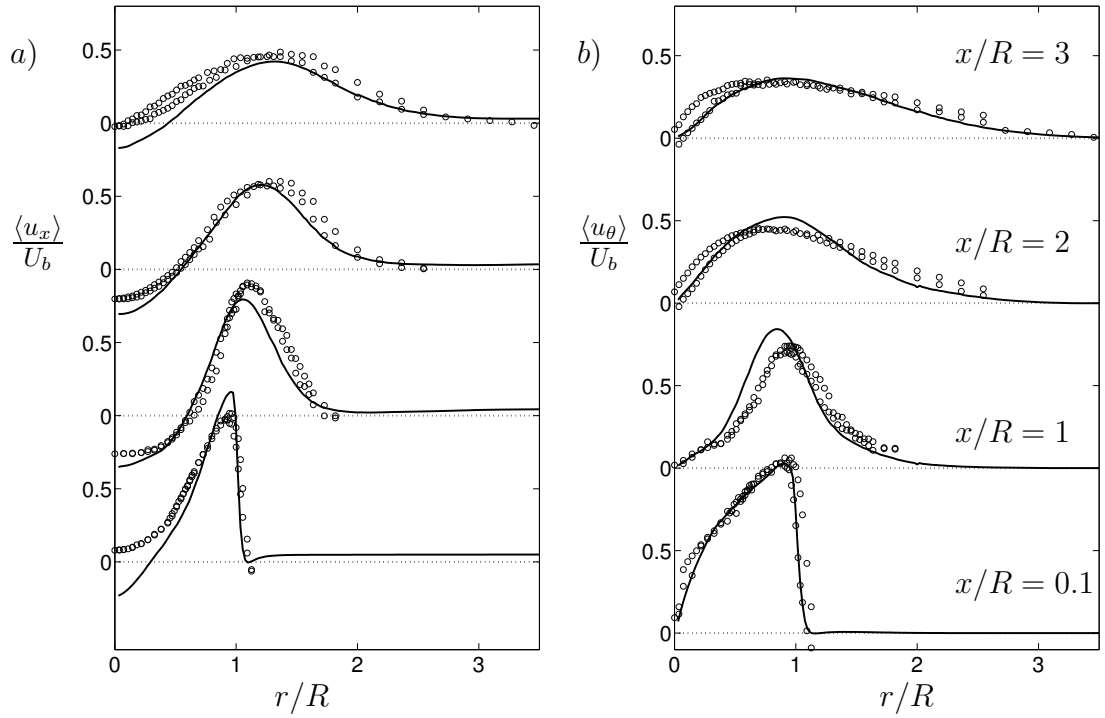

Figure 8.5: Radial profiles of mean velocity for $x_{pilot} = -0.73R$, NB5 $a)$ Axial velocity $b)$ Tangential velocity

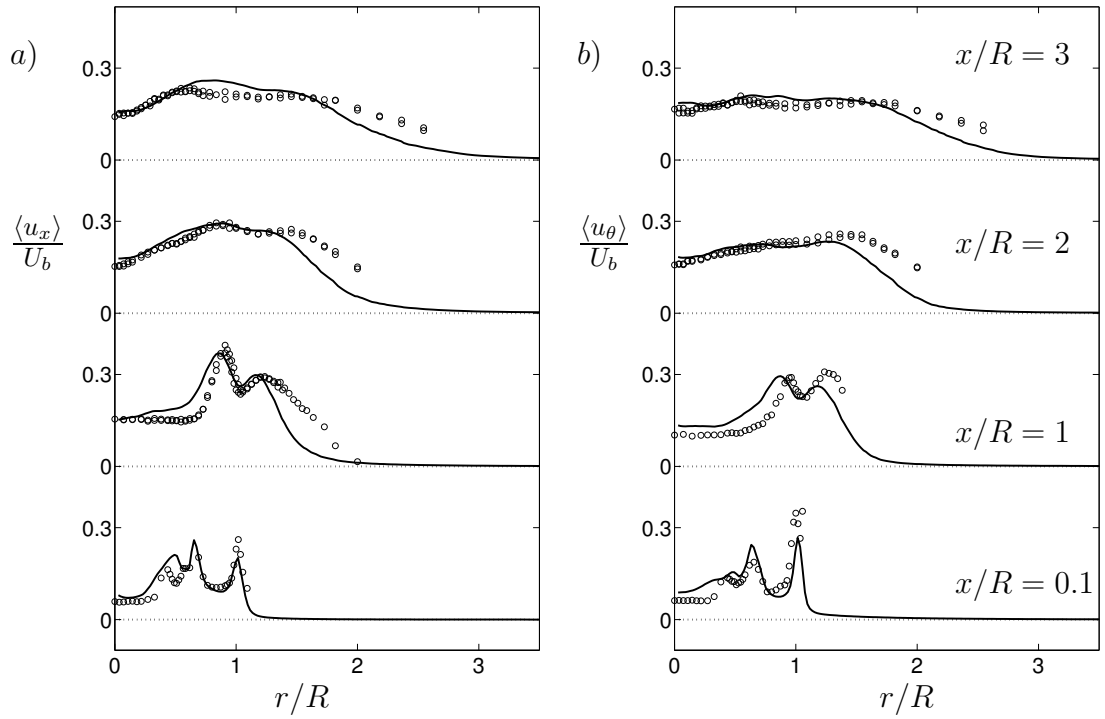

Figure 8.6: Radial profiles of RMS velocity for $x_{pilot} = 0$, NB4. $a)$ Axial velocity $b)$ Tangential velocity

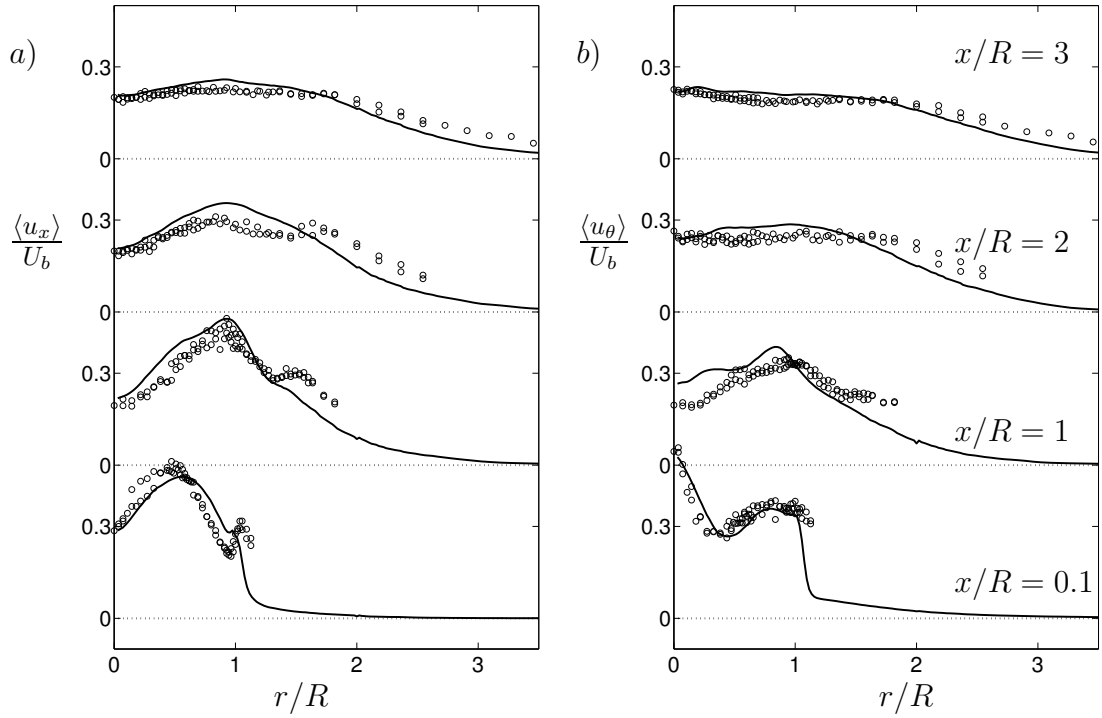

Figure 8.7: Radial profiles of RMS velocity for $x_{pilot} = -0.73R$, NB5. $a)$ Axial velocity $b)$ Tangential velocity

Some features are common in both cases, like the presence of a recirculation zone and the two shear layers. In the case $x_{pilot} = 0$, the turbulent fluctuations generated in these layers are clearly visible up to $x/R = 1$ in the profiles of RMS fluctuations by corresponding peaks (Fig. 8.6). In the case $x_{pilot} = -0.73R$ this feature is only observed in the profile of the axial fluctuations very close to the jet exit 8.7a. Note also that the level of fluctuations at $x/R = 0.1$ is much higher for $x_{pilot} = -0.73R$. In that case the maximum RMS is about $0.5U_b$ while in the case $x_{pilot} = 0$ it does not reach $0.3U_b$. Further downstream at $x/R = 3$ this difference has vanished and in both cases the maximum RMS fluctuation is close to $0.3U_b$, although the radial spreading of the profiles is larger in the case $x_{pilot} = -0.73R$.

8.2.3 Fluctuating kinetic energy

To conclude the description of the average flow, Fig. 8.8 displays contours of the fluctuating kinetic energy, using the same scale for both cases. It is obvious that the retraction of the pilot jet leads to a large increase in the level of the fluctuating energy. In the case $x_{pilot} = 0$ the fluctuating kinetic energy is concentrated in the

two shear layers mentioned above and the maximum level is $k_{max}/U_b^2 \sim 0.14$. In the case $x_{pilot} = -0.73R$ the kinetic energy is concentrated in three regions, just behind the inner part of the burner, at the beginning of the recirculation bubble (compare Fig. 8.8b and Fig. 8.3b) and in the region of the inner shear layer. The tangential and the radial velocity fluctuations contribute mainly to the concentration of kinetic energy at the beginning of the recirculation zone while the level of axial fluctuations at this location is lower. This is evidenced by the RMS profile of tangential velocity fluctuations, Fig 8.7b at $x/R = 0.1$, showing a pronounced local maximum at the symmetry axis. The radial fluctuations are not shown here but present a similar peak. The features observed here will be discussed below in connection with the vortical structures present in the respective flows.

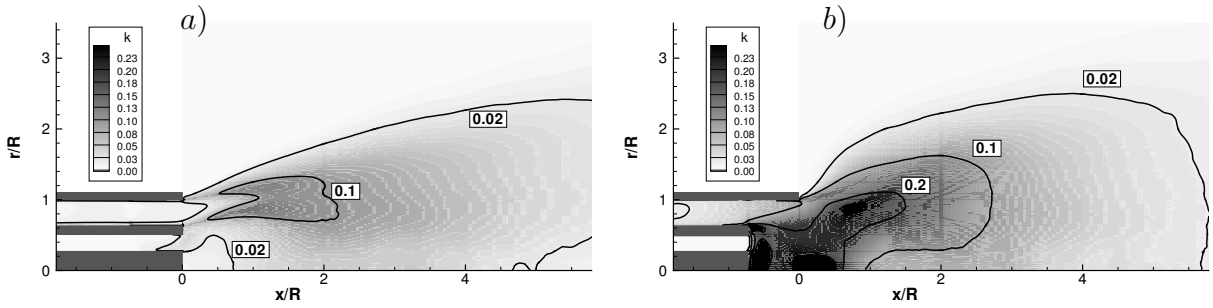

Figure 8.8: Fluctuating kinetic energy $a)$ $x_{pilot}/R = 0$ $b)$ $x_{pilot} = -0.73R$.

8.3 Instantaneous flow and spectra

8.3.1 Coherent structures

Fig. 8.9 shows iso-surfaces of pressure fluctuations for both cases visualizing the coherent structures of the flow. Fig. 8.9a and Fig. 8.9c display two different levels of p'' for the case $x_{pilot} = 0$, namely $p'' = -0.3$ and $p'' = -0.15$, respectively. Figs. 8.9b, d show the level $p'' = -0.3$ at two different instants in time for the case $x_{pilot} = -0.73$. The grey scale is again obtained using the criterion defined in Chapter 3.

Pronounced large-scale coherent structures are observed in the case of the retracted pilot jet, Fig. 8.9b, d. As in the case without inner jet, two types of structures can be observed in these pictures. Most of the time only one inner structure

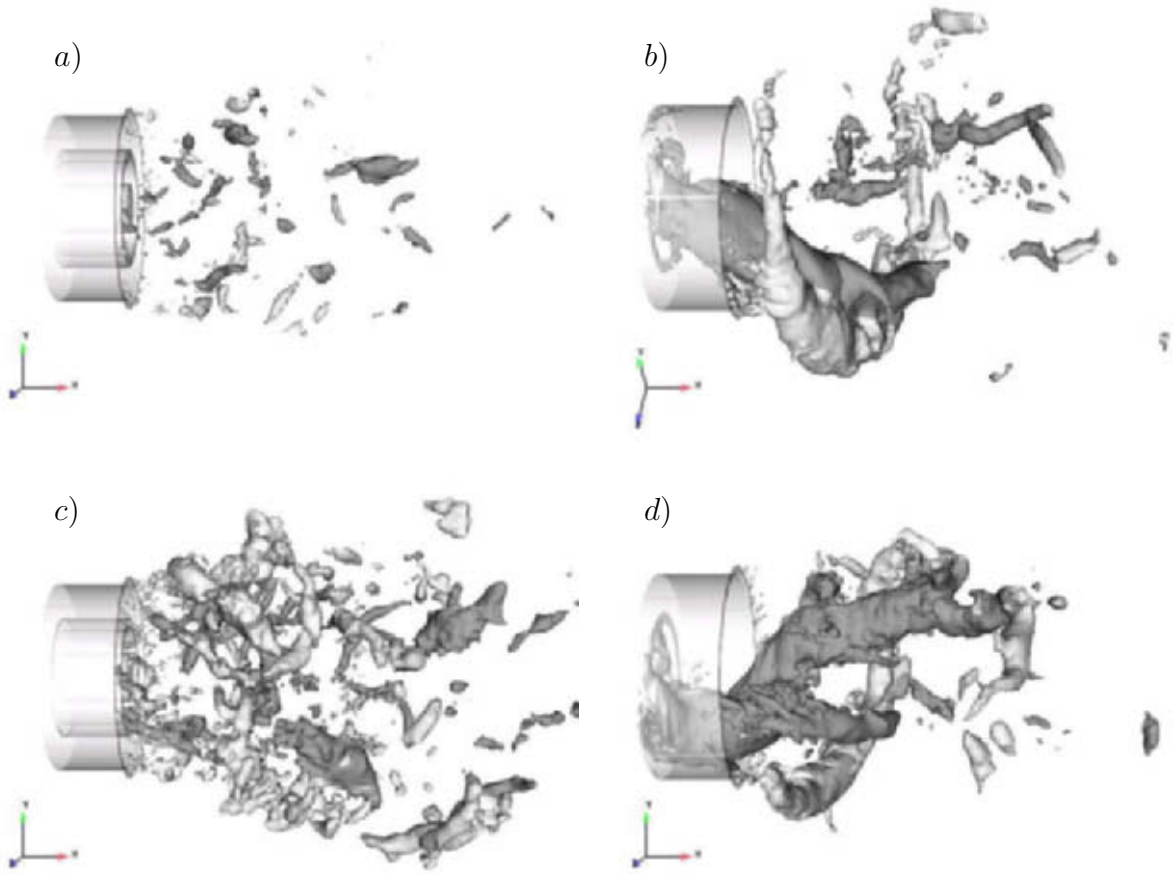

Figure 8.9: Coherent structures visualized using an iso-surface of pressure fluctuations. Left, $x_{pilot}/R = 0$. Right, $x_{pilot}/R = -0.73R$. $a, b, d)$ $p - \langle p \rangle = -0.3$. $c)$ $p - \langle p \rangle = -0.15$. Grey scale as explained in the text.

is visible and animations show that its rotation around the symmetry axis is very regular. At some instances, however, the inner structure branches, leading to two arms as shown in Fig. 8.9d. The leading one, in the direction of the rotation, is faster than the second one and takes over in terms of strength. The one behind disappears at the exit in less than half a rotation period and in the downstream field during another half period. In the case without retraction, $x_{pilot} = 0$, the structures are substantially smaller and more irregular as discussed in the previous chapter. In fact, if one compares the same level of pressure fluctuations $p'' = -0.3$, hardly any structure is visible in the flow, Fig. 8.9a. Increasing the pressure level to $p'' = -0.15$, small structures are visible, which exhibit small

coherence. Hence, in the case NB4 $x_{pilot} = 0$, the pilot jet destroys the large-scale structures. When the pilot jet is retracted to $x_{pilot} = -0.73R$ this is not observed. The cylindrical tube enclosing the main jet prevents the recirculation bubble from moving upstream to the central bluff body containing the exit of the pilot jet, Fig. 8.3b. This is also illustrated using the instantaneous axial velocity component displayed in Fig. 8.10 for both cases. The pilot jet therefore only "hits" the upstream front of the recirculation bubble but cannot penetrate into the inner shear layer where it would be able to impact on the coherent structures. The different coherent structures observed in both cases explain the different levels of fluctuating kinetic energy encountered close to the burner exit in Fig. 8.8.

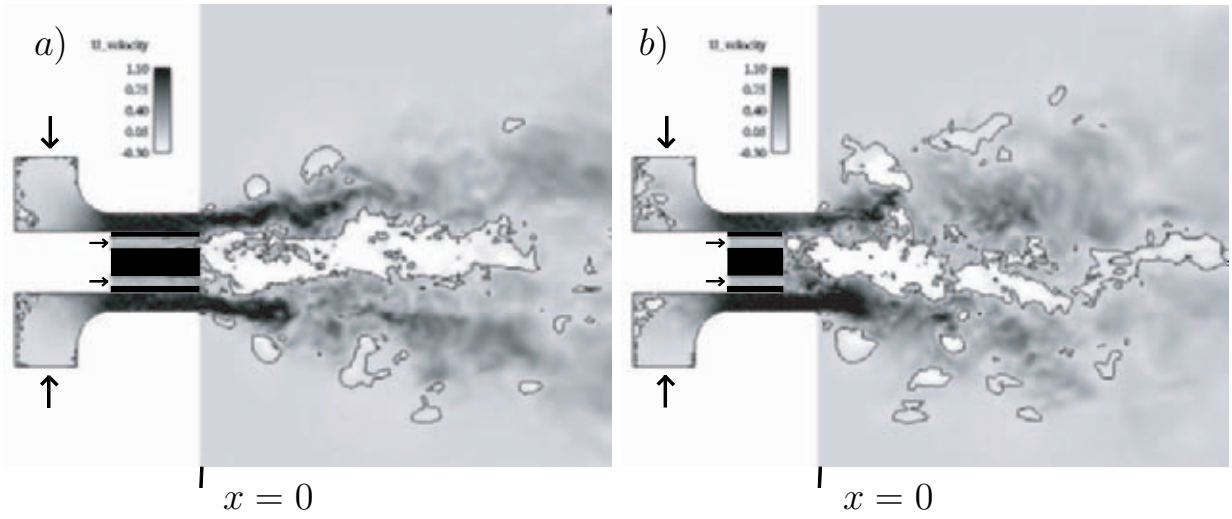

Figure 8.10: Instantaneous axial velocity in the region close to the jet exit. The black line is the boundary of the instantaneous recirculation zone $u_x = 0$. $a)$ NB4, $x_{pilot} = 0$. $b)$ NB5, $x_{pilot} = -0.73R$.

8.3.2 Spectra

In the experiment of Bender & Büchner (2005), time signals of velocity have been recorded at several radial positions close to the burner exit at $x/R = 0.1$ for the case $x_{pilot} = -0.73R$. The case $x_{pilot} = 0$ was not measured because in preliminary tests no instability was observed. During the simulation, velocity and pressure signals were recorded at the same positions for a duration of $80t_b$. Furthermore, signals were recorded for each of these $x-$ and $r-$positions at 12

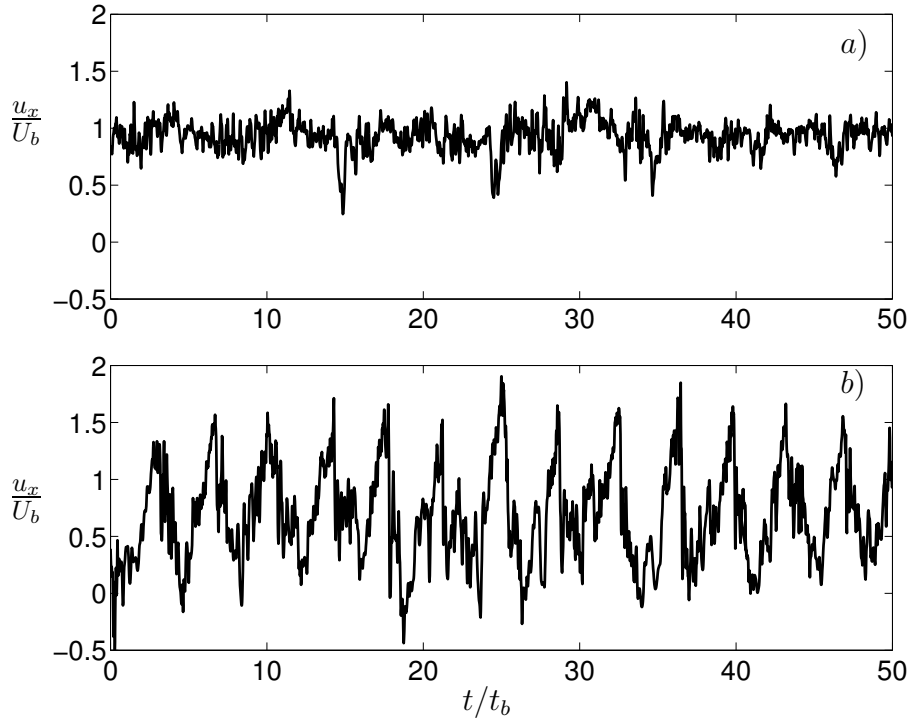

Figure 8.11: Time signals of axial velocity at $r/R = 0.73$, $x/R = 0.1$ recorded during the simulations. $a)$ $x_{pilot} = 0$. $b)$ $x_{pilot} = -0.73R$.

different angular locations over which additional averaging was performed. At the symmetry axis no angular averaging is possible and only one signal was recorded. At $r/R = 0.1$ and $r/R = 0.18$ only four angular signals were recorded. The spectra were obtained splitting each signal in three overlapping segments of length $40t_b$ multiplying it by a Hanning window and averaging over the segments.

The difference between the time signals of both cases is evident from Fig. 8.11. For $x_{pilot} = 0$, Fig. 8.11a, the signal exhibits the typical irregularity of a turbulent signal. Fig. 8.11b, on the other hand shows that for $x_{pilot} = -0.73R$ a flow instability has developed which causes a regular oscillation of the signal with large amplitude. The low frequency oscillations of this signal produce a pronounced peak in the power spectrum of the axial velocity fluctuations, Fig 8.12. The frequency of the principal peak is $f_{peak} = 0.25U_b/R$, which in the dimensional units of the experiment corresponds to a value of $f_{peak} = 102Hz$. The amplitude of the peak is very large, covering almost two decades in logarithmic scale. The total fluctuating energy is substantially larger than for $x_{pilot} = 0$, reflected by the larger integral under this curve. This is in line with the fluctuating kinetic energy contours of Fig. 8.8 and the RMS values of Figs. 8.6 and 8.7. In the case

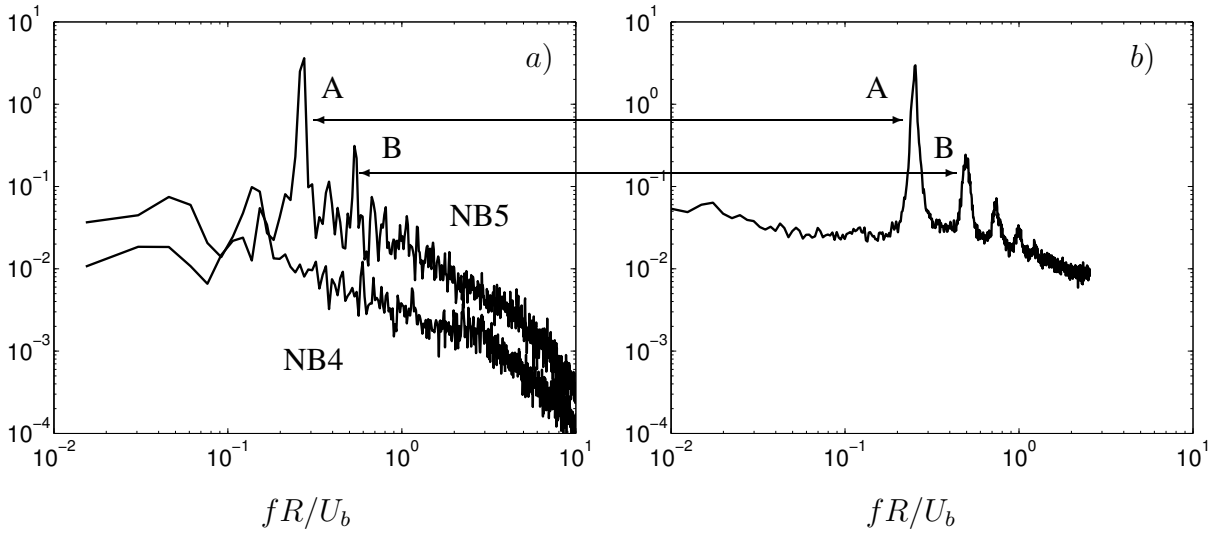

Figure 8.12: $a)$ Power spectrum of axial velocity fluctuations at $x/R = 0.1$, $r/R = 0.73$ from computations NB4 and NB5. $b)$ the same data for $x_{pilot} = -0.73R$ from the experiment.

$x_{pilot} = 0$, no pronounced peak is observed which confirms the preliminary experimental tests in which no flow instability was detected. The smaller peak which appears for $x_{pilot} = 0$ at a frequency $0.16U_b/R$ cannot be related to the small coherent structures observed in Fig. 8.9c because these structures have a shorter time scale which would correspond to higher frequencies. This finding deserves further investigation.

A comparison of the spectrum from the LES for $x_{pilot} = -0.73R$, Fig 8.12a, and the corresponding experimental spectrum in Fig 8.12b serves to further validate the simulations. The agreement for both frequency and amplitude of the dominant peak is remarkable (label A). Also the second harmonic is well predicted in the simulations (label B).

The amplitude of the power spectrum at the peak frequency is now considered. Fig. 8.13 shows this amplitude at the fundamental frequency f_{peak} as a function of the radial position at $x/R = 0.1$. The shape of the curves is different for the three velocity components. The simulation reproduces quite well the trends of the experiment. Only for $r/R < 0.2$ the simulation overpredicts the amplitudes. In that region the impact of azimuthal averaging is small (even non-existent at the axis) so that this could have an effect.

In Chapter 3 similar plots were reported for the Hillemanns configuration. Fig.

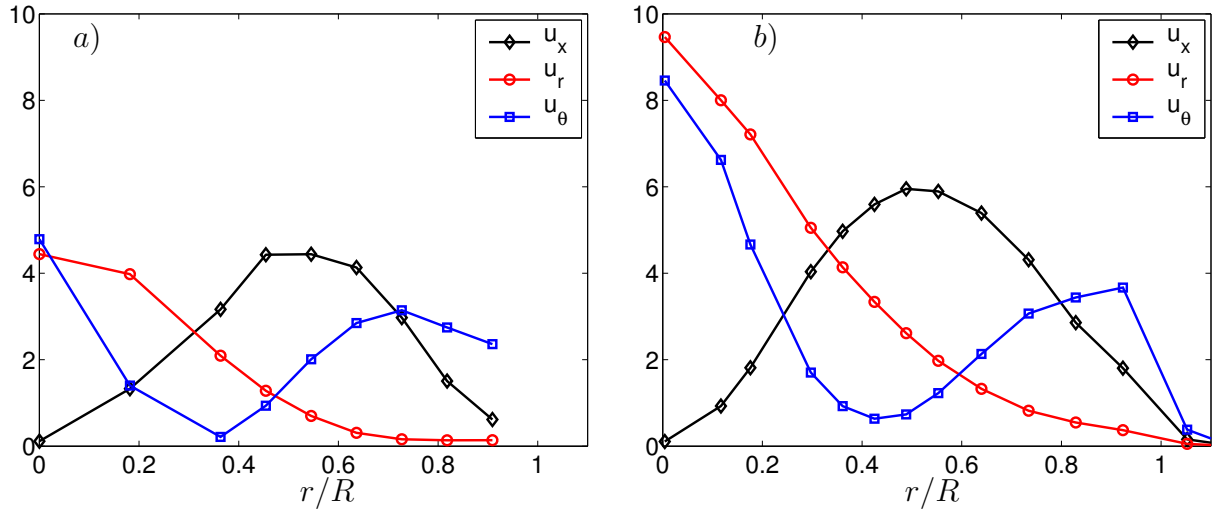

Figure 8.13: Amplitude of the power spectrum at the fundamental frequency f_{peak} at $x/R = 0.1$ as a function of the radial position for $x_{pilot} = -0.73R$. $a)$ experiment. $b)$ NB5.

3.32a displays this quantity obtained for the simulation H1. No experimental support was available for those plots. The similarity with the present configuration is however remarkable. It was shown in Chapter 3 that an important issue is the location of the minimum of the amplitude of the tangential velocity fluctuations. This minimum indicates the mean radial location of the centre of the inner structures. Therefore, it is noteworthy that the minimum is well reproduced in the simulation. The trends for the radial and axial velocity components are also the same in both configurations, taking into account that in the Hillemanns case the cylindrical centre body blocks the axial velocity fluctuations for $r/R < 0.5$ while this does not happen in the present configuration for $x_{pilot} = -0.73R$.

9 Analysis of coherent structures using conditional averages

In this chapter the analysis of coherent structures is further pursued by considering conditional averages. These allow to remove the irregularity of the turbulent motions and provide insights into the main characteristics of the coherent structures and the three-dimensional flow field.

9.1 Motivation

It has been shown in the previous chapters that large-scale structures rotating around the symmetry axis are present in the flow in most cases. Due to the high level of turbulence, the vortical structures are highly irregular as evidenced by the difference between Figs. 8.9b and 8.9d for NB5. The pronounced peak in the power spectrum, Fig. 8.12, indicates that the rotation of the structure is very regular in that case and allows the calculation of conditional averages. This feature is shared by many of the cases presented in this thesis, like the reference case H1 and the rest of high-swirl cases in Chapter 5. Two cases are considered in this chapter, H1 and NB5. The purpose of the conditional averages is to remove the irregularity induced by the turbulent motions. The method, which is described in the following section, consists basically in defining a coordinate system $y-z$ with origin at the symmetry axis which rotates with the structure and in performing the averaging procedure in this rotating coordinate system.

9.2 Procedure

In order to investigate the main characteristics of the coherent structures, instantaneous three-dimensional fields have been recorded. The details are summarized in Table 9.1, including the number of fields N, the separation in time of the fields

Sim.	N	$\Delta t/t_b$	τ/t_b
H1	199	0.5	99.5
NB5	180	0.8	144

Table 9.1: Number, separation in time and time span of fields recorded to perform conditional averages.

Δt and the time span τ covered by the fields for each case. From the values in Table 9.1 it is seen that, in each period of rotation of the structure, 5 fields have been recorded in NB5 and 7 in H1.

If the oscillations are truly periodic, the definition of the axes that rotate with the structure is straightforward, with a fixed angle of rotation in a fixed time. In the present case, however, the motion of the structure is only quasi-periodic and therefore the method has to be more elaborate. The centre of the structure has to be determined for each instantaneous field and a subsequent rotation of the field is performed, such that the centre of the vortex is always on the $y-$axis. This is equivalent to defining a coordinate system $y-z$ which rotates with the structure. In this case however the rotation rate does not need to be constant.

The method is illustrated in Fig. 9.1 and proceeds as follows. The radial location of the dominant inner structures in the transverse plane $x/R = 0.1$ is known from the previous discussion of the power spectrum, Figs. 8.13 and 3.32 (minimum of u_θ). In the present case $r/R = 0.35$ is used for NB5 and $r/R = 0.57$ for H1. The centre of the vortex is identified as the local minimum of the pressure fluctuations at that radial position. In case NB5 the coherent structure is very regular and the detection is simple. In H1 up to three of these coherent structures can co-exist at certain instants and in that case the dominant one is selected, Fig. 9.1. Then, the full three-dimensional field is rotated by an angle α, defined in Fig. 9.1, so that each field has the dominant vortex structure at the same location and standard averaging is performed. Midgley *et al.* (2005) used a similar method to analyze two-dimensional data from experiments on fuel injectors. Here, however, three-dimensional fields are available. Note that this procedure is fundamentally different from phase-averaging. There is no external trigger or internal frequency which would suggest to divide one rotation period into several

phases which would reduce therefore the amount of samples in each phase. Instead, all angles are statistically equivalent due to the cylindrical symmetry of the problem.

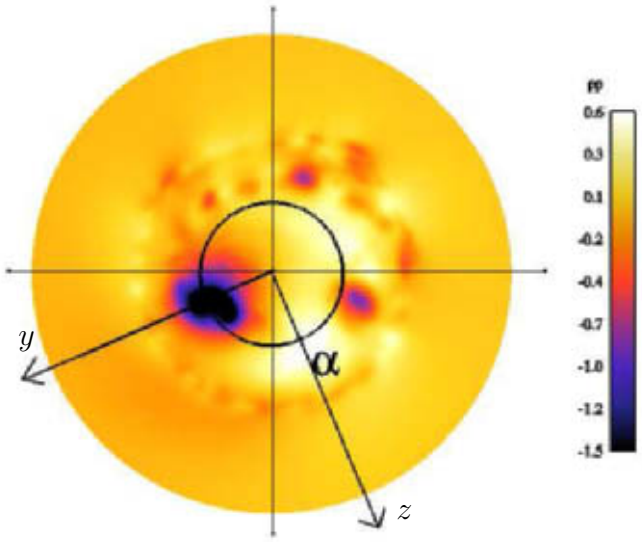

Figure 9.1: Illustration of the conditional averaging procedure. Color according to $p - \langle p \rangle$ from H1. The black circle indicates the points where the minimum of the pressure is looked for.

9.3 Results

In the following, conditionally averaged quantities are indicated with an upper index c. Fig. 9.2 show iso-surfaces of pressure fluctuations resulting from the conditional averaging procedure. For each case, two different levels are presented. It is clear that using this procedure the large-scale coherent structures have been substantially smoothed. In spite of the difference between the cases these plots show that essentially the same phenomena occur. The criterion which has been used to obtain the conditional averages involves only the inner structure. Nevertheless, the outer structure does not disappear with the conditional-averaging but appears at the same angular position demonstrating its link to the inner structure.

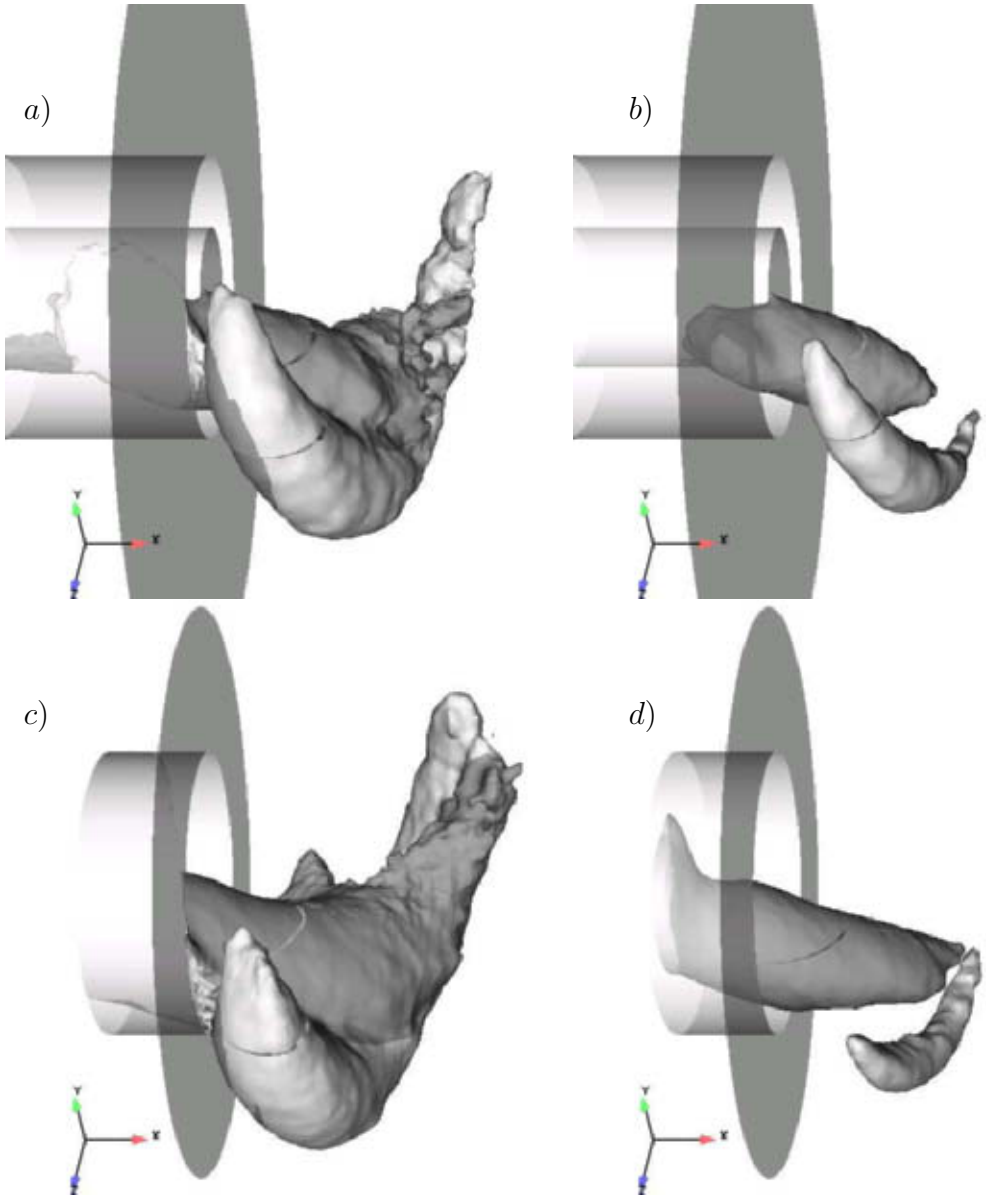

Figure 9.2: Coherent structures obtained using the conditional average flow field. Top, H1. Bottom, NB5. $a, c)$ $p^c - \langle p \rangle = -0.1$. $b)$ $p^c - \langle p \rangle = -0.2$. $d)$ $p^c - \langle p \rangle = -0.3$

Figs. 9.3 and 9.4 show two-dimensional cuts of the conditionally averaged flow for NB5 and H1, respectively. Streamlines of the flow field projected onto two planes are displayed. In Fig. 9.3c the streamlines are based on (u_x^c, u_r^c), in Fig. 9.3d on (u_r^c, u_θ^c), and the same in Fig. 9.4. The color represents p^c and the thick line indicates the contour line $u_x^c = 0$. The latter shows in all four graphs that the recirculation region is displaced off the symmmetry axis. The pressure minimum generated by the inner vortex structure is well visible in the $y-z-$plane together with the vortex motion surrounding it. (Figs. 9.3d and 9.4d)

The inner and outer structure are also visible in Figs. 9.3c and 9.4c. The inner structure shows up through the pressure minimum around $x/R = 0$ and $z > 0$. The outer structure is reflected by the recirculation regions and the spiralling or bending streamlines at the top and the bottom of the figure in NB5, but only at the top in H1. This shows that the outer structure is longer in case NB5. From the streamlines for $x \sim 0$ in both figures (c) it is also clear that the inner structure is correlated with high forward axial velocity, for $z > 0$, while the low axial velocity is located on the opposite side for $z < 0$. This is indicated also by the asymmetry of the recirculation region.

The pressure minimum is off the axis at $r/R \simeq 0.35$ in NB5 and $r/R \simeq 0.57$ in H1 (*a posteriori* justifying the choice of this radius for the conditioning) and by definition located on the $y-$axis. As displayed in Figs. 9.3d and 9.4d the streamlines spiral around a different point closer to the symmetry axis in case NB5, compared to case H1. The shape of the recirculation region is also different, while in NB5 lags behind the inner structure by about $130°$, in H1 it is simply deformed by the inner structure or lagging by about $180°$.

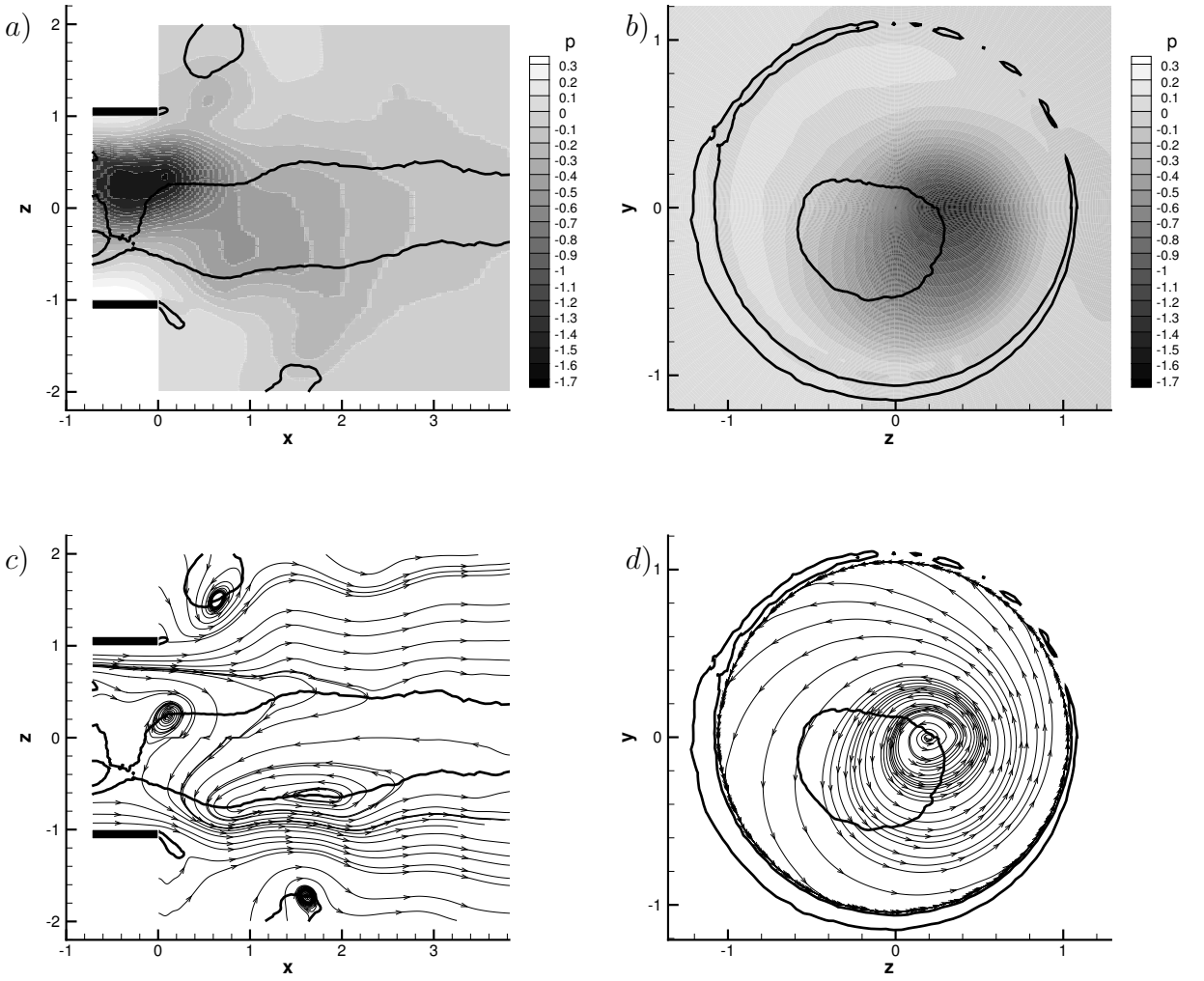

Figure 9.3: Two-dimensional cuts of the conditional average flow from NB5. Thick solid line, $u_x^c = 0$. Left, cut through the plane $y/R = 0$. Right, cut through the plane $x/R = 0.1$. Top, Color is given by p^c. Bottom, streamlines calculated using $c)$ u_x^c and u_r^c, $d)$ u_r^c and u_θ^c.

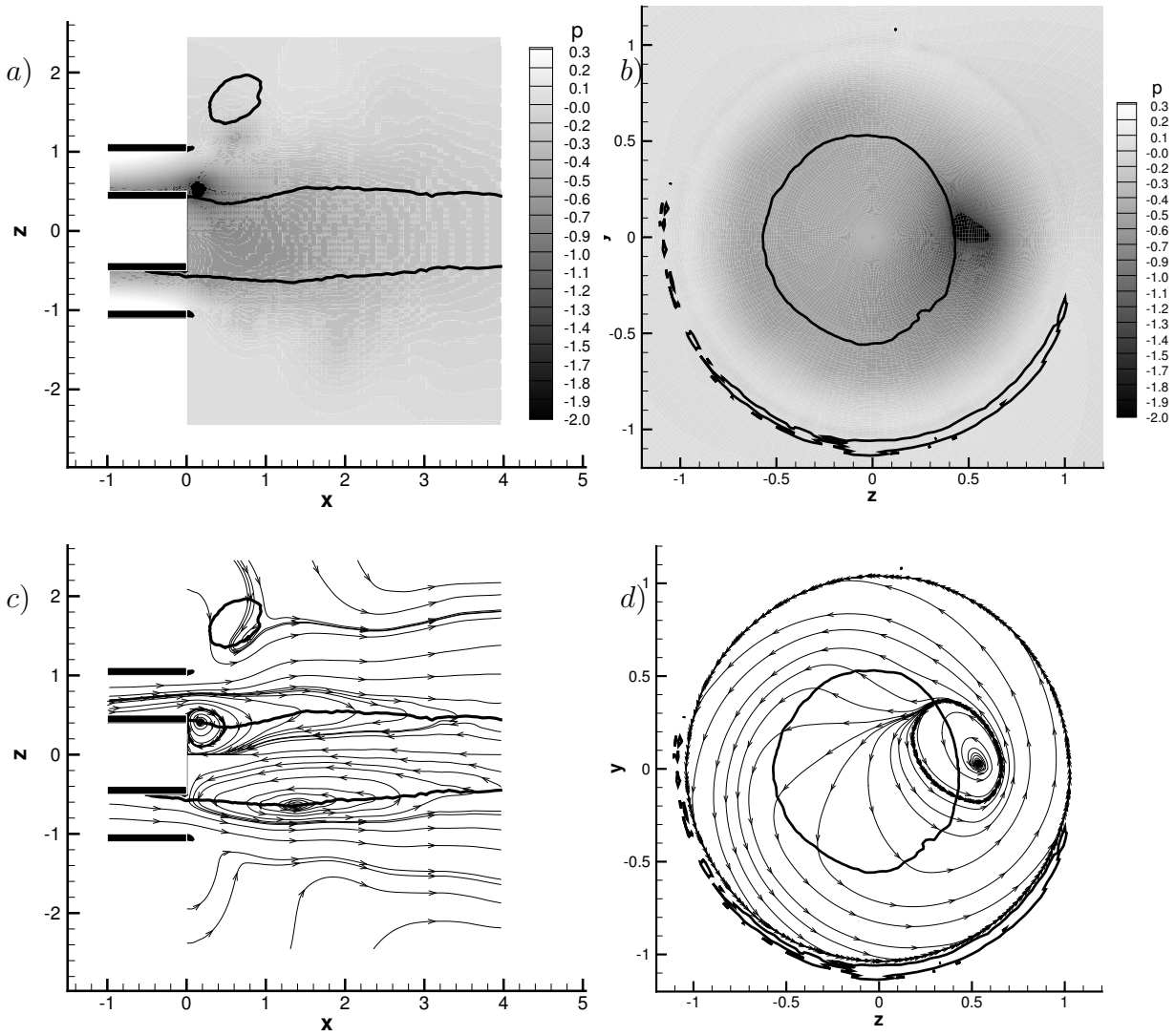

Figure 9.4: Two-dimensional cuts of the conditional average flow from H1. Thick solid line, $u_x^c = 0$. Left, cut through the plane $y/R = 0$. Right, cut through the plane $x/R = 0.1$. Top, Color is given by p^c. Bottom, streamlines calculated using $c)$ u_x^c and u_r^c, $d)$ u_r^c and u_θ^c.

The previous information is contained in a more quantitative way in Figs. 9.5-9.7, which show mean and conditional-averaged profiles of pressure and velocity at $x/R = 0.1$ and $x/R = 1$ for both cases, together with contour plots of the same quantities only in case NB5. Conditional-averaged profiles are shown along two lines. The first coincides with the centre of the structure. The second one is orthogonal to the first one. At $x/R = 0.1$ these lines are the $y-$ and $z-$axes by definition. At $x/R = 1$ this is not the case because of the helical shape of the structure. Hence a coordinate system is chosen such that the pressure minimum lies on one of its axes as indicated in Figs. 9.6b, d, f and labeled A and B.

In Figs. 9.5a and 9.7a the strength of the pressure minimum related to the centre of the structure is visible by comparison to the mean pressure. This difference is larger in H1 which seems to indicate that the structure is stronger in this case. However, downstream at $x/R = 1$ the difference is larger in NB5 (compare Figs. 9.6a and 9.7b). This indicates that in H1 the intensity of the structure is concentrated in a small region close to the jet exit while in NB5 it spreads over a longer region. The second minimum located radially outwards in both plots indicate the outer structure.

The conditionally averaged axial velocity u_x^c along the positive $y-$axis, hence in the inner structure, is higher than the mean axial velocity (Figs. 9.5c and 9.7c). This also happens at $x/R = 1$. The recirculation zone in NB5, as expected from the two-dimensional plots (Fig. 9.3), is displaced towards the opposite side, while this effect is not so pronounced in H1. The reason is, perhaps, that the inner vortex is closer to the symmetry axis in NB5, and this has a larger effect on the recirculation zone. In general, the profiles in the region indicated by $r < 0$ in Figs. 9.5-9.7 is closer to the mean flow in case H1 than in case NB5. This suggests that the perturbation induced by the inner structure is more local in case H1.

The features observed in the profiles of u_θ^c (Figs. 9.5e and 9.7e) are also similar in both cases. In Fig. 9.5e, the radial position at which the conditionally averaged tangential velocity u_θ^c at $y = 0$ equals the mean velocity, roughly corresponds to the minimum of the pressure. This is also expected because at the centre of the structure the fluctuations of the tangential velocity component have to vanish, as discussed in Chapter 3.

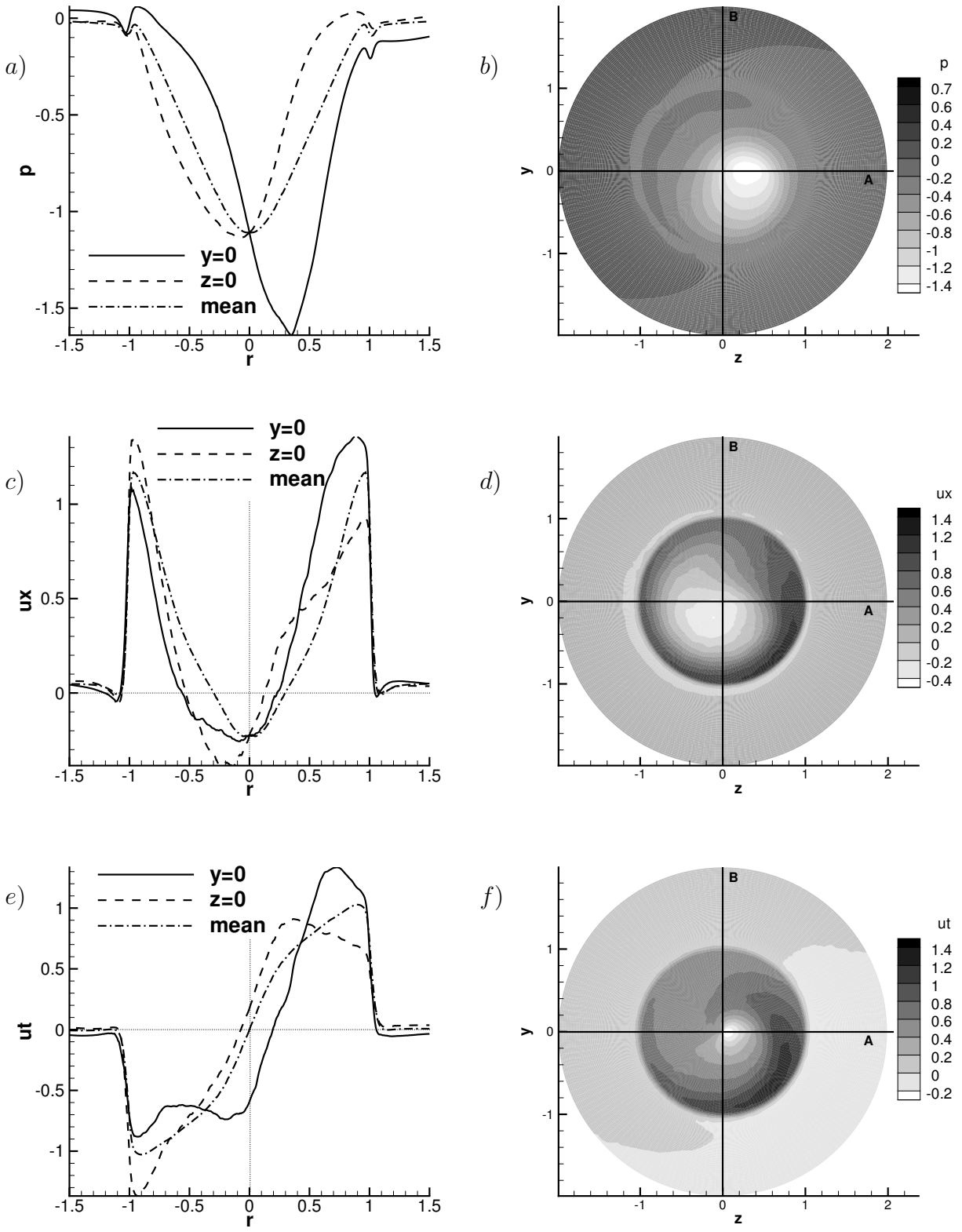

Figure 9.5: Profiles and contours at $x/R = 0.1$ from NB5. Top, pressure. Middle, axial velocity. Bottom, tangential velocity.

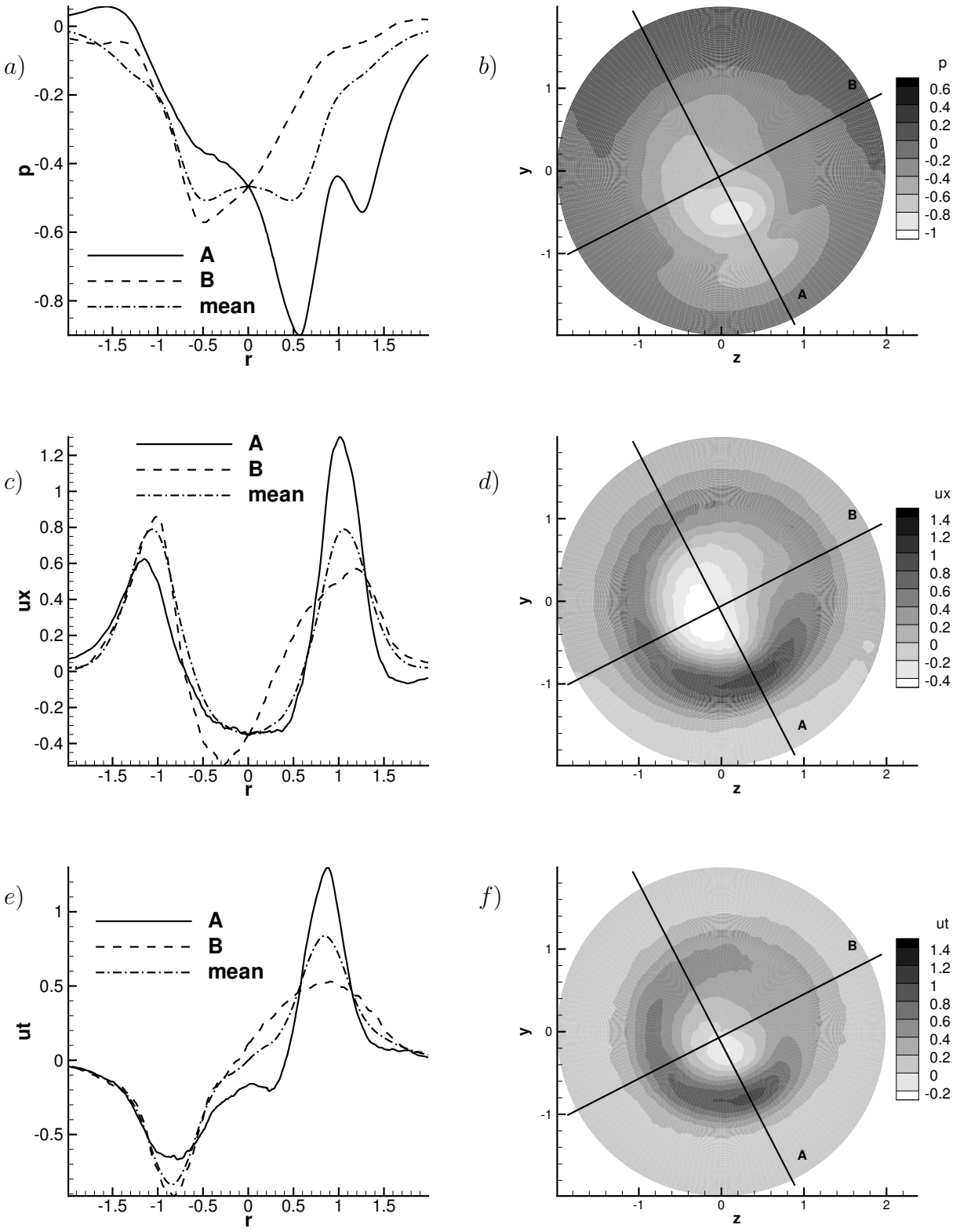

Figure 9.6: Profiles and contours at $x/R = 1$ from NB5. Top, pressure. Middle, axial velocity. Bottom, tangential velocity.

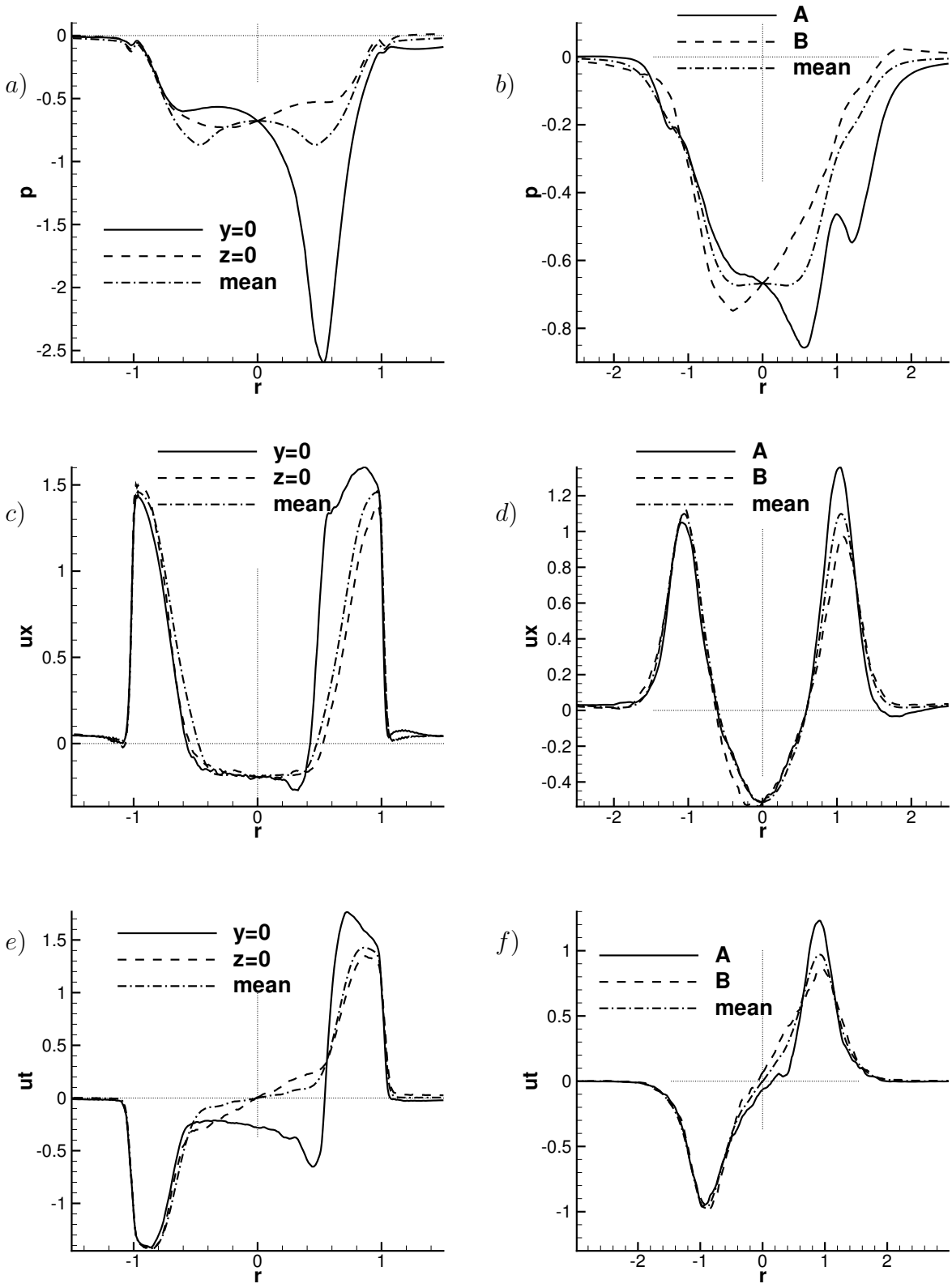

Figure 9.7: Profiles from H1. Top, pressure. Middle, axial velocity. Bottom, tangential velocity. Left, $x/R = 0.1$. Right, $x/R = 1$.

Finally, Fig. 9.8 shows the same plane as Fig. 9.3 and 9.4 but the color and streamlines are given by the equivalent Reynolds-decomposed quantities, i.e. color by $p^c - \langle p \rangle$ and streamlines by $(u_r^c - \langle u_r \rangle, u_\theta^c - \langle u_\theta \rangle)$. The thick line again represents $u_x^c = 0$. In this figure the region of low pressure fluctuations corresponds to the inner structure of Fig. 9.2. Note that it forms outside the boundary of the recirculation zone.

Yazdabadi *et al.* (1994) performed phase-averaged measurements in a cyclone dust separator and obtained similar plots as Figs. 9.5-9.7 for the velocity components. Their conclusion was that the reverse flow zone displaces the central vortex core to create the precessing vortex core. The reverse flow zone would then provide feedback for the precessing vortex core, and precess around the central axis behind the precessing vortex core. In the present case, Fig. 9.8 together with the discussion of Chapter 3 suggest an alternative explanation, although perhaps compatible with the previous one: The inner structure (precessing vortex core) is formed as an instability of the shear layer (Kelvin-Helmholtz instability). It is therefore formed on the boundary of the recirculation zone, Fig. 9.8, and advected by the mean flow. This structure then constrains the motion of the recirculation zone which is displaced off the symmetry axis and precesses behind the structure.

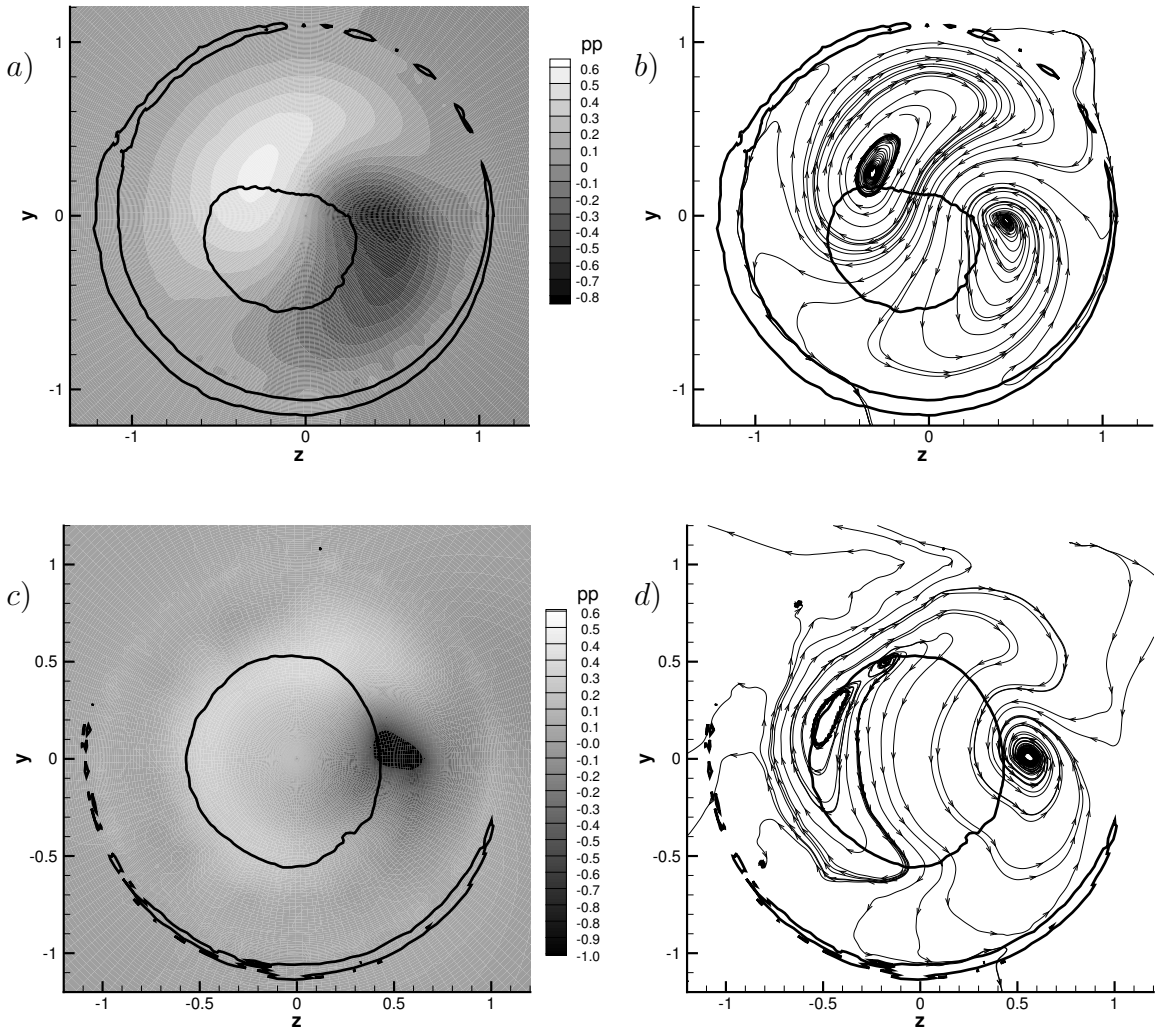

Figure 9.8: Two-dimensional cut through the plane $x/R = 0.1$ of the conditional average flow. Top, NB5. Bottom, H1. Thick solid line, $u_x^c = 0$. Left, Color is given by $p^c - \langle p \rangle$. Right, streamlines calculated using $u_r^c - \langle u_r \rangle$ and $u_\theta^c - \langle u_\theta \rangle$.

10 Summary, conclusions and recommendations for future work

Your ability to help others
may not be seen by all.

Fortune Cookie

10.1 Summary

In this thesis the flow in swirl-burner related geometries has been investigated using LES. The adequacy of the employed LES methodology has been demonstrated by various comparisons with corresponding experiments (Büchner & Petsch, 2004; Bender & Büchner, 2005). Very good agreement with the experimental data has been obtained for mean flow and turbulent fluctuations. Also, the low frequency range of the power spectral density of velocity fluctuations has been found to be in good agreement with the experiments. This suggests that the large-scale organized motions have been well captured in the simulations, allowing a more detailed physical interpretation of these motions than is possible from the experimental results. Analyses of the different vortex structures have been performed by a variety of post-processing techniques. Two- and three-dimensional visualizations, filtering, different types of averaging, spectra, auto-correlation functions, etc. were employed depending on the specific question to be answered.

Swirl flows constitute a challenging and practically relevant class of flows. They encompass a large number of phenomena, like recirculation zones, shear layers, flow instabilities, etc. These features are present in the simulations described in this thesis. In particular, the simplest configuration presented here is an unconfined annular swirling jet, at high Reynolds and Swirl numbers. For this configuration some of the modelling assumptions have been investigated. The influence of the sub-grid scale model, the grid and the co-flow boundary condition

have been assessed. Furthermore, different ways of providing the inflow conditions have been considered.

Using this simple configuration as reference, parametric studies have been performed. The influence of the level of swirl, an imposed oscillation and a pilot jet have been investigated. The sensitivity to the level of swirl has been performed by considering seven simulations in Chapter 5 covering a wide range. From no-swirl until high swirl including intermediate cases. Pulsating inflow has been discussed in Chapter 6 considering two cases which correspond to different idealized scenarios of pulsation which are realistic since the swirl-generating devices in a burner can be different. In one case only the axial velocity oscillates at the inflow. In the second both the axial and the tangential velocity components oscillate. Finally, the practically-relevant case of the addition of a pilot jet has been considered. Two cases have been studied. First, main and pilot jet exit at the same location. In the second one, the pilot jet is retracted into the inlet duct. In this case, the main jet is subject to a double expansion.

10.2 Conclusions

The simulations reported in the present thesis provide good quality data and important hints to mechanisms of instability.

For the reference case, large-scale coherent structures rotating around the symmetry axis have been identified. Two families of structures appear, an inner one oriented quasi-streamwise and located in the inner shear layer and an outer one oriented at a larger angle with respect to the $x-$axis and situated in the outer shear layer. The large-scale coherent structures are relevant to the mixing of heat and species in the near field of swirl burners. The Kelvin-Helmholtz instability has been identified as the major source for the generation of the coherent vortices. Furthermore, a clear connection between the velocity power spectra and the coherent structures has been established.

By varying the swirl level, it has been shown that jet growth, entrainment and decay are enhanced progressively as the degree of swirl is increased. It has been also shown that, as soon as the swirl is higher than $S > 0.7$, the characteristics of the large-scale coherent structures are similar. In the intermediate case $S = 0.55$,

however, only inner structures have been found. This suggests that the inner shear layer is more unstable than the outer one and the structures form first in the inner shear layer. With increasing swirl, the shear layers approach each other and the inner structures trigger the formation of the outer ones.

For the pulsating inflow investigations, it has been shown that the recirculation zone is mainly influenced by the oscillation of azimuthal velocity. In both cases considered, dominant vortex rings have been observed in the phase-averaged flow. The rotation rate of the instantaneous coherent structures is dominated by the oscillation of the azimuthal component. When the latter is fixed at the inlet, the structures rotate at a constant rate and pronounced peaks are observed in the spectra. When the flow oscillates azimuthally at the inlet, temporal spectra cannot be used to assess spatial structures. Analyses of the instantaneous pressure field have shown that the qualitative nature of the vortex structures is similar to that in the non-pulsating case. The coherence of the structures, in particular for the inner ones, is larger when only the axial velocity component oscillates.

Concerning the pilot jet, it has been shown that the mean flow is only little affected by the introduction of the pilot jet while the fluctuations show moderate differences near the outlet and close to the inner shear layer. Visualizations and spectra have shown, however, that although axial and angular momentum of this jet are small, it has a dramatic effect on the instantaneous vortex structures. When the pilot jet is retracted, on the other hand, the flow instabilities are substantially enhanced. The reason is that, in the first case, the pilot jet perturbs the inner shear layer avoiding the formation of large coherent structures, only short living structures are formed. In the second case, the perturbation of the inner shear layer does not occur because the tube enclosing the main jet prevents the recirculation bubble from moving upstream to the central bluff body.

In conclusion, a comprehensive investigation of isothermal swirling flows has been performed providing a detailed understanding of the underlying physics. After validation for one particular case, LES has been shown to be a suitable, predictive tool for parametric studies.

10.3 Recommendations for future work

In this thesis a number of different investigations on large eddy simulations of turbulent incompressible swirling jets have been performed successfully. There are important issues which have not been addressed in this work. In the following an overview of these issues is given.

First, it is worth to mention that the validation of the simulations have been performed in a small region very close to the burner exit due to the lack of experimental data further downstream. More experiments are needed to validate thoroughly the simulations, for example with respect to the length of the recirculation zone. Also it would be of interest to evaluate the influence of confinement by performing several simulations with walls at different locations and comparing with the unconfined simulations reported here.

From a fundamental point of view, the mechanisms of instability which have been proposed should be supported by stability analyses. Nowadays, a suitable approach is the so-called bi-global stability analysis (Theofilis, 2003). In linear stability research, the flow is decomposed into an steady (or time-periodic) *basic flow* upon which small-amplitude three-dimensional disturbances are permitted to develop. The advantage of bi-global analyses is that the basic flow is two-dimensional unlike more traditional approaches which usually employ the parallel flow assumption (Drazin & Reid, 1981). For the configurations studied in the present work, a two-dimensional basic flow is needed because of the spatial structure of the mean flow, i.e. the parallel flow assumption is not valid. It would therefore be interesting to consider the mean flow obtained from the LES as basic flow, with the azimuthal direction being homogeneous, using an additional eddy viscosity term like in del Álamo & Jiménez (2006). Alternatively, the basic flow could be obtained by performing a direct numerical simulation of the linearised two-dimensional equations of motion (see Theofilis (2003)). Two-dimensional in the sense that the equations only depend on x and r, and not in θ, although the three-velocity components must be retained in the equations.

In this thesis, the interest has been focused in high Reynolds number flows. Other investigators have shown that flow instabilities occur also at lower Reynolds number (Freitag & Klein, 2005). The irregularity induced by the turbulent mo-

tions decreases at lower Re and the characteristics of the large-scale coherent structures could be interpreted in an easier manner. Therefore, it would be interesting to perform direct numerical simulations of the present configuration at a lower Reynolds number.

A natural continuation of the present work is the study of mixing in the near field of swirl burners. Despite recent development in this direction (Freitag *et al.*, 2005; Wegner *et al.*, 2005), there is still a need of a deeper understanding of this phenomenon. In particular, it would be instructive to study the impact of the large-scale coherent structures on the mixing of a passive scalar by using the configurations of Chapter 8. This would allow the comparison of the mixing in a case with strong coherent structures and a case with weak coherent structures.

As mentioned in the introduction of the thesis, this work is part of a long-term research effort focused on unsteady combustion. It is therefore logical that the next step has to be related to the investigation of reactive flows, first, by using the G-equation as combustion model combined with simple models for the turbulent flame speed (Poinsot & Veynante, 2001). The configurations discussed in the present thesis are available for comparison, in particular, to evaluate how the combustion affects the formation of coherent structures and to study the unsteady heat release. In the long term, the objective of the project is to perform large eddy simulations of flow in model combustors using realistic Reynolds number ($Re \sim 10^5$) and high-quality combustion models in order to predict combustion instabilities and to clarify mechanisms of instability.

Bibliography

AKSELVOLL, K. & MOIN, P. 1995 Large-eddy simulation of turbulent confined coannular jets and turbulent flow over a backward facing step. Report No. TF-63. Thermosciences Division. Stanford University.

AKSELVOLL, K. & MOIN, P. 1996 Large-eddy simulation of turbulent confined coannular jets. *J. Fluids Mech.* **315**, 387–411.

DEL ÁLAMO, J. & JIMÉNEZ, J. 2006 Linear energy amplification in turbulent channels. In preparation.

DEL ÁLAMO, J., JIMÉNEZ, J., ZANDONADE, P. & MOSER, R. D. 2004 Scaling of the energy spectra in turbulent channels. *J. Fluids Mech.* **500**, 135–144.

ALEKSEENKO, S. V., KUIBIN, P. A., OKULOV, V. & SHTORK, S. I. 1999 Helical vortices in swirl flow. *J. Fluid Mech.* **382**, 195–243.

APTE, S., MAHESH, K., MOIN, P. & OEFELEIN, J. 2003 Large-eddy simulation of swirling particle-laden flows in a coaxial-jet combustor. *Int. J. Multiphase Flow* **29**, 1311–1331.

BATCHELOR, G. 1967 *An introduction to fluid mechanics*. Cambridge Univ. Press.

BENDER, C. & BÜCHNER, H. 2005 Noise emissions from a premixed swirl combustor. In *Proc. 12th Int. Cong. Sound and Vibration, Lisbon, Portugal*.

BENOCCI, C. & PINELLI, A. 1990 The role of the forcing term in the large eddy simulation of equilibrium channel flow. In *Engineering Turbulence Modelling and Experiments* (ed. W. Rodi & E. N. Ganić). Elsevier.

BILLANT, P., CHOMAZ, J. M. & HUERRE, P. 1998 Experimental study of vortex breakdown in swirling jets. *J. Fluid Mech.* **376**, 183–219.

BOCKHORN, H., FRÖHLICH, J. & SUNTZ, R. 2003 SFB 606 – a german research initiative on unsteady combustion. Ercoftac bulletin.

BRAUN, C. 2005 *Large-Eddy Simulation of turbulent flow over dunes*. Diploma thesis. Univ. Karlsruhe.

BREUER, M. & RODI, W. 1996 Large eddy simulation of complex turbulent flows of practical interest. In *Flow simulation with high performance computers II* (ed. E. Hirschel), *Notes on Numerical Fluid Mechanics*, vol. 52, pp. 258–274. Braunschweig: Vieweg.

BÜCHNER, H. 2005 Private communication.

BÜCHNER, H. & PETSCH, O. 2004 Experimental investigation of instabilities in turbulent premixed flames. In *Proc. 1st Int. Workshop on Unsteady Combustion. Karlsruhe. Germany*.

COATS, C. M. 1996 Coherent structures in combustion. *Prog. Energy and Comb. Sci.* **22**, 427–509.

DAHM, W., FRIELER, C. & TRYGGVASON, G. 1992 Vortex structure and dynamics in the near field of a coaxial jet. *J. Fluid Mech.* **241**, 371–402.

DEARDOFF, J. W. 1970 A numerical study of three-dimensional turbulent channel flow at large Reynolds number. *J. Fluid Mech.* **41**, 453–465.

DRAZIN, P. G. & REID, W. H. 1981 *Hydrodynamic stability*. Cam. Univ. Press.

DRUAULT, P., LARDEAU, S., BONNET, J. P., COIFFET, F., DELVILLE, J., LAMBALLAIS, E., LARGEAU, J. F. & PERRET, L. 2004 Generation of three-dimensional turbulent inlet conditions for large eddy simulation. *AIAA J.* **42** (3), 447–456.

DUBIEF, Y. & DELCAYRE, F. 2000 On coherent-vortex identification in turbulence. *Journal of Turbulence* **1**.

DURBIN, P. A. 2002 A perspective on recent developments in RANS modeling. In *Engineering Turbulence Modelling and Experiments 5* (ed. W. Rodi & N. Fueyo). Elsevier.

DURBIN, P. A. & PETTERSSON-REIF, B. A. 2001 *Statistical Theory and Modeling for Turbulent Flow*. John Wiley.

DÜSING, M., HAUSER, A., SADIKI, A. & JANICKA, J. 2002 LES of confined methane-air diffusion flames using oscillation inflow conditions. In *Proc. Int. Symp. Eng. Turbulence Modelling Measurements ETMM5, Mallorca, Spain* (ed. W. Rodi & N. Fueyo).

FREITAG, M. & KLEIN, M. 2005 Direct Numerical Simulation of a recirculating, swirling flow. *Flow, Turbulence and Combustion (in press)* .

FREITAG, M., KLEIN, M., GREGOR, M., NAUERT, A., GEYER, D., SCHNEIDER, C., DREIZLER, A. & JANICKA, J. 2005 Mixing analysis of a swirling recirculating flow using DNS and experimental data. In *Proc. 4th Int. Symposium on Turbulence and Shear Flow Phenomena. Williamsburg. USA*.

FRISCH, U. 1995 *Turbulence. The legacy of A. N. Kolmogorov*. Cambridge Univ. Press.

FRÖHLICH, J. 2005 *Large Eddy Simulation inkompressibler Strömungen*. Habilitationschrift Univ. Karlsruhe.

FRÖHLICH, J., DENEV, J. & BOCKHORN, H. 2004 Large eddy simulation of a jet in crossflow. In *Proc. 4th ECCOMAS Conference, Jyvskyl, Finland*.

FRÖHLICH, J., MELLEN, C. P., RODI, W., TEMMERMAN, L. & LESCHZINER, M. A. 2005 Highly resolved large-eddy simulation of separated flow in a channel with streamwise periodic constrictions. *J. Fluid Mech.* **526**, 19–66.

FRÖHLICH, J. & RODI, W. 2002 Introduction to large eddy simulation of turbulent flows. In *Closure Strategies for Turbulent and Transitional Flows.*. Cambridge University Press.

FRÖHLICH, J. & RODI, W. 2004 LES of the flow around a cylinder of finite height. *Int. J. Heat Fluid Flow* **25**, 537–548.

FROUD, D., O'DOHERTY, T. & SYRED, N. 1995 Phase averaging of the precessing vortex core in a swirl burner under piloted and premixed combustion conditions. *Combustion and Flame* **100**, 407–412.

GALLAIRE, F. & CHOMAZ, J. M. 2003 Mode selection in swirling jet experiments: a linear stability analysis. *J. Fluid Mech.* **494**, 223–253.

GARCÍA-VILLALBA, M., FRÖHLICH, J. & RODI, W. 2005 Large eddy simulation of turbulent confined coaxial swirling jets. In *Proc. 76. Jahrestagung der Gesellschaft für Angewandte Mathematik und Mechanik. Luxembourg*.

GERMANO, M., PIOMELLI, U., MOIN, P. & CABOT, W. 1991 A dynamic subgrid-scale eddy viscosity model. *Phys. Fluids* **3**, 1760–1765.

GEURTS, B. J. 2003 *Elements of Direct and Large-Eddy Simulation*. R.T. Edwards.

GUPTA, A., LILLEY, D. & SYRED, N. 1984 *Swirl Flows*. Abacus Press.

HABISREUTHER, P., BENDER, C., PETSCH, O., BÜCHNER, H. & BOCKHORN, H. 2005 Prediction of pressure oscillations in a premixed swirl combustor flow and comparison to measurements. In *Engineering Turbulence Modelling and Experiments 6* (ed. W. Rodi & M. Mulas). Elsevier.

HARVEY, J. K. 1962 Some observations of the vortex breakdown phenomenon. *J. Fluid Mech.* **14**, 585–592.

HILLEMANNS, R. 1988 Das Strömungs- und Reaktionsfeld sowie Stabilisierungeigenschaften von Drallflamen unter dem Einfluss der inneren Rezirkulationszone. PhD thesis, University of Karlsruhe.

HINTERBERGER, C. 2004 Dreidimensionale und tiefengemittelte Large-Eddy-Simulation von Flachwasserströmungen. PhD thesis, University of Karlsruhe.

HINTERBERGER, C., GARCÍA-VILLALBA, M. & RODI, W. 2004 LES of flow around the Ahmed body. In *Lecture Notes in Applied Mechanics and Computational Mechanics / The Aerodynamics of Heavy Vehicles: Trucks, Buses, and Trains* (ed. R. McCallen, F. Browand & J. Ross). Springer Verlag.

HUANG, Y., SUNG, H.-G., HSIEH, S.-Y. & YANG, V. 2003 Large Eddy Simulations of combustion dynamics of lean-premixed swirl-stabilized combustion. *J. of Propulsion and Power* **19** (5), 782–794.

HUSAIN, H. S., SHTERN, V. & HUSSAIN, F. 2003 Control of vortex breakdown by addition of near axis swirl. *Phys. Fluids* **15**, 271–279.

JAKIRLIĆ, S., HANJALIĆ, K. & TROPEA, C. 2002 Modeling rotating and swirling turbulent flows: a perpetual challenge. *AIAA J.* **40** (10), 1984–1996.

JEHONG, J. & HUSSAIN, F. 1995 On the identification of a vortex. *J. Fluid Mech.* **285**, 69–94.

JIMÉNEZ, J. 2000 Turbulence. In *Perspectives in fluid mechanics*. Cambridge Univ. Press.

JIMÉNEZ, J. 2003 Computing high-Reynolds number turbulence: will simulations ever replace experiments? *J. Turbulence* **4**.

JONES, W. P. 2005 Private communication.

KIM, W., MENON, S. & MONGIA, H. 1999 Large-eddy simulations of a gas turbine combustor flow. *Combustion science and technology* **143**, 25–62.

KLEIN, M., SADIKI, A. & JANICKA, J. 2003 A digital filter based generation of inflow data for spatially developing direct numerical or large eddy simulations. *J. Comp. Physics* **186**, 652–665.

KO, N. & KWAN, A. 1976 The initial region of subsonic coaxial jets. *J. Fluid Mech.* **73**, 305–332.

KOCH, R. 2004 Private communication.

KOLMOGOROV, A. 1941 The local structure of turbulence in imcompressible viscous fluids at very large Reynolds number. *Dokl. Akad. Nauk. SSSR* **300**, 301–305, reprinted in *Proc. R. Soc. London A*, **434**, 9-13, (1991).

KÜLSHEIMER, C. & BÜCHNER, H. 2002 Combustion dynamics of turbulent swirling flames. *Comb. Flame* **131**, 70–84.

KWAN, A. & KO, N. 1977 The initial region of subsonic coaxial jets. Part 2. *J. Fluid Mech.* **82**, 273–287.

LE, H., MOIN, P. & KIM, J. 1997 Direct numerical simulation of turbulent flow over a backward-facing step. *J. Fluids Mech.* **330**, 349–374.

LE-RIBAULT, C., SARKAR, S. & STANLEY, S. 1999 Large eddy simulation of a plane jet. *Phys. Fluids* **11**, 3069–3083.

LEIBOVICH, S. 1984 Vortex stability and breakdown: survey and extension. *AIAA J.* **22** (9), 1192–1206.

LEUCKEL, W. 1967 Swirl intensities, swirl types and energy losses of different swirl generating devices. IFRF Doc Nr. G 02/a/16.

LIEUWEN, T., TORRES, H., JOHNSON, C. & ZINN, B. 2001 A mechanism of combustion instability in lean premixed gas turbine combustors. *J. Eng. Gas Turbines and Power* **123**, 182–189.

LILLY, D. 1967 The representation of small-scale turbulence in numerical simulation experiments. In *Proc. IBM Scientific Computing Symp. on Environmental Sciences* (ed. H. H. Goldstine), pp. 195–210. Yorktown Heights, NY:IBM.

LILLY, D. 1992 A proposed modification of the Germano subgrid-scale closure method. *Phys. Fluids* **4**, 633–635.

LU, X., WANG, S., SUNG, H.-G., HSIEH, S.-Y. & YANG, V. 2005 Large Eddy Simulations of turbulent swirling flows injected into a dump chamber. *J. Fluid Mech.* **527**, 171–195.

LUCCA-NEGRO, O. & O'DOHERTY, T. 2001 Vortex breakdown: a review. *Prog. Energy and Comb. Sci.* **27**, 431–481.

LUND, T., WU, X. & SQUIRES, K. 1998 Generation of turbulent inflow data for spatially-developing boundary layer simulations. *J. Comp. Phys.* **140**, 233–258.

MCILWAIN, S. & POLLARD, A. 2002 Large eddy simulation of the effects of mild swirl on the near field of a round free jet. *Phys. Fluids* **14** (2), 653–661.

MICHELASSI, V., WISSINK, J. G., FRÖHLICH, J. & RODI, W. 2003 LES of flow around a low-pressure turbine blade with incoming wakes. *AIAA J.* **41** (11), 2143–2156.

MIDGLEY, K., SPENCER, A. & MCGUIRK, J. J. 2005 Unsteady flow structures in radial swirled fed fuel injectors. *J. Eng. Gas Turbines and Power* **127**, 755–764.

NEJAD, A., VANKA, S., FAVALORO, S., SAMIMY, M. & LANGENFELD, C. 1989 Application of laser velocimetry for characterization of confined swirling flow. *Journal of Engineering for Gas Turbines and Power* **111**, 36–45.

OLSSON, M. & FUCHS, L. 1996 Large eddy simulation of the proximal region of a spatially developing circular jet. *Phys. Fluids* **8**, 2125–2137.

O'NEIL, J. & MENEVEAU, C. 1997 Subgrid-scale stresses and their modelling in a turbulent plane wake. *J. Fluid Mech.* **349**, 253–293.

OPPENHEIM, A. & SCHAFER, R. 1989 *Discrete-Time Signal Processing*. Prentice Hall.

PANDA, J. & MCLAUGHLIN, D. 1994 Experiments on the instabilities of a swirling jet. *Phys. Fluids* **6**, 263–276.

PASCHEREIT, C., FLOHR, P., BOCKHOLTS, M. & POLIFKE, W. 2000*a* Fluid dynamic instabilities in a swirl stabilized burner and their effect on heat release fluctuations. In *Flow induced vibration* (ed. Ziada & Staubli), pp. 687–694.

PASCHEREIT, C., GUTMARK, E. & WEISENSTEIN, W. 1998 Structure and control of thermoacustic instabilities in a gas-turbine combustor. *Combustion science and technology* **138**, 213–232.

PASCHEREIT, C., GUTMARK, E. & WEISENSTEIN, W. 1999 Coherent structures in swirling flows and their role in acoustic combustion control. *Phys. Fluids* **11**, 2667–2678.

PASCHEREIT, C., GUTMARK, E. & WEISENSTEIN, W. 2000*b* Excitation of thermoacustic instabilities by interaction of acoustics and unstable swirling flow. *AIAA J.* **38**, 1025–1034.

PIERCE, C. 2001 Progress-variable approach for large-eddy simulation of turbulent combustion. PhD thesis, Stanford University.

PIERCE, C. & MOIN, P. 1998*a* Large eddy simulation of a confined coaxial jet with swirl and heat release. AIAA paper no. 98-2892.

PIERCE, C. & MOIN, P. 1998*b* Method for generating equilibrium swirling inflow conditions. *AIAA J.* **36** (7), 1325–1327.

PIOMELLI, U. & BALARAS, E. 2002 Wall-layer models for large-eddy simulations. *Annu. Rev. Fluid Mech.* **34**, 349–374.

PIOMELLI, U., CABOT, W. H., MOIN, P. & LEE, S. 1991 Subgrid-scale backscatter in turbulent and transitional flow. *Phys. Fluids* **3**, 1766–1771.

POINSOT, T. & VEYNANTE, D. 2001 *Theoretical and numerical combustion*. Edwards.

POPE, S. 2000 *Turbulent Flows*. Cambridge University Press.

POPE, S. B. 2004 Ten questions concerning the large-eddy simulation of turbulent flows. *New J. of Physics* **6**, 35.

REHAB, H., VILLERMAUX, E. & HOPFINGER, E. J. 1997 Flow regimes of large-velocity-ratio coaxial jets. *J. Fluid Mech.* **345**, 357–381.

RHIE, C. & CHOW, W. 1983 Numerical study of the turbulent flow past an airfoil with trailing edge separation. *AIAA J.* **21** (11), 1061–1068.

ROBACK, R. & JOHNSON, B. 1983 Mass and momentum turbulent transport experiments with confined swirling coaxial jets. NASA CR-168252.

RODI, W. 1993 *Turbulence models and their applications in hydraulics*, 3rd edn. IAHR Monograph Series.

RODI, W., GARCÍA-VILLALBA, M., STOESSER, T. & BRAUN, C. 2005 Flow over an axisymmetric three-dimensional hill (Large Eddy Simulation). In *Proc. 11th ERCOFTAC/IAHR workshop on refined turbulence modelling* (ed. T. Johansson & L. Davidson).

ROUX, S., LARTIGUE, G., POINSOT, T., MEIER, U. & BÉRAT, C. 2005 Studies of mean and unsteady flow in a swirled combustor using experiments, acoustic analysis and large eddy simulations. *Comb. Flame* **141**, 40–54.

RUITH, M. R., CHEN, P., MEIBURG, E. & MAXWORTHY, T. 2003 Three-dimensional vortex breakdown in swirling jets and wakes: direct numerical simulation. *J. Fluid Mech.* **486**, 331–378.

SAGAUT, P. 2002 *Large Eddy Simulation for incompressible flows*, 2nd edn. Springer.

SAGAUT, P., GARNIER, E., TROMEUR, E., LARCHEVÊQUE, L. & LABOURASSE, E. 2004 Turbulent inflow conditions for large eddy simulation of compressible wall-bounded flows. *AIAA J.* **42** (3), 469–477.

SANKARAN, V. & MENON, S. 2002 LES of spray combustion in swirling flows. *Journal of Turbulence* **3**.

SARPKAYA, T. 1971 On stationary and travelling vortex breakdowns. *J. Fluid Mech.* **45**, 545–559.

SARPKAYA, T. 1995 Turbulent vortex breakdown. *Phys. Fluids* **7** (10), 2301–2303.

SCHLICHTING, H. & GERSTEN, K. 1996 *Grenzschicht–Theorie*, 9th edn. Springer.

SCHLÜTER, J. 2000 Large eddy simulations of flow and mixing in jets and swirl flows: Application to a gas turbine. PhD thesis, Institut National Polytechnique de Toulouse.

SCHLÜTER, J., PITSCH, H. & MOIN, P. 2004 Large eddy simulation inflow conditions for coupling with Reynolds-averaged flow solvers. *AIAA J.* **42** (3), 478–484.

SCHNEIDER, C., DREIZLER, A. & JANICKA, J. 2005 Fluid dynamical analysis of atmospheric reacting and isothermal swirling flows. *Flow, Turbulence and Combustion* **74**, 103–127.

DA SILVA, C., BALARAC, G. & MÉTAIS, O. 2003 Transition in high velocity ratio coaxial jets analysed from direct numerical simulations. *Journal of Turbulence* **4**.

SMAGORINSKY, J. 1963 General circulation experiments with the primitive equations, Part I: The basic experiment. *Monthly Weather Review* **91**, 99–152.

SOMMERFELD, M. & QIU, H. 1991 Detailed measurement in a swirling particulate two-phase flow by a phase-doppler anemometer. *Int. J. Heat and Fluid Flow* **12** (1), 20–28.

STANLEY, S., SARKAR, S. & MELLADO, J. 2002 A study of the flow-field evolution and mixing in a planar turbulent jet using direct numerical simulation. *J. Fluids Mech.* **450**, 377–407.

STOESSER, T., FRÖHLICH, J. & RODI, W. 2003 Identification of coherent flow structures in open channel flow over rough bed using large eddy simulation. In *Proc. XXX IAHR Congress, Thessaloniki, Greece*.

STONE, H. 1968 Iterative solution of implicit approximations of multidimensional partial differential equations for finite difference methods. *SIAM J. Numer. Anal.* **5**, 530–558.

SYRED, N. & BEÉR, J. 1974 Combustion in swirling flows. *Combustion and Flame* **23**, 143–201.

SYRED, N., FICK, W., O'DOHERTY, T. & GRIFFITHS, A. 1997 The effect of the precessing vortex core on combustion in a swirl burner. *Combustion Science and Technology* **125**, 139–157.

SYRED, N., O'DOHERTY, T. & FROUD, D. 1994 The interaction of the precessing vortex core and reverse flow zone in the exhaust of a swirl burner. *Proc. Instn Mech Engrs* **208**, 27–36.

TANG, G., YANG, Z. & MCGUIRK, J. 2002 Large eddy simulation of isothermal confined swirling flow with recirculation. In *Engineering Turbulence Modelling and Experiments 5* (ed. W. Rodi & N. Fueyo). Elsevier.

TANG, S. & KO, N. 1994 Experimental investigation of the structure interaction in an excited coaxial jet. *Experimental Thermal and Fluid Science* **8**, 214–229.

TENNEKES, H. & LUMLEY, J. 1972 *A first course on turbulence*. MIT Press.

THEOFILIS, V. 2003 Advances in global linear instability analysis of nonparallel and three-dimensional flows. *Prog. Aerospace Sciences* **39**, 249–315.

WANG, P., BAI, X., WESSMAN, M. & KLINGMANN, J. 2004 Large eddy simulation and experimental studies of a confined turbulent swirling flow. *Phys. Fluids* **16** (9), 3306–3324.

WANG, S., HSIEH, S.-Y. & YANG, V. 2005 Unsteady flow evolution in swirl injector with radial entry. I. Stationary conditions. *Phys. Fluids* **17**, 045107.

WEGNER, B., JANUS, B., SADIKI, A., DREIZLER, A. & JANICKA, J. 2005 Study of flow and mixing in a generic GT combustor using LES. In *Engineering Turbulence Modelling and Experiments 6* (ed. W. Rodi & M. Mulas), pp. 731–740. Elsevier.

WEGNER, B., KEMPF, A., SCHNEIDER, C., SADIKI, A., DREIZLER, A., JANICKA, J. & SCHÄFER, M. 2004*a* Large eddy simulation of combustion processes under gas turbine conditions. *Prog. Computational Fluid Dynamics* **4**, 257–263.

WEGNER, B., MALTSEV, A., SCHNEIDER, C., SADIKI, A., DREIZLER, A. & JANICKA, J. 2004*b* Assesment of unsteady RANS in predicting swirl flow instability based on LES and experiments. *Int. J. Heat and Fluid Flow* **25**, 528–536.

WERNER, H. & WENGLE, H. 1993 Large-eddy simulation of turbulent flow over and around a cube in a plate channel. In *8th Symp. on Turb. Shear Flows*.

WICKER, R. & EATON, J. 1994 Near field of a coaxial jet with and without axial excitation. *AIAA J.* **32** (3), 542–546.

WILCOX, D. C. 2002 *Turbulence modelling for CFD*, 2nd edn. DCW Industries.

WILLE, M. 1997 Large eddy simulation of jets in cross flows. PhD thesis, Imperial College London.

WISSINK, J. G. 2003 DNS of separating, low Reynolds number flow in a turbine cascade with incoming wakes. *Int. J. Heat and Fluid Flow* **24**, 626–635.

WISSINK, J. G. & RODI, W. 2006 DNS of flow and heat transfer in a turbine cascade with incoming wakes. *submitted to J. Fluid Mech.* .

YAZDABADI, P., GRIFFITHS, A. & SYRED, N. 1994 Characterization of the PVC phenomena in the exhaust of a cyclone dust separator. *Exp. in Fluids* **17**, 84–95.

List of Tables

3.1 Overview of the simulations for the Hillemanns burner. Parameters are explained in the text. H2-H6 have an excess of swirl compared to the experimental flow conditions for historical reasons as discussed in the text. 32

4.1 Overview of the simulations to assess the inflow conditions. 75

5.1 Overview of the simulations performed to investigate the impact of the swirl number 84
5.2 Variation of characteristic quantities with the swirl parameter 86

6.1 Overview of the simulations performed to investigate the influence of pulsating inflow 102

7.1 Overview of the simulations performed to investigate the influence of an inner jet (IJ). 119

8.1 Overview of the simulations performed to investigate the influence of the retraction of the pilot jet. 128

9.1 Number, separation in time and time span of fields recorded to perform conditional averages. 142

List of Figures

1.1 Swirl burner used in the experiments of Bender & Büchner (2005). 6

3.1 Sketch of the burner taken from Hillemanns (1988) 28

3.2 Geometry of the computational domain and boundary conditions applied. 29

3.3 Development of the flow in the inlet duct region. a) Instantaneous axial velocity. b) Instantaneous fluctuating kinetic energy. 30

3.4 Computational grid. a) Axial plane, zoom near the jet exit. Every 4th grid line is shown. b) Cut in the $y-z$ plane through the entire domain with all grid lines being shown. c) same as b) but zoomed around the symmetry axis. d) strong zoom around the axis. 31

3.5 Average streamlines in an axial plane obtained from the simulation. 33

3.6 Vector plots in an axial plane. a) Average flow. b) Instantaneous flow. (Values are interpolated to a cartesian grid) 35

3.7 Influence of the grid. Radial profiles of mean velocity components at $x/R = 0.2$ and 2.0 (top to bottom as indicated in the rightmost column). Solid line, H3; dashed line, H2; symbols, experimental data from Büchner & Petsch (2004). Left, axial velocity, $\langle u_x \rangle / U_b$. Centre, tangential velocity, $\langle u_\theta \rangle / U_b$. Right, radial velocity, $\langle u_r \rangle / U_b$. Observe that the ranges of the vertical axis have been adjusted individually. 36

3.8 Influence of the grid. Radial profiles of rms velocity fluctuations at $x/R = 0.2$ and 2.0 (top to bottom as indicated in the rightmost column). Solid line, H3; dashed line, H2; symbols, experimental data from Büchner & Petsch (2004). Left, axial velocity, $\langle u_x^{rms} \rangle / U_b$. Centre, tangential velocity, $\langle u_\theta^{rms} \rangle / U_b$. Right, radial velocity, $\langle u_r^{rms} \rangle / U_b$. 37

3.9 Influence of the SGS model. Radial profiles of mean velocity components at $x/R = 0.2$ and 2.0 (top to bottom as indicated in the rightmost column). Solid line, H2; dashed line, H4; symbols, experimental data from Büchner & Petsch (2004). Left, axial velocity, $\langle u_x \rangle / U_b$. Centre, tangential velocity, $\langle u_\theta \rangle / U_b$. Right, radial velocity, $\langle u_r \rangle / U_b$. Observe that the ranges of the vertical axis have been adjusted individually. 38

3.10 Influence of the SGS model. Radial profiles of rms velocity fluctuations at $x/R = 0.2$ and 2.0 (top to bottom as indicated in the rightmost column). Solid line, H2; dashed line, H4; symbols, experimental data from Büchner & Petsch (2004). Left, axial velocity, $\langle u_x^{rms} \rangle / U_b$. Centre, tangential velocity, $\langle u_\theta^{rms} \rangle / U_b$. Right, radial velocity, $\langle u_r^{rms} \rangle / U_b$. 39

3.11 Radial profiles of eddy viscosity, ν_t/ν. $a)$ $x/R = 0.2$. $b)$ $x/R = 2.0$. Solid line, H3 with dynamic model on fine grid; dashed line, H4 with Smagorinsky model on coarse grid; dotted line, H2 with dynamic model on coarse grid. 40

3.12 Influence of the co-flow. Radial profiles of mean velocity components at $x/R = 0.2$ and 2.0 (top to bottom as indicated in the rightmost column). Solid line, Sim H4; dashed line, Sim H5; dotted line, Sim H6; symbols, experimental data from Büchner & Petsch (2004). Left, axial velocity, $\langle u_x \rangle / U_b$. Centre, tangential velocity, $\langle u_\theta \rangle / U_b$. Right, radial velocity, $\langle u_r \rangle / U_b$. Observe that the ranges of the vertical axis have been adjusted individually. 41

3.13 Influence of the co-flow. Radial profiles of rms velocity fluctuations at $x/R = 0.2$ and 2.0 (top to bottom as indicated in the rightmost column). Solid line, Sim H4; dashed line, Sim H5; dotted line, Sim H6; symbols, experimental data from Büchner & Petsch (2004). Left, axial velocity, $\langle u_x^{rms} \rangle / U_b$. Centre, tangential velocity, $\langle u_\theta^{rms} \rangle / U_b$. Right, radial velocity, $\langle u_r^{rms} \rangle / U_b$. 42

3.14 Radial profiles of mean velocity components at $x/R = 0.2, 1.0, 2.0$ and 3.0 (top to bottom as indicated in the rightmost column). Solid line, H1; open symbols, experimental data from Büchner & Petsch (2004); closed symbols, experimental data from Hillemanns (1988). Left, axial velocity, $\langle u_x \rangle / U_b$. Centre, tangential velocity, $\langle u_\theta \rangle / U_b$. Right, radial velocity, $\langle u_r \rangle / U_b$. To enhance readability the range of the vertical axis has been adjusted individually. 45

3.15 Radial distribution of the terms in the continuity equation for the averaged flow eqn. (3.2) at $x = 2R$. Solid line $q_1 = -r\partial\langle u_x \rangle \partial x$ estimated from the experiment. Dashed line q_1 from the simulation. Symbols $q_2 = \partial(r\langle u_r \rangle)\partial r$ estimated from the experiment. 46

3.16 Radial profiles of rms velocity fluctuations at $x/R = 0.2, 1.0, 2.0$ and 3.0 (top to bottom as indicated in the rightmost column). Solid line, H1; open symbols, experimental data from Büchner & Petsch (2004); closed symbols, experimental data from Hillemanns (1988). Left, axial component, u_x^{rms}/U_b. Centre, tangential component, u_θ^{rms}/U_b. Right, radial component, u_r^{rms}/U_b. 48

3.17 Isosurface of instantaneous pressure fluctuations, $p - \langle p \rangle = -0.3$. a) Original field computed in H1. b) Filtered field employed for visualization. 49

3.18 Isosurface of instantaneous pressure fluctuations (smoothed), $p - \langle p \rangle = -0.3$ from H1 at three instants in time. The colour is given by: $(\partial\langle u_x \rangle / \partial r) > 0$, dark; $(\partial\langle u_x \rangle / \partial r) < 0$, bright. Swirl is clockwise when looking upstream in axial direction. 50

3.19 Mean axial velocity $\langle u_x \rangle / U_b$ at $x/R = 0.2$. Dashed line, original simulation H1. Solid line, simulation with a lower level of swirl, $S = 0.85$. The arrows indicate the approximate width of the inner and outer shear layers for both simulations. The patches show the resulting radial separation between the inner and the outer shear layer. Light patch, original simulation H1. Dark patch, simulation with lower swirl. 52

3.20 Coherent structures from a simulation with a lower level of swirl, $S = 0.85$ at $x/R = -2$, visualized by instantaneous pressure fluctuations (unsmoothed), coloured as in Fig. 3.18. a) Side view. b) View from downstream. 52

3.21 $a - c$) Contour plots in a transverse plane at $x/R = 0.2$ and the same instant in time. The straight arrows point at the dominant PVC observed at this instant. The curved arrows indicate the sense of rotation. a) Instantaneous axial velocity fluctuations. b) Instantaneous pressure fluctuations. c) Instantaneous axial velocity component. The white line is a pressure fluctuation contour $p - \langle p \rangle = -0.7$ extracted from the data shown in b). The black line is the boundary of the recirculation zone $u_x = 0$. d) Idealized sketch of the PVC motion in the transverse plane. 54

3.22 Time signal at $x/R = 0.1$, $r/R = 0.6$. a) Axial velocity. b) Pressure. 55

3.23 Temporal cross-correlation of axial velocity and pressure fluctuations $\langle u_x''(t) p''(t + \Delta t) \rangle$ at $x/R = 0.1$, $r/R = 0.6$. 55

3.24 Coherent structures of the instantaneous flow as in Fig. 3.18 but the level of the iso-surface is $p - \langle p \rangle = -0.5$. Only the inner region $r < R$ is shown. The black lines represent stream ribbons of the averaged flow issued at different positions in the inner region of the jet around $r/R \sim 0.5$. 56

3.25 Spatial two-point autocorrelation as a function of angular separation at $x/R = 0.1$, $r/R = 0.6$. R11, axial velocity. R22, radial velocity. R33, tangential velocity. . . 58

3.26 Coherent structures of the instantaneous flow as in Fig. 3.18. The black lines represent stream ribbons of the averaged flow issued at $x/R = 0$, $r/R = 0.95$ and four angular positions with an angular distance of $\Delta\varphi = 90^o$. 59

3.27 Unsmoothed iso-surface of pressure fluctuations $p'' = -0.3$. It has been coloured according to the radial coordinate to highlight secondary structures in streamwise direction which are located at the outer boundary of the outer spiraling vortices. . 60

3.28 Power spectral density of axial velocity fluctuations at $x/R = 0.1$, $r/R = 0.6$. The straight line has a slope of $-5/3$. 61

3.29 Power spectral density of velocity fluctuations at $x/R = 0.1$, $r/R = 0.6$ in the experiment. At $x/R = 0.1$, $r/R = 0.605$ in H1. $a) - c)$ Simulation $d) - f)$ Experiment Büchner & Petsch (2004). $a)$ and $d)$ Axial velocity fluctuations. $b)$ and $e)$ Radial velocity fluctuations. $c)$ and $f)$ Azimuthal velocity fluctuations. . . 63

3.30 Power spectral density of velocity fluctuations at $x/R = 0.1$, $r/R = 0$. $a) - b)$ Simulation $c) - d)$ Experiment Büchner & Petsch (2004). $a)$ and $c)$ Axial velocity. $b)$ and $d)$ Radial velocity. (Note that all directions orthogonal to the centreline are statistically equivalent. Therefore only two spectra are shown in this figure.) . . . 64

3.31 PSD of velocity fluctuations at $x/R = 0.1$, $r/R = 0.594$. $a)$ Axial velocity fluctuations. Compare to Fig. 3.29a, d. $b)$ Tangential velocity fluctuations. Compare to Fig. 3.29c, f. 65

3.32 Value of the power spectrum at the fundamental frequency f_{peak} as a function of r/R. $a)$ $x/R = 0.1$, $b)$ $x/R = 0.4$ 65

3.33 Power spectral density of radial velocity fluctuations. Outer shear layer, solid line $x/R = 1.0$, $r/R = 1.2$. Inner shear layer, dashed line $x/R = 0.1$, $r/R = 0.6$. . . 67

4.1 Generation of inflow data. 70

4.2 Description of the three approaches for the specification of inflow conditions considered in the present chapter . The contour plots show the mean axial velocity component. 74

4.3 Radial profiles of mean velocity obtained with different inflow conditions. Left, axial velocity component. Right, tangential velocity component. $a)$ $x/R = 0.2$ $b)$ $x/R = 1$ $c)$ $x/R = 3$. H1, solid. H7, dashed. H8, dotted. 78

4.4 Radial profiles of RMS velocity obtained with different inflow conditions. Left, axial velocity component. Right, tangential velocity component. $a)$ $x/R = 0.2$ $b)$ $x/R = 1$ $c)$ $x/R = 3$. H1, solid. H7, dashed. H8, dotted. 79

4.5 Results with different inflow conditions. Left, iso-surfaces of pressure fluctuations. Right, PSD of axial velocity fluctuations at $x/R = 0.1$, $r/R = 0.6$. $a)$ H1. $b)$ H7. $c)$ H8. 80

5.1 Mean velocity deduced from the fluctuating inflow conditions imposed at $x/R = -2$ for different levels of swirl. The line styles are defined in Table 5.1. $a)$ Mean axial velocity. $b)$ Mean tangential velocity. 85

5.2 Streamlines of the average flow, solid lines. $\langle u_x \rangle = 0$, dashed line. $a)$ $S = 0$. $b)$ $S = 0.4$. $c)$ $S = 0.55$. $d)$ $S = 0.7$. $e)$ $S = 0.85$. $f)$ $S = 1$. $g)$ $S = 1.2$. 87

5.3 Streamlines of the average flow, solid lines. $\langle u_x \rangle = 0$, dashed line. Zoom close to the jet exit. $a)$ $S = 0.4$. $b)$ $S = 0.55$. 88

5.4 α, angle of the average flow with respect to the $x-$axis as detailed in the text. $a)$ $S = 0.4$. $b)$ $S = 0.55$. $c)$ $S = 0.7$. $d)$ $S = 0.85$. $e)$ $S = 1$. $f)$ $S = 1.2$. 89

5.5 Fluctuating kinetic energy. $a)$ $S = 0$. $b)$ $S = 0.4$. $c)$ $S = 0.55$. $d)$ $S = 0.7$. $e)$ $S = 0.85$. $f)$ $S = 1$. $g)$ $S = 1.2$. 90

5.6 Fluctuating kinetic energy. $a)$ S=0.85 $b)$ S=1 $c)$ S=1.2 91

5.7 Radial profiles of mean velocity for different swirl numbers. Left, axial velocity component. Right, tangential velocity component. $a)$ $x/R = 0.2$. $b)$ $x/R = 3$. $c)$ $x/R = 6$. To enhance readability the range of both axes has been adjusted individually. The line styles are defined in Table 5.1 93
5.8 Radial profiles of RMS velocity for different swirl numbers. Left, axial velocity component. Right, tangential velocity component. $a)$ $x/R = 0.2$. $b)$ $x/R = 3$. $c)$ $x/R = 6$. To enhance readability the range of both axes has been adjusted individually for each position. The line styles are defined in Table 5.1 94
5.9 Isosurfaces of pressure fluctuations $p'' = -0.3$. $a)$ S=0.4 $b)$ S=0.55 $c)$ S=0.7 $d)$ S=0.85 $e)$ S=1 $f)$ S=1.2 (f) 96
5.10 PSD of axial velocity fluctuations at $x/R = 0.1$, $r/R = 0.7$ for different swirl numbers. Arbitrary units are used in the vertical axis and the curves have been shifted vertically for readability. $a)$ Diagram with logarithmic axes. $b)$ The same diagram with linear axes. The line styles are defined in Table 5.1. 98
5.11 Radial profiles of the mean tangential velocity at $x/R = 0.2$ for the cases $S = 0.7$, 1 and 1.2. Symbols identify the middle of the shear layer as detailed in the text. . 99

6.1 Phase-averaged velocity at the inflow plane $x/R = -2$ at $r/R = 0.75$, i.e. in the middle of the annular duct, as a function of time over one period. $a)$ Axial component $\widetilde{u_x}/U_b$ and phases discussed below. $b)$ Tangential component $\widetilde{u_\theta}/U_b$. H16: circles. H17: squares. 103
6.2 Radial profiles of axial velocity u_x/U_b at $x/R = 0.1$ (left) and $x/R = 1$ (right). $a-b)$ Time-averaged velocity in H7. $c-d)$ Phase-averaged velocity in H16. $e-f)$ Phase-averaged velocity in H17. Phases as indicated in Fig.6.1. $\psi = 0$ ——. $\psi = 0.25$ —·—. $\psi = 0.5$ ·····. $\psi = 0.75$ – – –. 105
6.3 Profiles of tangential velocity u_θ/U_b at $x/R = 0.1$ (left) and $x/R = 1$ (right). $a-b)$ Time-averaged velocity in H7. $c-d)$ Phase-averaged velocity in H16. $e-f)$ Phase-averaged velocity in H17 Phases as indicated in Fig.6.1. $\psi = 0$ ——. $\psi = 0.25$ —·—. $\psi = 0.5$ ·····. $\psi = 0.75$ – – –. 106
6.4 Profiles of average radial velocity u_r/U_b at $x/R = 0.1$ (left) and $x/R = 1$ (right). $a-b)$ Time-averaged velocity in H7. $c-d)$ Phase-averaged velocity in H16. $e-f)$ Phase-averaged velocity in H17 Phases as indicated in Fig.6.1. $\psi = 0$ ——. $\psi = 0.25$ —·—. $\psi = 0.5$ ·····. $\psi = 0.75$ – – –. 108
6.5 Phased-averaged tangential vorticity $\widetilde{\omega_\theta}$ in a plane $\theta = const.$ 109
6.6 Turbulent kinetic energy k/U_b^2 in a plane $\theta = const.$ Top : H7 without pulsation. Left: Four phases from H16, Right: the same phases from H17. 110
6.7 Instantaneous coherent structures at $\psi = 0.25$ (arbitrary instant for H7). $a-c)$ Iso-surface of pressure fluctuations $p'' = -0.3$, $d-e)$ Iso-surface of pressure $p = -0.5$ for the same data sets. The color is determined by the sign of the radial gradient of the phase-averaged axial velocity (in H7 the time-average). 112

6.8 PSD of velocity fluctuations. a) PSD of axial velocity fluctuations at $x/R = 0.1$, $r/R = 0.6$. b) PSD of radial velocity fluctuations at $x/R = 0.9$, $r/R = 1.2$. Solid line: H7, circles: H16, squares: H17. Arbitrary units are used in the vertical axis. 113

7.1 Sketch of the new burner in configuration with tangential swirl generation (from Bender & Büchner (2005)) 116
7.2 Inflow conditions and geometry for the computations assembled in Table 7.1. Development of the fluctuating kinetic energy in the inlet duct for Sim NB3. Only the lower levels of k are considered as discussed in the text. 118
7.3 Influence of the pilot jet on the mean flow. Column 1: Streamlines of the average flow, solid lines. $\langle u_x \rangle = 0$, dashed line. Column 2: Fluctuating kinetic energy. (a) NB1. (b) NB2. (c) NB3. 120
7.4 Radial profiles of mean velocity and corresponding turbulent intensities. (a) $x/R = 0.1$. (b) $x/R = 1$. (c) $x/R = 3$. Row 1: Mean axial velocity. Row 2: Mean tangential velocity. Row 3: RMS axial velocity. Row 4: RMS tangential velocity. The line styles are defined in Table 7.1. Symbols represent experimental data of Bender & Büchner (2005). To enhance readability the range of the vertical axis has been adjusted individually. 122
7.5 Instantaneous coherent structures visualized using an iso-surface of the filtered instantaneous pressure deviation $p' = p - \langle p \rangle = -0.2$. (a) NB1. (a) NB2. (a) NB3. Colour is given by the sign of the radial gradient of the mean axial velocity. 124
7.6 PSD of radial velocity fluctuations at $x/R = 0.4$. (a) Location on the symmetry axis, $r/R = 0$. (b) Location in the inner shear layer, $r/R = 0.6$. Line styles are defined in Table 7.1. 125

8.1 Numerical setup and boundary conditions. Gray scale represents mean axial velocity $a)$ $x_{pilot} = 0$. $b)$ $x_{pilot} = -0.73R$. 128
8.2 Comparison of velocity profiles from simulations NB3 and NB4 at $x/R = 0.1$. Dashed line, NB3. Solid line, NB4. Symbols, experiment. $a)$ Mean axial velocity. $b)$ Mean tangential velocity. $c)$ RMS axial velocity. $d)$ RMS tangential velocity. . 129
8.3 Streamlines of the average flow in an axial plane $a)$ $x_{pilot} = 0$, NB4 $b)$ $x_{pilot} = -0.73R$, NB5. The dashed line indicate the location where $\langle u_x \rangle = 0$. 130
8.4 Radial profiles of mean velocity for $x_{pilot} = 0$, NB4 $a)$ Axial velocity $b)$ Tangential velocity 131
8.5 Radial profiles of mean velocity for $x_{pilot} = -0.73R$, NB5 $a)$ Axial velocity $b)$ Tangential velocity 132
8.6 Radial profiles of RMS velocity for $x_{pilot} = 0$, NB4. $a)$ Axial velocity $b)$ Tangential velocity 132
8.7 Radial profiles of RMS velocity for $x_{pilot} = -0.73R$, NB5. $a)$ Axial velocity $b)$ Tangential velocity 133
8.8 Fluctuating kinetic energy $a)$ $x_{pilot}/R = 0$ $b)$ $x_{pilot} = -0.73R$. 134

8.9 Coherent structures visualized using an iso-surface of pressure fluctuations. Left, $x_{pilot}/R = 0$. Right, $x_{pilot}/R = -0.73R$. $a, b, d)$ $p - \langle p \rangle = -0.3$. $c)$ $p - \langle p \rangle = -0.15$. Grey scale as explained in the text. 135
8.10 Instantaneous axial velocity in the region close to the jet exit. The black line is the boundary of the instantaneous recirculation zone $u_x = 0$. $a)$ NB4, $x_{pilot} = 0$. $b)$ NB5, $x_{pilot} = -0.73R$. 136
8.11 Time signals of axial velocity at $r/R = 0.73$, $x/R = 0.1$ recorded during the simulations. $a)$ $x_{pilot} = 0$. $b)$ $x_{pilot} = -0.73R$. 137
8.12 $a)$ Power spectrum of axial velocity fluctuations at $x/R = 0.1$, $r/R = 0.73$ from computations NB4 and NB5. $b)$ the same data for $x_{pilot} = -0.73R$ from the experiment. 138
8.13 Amplitude of the power spectrum at the fundamental frequency f_{peak} at $x/R = 0.1$ as a function of the radial position for $x_{pilot} = -0.73R$. $a)$ experiment. $b)$ NB5. 139

9.1 Illustration of the conditional averaging procedure. Color according to $p - \langle p \rangle$ from H1. The black circle indicates the points where the minimum of the pressure is looked for. 143
9.2 Coherent structures obtained using the conditional average flow field. Top, H1. Bottom, NB5. $a, c)$ $p^c - \langle p \rangle = -0.1$. $b)$ $p^c - \langle p \rangle = -0.2$. $d)$ $p^c - \langle p \rangle = -0.3$. 144
9.3 Two-dimensional cuts of the conditional average flow from NB5. Thick solid line, $u_x^c = 0$. Left, cut through the plane $y/R = 0$. Right, cut through the plane $x/R = 0.1$. Top, Color is given by p^c. Bottom, streamlines calculated using $c)$ u_x^c and u_r^c, $d)$ u_r^c and u_θ^c. 146
9.4 Two-dimensional cuts of the conditional average flow from H1. Thick solid line, $u_x^c = 0$. Left, cut through the plane $y/R = 0$. Right, cut through the plane $x/R = 0.1$. Top, Color is given by p^c. Bottom, streamlines calculated using $c)$ u_x^c and u_r^c, $d)$ u_r^c and u_θ^c. 147
9.5 Profiles and contours at $x/R = 0.1$ from NB5. Top, pressure. Middle, axial velocity. Bottom, tangential velocity. 149
9.6 Profiles and contours at $x/R = 1$ from NB5. Top, pressure. Middle, axial velocity. Bottom, tangential velocity. 150
9.7 Profiles from H1. Top, pressure. Middle, axial velocity. Bottom, tangential velocity. Left, $x/R = 0.1$. Right, $x/R = 1$. 151
9.8 Two-dimensional cut through the plane $x/R = 0.1$ of the conditional average flow. Top, NB5. Bottom, H1. Thick solid line, $u_x^c = 0$. Left, Color is given by $p^c - \langle p \rangle$. Right, streamlines calculated using $u_r^c - \langle u_r \rangle$ and $u_\theta^c - \langle u_\theta \rangle$. 153